

## ABSTRACT

Title of dissertation: THE FLUID DYNAMICS OF  
MAYFLY NAIADS

Khaled Abdelaziz, Doctor of Philosophy, 2014

Dissertation directed by: Professor Kenneth Kiger  
The Mechanical Engineering Department

During their aquatic phase, mayflies *Centroptilum triangulifer* use a series of tracheal gills to facilitate gas exchange. Recent experimental studies on nymphal mayflies have identified two coupled features associated with the ontogenic progression of their ventilatory kinematics: 1) there is an abrupt shift from a rowing mechanism in small instars to a flapping mechanism in larger instars, and 2) the flapping mechanism is associated with the development of a flexural hinge that permits the passive movement of a distal flap. The primary role of the tracheal gills is tied to ventilation rather than locomotion. As such, it is not yet understood why such a transition happens and which performance metric is improved, if any. Hence, the goal of the current research is to investigate both features using numerical simulations.

First, a computational model of the mayfly is built from a dissected animal. Then, a 3-level prescribed kinematic chain is introduced to a previously in-house developed and in-house validated explicit parallel Navier-Stokes solver where both the advective and diffusive terms are advanced explicitly using a third-order, low-storage, Runge-Kutta scheme. Finally, an immersed boundary method based on a

moving least squares reconstruction is implemented to enforce the correct moving boundary conditions.

Two different parametric spaces are constructed. The first one investigates the transition from rowing to flapping kinematics, the morphological effects on the flow field and on the proposed performance parameters while the second aims to provide an explanation for the hinge development.

Two metrics based on control volume analysis are proposed to quantify the performance of each numerical case. The first metric is simply the mechanical efficiency of the energy transfer from the moving gills to the surrounding flow field while the second incorporates the mass flow rate across the control surface. The second metric is promising because it is able to provide a plausible explanation of both features by showing that the rate of work done by the mayfly is diminished throughout ontogeny with respect to the induced mass flow rate.

THE FLUID DYNAMICS OF  
MAYFLY NAIADS

by

Khaled Abdelaziz

Dissertation submitted to the Faculty of the Graduate School of the  
University of Maryland, College Park in partial fulfillment  
of the requirements for the degree of  
Doctor of Philosophy  
2014

Advisory Committee:  
Professor Kenneth Kiger, Chair  
Professor Elias Balaras  
Professor Peter Bernard  
Professor James Duncan  
Professor Jeffrey Shultz, Dean's Representative

© Copyright by  
Khaled Abdelaziz  
2014

## Dedication

To GOD, the Watchful.

To Mankind, in peace.

To my deceased father, from whom I learned my first key strokes.

To my mother, for going beyond limits in raising her children.

To my brother, for his support from the moment I stepped foot in JFK.

To my sister, for her continuous encouragement.

To Mariam and Jannah, my adorable nieces.

To Ryaan, my nephew and the newest family member.

## Acknowledgments

I would like to express my sincere appreciation to my advisors, Professor Elias Balaras and Professor Kenneth Kiger, for their continuous support during the course of my graduate studies at the University of Maryland. Professor Balaras provided me with invaluable scientific expertise and gave me the chance to work with his CFD team and with state-of-the-art computational resources. My deepest gratitude to Professor Kenneth Kiger for his never-ending motivation, insight, inspiration, constructive feedback, and for effectively and enthusiastically teaching me courses in viscous flows and experimental techniques.

I take this opportunity to express my gratitude to Professors James Duncan, Peter Bernard and Jeffrey Shultz for agreeing to serve on my PhD dissertation committee and for providing helpful feedback on my research proposal. Professors James Duncan and Peter Bernard have also inspired me throughout many fluid mechanics courses. I also wish to acknowledge the help provided by Professor Jeffrey Shultz for supplying the high-resolution images and segments of the mayfly naiad.

I would like to thank my lab mates Marcos Vanella and Nikolaos Beratlis, for their help and support at the beginning of my graduate studies and for providing me with useful numerical codes. I also thank my fellow lab mates Grigorios Panagakos, Don Daniel, and Clarence Baney for their helpful discussions and moral support.

Last but not least, I would like to acknowledge the technical and prompt help of Melvin Fields our IT coordinator. I also thank Dylan Hazelwood and Dan Wysling for their IT support.

## Table of Contents

List of Tables	vi
List of Figures	vii
List of Abbreviations	ix
1 Introduction	1
1.1 What is a Mayfly?	1
1.2 Motivation	3
1.3 Objectives	5
1.4 Literature Review and Prior Work	5
1.4.1 Rowing and Flapping	7
1.4.2 The Metachronal Wave	14
1.4.3 Advances in Mayfly Larvae	18
1.5 Research Outline	20
2 Mathematical Modeling	21
2.1 Surface Modeling of the Mayfly Nymph	21
2.2 The Prescribed Kinematics	28
2.2.1 The Kinematic Chain	29
2.2.2 The Flapping Kinematics	41
2.2.3 The Rowing Kinematics	42
2.3 Governing Equations	47
2.4 Performance Metrics	50
2.4.1 Mechanical Efficiency	51
2.4.2 Specific Mass Flow Rate	52
3 Numerical Methodologies and Validation	54
3.1 Spatial and Temporal Discretization	54
3.2 Treatment of Immersed Boundaries	57
3.2.1 MLS Reconstruction	59
3.2.2 Evaluation of Surface Forces	62
3.3 Computational Setup	64

3.4	Comparison with Experiments . . . . .	66
3.4.1	Comparison with <i>in-vivo</i> Experiments . . . . .	67
3.4.2	Comparison with Robotic Experiments . . . . .	80
3.5	Parametric Spaces . . . . .	85
4	Results I: The Rowing-Flapping Transition . . . . .	88
4.1	Introduction . . . . .	88
4.2	General Description of the Time-averaged Flow Fields . . . . .	89
4.3	Dynamics of Rowing and Flapping . . . . .	92
4.3.1	Flapping Dynamics at $Re_\omega = 21.6$ . . . . .	93
4.3.2	Rowing Dynamics at $Re_\omega = 21.6$ . . . . .	101
4.4	Viscous and Inertial Effects . . . . .	104
4.5	Planform Morphology . . . . .	115
4.6	Micro-pumping and Performance Metrics . . . . .	122
4.6.1	Mechanical Efficiency . . . . .	125
4.6.2	Specific Mass Flow Rate . . . . .	132
5	Results II: Flexibility and the Role of the Hinge . . . . .	150
5.1	Introduction . . . . .	150
5.2	Qualitative Investigation . . . . .	152
5.3	Quantitative Assessment . . . . .	159
5.4	Last Remarks . . . . .	167
6	Conclusions and Future Work Suggestions . . . . .	170
A	Published Article: Experiments in Fluids . . . . .	175
	Bibliography . . . . .	188

## List of Tables

3.1	Parametric space used to explore the rowing-flapping transition . . .	86
4.1	Mass flow rates for flapping at $Re_\omega = 21.6$ and rowing at $Re_\omega = 2.3$ .	91
4.2	Normalized specific mass flow rate for control volume 2 . . . . .	138

## List of Figures

1.1	Two different phases of mayfly <i>C. triangulifer</i> . . . . .	2
1.2	Typical motion of cilium. Photomicrograph of a live copepod . . . . .	15
2.1	High-resolution raster images of <i>C. triangulifer</i> and cross sections . . . . .	23
2.2	Computational model of <i>C. triangulifer</i> . . . . .	24
2.3	Gill morphology . . . . .	25
2.4	Illustration of the kinematic chain . . . . .	31
2.5	Illustration of the forward transformation between levels 1 and 2 . . . . .	35
2.6	Schematic of position vectors in different levels . . . . .	38
2.7	Prescribed mayfly flapping kinematics for gill 4 . . . . .	43
2.8	Eulerian angles for mayfly flapping kinematics . . . . .	44
2.9	Prescribed mayfly rowing kinematics for gill 4 . . . . .	45
2.10	Eulerian angles for mayfly rowing kinematics . . . . .	46
2.11	Schematic of control volume . . . . .	50
3.1	Schematic of computational Domain . . . . .	66
3.2	Comparison of the velocity magnitude for flapping at $Re_\omega = 21.6$ . . . . .	69
3.3	Comparison of $u$ for flapping at $Re_\omega = 21.6$ . . . . .	71
3.4	Comparison of $v$ for flapping at $Re_\omega = 21.6$ . . . . .	72
3.5	Comparison of $\omega_z$ for flapping at $Re_\omega = 21.6$ and $t/\tau = 0.102$ . . . . .	74
3.6	Comparison of $\omega_z$ for flapping at $Re_\omega = 21.6$ and $t/\tau = 0.326$ . . . . .	75
3.7	Comparison of the velocity magnitude for rowing at $Re_\omega = 2.3$ . . . . .	79
3.8	Comparison of the instantaneous fields for rowing at $Re_\omega = 2.3$ . . . . .	81
3.9	Illustration of computational setup and slice at $z/L = 1.3$ . . . . .	82
3.10	Comparison with robotic experiments for rowing at $Re_\omega = 17.6$ . . . . .	84
4.1	Time-averaged flow fields for rowing and flapping . . . . .	90
4.2	Instantaneous flapping dynamics at $Re_\omega = 21.6$ . . . . .	95
4.3	Flapping dynamics at $Re_\omega = 21.6$ and $t/\tau = 0.65$ . . . . .	97
4.4	Pathlines for flapping kinematics at $Re_\omega = 21.6$ . . . . .	100
4.5	Instantaneous rowing dynamics at $Re_\omega = 21.6$ . . . . .	102
4.6	Effect of $Re_\omega$ on $\omega_z$ for flapping kinematics . . . . .	107
4.7	Effect of $Re_\omega$ on $\omega_z$ for rowing kinematics . . . . .	108

4.8	Pathlines for flapping kinematics at $Re_\omega = 21.6$ and $Re_\omega = 1.0$ . . . . .	111
4.9	Pathlines for rowing kinematics at $Re_\omega = 21.6$ and $Re_\omega = 1.0$ . . . . .	113
4.10	Effects of planform morphology on flow fields at $Re_\omega = 21.6$ . . . . .	118
4.11	Effects of planform morphology on flow fields at $Re_\omega = 21.6$ . . . . .	119
4.12	Mechanical efficiency, $\eta$ , for 3 control volumes . . . . .	127
4.13	Viscous and pressure work rate on the ventral plane . . . . .	131
4.14	Specific mass flow rate, $\xi$ , for CV1 . . . . .	135
4.15	Specific mass flow rate, $\xi$ , for CV1 (normalized axis) . . . . .	139
4.16	Sensitivity of specific mass flow rate, $\xi$ , to the control volume size . . . . .	141
4.17	Quantitative mass flow rate analysis around the mayfly . . . . .	143
4.18	Quantitative mass flow rate analysis around the mayfly (%) . . . . .	144
5.1	Time-averaged vorticity component $\omega_z$ for $Re_\omega = 21.6$ . . . . .	153
5.2	Time-averaged normalized velocity magnitude for $Re_\omega = 21.6$ . . . . .	154
5.3	Pathlines integration for gill pair 4 at $Re_\omega = 21.6$ . . . . .	157
5.4	Specific mass flow rate, $\xi$ , for the parametric space (normalized axis) . . . . .	160
5.5	Rate of work done for flapping using gill pair 4 at $Re_\omega = 21.6$ . . . . .	163
5.6	Viscous and pressure work rate on left gill 4 . . . . .	165

## List of Abbreviations

CV	: Control Volume
CS	: Control Surface
FFT	: Fast Fourier Transform
DFFT	: Discrete Fast Fourier Transform
FOR	: Frame of Reference
IB	: Immersed Boundary
LHS	: Left Hand Side
MLS	: Moving Least Squares
MPI	: Message Passing Interface
NSE	: Navier-Stokes Equations
PDE	: Partial Differential Equation
RHS	: Right Hand Side
RK3	: Runge-Kutta 3 <sup>rd</sup> order
SP	: Stroke Plane
wrt	: with respect to
+ve	: Positive
-ve	: Negative
Anterior	: Of or near the head end of the mayfly
Coronal	: Divides the body into ventral and dorsal sections
Dorsal	: Belonging to or near the upper surface of the mayfly
Medial	: Dividing the mayfly into right and left halves
Posterior	: Located at or towards the rear of the mayfly
Sagittal	: Located in a plane that is parallel to the medial plane
Transverse	: Divides the body into superior and inferior parts
Ventral	: Belonging to or near the belly surface of the mayfly
<i>C. triangulifer</i>	: <i>Centroptilum triangulifer</i>
$c$	: cosine function
$s$	: sine function
$A$	: Peak-to-peak amplitude
$L$	: Gill length and reference length in NSE
$f$	: Frequency
${}^N\mathbf{r}^M$	: Position vector from frame N to point M
$t^*$	: Physical time
$t$	: Dimensionless time
$U$	: Reference velocity in NSE
$\mathbf{u}$	: Dimensionless velocity vector

$\mathbf{x}$	: Dimensionless Cartesian position vector
${}^X\boldsymbol{\alpha}_Z^Y$	: angular acceleration of frame Y relative to frame X in Z frame
$\beta$	: Stroke plane inclination angle
$\gamma$	: Hinge flexion angle
$\epsilon$	: Stroke plane lateral offset angle
$\eta$	: Mechanical efficiency
$\theta$	: Stroke plane deviation angle
$\lambda$	: Proximal-distal inclination angle
$\mu$	: Dynamic viscosity
$\nu$	: Kinematic viscosity
$\xi$	: Specific mass flow rate
$\rho$	: Fluid mass density
$\tau$	: Beating Period
$\phi$	: Angle that modifies the pitch
$\psi$	: In-plane beating angle
${}^X\boldsymbol{\omega}_Z^Y$	: angular velocity of frame Y relative to frame X in Z frame
$Re_\omega = fL^2/\nu$	: Oscillating Reynolds number
$Re_f = fAL/\nu$	: Flapping Reynolds number
$Re_L = UL_{body}/\nu$	: Translation Reynolds number
$St = fL/U$	: Strouhal number
$Pé = LU/D$	: Péclet Number

## Chapter 1: Introduction

### 1.1 What is a Mayfly?

Mayflies are classified in the insect order Ephemeroptera, meaning in Greek “lasting but one day”. The name refers to the fact that the winged adults live only one to two days. Mayfly adults are winged, terrestrial and are also referred to as imagoes (sexually mature). Mayflies are unique in having a winged subimago stage (sexually immature). Early in their life -referred to as larvae, naiads or nymphs-, mayflies are aquatic (Fig. 1.1). Most of a mayfly’s life cycle is spent as a naiad. Naiads are found in wetlands, ponds, lakes, slow or swift flowing streams and rivers. There are many species of mayflies, and they are very common and diverse in river habitats. Many species are relatively intolerant of pollution. The chief importance of mayflies in the ecosystem lies in their value in breaking down organic matter and as food for fish, although they are also food for many other animals, including amphibians, birds, spiders and insects.

Mayfly naiads possess gills, which can be divided into two types: the plate-like abdominal gills and the accessory gills. From a biological standpoint, the abdominal gills have been studied in detail, and a variety of functions have been documented, among which are respiration, osmoregulation, locomotion, water circulation, protec-



(a)



(b)

Figure 1.1: Two different phases of mayfly *C. triangulifer*. (a) Aquatic phase, photograph courtesy of David Funk. (b) Terrestrial phase.

tion and maintenance of the position of the body [84]. Accessory gills have other characteristics that distinguishes them from the abdominal gills. For example, they are thread-like or finger-like filaments or tufts, never plate-like. Also, they are situated on the head and/or thorax, never on the abdomen. Most genera of Baetidae (small minnow mayflies) lack these accessory gills and the species under consideration in this research (*Centroptilum triangulifer*) is not any different. According to the Integrated Taxonomic Information System ([www.itis.gov](http://www.itis.gov)), the taxonomic hierarchy of the species under consideration is: Animalia (Kingdom); Arthropoda or jointed-foot (Phylum); Hexapoda (Subphylum); Insecta (Class); Pterygota or winged insects (Subclass); Palaeoptera or ancient winged insects (Infraclass); Ephemeroptera or mayflies (Order); Pisciforma (Suborder); Baetidae (Family); *Centroptilum* (Eaton 1869) (Genus), *Centroptilum triangulifer* (McDunnough, 1931) (Species).

## 1.2 Motivation

A typical feature of the mayfly naiad is the presence of 7 pairs of abdominal gill plates on the lateral dorsal region of the abdomen. In many species, these plates actively beat in a metachronal fashion to produce an external current that aids in the circulation of fresh oxygenated water and allows mayflies to tolerate fluctuations in oxygen concentrations [3]. More recent studies documented the ventilatory kinematics of the nymphal mayfly *C. triangulifer* [57–59]. In these studies, two distinctive and coupled features associated with the ontogenic progression of the ventilatory kinematics of this specific species (*C. triangulifer*) have been identified: 1) there is an abrupt shift from a rowing mechanism in small instars to a flapping mechanism in larger instars, and 2) the flapping mechanism exhibited the development of a flexural hinge that allowed for the passive movement of a distal flap. The reported oscillating  $Re_\omega$  ranged from 2.0 to 22.0. This was the first study to reveal that a switch from a rowing mechanism to a flapping mechanism can occur systematically in the same species as it molts or grows and therefore highlighting the effect of increasing the  $Re$ , and possibly morphology, on beating kinematics.

*Centroptilum triangulifer* therefore presents a very interesting problem for both areas of fluid mechanics and biology. For the former, *C. triangulifer* operates in the transitional regime where a demarcation from a viscosity-dominated flow to an inertia-dominated flow is known to occur. Examining the behavior of *C. triangulifer* may shed more light on how important gait changes are, in order to escape viscosity, increase mechanical efficiency or thrust, or enhance water circulation. For the latter,

*C. triangulifer* traverses the biologically intermediate regime ( $1 < Re_L < 100$ ) where it is known that below this regime ( $Re_L < 1$ ), rowing is exclusively used by the biological taxa while above this regime ( $Re_L > 100$ ), flapping is predominantly used. Indeed much research has been conducted that aims to link rowing mechanisms to viscous flows and flapping mechanisms to inertial flows, but it is unwarranted to generalize previous hypotheses especially that rowing is often used at  $Re_L > 100$  and, in some cases, is associated with better maneuverability, higher thrust or intermittent burst-and-coast. Mayfly larvae might be optimizing for respiration rather than thrust or mechanical efficiency and therefore presents a different type of a problem.

What makes the problem even more appealing is its applied engineering perspective, where understanding the micro-circulation dynamics around mayfly nymphs can help improve future generations of distributed and autonomous micro-scale chemical sensor networks, which often require an external convective current to achieve rapid and reliable performance. Such requirement was concluded by a recent report by the National Academy of Sciences [71]. Micro-scale sensors are usually limited by diffusion which calls for the use of a convective sampling system to enhance performance, and indeed, use of such systems has shown over an order of magnitude decrease in response time when implemented [48, 56, 63, 70]. Bio-inspired sensors have exciting applications in micro-fluidic devices, which was recently demonstrated by fabricated artificial cilia consisting of electro-statically actuated polymer structures. The device showed substantial fluid flow experimentally [13], which was also modeled numerically [5]. Worth mentioning is that conventional centrifugal pumps, for example, are typically ineffective at low  $Re$  and have only been miniaturized to a limited extent [45],

which paves the road towards unconventional designs for micro-pumping.

### 1.3 Objectives

The objective of the current work is to determine why the transition from a rowing-like mechanism to a flapping-like mechanism occurs in *C. triangulifer*, to possibly corroborate previous experimental results [57–59] and present new ideas or hypotheses. The research also aims to shed more light on the more general question as to why rowing is exclusively used as one approaches the viscosity-dominated flows. Using solely numerical techniques, the goal is to simulate hypothetical scenarios that were impossible to obtain using *in-vivo* experiments such as rowing at high  $Re_\omega$  or flapping at low  $Re_\omega$  or flapping without a flexural hinge, and interpret the numerical results in order to explain the systematic behavior of growing nymphs. These hypothetical scenarios could be obtained using robotic mayflies, but given the complicated nature of the kinematics, the metachronal wave, and the three-dimensionality of the flow field, this approach presents a different set of challenges.

### 1.4 Literature Review and Prior Work

This section provides a comprehensive overview of prior work related to my research, presents the problem in greater depth and familiarizes the reader with the different aspects related to it as, for example, the highly viscous nature of creeping flows. The multidisciplinary problem is tied to what could be optionally classified into three different categories of research. The first research area is basically the rowing

and flapping axis in the biological taxa, which has been under investigation for many decades. The rowing-flapping axis is largely, if not entirely, an aquatic phenomenon and is rarely discussed in the flight literature [74] since most flight literature deals with flapping flight. Rowing and flapping, however, in the context of enhancing micro-mixing or micro-pumping efficiency is almost nonexistent and therefore is the primary contribution from my work. Second, a need to assess the performance of the micro-mixing of the mayflies rose, and given the possible applicability towards bio-inspired and autonomous sensors, the second research area is basically articles related to micro-scale sensors and lab-on-a-chip devices aiming to look primarily into how these sensors are being evaluated (e.g. response time, effectiveness, energy consumption, etc.). Both these areas have been synthesized in order to present a coherent description of the rowing-flapping dichotomy and the metachronal wave in sections 1.4.1 and 1.4.2 respectively. The last research area pertains to the numerical methodologies used to perform the simulations, which relies primarily on the immersed boundary technique [4, 69], which will be presented in Chapter §3.

The following subsections are divided as follows. First, prior work on rowing and flapping is reviewed in §1.4.1. Second, a description of the metachronal wave and how it may affect the flow field is presented in §1.4.2. Third and last, advances pertaining to mayfly larvae specifically is presented, and its relation to rowing, flapping and the metachronal wave is discussed in §1.4.3.

### 1.4.1 Rowing and Flapping

The primary distinction between rowing and flapping is made by comparing the direction of the net force generation (thrust) with respect to the stroke plane. Flapping strokes are characterized by an appendage motion perpendicular to the direction of the net force generation, while rowing strokes are characterized by predominant motion in the direction of net force generation. With the primary objective of the mayfly larva under consideration being different than locomotion, the difference between rowing and flapping is tweaked by simply comparing the direction of the mean flow (instead of the thrust) with the motion of the gills. If the mean flow is perpendicular to the motion of the gills, then the beating kinematics are classified as a flapping mechanism. On the contrary, if the direction of the mean flow is almost parallel to the motion of the gills, then the kinematics are classified as a rowing mechanism. In order to remove any confusion that may arise from the distinction between rowing and flapping, it is emphasized that rowing and flapping are idealized extremes of a continuum [74]. In other words, there exist many sets of kinematics that produce mean flow (or thrust) in directions that are not necessarily parallel or perpendicular to the appendages motion as for example in mayfly naiads in their intermediate regime [59]. Flapping strokes are usually symmetric while rowing strokes introduce some asymmetry. The asymmetry in rowing can be classified into temporal and spatial asymmetry. Temporal asymmetry is introduced by using a power stroke and a recovery stroke where the recovery stroke is slower in order to reduce drag. Temporal asymmetry is known to fail in the Stokesian regime (scallop theorem [53]). Spatial

asymmetry is introduced by changing the shape or profile of the appendage during the recovery stroke in an attempt to reduce drag. This is accomplished through articulation of the appendage (remipede), actuated flexion (cilia in the ctenophore) or retraction of setae on the limb (*Artemia*, remipede) [57]. Spatial symmetry may also be broken by the surrounding fluid domain as for example when beating near a wall (see for example [46]).

The subject of rowing and flapping is rarely discussed in the flight literature and most research on insect flight has been done on flapping flight. There has been a mention that the smallest flying insects swim, or row, in air but then the geometry of rowing would be quite different from that occurring in aquatic flight [74]. In his review of unsteady mechanisms of aquatic and aerial locomotion (intermediate and high Reynolds number), Dickinson [14] pointed out that the separate histories of the two fields (aerial and aquatic locomotion) serve as an obstruction to a useful and powerful synthesis of the knowledge gained throughout the previous decades. For example the concept of added mass is variably called 'added mass', 'added mass inertia', 'virtual mass', 'acceleration reaction' within the biological literature. Nevertheless, the abundant literature about insect flapping flight provides profound interpretations to the inertia-dominated regime and something to look for in the transitional regime encountered in this research. One important lesson to learn from insect flight literature is that non steady-state (instead of quasi-steady) approaches are currently much more common in analysis, due in large part to the influence of Torkel Weis-Fogh in the 1970s [76] and more recently of Charlie Ellington and his colleagues [21–25]. This is due to the fact that quasi-steady analysis failed to explain many insect flights, for

example by frequently underestimating the lift coefficient. A numerical solution of the full unsteady Navier-Stokes equations is the best approach given the availability of higher computing power.

Another nomenclature is repeatedly associated with rowing and flapping kinematics, which is the “drag-based” and “lift-based” propulsion respectively. I speculate that the terms loosely originated to indicate or imply that the low Reynolds number regime is dominated by viscous drag and therefore a “drag-based” propulsion or mechanism, while the high Reynolds number regime is dominated by inertia forces producing lift and therefore the term “lift-based” propulsion or mechanism. This nomenclature may be misleading. After all, how can a drag-based mechanism produce lift (needed at least to sustain weight in non-neutrally buoyant animals or flying insects) if by formal definition drag and lift are orthogonal to each other? On the other hand, at high Reynolds numbers, part of the pressure forces contributes to the drag, known as form drag which is clearly not implied by the term “lift-based”. At best, the nomenclature may be a good approximation in a heuristic model of heaving and pitching plates but numerous mechanisms, including viscous stresses, bound circulation, flow separation, fin-vortex interactions, fin inertia, added mass (acceleration reaction) forces, and jet-like (squeeze) forces, potentially contribute to the force balance in *both* rowing and flapping foils that makes it unwise to distinguish beating or locomotion mechanisms using only these two terms. Again, the “drag-based” and “lift-based” distinction seem to work only for idealized extremes. As Walker put it: “The drag vs. lift dichotomy, then, while useful as an elementary model, both confounds and obscures the different sources of forces on real oscillating fins.” [74], which

was emphasized earlier by Dickinson [14]. A detailed presentation of such unsteady forces associated with inertia-dominated flows, may be found in [11, 55, 75].

In one of the more recent and rich technical articles that examines the rowing-flapping dichotomy, Walker presented a comprehensive comparative study of rowing and flapping [72]. Based on the available data, Walker showed that rowing occurs throughout the range of biologically intermediate  $Re$  ( $1 < Re < 100$ ). On the other hand, flapping is restricted to  $Re > 10$ . In addition, for neutrally buoyant animals, the data suggested that flapping is restricted to  $Re > 100$ . Walker pointed out that the minimum  $Re$  for flapping appendages should be accepted cautiously because of the scarcity of the data on the most relevant animals. In other words, the critical Reynolds number shall not be extended to all biological entities in general and certainly not to *C. triangulifer*. Using the blade-element method and despite the simplicity of his model, Walker concluded that the results predict (or retrodict) both the exclusive use of a rowing stroke below a cut-off  $Re$  of about 20 and the reliance on a reduced area and span during the recovery stroke of small rowing animals.

The problem has been also approached by Childress and Dudley [12] using experiments and several simplified theoretical models. They performed experiments on the swimming of the shell-less pteropod mollusc *Clione antarctica*, which achieves locomotion using ciliated surfaces alone (rowing) or using a pair of flapping wings. It was proposed that forward, reciprocal flapping flight is impossible below some finite critical value of the Reynolds number provided the motion of the insect be fully determined by that dimensionless number. They substantiated their findings using theoretical approaches, namely a modified Oseenlet model and a venetian blind flap-

ping model. The former showed a critical Reynolds number of 33 for an approximate two-dimensional wing model, while the latter showed it to be 9.23 for a spatial period of 1.

In yet another simple and elegant experimental approach, and employing a rotational horizontal flat rectangular wing, Vandenberghe [66, 67] was able to show that flapping flight occurs as a symmetry-breaking bifurcation from a pure flapping state with no prior horizontal motion. A sharp bifurcation to flapping flight for a frictionless system in the range  $20 < Re_f < 55$  was indicated. Visualization of the flow field around the heaving and plunging foil showed a symmetric pattern below transition, while above threshold, an inverted von Kármán vortex street was observed in the wake of the wing.

Another numerical study shows that flapping has a higher mechanical efficiency for all biologically relevant swimming speeds and therefore it was suggested that flapping is usually employed by animals that require energy conservation such as during migration (e.g. adult green turtles and loggerheads), while rowing maximizes maneuverability such as acceleration, turning and braking such as during escape swimming or feeding [73]. The existence of both flapping and rowing in the intermediate regime and the occasional rowing in the inertial regime might be explained by the fact that the optimized parameter or parameters are not known. After all, locomotion is not only about getting efficiently from one point to another, but also a complex and flexible system of behavior required for feeding, courtship, escape [14] and migration.

[1] used *in-silico* experiments and in particular the vorticity stream function to study a 2D flapping ellipsoidal body. By introducing a perturbation normal to the

flapping direction, they showed that at sufficiently large  $Re_f$ , unidirectional locomotion emerges as an attracting state. The onset of the instability (steady locomotion) depended on the aspect ratio of the body and appeared to be independent of the density ratio. They also showed that for sufficiently small  $Re_f$ , horizontal motions imposed transiently on the flapping body rapidly dissipate and the fluid resumes a qualitative left-right symmetry.

Now that it is established that a transition to rowing at low Reynolds numbers must exist [12, 67, 72, 73], the question becomes why is flapping flight “prohibited” at low Reynolds numbers? To answer that, one must first look into how really “viscous” a fluid can get as one approaches the Stokes regime and how bad it is for living organisms. First, an organism is confronted with a large viscous drag and its inertia plays no role. To give an example, an organism with one micron order that is moving with a typical biological speed of  $30\mu\text{m}/\text{s}$  will coast for  $0.1\text{\AA}$  in  $0.6\mu\text{s}$  to a complete stop. This is a tremendous deceleration of  $450\text{m}/\text{s}^2$ . In other words, the organism stops instantaneously once the external force is removed (the distance coasted is 5 orders of magnitude less than that of the organism size). Simply speaking if an organism needs to move in a Stokesian realm, it has to keep propelling itself all the time. Coasting is just not possible. Viscous flows are not easily intuitively grasped simply because they are not encountered on a daily basis, as opposed to other inertia-dominated flows (swimming, driving a car, insect flight, water faucet, etc.). A second characteristic of the Stokesian realm is the low mechanical efficiency associated with moving organisms. For example, a sphere driven by a helical propeller in a creeping flow has a mechanical efficiency of only 1%. Nevertheless, it was pointed

out that the energy exerted in locomotion still represents a minute amount of an organism's metabolism and that efficiency may not be of primary concern [53]. The third important aspect of creeping flows is the kinematical reversibility resulting from the linearity of its basic differential equations. In other words, any creeping flow solution is indistinguishable from its solution if the flow direction is reversed [77]. This paves the road to why symmetrical flapping would not work in the Stokesian realm and was further solidified by the famous scallop theorem: A neutrally buoyant organism exhibiting time-reversal symmetry is a non-swimmer in the Stokesian realm [11]. The scallop theorem could be traced back to the famous lecture by Purcell [53] where it was also shown that with only one degree of freedom in configuration space, one can only have reciprocal motion and therefore swimming is not possible at low  $Re$ .

So how can an organism propel itself in the Stokesian realm? One way is to introduce some asymmetry in the oscillating appendage other than time asymmetry (scallop theorem). Such asymmetry can be accomplished by changing the appendage shape or profile during the recovery stroke, which, in turn, might help reduce the viscous drag. This mechanism is sometimes referred to as non-reciprocal drag-based propulsion. One abundant example is cilia (Figure 1.2a). A cilium (Latin for eyelash) has a diameter of order  $0.2\mu m$  and a typical length that varies from  $2\mu m$  to  $15\mu m$ . Cilia are found in humans (lining of the trachea to sweep mucus, Fallopian tubes to move ovum). They are also found in a diversity of aquatic animals like ctenophores (comb jellies) [6] and molluscs [12]. To achieve asymmetry, a cilium moves approximately as a straight rod during the effective stroke, while during the recovery stroke, it rolls close to the surface in a tangential motion. The mechanical work done of

cilia during the effective stroke was modeled computationally and was shown to be approximately five times the amount of work done during the recovery stroke [31].

Another way to introduce spatial asymmetry is achieved by articulation of the appendages as in remipede (Remipedia: Latin for oar-footed) [40], or retraction of setae (Latin for bristle) on the limb as in *Artemia* (brine shrimp) [78, 79] and remipede. The most recent study on *C. triangulifer* showed that at its low  $Re$  end, the gills are fairly stiff offering little chance to change its shape. Therefore, the spatial asymmetry is introduced by changing the gills pitch during the recovery stroke in order to “feather“ them into the incoming flow and minimize the drag [57].

A recent article has classified asymmetry into temporal, spatial and orientational asymmetry [38], where temporal asymmetry means that one of the half strokes lasts longer than the other, spatial asymmetry is when the shape of the appendage changes between power and recovery strokes (e.g. cilia), and orientational asymmetry is the asymmetry introduced with respect to the channel boundaries for example. The temporal asymmetry is known to be ineffective in the Stokesian regime (scallop theorem) since both half strokes occur in a highly viscous regime. A system achieving “configurational” symmetry (the three aforementioned symmetries) will not generate a net flow or thrust in the Stokesian realm [38].

#### 1.4.2 The Metachronal Wave

An animal having multiple appendages has one more degree of freedom, which is the phase lag between its beating appendages. On some occasions, appendages beat

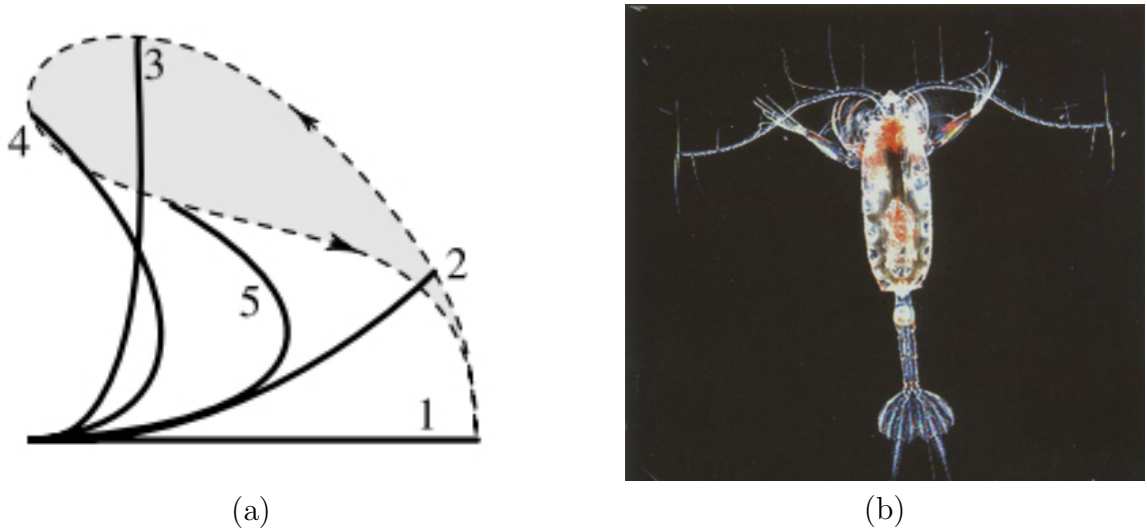


Figure 1.2: (a) Typical asymmetric motion of a cilium. The dashed lines represent the trajectory of the tip of an individual cilium [39]. (b) Photomicrograph of a live copepod, *Euchaeta norvegica* [83].

in phase, but in most scenarios, there is a phase lag between the beating appendages that introduces a spatial wave, which travels along the animal in what is known among biologists as a metachronal wave. A metachronal wave that travels in the same direction as the power stroke is called a symplectic metachronal wave. On the contrary, a metachronal wave that travels in the opposite direction of the effective stroke is termed an antiplectic metachronal wave. An ametachronal wave is different from the typical metachronal wave in that many consecutive legs beat in the same phase. Many research articles investigated the benefits of metachronal waves using either a numerical approach or an experimental one.

On the modeling side, Gueron modeled multiciliary configurations. It was found that when two adjacent cilia start beating at different phases, they became synchronized within several beating periods which was also observed in experiments when two flagella are brought into close proximity. The models also showed that an ap-

proximately antiplectic wave pattern evolved autonomously and it was conjectured that metachronism in cilia may occur, at least partially, as an organized phenomenon due to the hydrodynamic interactions between neighboring cilia [30, 32]. In other words, the metachronal wave occurs as a result of the fluid-structure interaction and the proximity of the cilia to each other. Later it was shown that having neighboring cilia beat metachronally is energetically advantageous [31]. Using a coupled magneto-mechanical solid-fluid computational model, Khaderi et al. [39] showed that artificial cilia beating metachronally enhance the fluid flow and that antiplectic metachrony leads to a considerable flow enhancement compared to symplectic metachrony, but only when the cilia spacing is small.

On the experimental side, the flow of water around the comb plates of *Pleurobrachia pileus* (phylum Ctenophora, class Tentaculata (comb jellies)) was studied [6]. Typical ctenophores swim by means of eight rows of comb plates where each comb plate resembles a rectangular paddle and is composed of a hundred thousand or more cilia. A typical power stroke of the comb plate has a Reynolds number of 9. Using suspended plastic beads and digitized high-speed films, it was shown that the antiplectic motion of the comb plates smooths out the otherwise intermittent flow enabling the jelly to impart greater momentum to the flow. Otherwise said, the comb plates work together by capturing particles accelerated by the preceding comb plate. There was no quantitative approach to compute the efficiency, but qualitative investigation of the flow field suggested that antiplectic metachronism may be responsible for the progressive acceleration of water to a much higher speed than would be possible with a single paddle thereby increasing the mechanical efficiency. It is interesting to mention

that the beating frequency of *Pleurobrachia pileus* could be controlled externally by a fine glass needle depressing against the shaft of the first comb plate at the aboral (back) end.

Studies on individual species that transit the biologically intermediate regime have shown that different types of metachronal waves may be used depending on the life situation. For example, remipede crustaceans beat with one set of appendages using a synchronized ametachronal stroke pattern during escape, while they beat with another set of appendages using a metachronal stroke during cruising and swimming. The copepod *Temora longicornis* forages using a metachronal rowing stroke with the first three of its five feeding appendages while the other two row synchronously, but rows with its swimming legs during escape with a metachronal power stroke and synchronized recovery stroke [65]. Copepods have been studied extensively to investigate the different types of propulsion and metachronal waves [34–37, 65, 83].

Many mayfly species use a metachronal wave or rhythm to beat their gills [3, 15–18, 20, 57–59], but only recent studies have revealed that *C. triangulifer* not only uses an antiplectic metachronal wave, but also switches systematically throughout ontogeny [57–59] from a rowing mechanism to a flapping mechanism thereby bringing an interesting problem into light where transition from antiplectic metachronal rowing to metachronal flapping is occurring. In the following section, previous work on mayfly larvae is reviewed.

### 1.4.3 Advances in Mayfly Larvae

The rhythmical movements of tracheal gills could be traced all the way back to Babák and Foustka [3] where they performed experiments on many arthropods including Ephemeroptera larvae. Babák and Foustka showed that the different beating frequencies were dependent on the oxygen content of the water. They observed a frequency of  $200bpm$  (beat per minute) in previously boiled water,  $100bpm$  in normal running water and as low as  $3.5bpm$  in well-aerated water. It was also indicated that the lower oxygen content affects the beating amplitude.

In 1932, Eastham [15] presented in detail the water currents generated by nymphal gill movements for five different mayfly species. He speculated that tracheal gills moving in a metachronal rhythm create differences of pressure in the inter-gill spaces leading to a period of suction followed by a period of compression. Using suspended mud, cultures of ciliate protozoa, and a stroboscope, he was also able to provide crude visualizations of the currents produced by three different species (*Caenis horaria* in 1934 [16], *Leptophlebia marginata* in 1936 [17] and *Ecdyonurus venosus* in 1937 [18]). In 1938, Eastham [19] also studied a species that is quite different from those previously investigated [15–18], namely, the nymphs of *Ephemera danica* which lives in burrows in the sandy mud of flowing waters. He showed that gills move in metachronal rhythm that starts backwards, and set up currents, which are symmetrical with the body axis. In 1958, Eastham made another contribution to mayflies [20] when he presented the nymph of *Chloeon dipterum* L., described its bilamellate gills, its metachronal rhythm, the currents produced by the gills over the

body, and its muscular mechanisms, which makes these and swimming possible. Eastham illustrated again the periods of suction followed by periods of squeezing between the posterior lamella of one gill and the anterior lamella of the next. He also showed that the normal musculature is modified to provide direct muscles to gill bases and to enable swimming using rhythmical movements of the abdomen. In his literature about nymphal mayflies, Eastham never mentioned an abrupt switch or change in gill kinematics or shape within the same species.

It was not until recently, however, that more quantitative information started to emerge. Sensenig, Kiger & Shultz [58] used Particle Image Velocimetry (PIV) to investigate the fluid dynamics of *C. triangulifer*. In particular, the velocity fields as well as the gill kinematics were measured for 13 mayfly naiads with ages ranging from 20 to 42 days, and gill lengths ranging from  $0.25\text{mm}$  to  $0.77\text{mm}$ . The corresponding oscillating  $Re$  ranged from 2.1 to 21.6. The results are presented in detail in [57] and it is this quantification of the biological model system that makes up one of the cornerstones of the upcoming computational study.

In a follow up study, Sensenig, Kiger & Shultz [59], investigated the hydrodynamic pumping mechanism, also termed “phased vortex pump”. They hypothesized that rowing should be favored when the radius of the vortices shed by the gills exceeds the inter-gill spacing, while flapping should be favored when the vortices radius is smaller than the inter-gill spacing. Their results showed that the vortices radius decreases relative to the inter-gill spacing during mayfly growth, and therefore a transition point exists during ontogeny. The vortices were defined within each PIV frame as those spatial regions where vorticity exceeded 25% of the peak value observed

during the complete beating cycle.

## 1.5 Research Outline

The goal of the current research is to investigate the transition from a rowing type of kinematics to a flapping type of kinematics in *C. triangulifer*, where the flapping kinematics is coupled with an increased gill flexibility and the development of a distal flap. The outline of the thesis is as follows. §2 describes the 3D modeling of the mayfly nymph, the 3-level kinematic chain used to prescribe the gill kinematics, the flapping and rowing kinematics in *C. triangulifer*, the mathematical modeling and the performance metrics used. §3 will briefly describe the numerical methodologies along with the immersed boundary formulation. This will be followed by comparisons with previous experimental results. §4 will present the results for the first parametric space that was designed to investigate the rowing-flapping transition, while §5 will investigate in more detail the effect of the flexural hinge. Finally, §6 summarizes the conclusions along with possible future extensions.

## Chapter 2: Mathematical Modeling

The goal of this work is to model the laminar micro-circulation of water around mayfly larvae using mass and momentum conservation laws. Therefore, four major milestones were accomplished. First, an accurate mayfly 3D model was created from a dissected animal. Second, the gill kinematics have been translated into a set of Eulerian angles, which were implemented into the mathematical model using a 3-level kinematic chain. The first and second milestones basically enable the introduction of the time-varying boundary conditions into the governing equations. Therefore, the third milestone was implementing the 3D model and the prescribed kinematics into the mathematical modeling, where both mass and momentum conservation laws are satisfied. The last milestone deals with the quantitative assessment of the micro-circulation around the mayfly nymphs. Sections 1 through 4 present milestones 1 through 4 respectively. The numerical methodologies will be introduced in §3.

### 2.1 Surface Modeling of the Mayfly Nymph

In order to implement the mayfly nymph into the numerical solver, it was necessary to build an accurate 3D model. The groundwork for the solid modeling was 4 high-resolution raster images of the mayfly nymph, which were provided by Professor

J. Shultz <sup>1</sup>. These images represent the ventral (bottom), dorsal (top), lateral (side) perspectives of the mayfly, magnified under the microscope with a magnification factor of 32, 25 and 32 respectively (see Figures 2.1b and 2.1c). A high-resolution image was also provided for the caudal filaments <sup>1</sup>. In addition to these, 10 posterior and 10 anterior sections were provided for 10 segments along the mayfly's abdomen (Figure 2.1a) which were obtained by patiently and artfully dissecting one nymph under the microscope using a drawing tube<sup>1</sup>.

The raster images and segments were then imported to a CAD software (AutoCAD 2008). Splines were visually fitted in order to vectorize the 20 sections and the main body longitudinal axis. Only one half of each segment was vectorized then mirrored by the medial plane in order to guarantee symmetry (otherwise, undesirable asymmetry will be introduced into the numerical solver). Care has been given to insure the smoothness of the sections at the medial plane by having tangents that are as close as possible to being normal to the medial plane. Using the lateral view of the nymph (Figure 2.1c), the location of each section has been identified and the 20 section have been positioned on the longitudinal axis. Then, each of the 20 sections has been rotated so that its plane lies normal to the longitudinal axis. Five more sections for the thorax and head have been created using the raster images making the total number of sections 25. The end result of these CAD operations is shown in Figure 2.2a. Finally, all the 25 sections have been input to the AutoCAD command "*loft*", which reconstructed the surface of the mayfly using interpolation techniques. After some considerable processing time, the complicated surface of the mayfly ab-

---

<sup>1</sup>Professor Jeffrey Shultz, Entomology Department, University of Maryland, College Park.

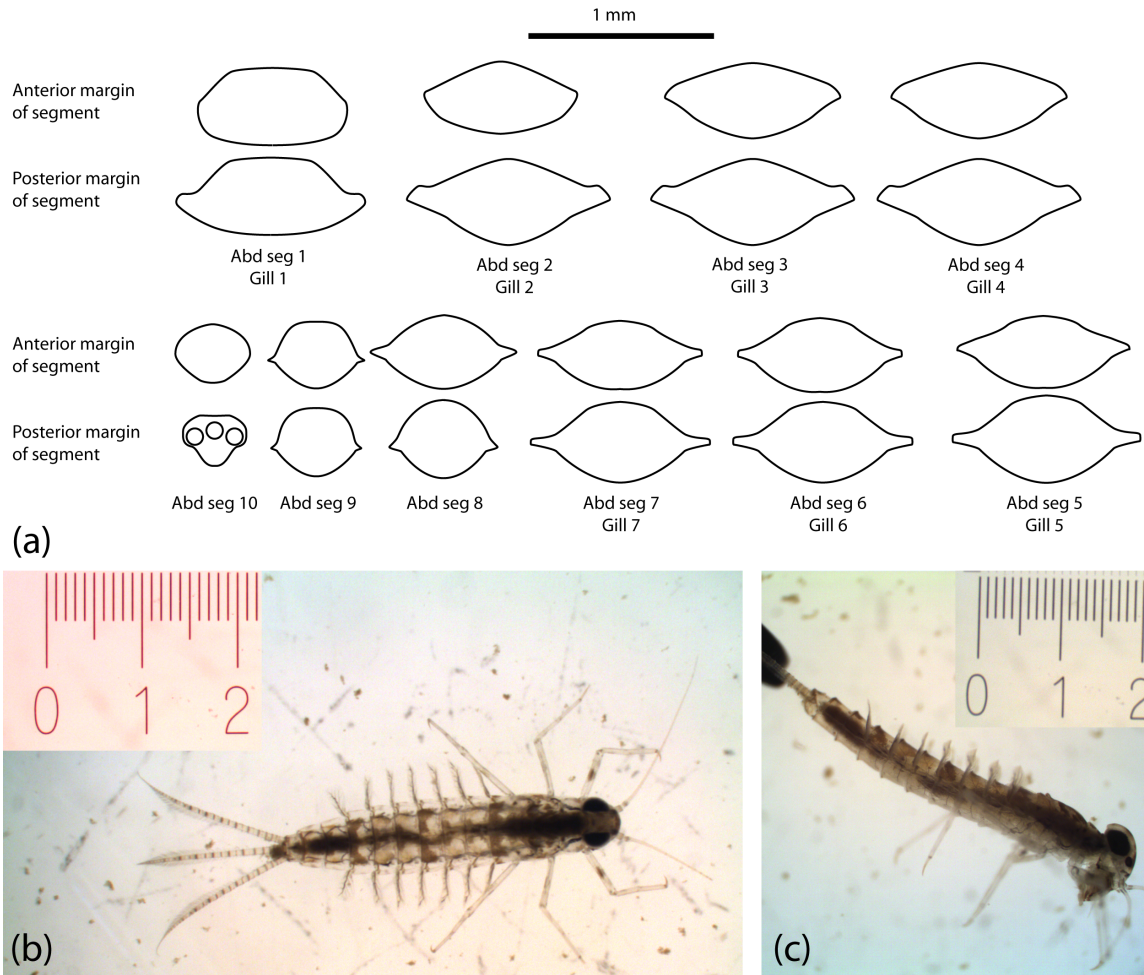


Figure 2.1: High-resolution raster images of *C. triangulifer* and cross sections. (a) Posterior and anterior margins of 10 abdomen segments of the mayfly nymph. Sections were traced using a drawing tube attached to a high-magnification dissecting microscope. (b) Dorsal view of the mayfly nymph at 25X (ruler in *mm*). (c) Lateral view of the mayfly nymph at 32X (ruler in *mm*).

domen, thorax and head emerged and the tapered nature of each segment and the “bulges” at the gills roots conformed to what had been seen under the microscope<sup>1,2</sup>. The final rendered version of the mayfly nymph is shown in Figure 2.2b. Noteworthy is that mayfly antenna, legs and caudal filaments were not included in the model since

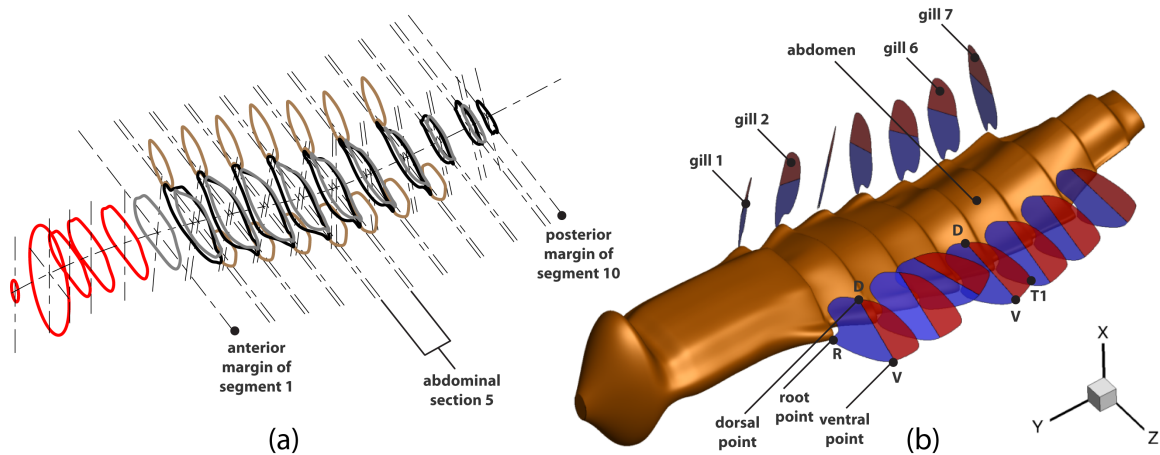


Figure 2.2: Computational model of *C. triangulifer* nymph. (a) 25 sections created in modeling software. Black: posterior sections. Grey: anterior sections. Red: thorax and head sections. Gills shown are decreasing in size towards the head and the tail (shown for illustration only). (b) Rendered version of *C. triangulifer* nymph showing different landmarks on the gills: (R) Root, (V) Ventral, (D) Dorsal and (T1) Tip. Blue: proximal plate. Red: distal plate.

their contribution to the fluid mechanics of the problem are negligible.

In order to create the mayfly gills, the same but simpler procedure has been followed. First, the raster images of the tracheal gills <sup>1</sup> are imported to AutoCAD, then splines are fitted visually in order to vectorize the gill shape. Figure 2.3 shows both raster and vectorized pictures of the different gill planforms used throughout the study.

The variation in the gill planform from younger nymphs to older nymphs was thought to have a marginal effect on the flow field. While this turned out to be generally true, its effect on the proposed performance parameters could not be overlooked. In particular, the mean flow direction and vortices configuration were not affected by the planform variation, but the work done by the gills as well as the induced mass

<sup>1</sup>Professor Jeffrey Shultz, Entomology Department, University of Maryland, College Park, MD.

<sup>2</sup>Professor Andrew T. Sensenig, PhD, Tabor College, Hillsboro, KS

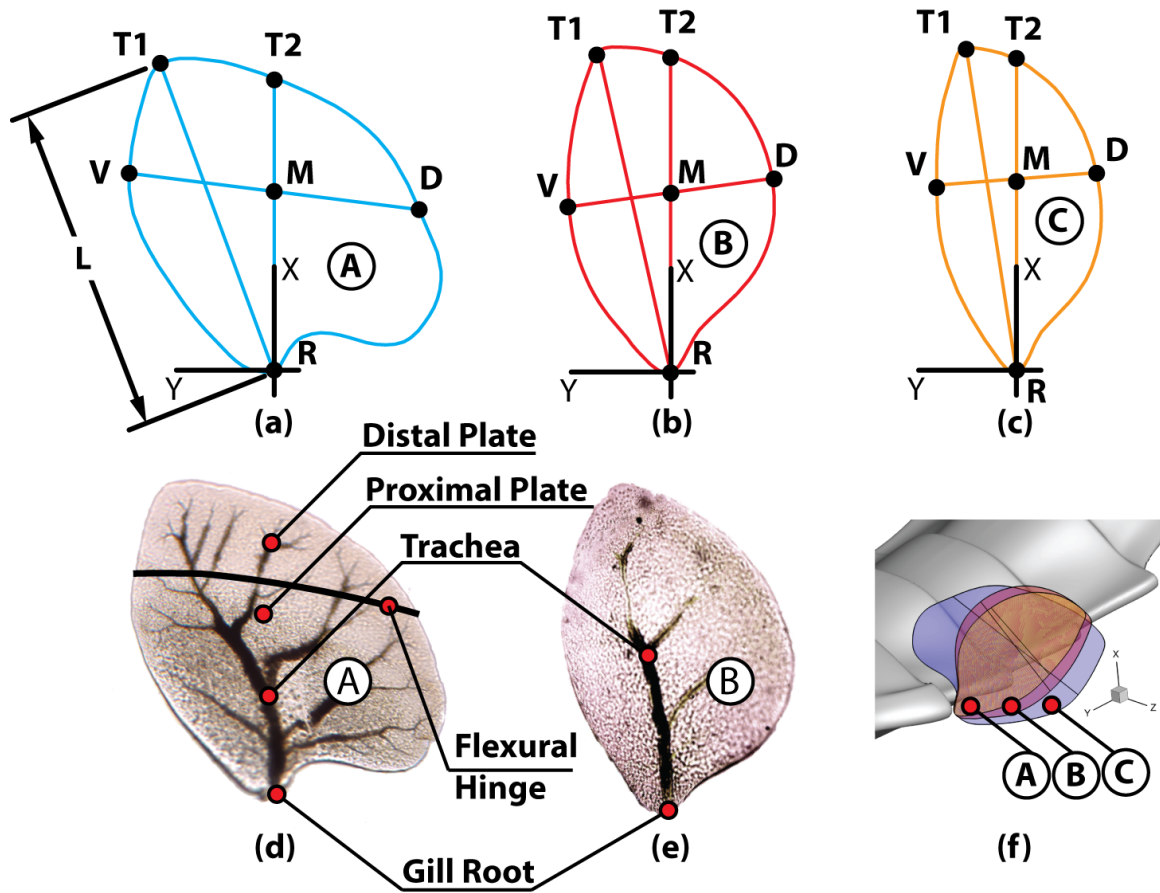


Figure 2.3: Gill morphology. (L)Gill length. (R)Root. (V)Ventral. (D)Dorsal. (M)Midchord. (T1)Gill Tip. (T2)Intersection of gill edge with  $\overrightarrow{RM}$ . (a) Computational model of planform A (older nymphs). (b,c) Computational models of planforms B and C (younger nymphs). (d,e) Actual planforms A and B [58]. (f) Computational model of all planforms at mean position for rowing (Gill 4). Planforms A, B and C have an area of 0.638, 0.449, and 0.356 (length squared) and an aspect ratio of 1.57, 2.23, and 2.81 respectively.

flow rate was strongly dependent on the planform. As a result, the gill planform was treated as an independent variable and three different planforms were selected to perform the simulations. The first planform corresponds to adult nymphs, while the other two relate to younger nymphs.

Figure 2.3d shows Planform A, which is the actual gill planform of adult nymphs, which utilize flapping kinematics. The branching trachea structure emerging at the

gill root is clear and interestingly presents a good analogy with vascular systems and branched water networks. The curved flexural hinge splits the gill into proximal and distal plates where the proximal plate is the plate in proximity of the gill root. The vectorized or computational version of Planform A is shown in Figure 2.3a. Point 'R' is the root of the gill, where it attaches to the mayfly abdomen. Point 'D' is termed the dorsal point, i.e. the point of intersection of the dorsal edge with the flexural hinge  $\overline{VD}$ . Likewise, point 'V' is termed the ventral point, i.e. the point of intersection of the ventral edge with the flexural hinge  $\overline{VD}$ . Point 'T1' is the tip of the gill, defined as the furthest point from the root 'R'. Point 'M' is the "mid-chord", while point 'T2' is the extension of segment  $\overline{RM}$ . The importance of all these points arises from the fact that four of them ('R', 'D', 'V' and 'T1') have been tracked experimentally to extract the gill kinematics, which will be discussed in more detail in the next section. These points are also shown in Figure 2.2b, in order to give a clear perspective of the mean orientation of the flapping gills with the respect to the abdomen. Segment  $\overline{VD}$  is the approximation of the flexural hinge that develops in the gills. The flexural line again splits the gill into its proximal (defined by points 'R', 'V', and 'D') and distal (defined by 'V', 'T1', and 'D') plates. The in-plane curvature of the flexural hinge has been idealized into a straight line owing primarily to the rigidity assumption of the gill plates.

The actual and vectorized versions of Planform B are shown in Figure 2.3e and 2.3b respectively. Planform B is representative of younger naiads, which use a rowing mechanism. Planform B is narrower compared to planform A and does not possess the bulge seen in Planform A near the root. In other words, the dorsal edge

(specifically between point 'R' and point 'D') is the major contributing factor in the planform change. Again, in extracting the gill kinematics, the four points 'R', 'D', 'V' and 'T1' were used to track the gill. For rowing kinematics, the flexural hinge angle is negligibly small and therefore was neglected in rowing simulations.

During the course of study, and after implementing planforms A and B, the effect of the gill shape on the proposed performance parameters became increasingly pronounced. A mayfly naiad molts more than a few times, and as it switches from rowing kinematics to beating kinematics, the gill planform also changes from planform A to B. While only two gill planforms were supplied by my collaborators in the Entomology Department, it is not valid to assume that the mayfly abdomen and gill shapes are "statistically convergent". After all, only one mayfly has been dissected and only one gill per planform has been drawn. When extracting the gill plate kinematics (Eulerian angles), I had to assume that the gill shape (but not the length) in Figure 2.3a-b remains similar for *all* six pairs of moving gills and for *any* mayfly. By looking at the average lengths of segments  $\overline{RV}$ ,  $\overline{RD}$  and  $\overline{VD}$  in the experiments, it was clear that this is not true. In other words, there is an amount of uncertainty in the shape of the gill. In fact, a gill with a higher aspect ratio would yield a better representation of the rowing kinematics. In light of that, planform C was devised. Planform C was obtained by scaling down planform B by 25% but only in a direction perpendicular to  $\overline{RT_1}$ . This effectively increased the gill aspect ratio further, which is illustrated in Figure 2.3c.

The three planforms are superimposed and shown in Figure 2.3f for gill 4 at its mean location for the rowing kinematics. Note that the local gill axis defined by  $\overline{RT_2}$

coincides for all 3 planforms, i.e midpoints of segment  $\overline{DV}$  are collinear. All the gills shown in Figure 2.3 have been scaled to have the same length in order to highlight their morphological or numerical differences. However, a typical gill length of older nymphs (planform A) is of order  $0.7mm$ , while that of younger nymphs (planform B or C) is of order  $0.3mm$ . Planforms A, B and C have areas of 0.638, 0.449, and 0.356 (length squared) respectively. The aspect ratio of planforms A,B and C, defined as the gill surface area divided by the square of the gill length, is 1.57, 2.23, and 2.81 respectively.

The following step was to create a surface mesh (Lagrangian mesh) for the mayfly nymph and the different gills. In other words, the vectorized version of the mayfly and the gills need to be transformed into the discrete space. In order to accomplish this, the AutoCAD drawings have been exported as Standard ACIS Text and imported into a meshing software (Gambit 2.4.6) where the geometry has been checked, cleaned then meshed. Details on the numerical methodologies will be presented in the §3.

## 2.2 The Prescribed Kinematics

In this section, the kinematic chain used to prescribe the different kinematics is presented. A fluid-structure interaction model would have required parameters that were not readily available at the beginning of the study as for example the mass distribution of the gill plates or elasticity parameters that describe the distal plate flexing. The interaction between the different gills becomes increasingly important at

lower  $Re$  and the structural properties will have more pronounced effects. Also, it is not known that these properties will be the same for all 7 pairs of gills. More interestingly, it is known if these structural properties remain constant throughout ontogeny. The gills of older nymphs (planform A) are known to be more flexible than those of younger nymph (planform B). The unavailability and the introduced uncertainty in the structural properties, if it were available, coupled with the uncertainty in the gill shape, kinematics and the variability of mayflies would further complicate the analysis of the results. In addition to its computational cost, introducing a fluid-structure interaction model was neither desirable nor feasible. Therefore, prescribed kinematics present a much simpler and more direct approach especially with the availability of the experimental data (kinematics and flow fields).

### 2.2.1 The Kinematic Chain

In this section, the kinematic chain is discussed in four steps. First a description of the kinematic chain itself, the different rigid bodies involved and the transformation matrices resulting from the multi-body system. Second, a short derivation of the absolute angular velocities of the different bodies. This is followed by a derivation of the absolute angular accelerations. The last step introduces the equations required to compute the absolute linear velocity and acceleration of any point in the kinematic chain.

The kinematic chain is illustrated in Figure 2.4 and consists of 3 levels, where the 1<sup>st</sup> level describes the orientation of the mayfly body 'M' (abdomen, thorax and

head) with respect to the inertial Frame of Reference (FOR) 'N' ( $0^{th}$  level), the  $2^{nd}$  level describes the orientation of the gill proximal plates 'G' with respect to the mayfly body ( $1^{st}$  level) and the  $3^{rd}$  level describes the orientation of the distal plates 'D' with respect to the proximal plate ( $2^{nd}$  level). For the flapping kinematics, both the  $2^{nd}$  and  $3^{rd}$  levels introduce time-dependent angles and are required to fully describe the gills motion. In the rowing case however, the  $3^{rd}$  level is not required since the entire gill is treated as one *single* rigid plate. This was easily executed by setting the hinge angle  $\gamma(t) = 0$  when simulating the rowing kinematics.

In the kinematic chain, three body-attached coordinate systems or FORs are used. These are 'M', 'G', and 'D' for levels 1, 2 and 3 respectively. A series or a sequence of Eulerian angles is performed in order to compute the location of a child body in level (l) with respect to its parent body in level (l-1) along with its angular velocities and accelerations. The first coordinate system  $M\{x_m, y_m, z_m\}$  is attached to the mayfly body and its origin lies at the symmetry (medial) plane on the midpoint of the segment connecting the attachment points of gill pair 4. The second coordinate system is attached to the root any of the proximal plates 1 through 7 and is denoted by  $G\{x_g, y_g, z_g\}$ . The third coordinate system is attached to any of the distal plates 1 through 7 with its origin at the midpoint of  $\overline{DV}$  and is denoted by  $D\{x_d, y_d, z_d\}$  (see Figure 2.4). Although a different amount of translation is required to reach each gill root from 1 to 7 from level 1, the transformation matrix for the rotation sequence is exactly the same. The same applies for the distal plates. In other words, there is only one transformation matrix in going from level 1 to level 2 and only one transformation matrix in going from level 2 to level 3. Only the numerical values of these matrices

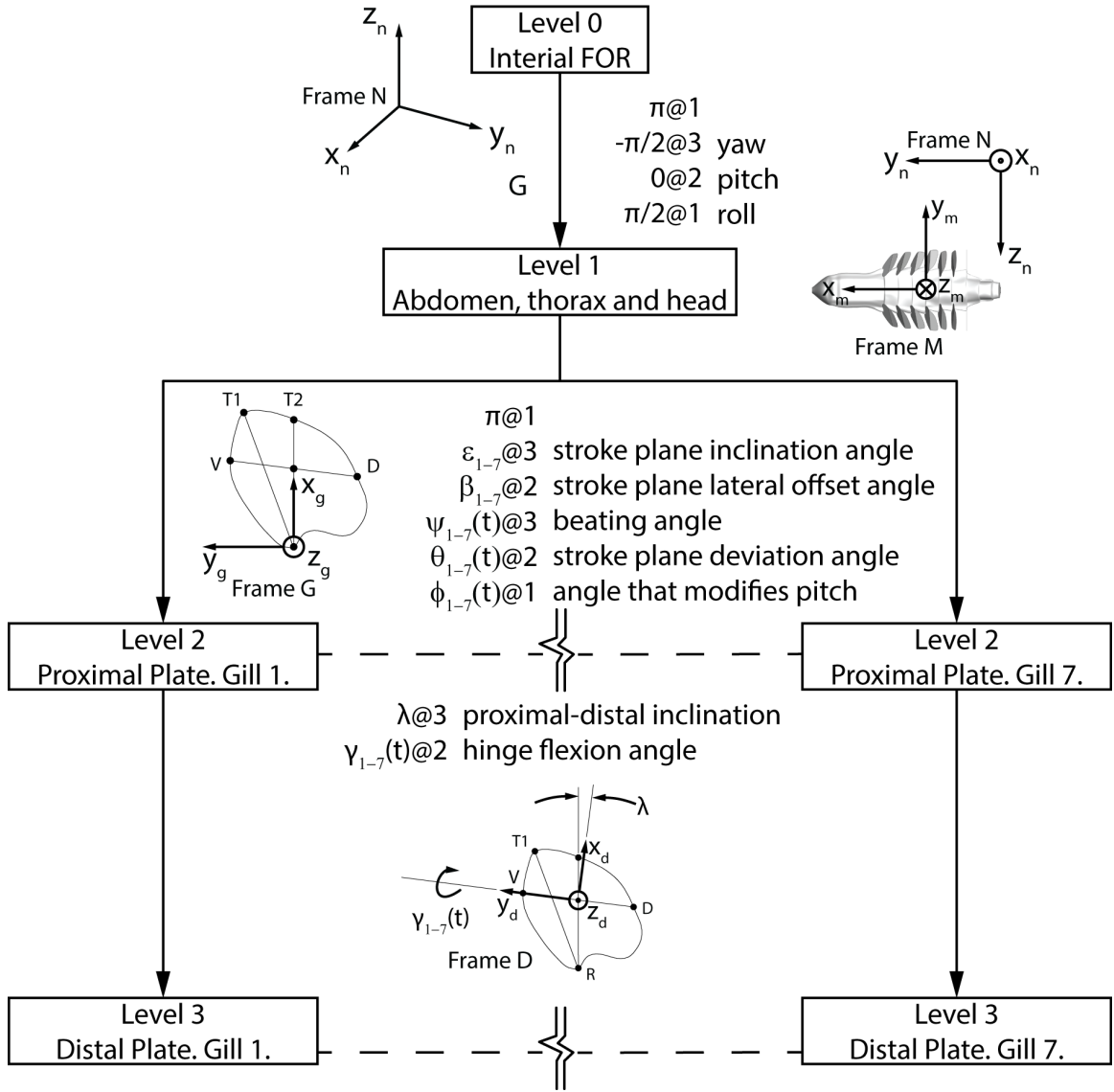


Figure 2.4: Illustration of kinematic chain. Level 0  $\{x_n, y_n, z_n\}$ : Inertial FOR. Level 1  $\{x_m, y_m, z_m\}$ : Mayfly abdomen, thorax and head. Level 2  $\{x_g, y_g, z_g\}$ : Proximal plate of gill. Level 3  $\{x_d, y_d, z_d\}$ : Distal plate of gill. Rotation sequence shown is for the forward transformation from the inertial FOR down to the distal plates. Level 1 is useful for orienting the mayfly inside the Eulerian domain and is not time-dependent. Level 2 has 3 time-dependent angles  $\psi(t)$ ,  $\theta(t)$  and  $\phi(t)$  signifying the beating angle, the stroke plane deviation angle and the angle that modifies the pitch. Level 3 has only one time-dependent angle  $\gamma(t)$ , which signifies the hinge flexion angle. Right hand rule is strictly followed to assign signs to different angles.

will differ depending on the type of kinematics used and the gill number. Worth mentioning is that gill pair 7 is not moving and that gills 1 through 6 have similar kinematics but different values for  $\epsilon$ ,  $\beta$ ,  $\psi(t)$ ,  $\theta(t)$ ,  $\phi(t)$  and  $\gamma(t)$ . FOR 'M' is used to describe the location of the mayfly body with respect to the inertial FOR 'N'. The transformation to level 'M' adds more flexibility because it allows for different orientations of the mayfly body within the Eulerian domain. The transformation was implemented to also allow future extensions of the code (insect flight). The transformation from the inertial FOR 'N' to the mayfly FOR 'M' is achieved by a  $180^\circ$  rotation with respect to the 1 axis, followed by a 3-2-1 Eulerian angle sequence with  $\psi_m(t)$ - $\theta_m(t)$ - $\phi_m(t)$  . This is the typical flight mechanics coordinate transformation (yaw, pitch and roll respectively) and yields a singularity for pitch angles multiple of  $\pi/2$ . In the current work, the values of  $\psi_m(t)$ ,  $\theta_m(t)$ , and  $\phi_m(t)$  were kept constant at  $-\pi/2$ , 0, and  $\pi/2$ . The transformation matrix from 'N' to 'M' is given by:

$$[T_{MN}] = \begin{bmatrix} c\theta c\psi & -c\theta s\psi & s\theta \\ s\phi s\theta c\psi - c\phi s\psi & -s\phi s\theta s\psi - c\phi c\psi & -s\phi c\theta \\ c\phi s\theta c\psi + s\phi s\psi & -c\phi s\theta s\psi + s\phi c\psi & -c\phi c\theta \end{bmatrix} = \begin{bmatrix} 0 & 1 & 0 \\ 0 & 0 & -1 \\ -1 & 0 & 0 \end{bmatrix} \quad (2.1)$$

where  $s()$  and  $c()$  are the sine() and cosine() functions respectively. Level 1 may be interpreted as follows: 1) a positive rotation about the 1 axis in level 1 translates to a positive rotation about the inertial 2 axis. 2) a positive rotation about the 2 axis in level 1 translates to a negative rotation about the inertial 3 axis. 3) a positive rotation about the 3 axis in level 1 translates to a negative rotation about the inertial 1 axis.

FOR 'G' is used to describe the location of any of the proximal plates 1 through

7  $G\{x_g, y_g, z_g\}$  with respect to the mayfly body  $M\{x_m, y_m, z_m\}$ . The transformation from the mayfly system 'M' to the proximal plates system 'G' is achieved in 3 steps with a total of 6 rotations as illustrated in Figure 2.5. First, a rotation of  $\pi$  about 1. This was primarily done to restore the axis orientation used in previous experimental work. Second, a 3-2 rotation of  $\epsilon$  (stroke plane lateral offset angle) and  $\beta$  (stroke plane inclination angle), which describe the location of the stroke plane (SP). Finally a 3-2-1 Eulerian rotation of  $\psi(t)$ ,  $\theta(t)$ , and  $\phi(t)$ , which signifies the in-plane beating angle, the stroke plane deviation angle and the pitch respectively. The transformation matrix of this 1-3-2-3-2-1 sequence is:

$$[T_{GM}] = \begin{bmatrix} T_{11} & T_{12} & T_{13} \\ T_{21} & T_{22} & T_{23} \\ T_{31} & T_{32} & T_{33} \end{bmatrix} \quad (2.2)$$

where:

$$T_{11} = -c\theta(s\epsilon s\psi - c\beta c\epsilon c\psi) - c\epsilon s\beta s\theta$$

$$T_{12} = s\beta s\epsilon s\theta - c\theta(c\epsilon s\psi + c\beta c\psi s\epsilon)$$

$$T_{13} = c\beta s\theta + c\psi s\beta c\theta$$

$$T_{21} = -c\phi(c\psi s\epsilon + c\beta c\epsilon s\psi) - s\phi(s\theta(s\epsilon s\psi - c\beta c\epsilon c\psi) - c\epsilon s\beta c\theta)$$

$$T_{22} = -s\phi(s\theta(c\epsilon s\psi + c\beta c\psi s\epsilon) + s\beta c\theta s\epsilon) - c\phi(c\epsilon c\psi - c\beta s\epsilon s\psi)$$

$$T_{23} = -s\phi(c\beta c\theta - c\psi s\beta s\theta) - c\phi s\beta s\psi$$

$$T_{31} = s\phi(c\psi s\epsilon + c\beta c\epsilon s\psi) - c\phi(s\theta(s\epsilon s\psi - c\beta c\epsilon c\psi) - c\epsilon s\beta c\theta)$$

$$T_{32} = s\phi(c\epsilon c\psi - c\beta s\epsilon s\psi) - c\phi(s\theta(c\epsilon s\psi + c\beta c\psi s\epsilon) + s\beta c\theta s\epsilon)$$

$$T_{33} = s\beta s\phi s\psi - c\phi(c\beta c\theta - c\psi s\beta s\theta)$$

FOR 'D' is used to describe the location of any of the distal plates 1 through 7  $D\{x_d, y_d, z_d\}$  with respect to its parent proximal plate  $G\{x_g, y_g, z_g\}$ . Level 'D' is simply a 3-2 transformation with  $\lambda$  and  $\gamma(t)$ , where  $\lambda$  is the angle which aligns the 2 axis with the flexural hinge line,  $\overline{DV}$ , and  $\gamma(t)$  is the time-dependent hinge flexural angle, which defines the deflection or the flexion of the distal plate with respect to its parent proximal plate. The angles are illustrated in Figure 2.4. The resulting transformation from the 'G' FOR to the 'D' FOR is:

$$[T_{DG}] = \begin{bmatrix} c\gamma c\lambda & c\gamma s\lambda & -s\gamma \\ -s\lambda & c\lambda & 0 \\ c\lambda s\gamma & s\gamma s\lambda & c\gamma \end{bmatrix} \quad (2.3)$$

Equations (2.1), (2.2), and (2.3) define the transformation matrices between any two consecutive levels and therefore enable the transformation of any vector quantity between the inertial FOR 'N' and any other FOR ('M', 'G', or 'D') using equations similar to the following:

$$[\mathbf{T}_{NM}] = [\mathbf{T}_{MN}]^T \quad (2.4)$$

$$[\mathbf{T}_{NG}] = [\mathbf{T}_{NM}][\mathbf{T}_{MG}] = [\mathbf{T}_{GN}]^T = [\mathbf{T}_{MN}]^T[\mathbf{T}_{GM}]^T \quad (2.5)$$

$$[\mathbf{T}_{ND}] = [\mathbf{T}_{NM}][\mathbf{T}_{MG}][\mathbf{T}_{GD}] = [\mathbf{T}_{DN}]^T = [\mathbf{T}_{MN}]^T[\mathbf{T}_{GM}]^T[\mathbf{T}_{DG}]^T \quad (2.6)$$

The next step in the kinematic analysis of this mechanical system is to compute the angular velocities of the different bodies in terms of the time derivatives of the Eulerian angles. In general, the angular velocity of some frame 'Y' with respect to another frame 'X' may be expressed in terms of the time derivatives of those Eulerian

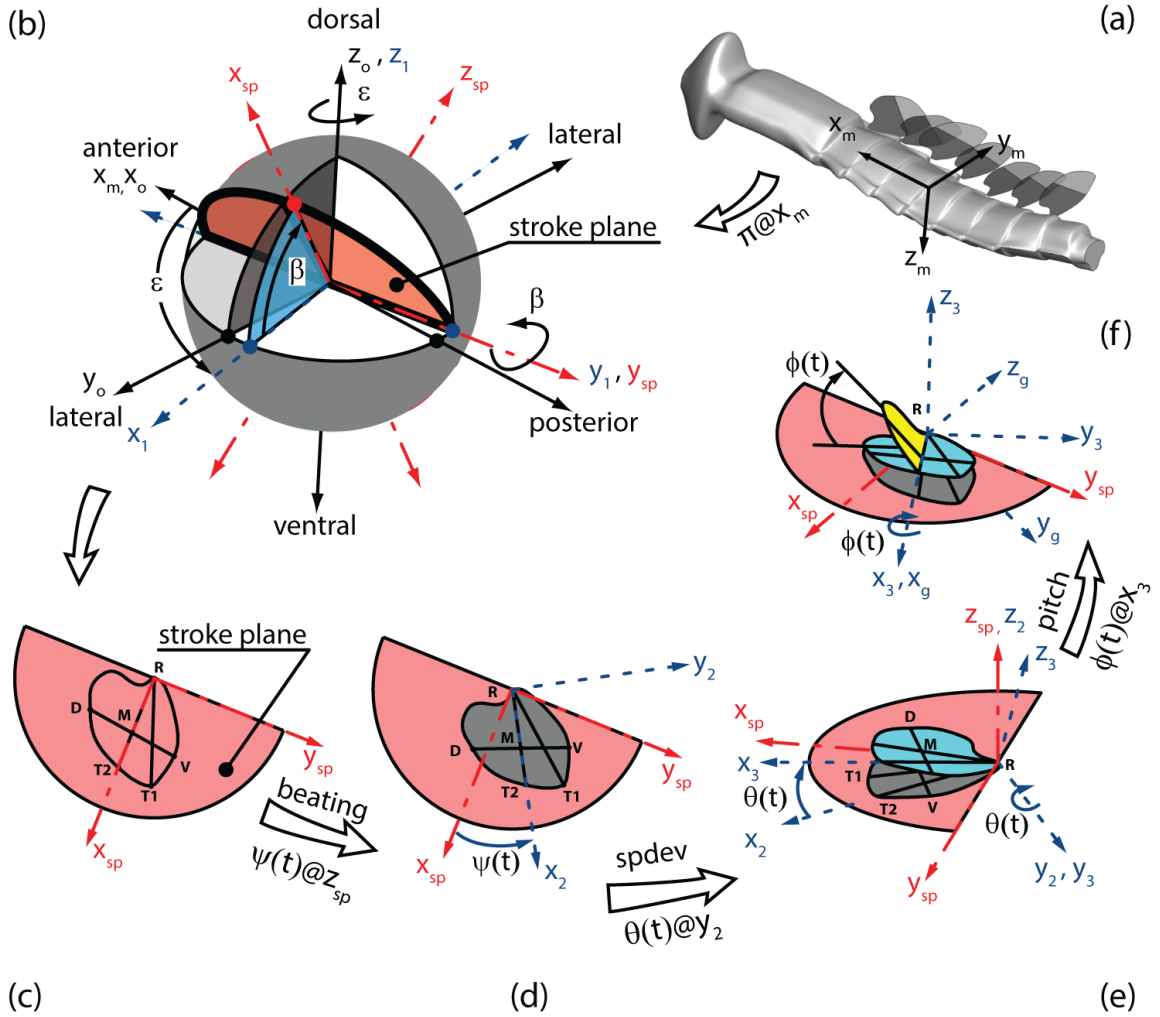


Figure 2.5: Illustration of the forward transformation from the mayfly local FOR  $M\{x_m, y_m, z_m\}$  to any local left gill FOR  $G\{x_g, y_g, z_g\}$ . The sequence is a 1 – 3 – 2 – 3 – 2 – 1 Eulerian sequence with  $\pi - \epsilon - \beta - \psi(t) - \theta(t) - \phi(t)$ , where  $\epsilon$  is the lateral offset angle,  $\beta$  is the stroke plane inclination angle,  $\psi(t)$  is the beating angle,  $\theta(t)$  is the stroke plane deviation angle and  $\phi(t)$  is then angle that modifies the pitch. The illustration shown is for  $\epsilon = 100^\circ, \beta = -60^\circ, \psi = 30^\circ, \theta = -15^\circ, \phi = -45^\circ$ . (a) Isometric view of mayfly naiad with its local FOR, left row of gills omitted. (b) Isometric view (matching view in (a)) of the stroke plane  $\{x_{sp}, y_{sp}, z_{sp}\}$  after the 1 – 3 – 2 rotation of  $\pi, \epsilon = 100^\circ, \beta = -60^\circ$ . (c) Perpendicular view of the stroke plane showing the in-plane gill ( $\psi = 0^\circ, \theta = 0^\circ, \phi = 0^\circ$ ). (d) Gill location  $\{x_2, y_2, z_2\}$  after beating of  $\psi = 30^\circ$ . (e) Gill location before  $\{x_2, y_2, z_2\}$  and after  $\{x_3, y_3, z_3\}$  a stroke plane deviation of  $\theta = -15^\circ$ . (f) Gill location before  $\{x_3, y_3, z_3\}$  and after  $\{x_g, y_g, z_g\}$  a pitch of  $\phi = -45^\circ$ . Gill at  $\{x_2, y_2, z_2\}$  is also shown (axis omitted for clarity).

angles used to rotate between 'Y' and 'X' in some frame 'B' in the form  ${}^X\boldsymbol{\omega}_B^Y = \mathbf{M}\dot{\boldsymbol{\Phi}}$  where the definition frame 'B' is usually one of the frames 'X' or 'Y'. This is obtained by expressing the components of the angular velocity vector  $\boldsymbol{\omega}$  in terms of only one FOR rather than in terms of all the FORs involved in the rotation sequence, which normally results from an Eulerian sequence. The angular velocity of the proximal gill plate 'G' with respect to the mayfly 'M' expressed in the mayfly frame 'M' is denoted  ${}^M\boldsymbol{\omega}_M^G = \mathbf{M}_{(\theta,\psi)}\dot{\boldsymbol{\Phi}}_{(\dot{\phi},\dot{\theta},\dot{\psi})}$  and reads:

$${}^M\boldsymbol{\omega}_M^G = \begin{bmatrix} c\beta c\epsilon c\theta c\psi - s\epsilon c\theta s\psi - s\beta c\epsilon s\theta & -c\beta c\epsilon s\psi - s\epsilon c\psi & s\beta c\epsilon \\ -c\beta s\epsilon c\theta c\psi - c\epsilon c\theta s\psi + s\beta s\epsilon s\theta & c\beta s\epsilon s\psi - c\epsilon c\psi & -s\beta s\epsilon \\ s\beta c\theta c\psi + c\beta s\theta & -s\beta s\psi & -c\beta \end{bmatrix} \begin{Bmatrix} \dot{\phi} \\ \dot{\theta} \\ \dot{\psi} \end{Bmatrix} \quad (2.7)$$

Similarly, the angular velocity of the distal gill plate 'D' with respect to the proximal gill plate 'G' expressed in the proximal gill frame 'G' is denoted  ${}^G\boldsymbol{\omega}_G^D = \mathbf{M}_{(\lambda)}\dot{\boldsymbol{\Phi}}_{(\dot{\gamma})}$  and reads:

$${}^G\boldsymbol{\omega}_G^D = \begin{bmatrix} 0 & -s\lambda & 0 \\ 0 & c\lambda & 0 \\ 0 & 0 & 0 \end{bmatrix} \begin{Bmatrix} 0 \\ \dot{\gamma} \\ 0 \end{Bmatrix} = \begin{Bmatrix} -s\lambda\dot{\gamma} \\ c\lambda\dot{\gamma} \\ 0 \end{Bmatrix} \quad (2.8)$$

Equations (2.7) and (2.8) fully describe the angular velocities of the proximal and distal plates of the gill respectively. Specifically it describes the relative angular velocity between a child (level  $l$ ) and its parent (level  $l - 1$ ). Although the angular velocities are expressed in different FORs, the transformation matrices introduced in (2.1), (2.2) and (2.3) along with the relations in (2.4) allows the expression of the angular velocities in any FOR and in the inertial FOR 'N' in particular. The absolute

angular velocities are calculated by use of the addition theorem [28,47]:

$${}^N\boldsymbol{\omega}_N^l = {}^N\boldsymbol{\omega}_N^{l-1} + {}^{l-1}\boldsymbol{\omega}_N^l \quad 1 \leq l \leq 3 \quad (2.9)$$

where  $l$  is the level number.

The next step in the kinematic analysis of this mechanical system is to compute the absolute angular accelerations of the different bodies in terms. With the angular velocity of the different frames known, it is possible to calculate the angular acceleration with the respect to the inertial FOR 'N' using the fundamental composition rule for the absolute angular acceleration [7]:

$${}^N\boldsymbol{\alpha}_N^l = {}^N\boldsymbol{\alpha}_N^{l-1} + {}^{l-1}\boldsymbol{\alpha}_N^l + {}^N\boldsymbol{\omega}_N^{l-1} \times {}^{l-1}\boldsymbol{\omega}_N^l \quad 1 \leq l \leq 3 \quad (2.10)$$

where  $l$  is the level. The angular acceleration of a child with respect to its parent is computed using Coriolis theorem as follows:

$${}^N\boldsymbol{\alpha}_N^M = \frac{d}{dt} {}^N\boldsymbol{\omega}_N^M = \mathbf{0} \quad (2.11)$$

$$\begin{aligned} {}^M\boldsymbol{\alpha}_M^G &= \frac{d}{dt} {}^M\boldsymbol{\omega}_M^G \\ &= \frac{d}{dt} {}^M\boldsymbol{\omega}_M^G + {}^N\boldsymbol{\omega}_M^M \times {}^M\boldsymbol{\omega}_M^G \\ &= \mathbf{M}_{(\theta,\psi)} \ddot{\Phi}_{(\phi,\dot{\theta},\dot{\psi})} + \dot{\mathbf{M}}_{(\theta,\psi)} \dot{\Phi}_{(\phi,\dot{\theta},\dot{\psi})} \end{aligned} \quad (2.12)$$

$$\begin{aligned} {}^G\boldsymbol{\alpha}_G^D &= \frac{d}{dt} {}^G\boldsymbol{\omega}_G^D \\ &= \frac{d}{dt} {}^G\boldsymbol{\omega}_G^D + {}^N\boldsymbol{\omega}_G^G \times {}^G\boldsymbol{\omega}_G^D \\ &= \mathbf{M}_{(\lambda)} \ddot{\Phi}_{(\dot{\gamma})} + \dot{\mathbf{M}}_{(\lambda)} \dot{\Phi}_{(\dot{\gamma})} + {}^N\boldsymbol{\omega}_G^G \times {}^G\boldsymbol{\omega}_G^D \end{aligned} \quad (2.13)$$

Equations (2.10) through (2.13) completely define the absolute angular accelerations

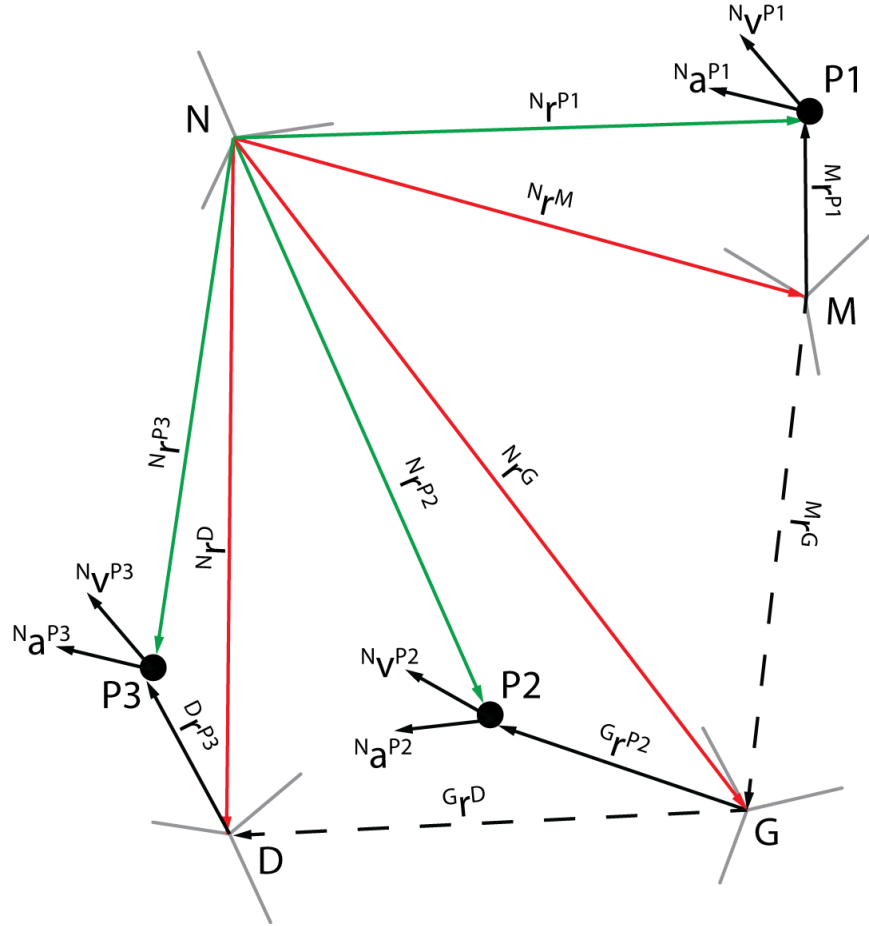


Figure 2.6: Schematic of position vectors in different levels. P1: Point in level I. N, M, G and D: Inertial, Mayfly, Gill and Distal plate frames of reference.  ${}^i\mathbf{r}^{Pl}$ : Position vector from FOR  $i$  to point Pl.  ${}^i\mathbf{v}^{Pl}$ ,  ${}^i\mathbf{a}^{Pl}$ : Velocity and acceleration of point Pl with respect to frame  $i$  respectively.

of the entire kinematic chain with the help of the transformation relations in (2.4).

With the absolute angular velocity and acceleration of all bodies (proximal 'G' and distal 'D' plates) determined, the last step is to compute the absolute position, linear velocity and linear acceleration of any point in the chain. With reference to Figure 2.6, the position vector for points 'P1', 'P2' and 'P3' lying on the mayfly 'M',

proximal plate 'G' and the distal plate 'D' respectively can be expressed as:

$$N_{\mathbf{r}^{P1}} = N_{\mathbf{r}^M} + M_{\mathbf{r}^{P1}} \quad (2.14)$$

$$\begin{aligned} N_{\mathbf{r}^{P2}} &= N_{\mathbf{r}^M} + M_{\mathbf{r}^G} + G_{\mathbf{r}^{P2}} \\ &= N_{\mathbf{r}^G} + G_{\mathbf{r}^{P2}} \end{aligned} \quad (2.15)$$

$$\begin{aligned} N_{\mathbf{r}^{P3}} &= N_{\mathbf{r}^M} + M_{\mathbf{r}^G} + G_{\mathbf{r}^D} + D_{\mathbf{r}^{P3}} \\ &= N_{\mathbf{r}^D} + D_{\mathbf{r}^{P3}} \end{aligned} \quad (2.16)$$

The corresponding linear velocity of any point lying on these rigid bodies may be respectively expressed as:

$$N_{\mathbf{v}^{P1}} = N_{\mathbf{v}^M} + N_{\boldsymbol{\omega}^M} \times M_{\mathbf{r}^{P1}} \quad (2.17)$$

$$N_{\mathbf{v}^{P2}} = N_{\mathbf{v}^G} + N_{\boldsymbol{\omega}^G} \times G_{\mathbf{r}^{P2}} \quad (2.18)$$

$$N_{\mathbf{v}^{P3}} = N_{\mathbf{v}^D} + N_{\boldsymbol{\omega}^D} \times D_{\mathbf{r}^{P3}} \quad (2.19)$$

Similarly, the corresponding linear acceleration of any point lying on these rigid bodies may be respectively expressed as:

$$N_{\mathbf{a}^{P1}} = N_{\mathbf{a}^M} + N_{\boldsymbol{\alpha}^M} \times M_{\mathbf{r}^{P1}} + N_{\boldsymbol{\omega}^M} \times (N_{\boldsymbol{\omega}^M} \times M_{\mathbf{r}^{P1}}) \quad (2.20)$$

$$N_{\mathbf{a}^{P2}} = N_{\mathbf{a}^G} + N_{\boldsymbol{\alpha}^G} \times G_{\mathbf{r}^{P2}} + N_{\boldsymbol{\omega}^G} \times (N_{\boldsymbol{\omega}^G} \times G_{\mathbf{r}^{P2}}) \quad (2.21)$$

$$N_{\mathbf{a}^{P3}} = N_{\mathbf{a}^D} + N_{\boldsymbol{\alpha}^D} \times D_{\mathbf{r}^{P3}} + N_{\boldsymbol{\omega}^D} \times (N_{\boldsymbol{\omega}^D} \times D_{\mathbf{r}^{P3}}) \quad (2.22)$$

In investigating the fluid dynamics of mayfly naiads, two sets of mayfly kinematics representative of flapping and rowing were under consideration, both extracted from the experimental measurements [57]. A description of both sets follows. In both sets, the beating cycle is split into two parts: 1) *retraction*, where the proximal plate

is moving towards the rear of the insect, and 2) *protraction*, where the proximal plate is moving towards the head. This notion is most comparable to the down-stroke and the up-stroke half-strokes in flapping flight literature because it implies a direction of motion rather than a function. The notion of a power stroke and a recovery stroke is not useful in flapping kinematics because both half-strokes are equally important and both half-strokes contribute to the induced micro-pumping. The power and recovery half-strokes notion, however, can be applied to the rowing kinematics since each half stroke has a distinguishable function.

In both sets, the kinematics of gill pairs 1 to 6 in the array are similar in terms of magnitude and frequency, and only differ in terms of their mean positions with respect to the body; gills towards the head of the insect are positioned closer to the abdomen (higher lateral offset angle,  $\epsilon$ , for SP definition). In both sets, gill pair number 7 is not moving and is, therefore, believed to act as a buffer to enhance performance. The phase lag between any two consecutive gills is approximately  $90^\circ$ , with the gills at the back having the lead. Whenever the mayfly naiad starts to beat its gills, it starts by beating gill pair 6. The metachronal wave starts posteriorly at gill pair number 6 and progresses forward towards the head of the animal. The actual frequency of the gills varies from  $20Hz$  to  $37Hz$  and no correlation could be made with the mayfly size or age [58]. Noteworthy is that experimental results from an idealized rowing robotic model of the mayfly naiad at  $Re_\omega = 17.4$  showed that the  $90^\circ$  phase lag produces the highest efficiency for the rowing case when compared to phase lags of  $0^\circ$ ,  $180^\circ$  and  $270^\circ$  [44]. In other words, it is possible that the  $90^\circ$  phase lag is nature's choice to optimize the induced micro-pumping. Both sets of kinematics are presented next.

## 2.2.2 The Flapping Kinematics

The flapping kinematics of gill 4 is illustrated in Figure 2.7. Part (a) of the figure shows an entire period of the gill as projected onto an  $xy$ -plane (the median plane or the symmetry plane), while parts (b) and (c) show gill 4 during retraction and protraction respectively. The projection onto the  $xy$ -plane is a good representation of the actual kinematics, i.e. antero-posterior (along  $y$ ) and dorso-ventral (along  $x$ ) motion represents the dominant motion. Frames 1 and 3 depict the extreme positions of the proximal plate, while frames 4 and 2 depict mid-retraction and mid-protraction respectively. The first thing to note about the flapping kinematics is that the motion of the proximal plate is almost symmetric. It takes 48% of a cycle to protract and 52% of to retract. In addition, looking at any two time frames in Figure 2.7a that lie in the same vertical column (e.g. 0.55 and 0.65) the segments  $\overline{DV}$  (red) and  $\overline{RM}$  (black) are always parallel, which again highlights the symmetry of motion of the proximal plate around its mean position. The segments in lighter dashed shades (gray and light red), which represent the position of the gill 0.025 earlier in the period, demonstrate that the acceleration of the proximal plate is the same during retraction and protraction. For this particular gill, the mean pitch angle is  $-92^\circ$  with a range of only  $6^\circ$ . The beating angle has a mean of  $-22^\circ$  and an amplitude of  $22^\circ$ . The range of the stroke plane deviation is  $3^\circ$ . It is evident from these numbers that the motion is dominated by the beating angle with relatively little pitch variation or stroke plane deviation. Finally, the motion of the distal plate relative to the hinge can also be seen in the figure. The hinge flexion angle varies from  $10^\circ$  at  $t/\tau = 0.45$  to  $65^\circ$  at  $t/\tau = 0.8$ . As

a result, the mean position of the distal plate is not parallel to the mean position of the proximal plate. A plot of the different angles describing the motion of all the 6 gills is shown Figure 2.8.

### 2.2.3 The Rowing Kinematics

The rowing kinematics for the same gill (number 4) are illustrated in Figure 2.9. The stroke plane in this case is inclined  $-53^\circ$  from the  $yz$  plane. Compared to flapping, there is no symmetry between the protraction and retraction part of the cycle. It takes 38% of the cycle for the gill to retract and 62% of the cycle to protract. The beating angle has a range of  $47^\circ$  over the entire period, which is more than twice the flapping beating range ( $22^\circ$ ). The presence of much higher accelerations during retraction is evident, as manifested by the larger lag between the black and gray lines (i.e.  $t = 0.3 - 0.4$ ). In addition, the pitch angle has a range of  $37^\circ$ , which is more than six times that of the flapping. The mean pitch is  $-90^\circ$  during retraction,  $-70^\circ$  during protraction, and  $-78^\circ$  for the entire period. In summary, the rowing motion is characterized by higher beating, accelerations, pitching and stroke plane deviation. The experiments have shown that the mean flow field is directed parallel to the stroke plane. In fact, the retraction is the power stroke where the fluid is being pushed towards the back and the bottom of the insect with an average pitch of  $-90^\circ$ , while the protraction is obviously a recovery stroke where the gill plate is feathering into the mean flow with a mean pitch of  $-70^\circ$  to -possibly- attempt to minimize the work done by the mayfly and enhance the efficiency. A plot of the different angles

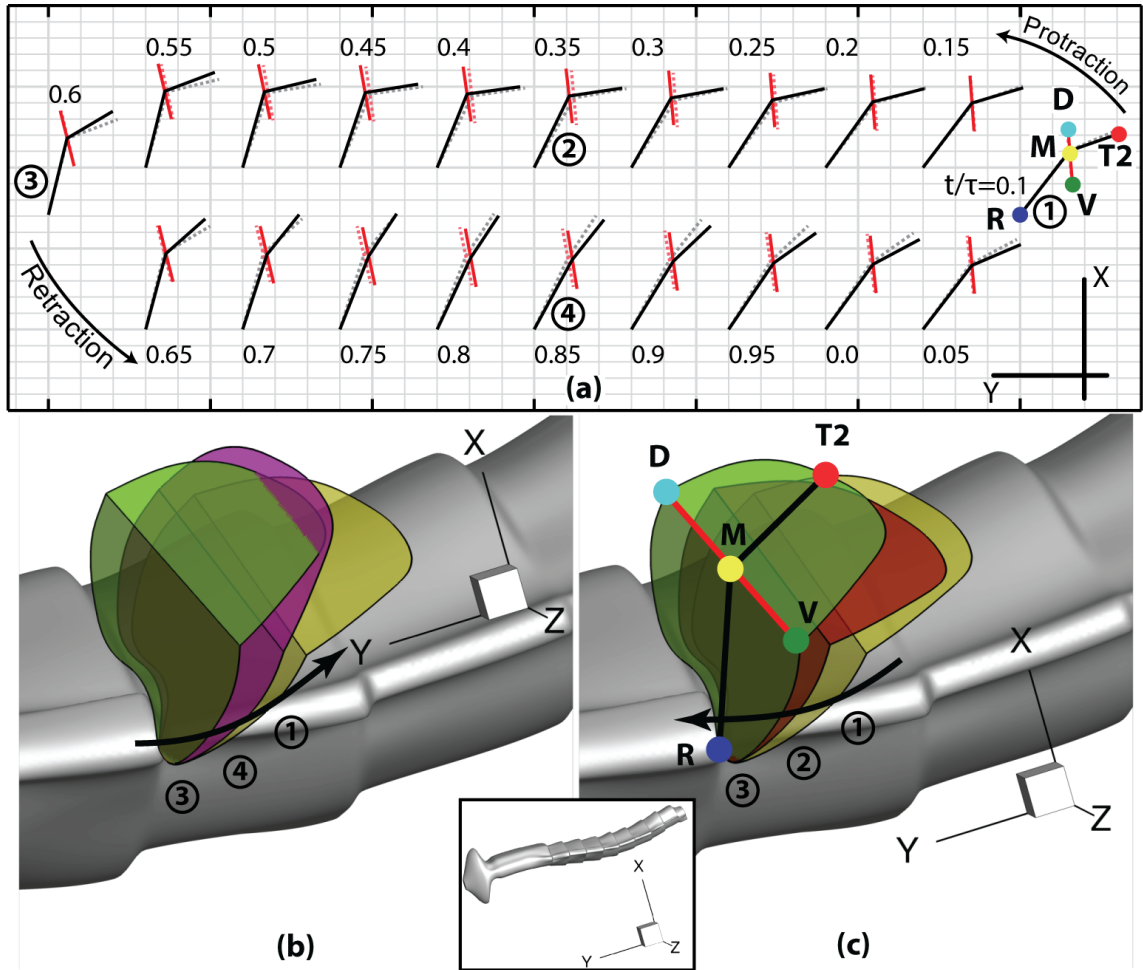


Figure 2.7: Prescribed mayfly flapping kinematics for gill 4. (a) Kinematics projected onto xy plane. Dashed trails in lighter shades are 0.025 earlier in the beating period ( $\tau = 1$ ). (b) Retraction (3D perspective). (c) Protraction (3D perspective). Inset illustrates the 3D perspective for parts (b) and (c). ①, ③: Extreme positions of proximal plate. ②: Mid-protraction. ④: Mid-retraction.

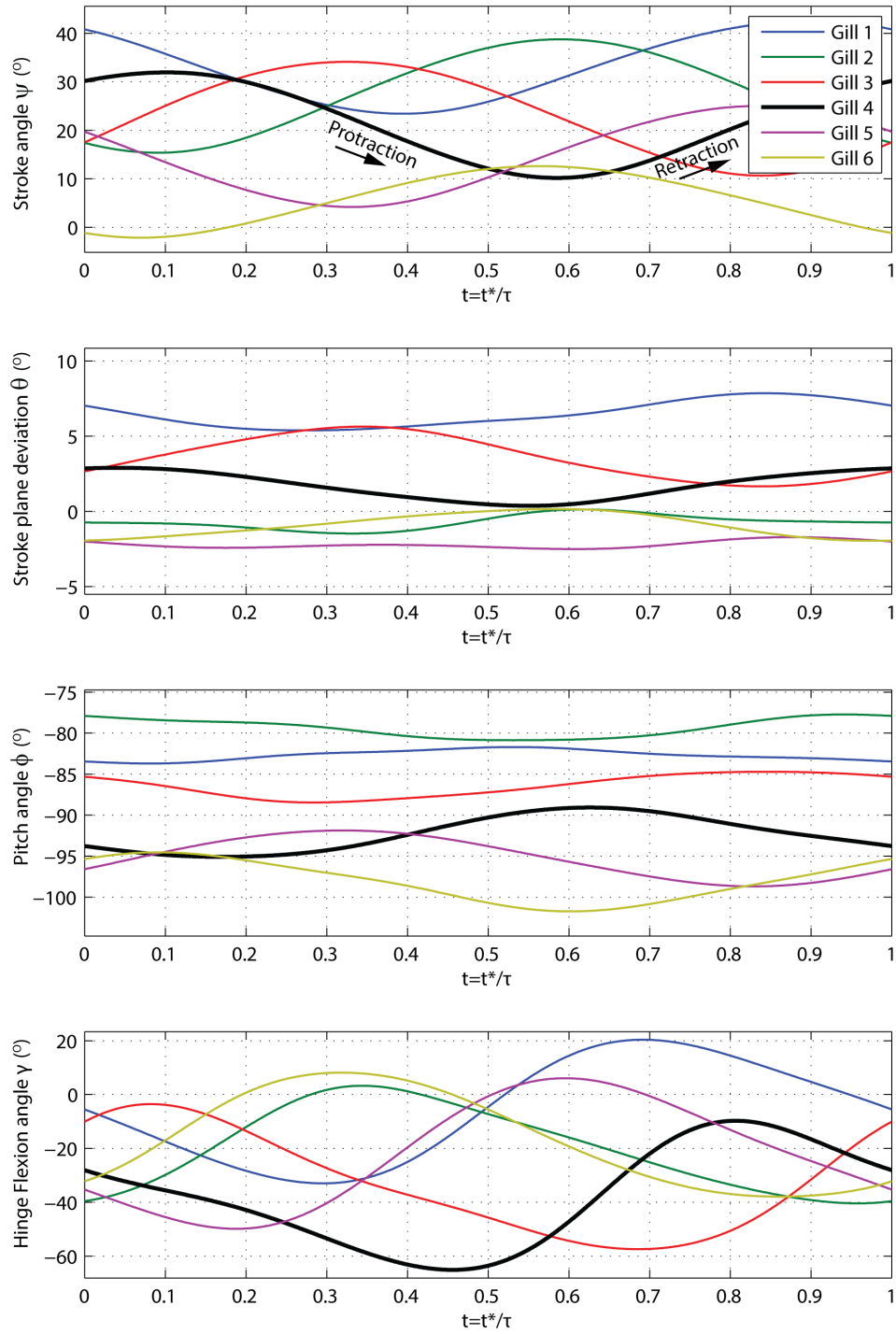


Figure 2.8: Eulerian angles for mayfly flapping kinematics (°). Top to bottom: Stroke or beating angle  $\psi_{1-6}(t)$ . Stroke plane deviation angle  $\theta_{1-6}(t)$ . Pitch angle  $\phi_{1-6}(t)$ . Hinge flexion angle  $\gamma_{1-6}(t)$ .

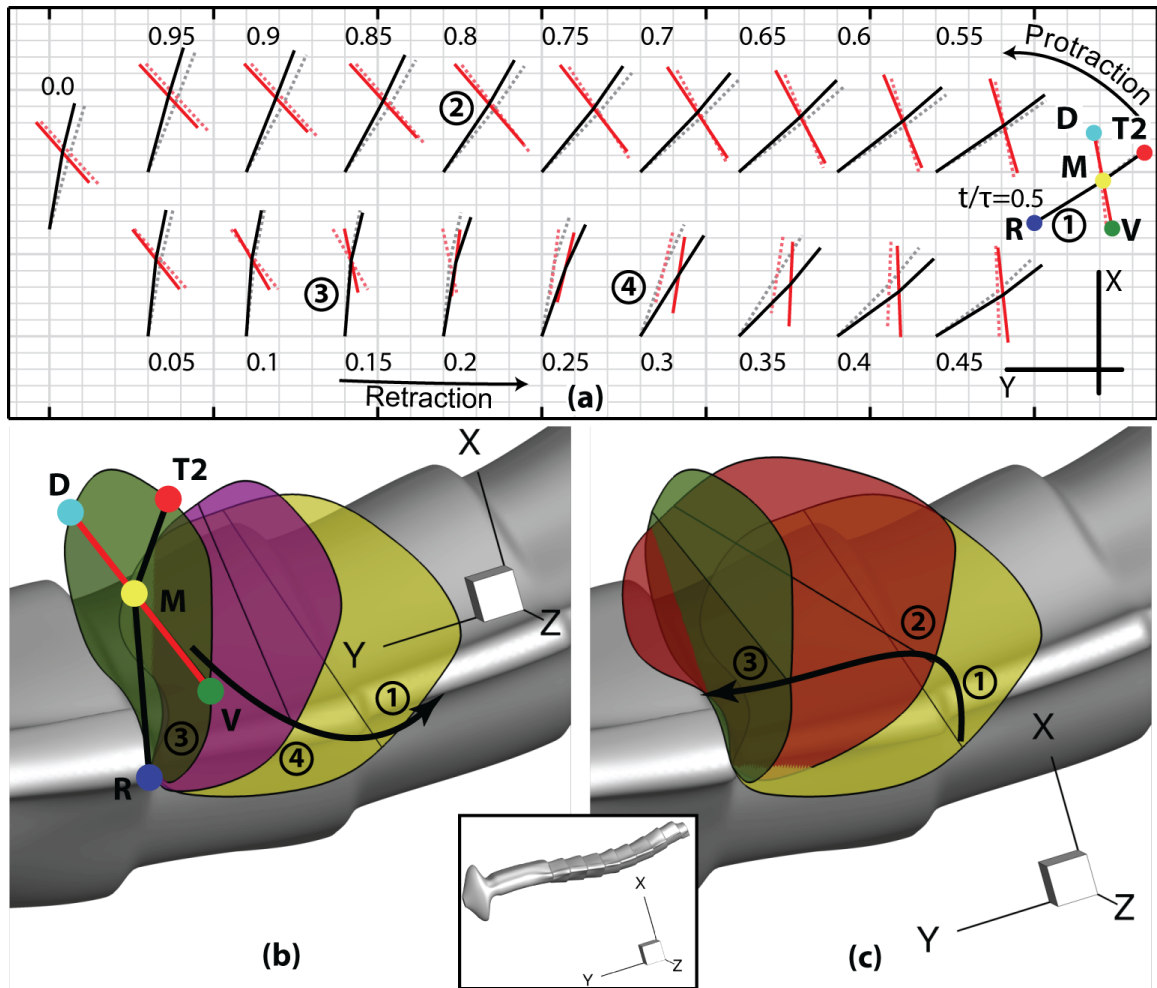


Figure 2.9: Prescribed mayfly rowing kinematics for gill 4. (a) Kinematics projected onto xy plane. Dashed trails in lighter shades are 0.025 earlier in the beating period ( $\tau = 1$ ). (b) Retraction (3D perspective). (c) Protraction (3D perspective). Inset illustrates the 3D perspective for parts (b) and (c). ①, ③: Extreme positions of proximal plate. ②: Mid-protraction. ④: Mid-retraction.

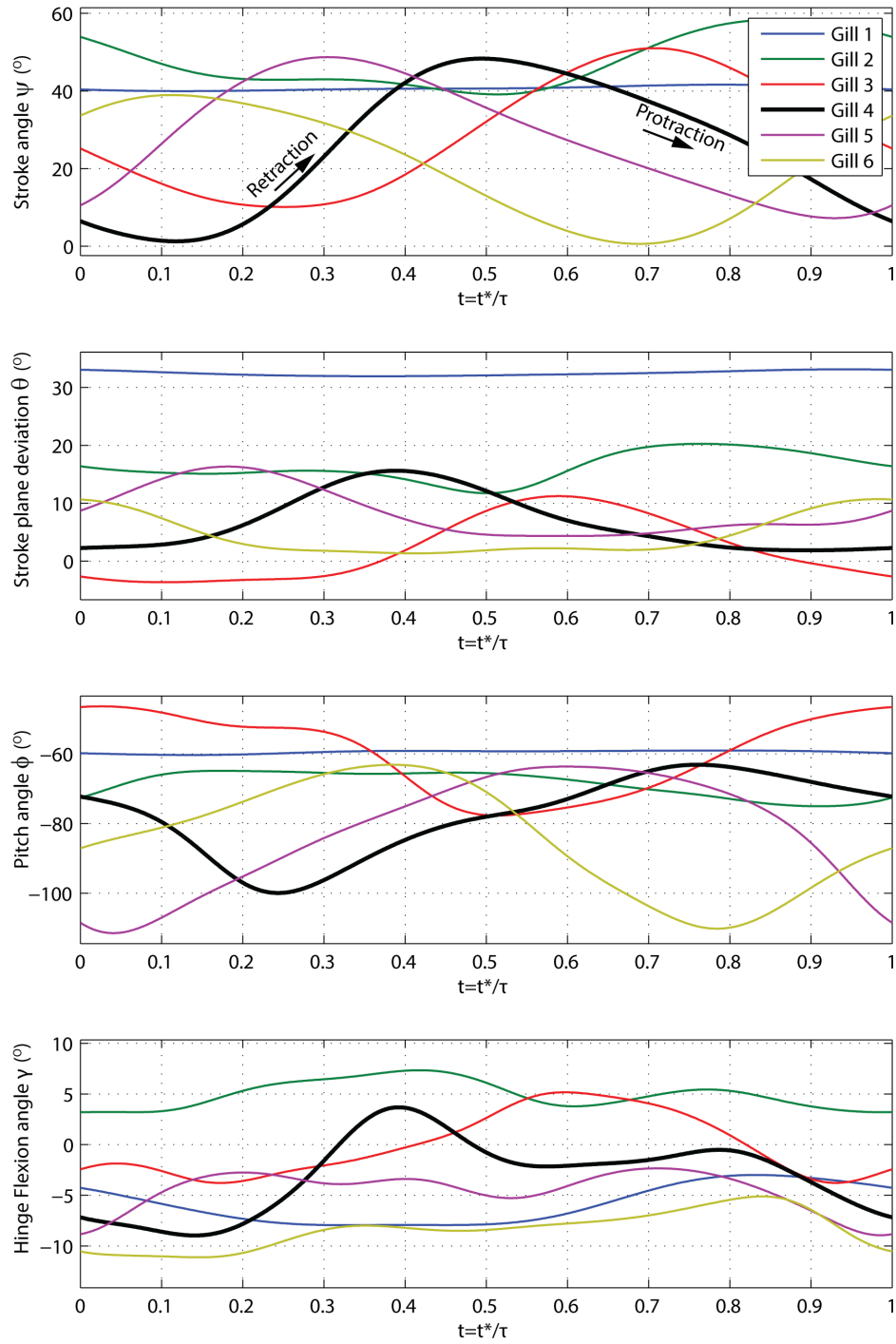


Figure 2.10: Eulerian angles for mayfly rowing kinematics ( $^\circ$ ). Top to bottom: Stroke or beating angle  $\psi_{1-6}(t)$ . Stroke plane deviation angle  $\theta_{1-6}(t)$ . Pitch angle  $\phi_{1-6}(t)$ . Hinge flexion angle  $\gamma_{1-6}(t)$ .

describing the motion of all the 6 gills is shown Figure 2.10. Noteworthy is that gill 1 is almost not moving and that the kinematics of gill 2 are not that similar to the remaining gills 3 to 6.

## 2.3 Governing Equations

Ideally, the physics of the problem would be investigated by solving for mass conservation, momentum conservation, and dissolved gases (oxygen) transport. However, the diffusion properties through the gills surface as well as the exact physiology inside the tracheal tubes is not well studied. In other words, one would have to solve for oxygen consumption (by simulating metabolism chemically for example) inside the mayfly in order to force the correct transport boundary conditions on the surrounding water. In addition, the exact solution of oxygen transport at such low  $Re$  and high  $Pe$  is cost-prohibitive. The estimated computational time is about 3 years if the same parametric spaces were to be carried out, not including the time needed to develop and validate the numerical codes. Therefore, including transport was beyond the scope of the current work, and, as a first approach, only mass and momentum conservation around the mayfly is considered. In light of that, the PDEs governing the problem are simply the continuity equation and the Navier-Stokes equations for incompressible Newtonian fluids, which in Cartesian coordinates read:

$$\frac{\partial u_i}{\partial x_i} = 0 \quad (2.23)$$

$$\frac{\partial u_i}{\partial t} + \frac{\partial(u_i u_j)}{\partial x_j} = -\frac{\partial p}{\partial x_i} + \frac{1}{Re_\omega} \frac{\partial^2 u_i}{\partial x_j \partial x_j} + f_i \quad i = (1, 2, 3) \quad (2.24)$$

where all the independent  $(\mathbf{x}, t)$  and dependent  $(\mathbf{u}, p)$  variables are dimensionless,  $x_i$  is the Cartesian coordinate in the  $i^{th}$  direction,  $u_i$  is the velocity component in the  $i^{th}$  direction,  $p$  is the pressure,  $f_i$  represents an external body force field used to implement the correct boundary conditions (will be introduced in §3).  $Re_\omega$  is the oscillating Reynolds number defined as  $Re_\omega = fL^2/\nu$  where  $f$  is the gill beating frequency,  $L$  is the gill length, and  $\nu$  is the kinematic viscosity. Both equations 2.23 and 2.24 were non-dimensionalized using the gill length,  $L$ , as a characteristic length scale, the beating period,  $\tau$  ( $= 1/f$ ), as a characteristic time scale, and  $U = Lf$  as a characteristic velocity scale with inertial scaling for the pressure gradient term ( $p_{ref} = \rho L^2 f^2$ ).

In the process of non-dimensionalizing the momentum equation, it is customary to relate the reference time ( $\tau$  or  $1/f$ ), the reference length ( $L$ ) and the reference velocity ( $U$ ) (i.e.  $U = fL$ ). This results in only one dimensionless group representing the ratio between the inertial forces and the viscous forces, which is the famously known Reynolds number. While this is may be a mathematical convenience, it may truncate some of the physics of the problem. Keeping the reference time, length and velocity unrelated will result, for example, in  $St = fL/U$  sitting next to the non-dimensionalized local acceleration. Now, it is common to associate  $St$  with the vortex shedding frequency ( $f$ ) as in the von Kármán street vortex behind bluff bodies or the inverted von Kármán street vortex associated with flapping bodies or even in flow meters. The question that arises now is what does  $St$  mean if there is no vortex shedding? i.e. the vortices are always attached to the body (which happens at the lower end of  $Re_\omega$  in my parametric space) or there are no vortices at all. In

light of that, I found it more insightful to distinguish between *Eulerian* inertia and *convective* inertia rather than *just* inertia. This may be thought of as an extension of the well-understood local and convective accelerations by multiplying by the "mass" of the fluid particle. Therefore, with the correct normalization and for small  $St$ , the fluid particle changes its inertia as it flows (*convects*) along its pathline (convective inertia  $>$  local inertia). On the contrary, for large  $St$ , the flow moves like a plug and there is a collective movement of the flow (local inertia  $>$  convective inertia). An example of large  $St$  flows is the unsteady Stokes flow. In unsteady flows or steady oscillatory flows, when  $St$  is close to unity (low end of  $Re_\omega$  in experimental studies [58]), there is a competition or balance between the *Eulerian* (also *local*) inertia and the *convective* inertia. For more insight about dimensional analysis, scaling, and orders of magnitude, the reader may consult [2]. Noteworthy is that  $St$  may also be regarded as the ratio between the frequency parameter ( $L^2/\nu\tau$ ) and Reynolds number. In light of that,  $Re_\omega$  introduced in (2.24) may be interpreted in many ways:

- ratio of the Eulerian inertia ( $\rho L^3 U/\tau$ ) to the viscous forces ( $\mu(U/L)L^2$ )
- ratio of the convective inertia ( $\rho L^3 U^2/L$ ) to the viscous forces ( $\mu(U/L)L^2$ )
- ratio of a characteristic length scale ( $L$ ) to a diffusive length scale (Oseen length  $= \nu/Lf$ )

All the mathematical tools are now ready for implementation in a discrete environment. The details of the numerical scheme along with the immersed boundary formulation will be introduced in §3. In the next section, two different metrics used to assess the micro-pumping of mayfly naiads are introduced.

## 2.4 Performance Metrics

In insect locomotion (i.e. flapping flight), it is usually straightforward to define performance metrics based on the generation of aerodynamic forces such as drag and lift. Simple models examining the mechanical efficiency for propulsion (work done to move the animal divided by the work done on the fluid) have shown that a switch from flapping to rowing kinematics is favored as one decreases the  $Re$  below 20 [12]. Mayfly nymphs, however, are not generating forces for the purpose of propulsion, but instead are flapping their gills to circulate water around them and enhance oxygen absorption. Therefore, it was necessary to create or look into novel performance metrics that could be computed based on the current model (mass and momentum conservation). With the nature of the flow field, a control volume approach such as the one shown in Figure 2.11 was devised and two performance metrics have been introduced.

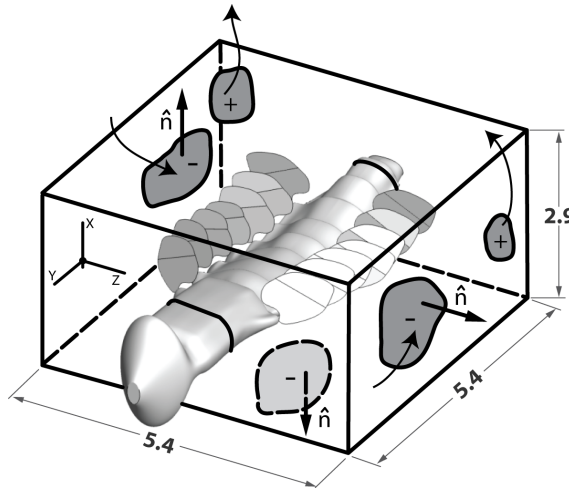


Figure 2.11: Schematic of control volume. Control volume encompasses the entire array of moving gills.

### 2.4.1 Mechanical Efficiency

One can define an efficiency similar to that of a hydraulic pump, which can be derived from the mechanical energy conservation equation:

$$\frac{d}{dt^*} \int E^* dV^* + \int E^* \mathbf{u}^* \cdot d\mathbf{A}^* = \int u_i^* \tau_{ij}^* dA_j^* - \int \phi^* dV^* \quad (2.25)$$

where  $E^* = 0.5\rho u_i^* u_i^*$  is the kinetic energy per unit volume,  $\tau_{ij}^* = -p^* \delta_{ij} + 2\mu e_{ij}^*$  is the stress tensor,  $\phi^* = 2\mu e_{ij}^* e_{ij}^*$  is the rate of viscous dissipation,  $e_{ij}^* = 0.5(\partial u_i^* / \partial x_j^* + \partial u_j^* / \partial x_i^*)$  is the strain rate tensor and the star superscript denotes dimensional variables [41]. Equation (2.25) is non-dimensionalized using the same reference parameters introduced in (2.23) and (2.24) ( $\rho L^5 f^3$ ) which yields:

$$\frac{d}{dt} \int E dV + \int E \mathbf{u} \cdot d\mathbf{A} = \int u_i \tau_{ij} dA_j - \int \phi dV, \quad (2.26)$$

where  $E = 0.5u_i u_i$ ,  $\tau_{ij} = -p\delta_{ij} + 2e_{ij}/Re_\omega$ ,  $\phi = 2e_{ij}e_{ij}/Re_\omega$ ,  $e_{ij} = 0.5(\partial u_i / \partial x_j + \partial u_j / \partial x_i)$ , where  $\mathbf{u}$ ,  $p$ ,  $\mathbf{x}$  and  $t$  are dimensionless as previously introduced in (2.23) and (2.24). Equation (2.26) is then time averaged over an entire beating period. The term corresponding to adding power to the control volume is identified, which is the time-averaged rate of work done by the moving gills. Also, the two terms corresponding to the rate of work done by the control volume are identified, which are the time-averaged kinetic energy flux through the control volume and the time-averaged rate of work done by the control volume on the remaining outer domain. The mechanical efficiency can now be defined as the ratio between the time-averaged output power and the time-averaged input power, where the difference between these is simply the time-averaged rate of viscous dissipation or the rate of energy loss throughout the

control volume averaged over an entire beating cycle. The mechanical efficiency can be expressed as follows:

$$\eta(\%) = \frac{\overline{\int_{outer} E\mathbf{u} \cdot d\mathbf{A}} - \overline{\int_{outer} u_i\tau_{ij}dA_j}}{\overline{\int_{gills} u_i\tau_{ij}dA_j}} \times 100 \quad (2.27)$$

where 'outer' refers to the surface defined by the six planes corresponding to the rectangular control volume in Figure 2.11, and 'gills' refer to the surface of the gills. The overbar denotes time-averaged quantities. Note that the kinetic energy flux through the control surfaces around the gills is zero owing to the assumed zero thickness of the gill plates. The mechanical efficiency,  $\eta$ , is analogous to that of a hydraulic pump where the denominator is the shaft input power while the numerator is the energy flux in the fluid and stress work done on the outer control volume boundary.

#### 2.4.2 Specific Mass Flow Rate

With reference to the same control volume shown in Figure 2.11, a second performance parameter is introduced; the specific mass flow rate,  $\xi$ .  $\xi$  is defined as follows:

$$\xi = \frac{\overline{\dot{m}}}{\dot{W}_{gills}}, \quad (2.28)$$

where

$$\dot{m} = \begin{cases} \int_{outer} \rho\mathbf{u} \cdot d\mathbf{A} & \text{if } \mathbf{u} \cdot d\mathbf{A} > 0 \\ 0 & \text{otherwise} \end{cases}, \quad (2.29)$$

and

$$\dot{W}_{gills} = \int_{gills} u_i\tau_{ij}dA_j \quad (2.30)$$

where  $\dot{m}$  is the mass flow rate leaving the control volume, and  $\dot{W}_{gills}$  is the rate of work done by the six pairs of gills.  $\xi$  is interpreted as the dimensionless time-averaged mass flow rate towards the mayfly divided by the dimensionless time-averaged rate of work done by the gills. It can be argued that the mass flow rate towards the mayfly is associated with the oxygen absorption by the gills. Therefore, the higher  $\xi$ , the better the performance, since in an average sense, higher oxygen absorption is achieved per unit power. The results of both metrics will be presented in §4 and §5.

## Chapter 3: Numerical Methodologies and Validation

In this chapter, the numerical methodologies and the computational setup used to solve for the laminar flow around mayfly nymphs are presented. This includes the domain spatial discretization, the time advancement scheme and the immersed boundary formulation used to implement the boundary conditions on the fluid. This will be followed by comparisons with *in-vivo* and robotic PIV experiments.

### 3.1 Spatial and Temporal Discretization

The equations governing the laminar flow of water around the mayfly were previously introduced in §2.3 and read:

$$\frac{\partial u_i}{\partial x_i} = 0 \quad (3.1)$$

$$\frac{\partial u_i}{\partial t} + \frac{\partial(u_i u_j)}{\partial x_j} = -\frac{\partial p}{\partial x_i} + \frac{1}{Re_\omega} \frac{\partial^2 u_i}{\partial x_j \partial x_j} + f_i \quad i = (1, 2, 3) \quad (3.2)$$

where  $f_i$  is a the forcing function in the  $i^{th}$  direction and is non-zero near the solid boundaries.

The above conservation laws are solved using a finite differencing approach with a standard second-order central-difference scheme on a Cartesian staggered grid. In a staggered arrangement, the pressure and other scalar variables are located at the

center of the grid cell, while velocity components are located at the cell face centers. The most important advantage of staggered grids over collocated grids is the stronger coupling between the pressure and the velocities, which avoids the so-called odd-even decoupling between the pressure and the velocity. The numerical approximation on a staggered grid is also conservative of kinetic energy [27]. Staggered grids, however, can be trickier to implement, since 4 grids are involved in computing the different gradients.

As for time advancement, a fractional time step method is used to integrate the unsteady momentum equation. In particular, the low-storage third-order Runge-Kutta (RK3) scheme is used:

$$\frac{\hat{u}_i - u_i^{n-1}}{\Delta t} = \gamma_k A(u_i^{n-1}) + \rho_k A(u_i^{n-2}) - \alpha_k \frac{\partial p^{n-1}}{\partial x_i} + f_i^{n-1} \quad (3.3)$$

$$\frac{\partial^2 \phi^n}{\partial x_i \partial x_i} = \frac{1}{\alpha_k \Delta t} \frac{\partial \hat{u}_i}{\partial x_i} \quad (3.4)$$

$$u_i^n = \hat{u}_i - \alpha_k \Delta t \frac{\phi^n}{x_i} \quad (3.5)$$

$$p^n = p^{n-1} + \phi^n \quad (3.6)$$

where  $n$  is the time subscript and ranges from 1 to 3 for the RK3 scheme,  $\Delta t$  is the time step and  $f_i^{n-1}$  is the forcing function. The velocity  $\hat{u}_i$  is the intermediate velocity, which does not satisfy the continuity equation. Therefore, the Poisson equation (3.4) is solved and the scalar  $\phi$  is used to project  $\hat{u}_i$  into a solenoidal (divergence-free) field. The spatial operator  $A$  contains the convective and viscous fluxes which are evaluated at the cell faces. The discretization of the above equations on a staggered grid in the computational space is described in detail in [8, 80]. The coefficients for

the RK3 scheme are:

$$\alpha_1 = 8/15, \gamma_1 = 8/15, \rho_1 = 0$$

$$\alpha_2 = 2/15, \gamma_2 = 5/15, \rho_2 = -17/60$$

$$\alpha_3 = 1/15, \gamma_3 = 3/4, \rho_3 = -5/12$$

with:

$$\sum_{k=1}^3 \alpha_k = \sum_{k=1}^3 (\gamma_k + \rho_k) \quad (3.7)$$

In addition, the following stability criterion (or the generalized CFL number including the time step constraint from the viscous terms) is adopted [8, 80]:

$$CFL = \Delta t \left[ \frac{|u|}{\Delta x} + \frac{|v|}{\Delta y} + \frac{|w|}{\Delta z} + 2\nu \left( \frac{1}{\Delta x^2} + \frac{1}{\Delta y^2} + \frac{1}{\Delta z^2} \right) \right] \quad (3.8)$$

Theoretically, the stability limit for RK3 is  $\sqrt{3}$ . However, the actual *CFL* number may be lower because the cross-derivatives are not included in the stability analysis. Consequently, in all simulations, a *CFL* = 1.0 was found to yield a stable solution.

The Poisson equation shown in vector form in (3.4) can be expressed in discrete form in Cartesian coordinates as:

$$\left( \frac{\partial^2}{\partial^2 x} + \frac{\partial^2}{\partial^2 y} + \frac{\partial^2}{\partial^2 z} \right) \phi_{i,j,k} = g_{i,j,k} = \frac{1}{\alpha_n \Delta t} \frac{\partial \hat{u}_i}{\partial x_i} \quad (3.9)$$

where  $n$  is the sub-step index for RK3 and  $\phi = p^n - p^{n-1}$ . With a second order spatial discretization, the 3-dimensional discretized version of the Poisson equation results in a hepta-diagonal coefficient matrix, which is extremely expensive to invert directly. A common approach to alleviate the computational cost is to apply a Discrete Fast Fourier Transform (DFFT) to the Poisson equation (3.9) in order to reduce the hepta-diagonal coefficient matrix into a penta-diagonal or even tri-diagonal matrix. For

example, applying a DFFT in the y-direction transforms (3.9) into a set of two-dimensional Helmholtz equations in the uncoupled wave number space:

$$\left( \frac{\partial^2}{\partial^2 x} + k'_l + \frac{\partial^2}{\partial^2 z} \right) \hat{\phi}_{i,j,k} = \hat{g}_{i,j,k} \quad (3.10)$$

where  $k'_l$  is the modified wave number and is expressed as:

$$k'_l = \frac{2}{\Delta y^2} \left[ 1 - \cos \left( \frac{2\pi l}{N_y} \right) \right] \quad (3.11)$$

where  $l$  is the wave number,  $\Delta y$  is the cell size in the y-direction and  $N_y$  is the number of grid cells in the y-direction not including the ghost cells. Since the above equation includes derivatives only in the x-direction and z-direction, the resulting coefficient matrix is penta-diagonal. Hence, a set of  $N_y$  uncoupled equations in wave space may be solved independently. This procedure was implemented using the FFTPACK library and FISHPACK library, in which a generalized cyclic reduction algorithm ('BLKTRI') is used [61, 62]. The solution is transformed back to the physical space by taking the inverse DFFT of  $\hat{\phi}$ .

The use of DFFT in some direction comes with a known caveat, in that the flow must be homogeneous and periodic in that direction. In addition, the numerical grid must be uniform in that direction. Noteworthy is that DFFT routines are optimized when the number of points can be factored to the smallest prime numbers.

## 3.2 Treatment of Immersed Boundaries

Over the past decades, a variety of non-boundary-conforming methods with various degrees of accuracy and complexity have been proposed, among which are

the Cartesian cut-cell formulations and the immersed boundary (IB) methods. The IB formulation was pioneered by Peskin [51, 52] and has been receiving an increased attention over the past decade [4, 8, 68, 69, 80–82].

IB methods provide a way to impose no-slip boundary conditions on immersed surfaces that do not conform to the Eulerian grid. The velocity field is reconstructed around these surfaces by applying a force field ( $f_i$ ) on the discrete momentum equations in order to satisfy the correct no-slip boundary condition. The most important feature of the IB methods is that the Eulerian grid (grid where fluid conservation laws must be satisfied) need not to relate in a special way to the Lagrangian grid (grid defining the immersed boundary), except that the moving Lagrangian grid must be sufficiently dense with respect to the fixed Eulerian grid. If the Lagrangian grid happens to be too coarse with respect to the Eulerian grid, the no-slip boundary conditions will be incorrectly represented. The simplicity of the IB method facilitates the numerical integration of the Navier-Stokes equations and is usually applied within a fractional time step method.

In 'direct forcing' IB methods, the forcing is done in the discrete equations defined on the Eulerian grid, and it is defined such that the boundary conditions are satisfied on the boundary itself [4, 26]. These methods are attracting because their ease of implementation in existing finite differences or finite volumes formulations. However, moving immersed boundaries introduce additional complications to direct forcing methods, which leads to hydrodynamic forces that lack smoothness and, therefore, stability [64, 81]. A different approach in IB methods is to compute the forcing function on the Lagrangian (moving) grid and then 'transfer' this function to the Eu-

lerian grid. This approach is introduced next, where the transfer is performed using the Method of Least Squares (MLS).

### 3.2.1 MLS Reconstruction

In the formulation proposed by Uhlmann [64], the direct forcing function is computed on each Lagrangian marker, rather than on the Eulerian grid nodes. However, Uhlmann’s formulation was tailored to a specific problem and provided only integral quantities of the hydrodynamic forces. Based on the formulation by Uhlmann and ideas presented in [42, 49], Vanella [68, 69] proposed a direct forcing scheme that utilizes a versatile MLS approximation in order to build the transfer functions between the Eulerian and the Lagrangian grids. The MLS approximation can be applied to arbitrary moving or deforming bodies. Vanella also proposed a method to compute the local traction forces. The overall formulation utilizes very compact stencils and, without compromising accuracy and robustness, gives results that are identical to ‘sharp’ direct forcing methods. A short description of the formulation is given hereunder. Further details can be found in [68, 69] and [49].

First, the velocity component in the  $i^{th}$  direction on a Lagrangian marker is approximated in its support domain by:

$$\tilde{U}_i(\mathbf{x}) = \sum_{j=1}^m p_j(\mathbf{x}) a_j(\mathbf{x}) = \mathbf{p}^T(\mathbf{x}) \mathbf{a}(\mathbf{x}) \quad (3.12)$$

where  $\tilde{U}_i(\mathbf{x})$  is the approximated velocity of the Lagrangian marker in the  $i^{th}$  direction,  $\mathbf{p}^T(\mathbf{x})$  is the basis functions vector of length  $m$ ,  $\mathbf{a}(\mathbf{x})$  is the vector of coefficients and  $(x)$  is the position vector of the Lagrangian marker. A linear basis,  $\mathbf{p}^T(\mathbf{x}) =$

$[1 \ x \ y \ z]$ , was found to be a cost efficient choice that preserves the second order spatial discretization scheme. Also, a support domain of approximately 2.4 the grid spacing in each direction was found to be sufficient.

Second, to obtain the coefficient vector  $\mathbf{a}(\mathbf{x})$ , a weighted  $L2$ -norm is defined:

$$J = \sum_{k=1}^{ne} W(\mathbf{x} - \mathbf{x}^k) [\mathbf{p}^T(\mathbf{x}^k)\mathbf{a}(\mathbf{x}) - \hat{u}_i^k]^2 \quad (3.13)$$

where  $\mathbf{x}^k$  is the position vector of the Eulerian point  $k$  in the Eulerian interpolation stencil,  $ne$  is the total number of Eulerian grid points in the interpolation stencil,  $\hat{u}_i^k$  is the intermediate velocity in the  $i^{th}$  direction (calculated from (3.3)) for an Eulerian grid point  $k$ , and  $W(\mathbf{x} - \mathbf{x}^k)$  is a known weighting function that uses cubic splines.

The solution of the minimization problem yields the shape function  $\Phi(\mathbf{x})$  of the Lagrangian marker  $l$ , which is a column vector of length  $ne$ . The velocity component of the Lagrangian marker in the  $i^{th}$  can now be calculated from:

$$\tilde{U}_i(\mathbf{x}) = \sum_{k=1}^{ne} \phi_k^l \hat{u}_i^k = \Phi^T(\mathbf{x}) \hat{\mathbf{u}}_i^k \quad (3.14)$$

where  $ne$  is the total number of Eulerian grid points in the interpolation stencil and  $\phi_k^l$  is the value of the shape function corresponding to the Lagrangian marker  $l$  and Eulerian grid point  $k$ .

Third, the amount of forcing required on the Lagrangian marker in the  $i^{th}$  direction is computed from:

$$F_i^n = \frac{U_i^d - \tilde{U}_i}{\Delta t} \quad (3.15)$$

where  $U_i^d$  is the desired velocity of the Lagrangian marker (boundary condition) in the  $i^{th}$  direction.

With that, the forcing function is computed on all the Lagrangian markers and the last step is to transfer the forcing function  $F_i^n$  back to the Eulerian grid. By requiring that the total force acting on the fluid not to change by the transfer, the forcing function on the Eulerian grid points can be computed from:

$$f_i^k = \sum_{l=1}^{nl} c_l \phi_k^l F_i^l \quad (3.16)$$

where  $c_l$  is a scaling factor related to the average volume associated with the Lagrangian markers and the average volume of the Eulerian grid cells [49, 68, 69].

In practice, the MLS formulation works in the following steps: 1) Locate a Lagrangian marker to enforce its no-slip boundary condition. 2) Locate the nearest Eulerian neighbor to that Lagrangian marker using bisection routines. 3) Build an interpolation stencil that consists of a minimum of 5 points for 3D problems (3.12). 4) Find the minimum weighted  $L2$ -norm of the difference between the Eulerian intermediate velocity field  $\hat{u}_i$  and their regressed values  $\tilde{U}_i$  (defined by (3.13)), which yields the MLS shape functions  $\Phi(\mathbf{x})$ . 5) Use the shape functions to transfer (interpolate) the Eulerian velocity field  $\hat{u}_i$  to the Lagrangian marker  $\tilde{U}_i$  (3.14). 6) Compute the amount of Lagrangian forcing required to satisfy its boundary condition (3.15). 7) Rescale the shape functions by way of conserving the total force to be transferred. 8) Transfer (interpolate) the forcing function back to the Eulerian stencil (3.16). 9) Loop on all the Lagrangian markers and sum the forcing field on the neighboring Eulerian points. 10) Repeat for each direction  $i$ .

### 3.2.2 Evaluation of Surface Forces

Non-boundary conforming formulations are faced with complications in computing the hydrodynamic forces generated by the surrounding fluid. This is because the Eulerian and the Lagrangian grid are almost never aligned. Once the force field is computed from (3.16), Uhlmann [64] proposed a formulation for computing the hydrodynamic forces on rigid bodies provided that all interior points are treated properly. However, Vanella [68, 69] proposed a different approach for the general case of moving or deforming bodies, which is based on the MLS formulation discussed previously. The hydrodynamic force per unit area on a surface element in the  $i^{\text{th}}$  direction may be computed directly from the flow field around the body by:

$$f_i^H = \tau_{ij} n_j = [-p\delta_{ij} + 2Re_\omega^{-1} e_{ij}] n_j \quad (3.17)$$

where

$$e_{ij} = \frac{1}{2} \left( \frac{\partial u_i}{\partial x_j} + \frac{\partial u_j}{\partial x_i} \right) \quad (3.18)$$

and  $n_j$  is the direction cosine of the unit normal vector in the  $x_j$  direction. Equation (3.17) has been non-dimensionalized using the same reference variables introduced in the non-dimensionalization of the continuity (2.23), momentum (2.24) and energy (2.26) equations, i.e. inertial scaling for the pressure  $\rho L^2 f^2$ ,  $fL$  for the reference velocity and  $f$  for the reference time. The use of (3.17) requires the knowledge of  $p$  and  $\partial u_i / \partial x_j$  on the body surface. However, the MLS formulation outlined in §3.2.1 underestimates the actual traction forces due to the smoothness introduced in the velocity field. Therefore, to find the pressure on a Lagrangian marker  $l$  and assuming

a linear velocity variation near the immersed bodies,  $\partial p/\partial n$  is first evaluated from [81]:

$$\frac{\partial p}{\partial n} = -\frac{D\mathbf{u}}{Dt} \cdot \mathbf{n} \quad (3.19)$$

where  $\mathbf{n}$  is the unit normal vector passing through the Lagrangian marker  $l$  and  $D\mathbf{u}/Dt$  is the absolute linear acceleration of the marker  $l$ . The value of the pressure at the surface can then be obtained from:

$$p^l = p^e - \frac{\partial p}{\partial n} h_n \quad (3.20)$$

where  $p^e$  is the pressure at point  $e$  in the Eulerian domain, which lies on the unit normal  $\mathbf{n}$  at distance  $h_n$ , where  $h_n$  is the average grid spacing at point  $e$ .

To find the velocity gradients  $\partial u_i/\partial x_j$ , the same MLS reconstruction discussed in §3.2.1 is used, but instead of reconstructing (interpolating) the velocity components, the gradients themselves are reconstructed using derivatives of the shape functions. The velocity gradients on the immersed bodies can then be computed from:

$$\frac{\partial U_i}{\partial x_j} = \sum_{k=1}^{ne} \frac{\partial \phi_k}{\partial x_j} u_i \quad (3.21)$$

where  $ne$  is the number of Eulerian grid points in the interpolation stencil and  $\partial \phi_k/\partial x_j$  results from the solution of a minimization problem similar to (3.13). Assuming a linear variation of the velocity near the body, the derivatives,  $\partial U_i/\partial x_j$ , coming from equation (3.21) are a good approximation of the derivatives  $\partial u_i/\partial x_j$  at the surface.

The evaluation of the surface forces is generally more computationally expensive per time step than the evaluation of the forcing functions because it requires the reconstruction of the 9 components of the velocity gradient tensor while the computation of the forcing functions requires only the reconstruction of the 3 velocity

components. Fortunately, the surface forces don't need to be evaluated at each time step in the current framework of prescribed kinematics.

### 3.3 Computational Setup

The numerical tools are almost ready to perform the simulations. To recap, both the continuity equation and the Navier-Stokes equations (3.2) are solved on a staggered grid where the advective and diffusive terms are evaluated using second order differencing and time is advanced using a fractional step method, namely the low-storage Runge-Kutta scheme (3.3). An IB method is used to implement the moving boundary conditions, which use a MLS reconstruction technique to transfer the forcing between the Eulerian and Lagrangian meshes. The numerical solver was parallelized using a domain decomposition strategy [8]. The code was compiled and executed on the University of Maryland High Performance Computing Cluster (Deepthought). The code was developed in FORTRAN90, uses the MPIF90 library and is executed on Intel's Xeon processors with Linux RedHat. Details about the computational setup used to simulate the mayfly nymphs follows.

A surface mesh of the mayfly computational model introduced in §2.1 was created using Gambit (Gambit 2.4.6). Triangular elements were clustered near the gill roots, where the surface geometry is most complex. The mesh was checked for quality (skewness, regularity and inverted elements). In the end, the surface of the mayfly abdomen, thorax and head required 659216 triangular elements (329610 nodes) to describe it. Coarser meshes resulted in highly skewed elements near the surface ridges

or even elements that don't describe the surface correctly. On the other hand, only 118580 elements were needed to describe the 14 proximal plates and 79072 elements to describe the 14 distal plates (planform A) making the total number of elements required to fully describe the immersed boundaries 856868 elements.

The Lagrangian grid was then immersed into a computational domain, which is a rectangular prism with dimensions  $10L \times 30L \times 20L$  in the  $x$ ,  $y$  and  $z$  directions respectively as illustrated in Figure 3.1. The mayfly nymph lies longitudinally along the  $y$ -axis. Plane  $z = 0$  is the median plane (plane of symmetry) of the mayfly with the left row of gills on the positive side of the  $z$ -axis. The  $x$ -axis is pointing dorsally (upwards) from the origin.

As for the domain boundary conditions, the bottom wall is modeled as a no-slip wall, while the other five walls are modeled as slip walls. It is worth pointing out that the computational domain is sufficiently large to minimize effects of the domain boundaries on the inner flow field. In fact, the bounding box encompassing the six pairs of moving gills represents less than 0.2% of the domain by volume. The domain is discretized with  $200 \times 1200 \times 400$  points in  $x$ ,  $y$  and  $z$  directions respectively (96 million points total). Stretching is applied to cluster points in the region around the mayfly. The cells size were designed so that 40 of them would span the entire gill length when it is in an orthogonal plane. The code is typically executed using a minimum of 100 processors. A typical sampling output yields approximately 300GB of data saved for further post processing. Time discretization resulted in 562 time steps per cycle for the highest Reynolds number ( $Re_\omega = 21.6$ ) and 10091 time steps per cycle for the lowest Reynolds number ( $Re_\omega = 1.0$ ) making the computational

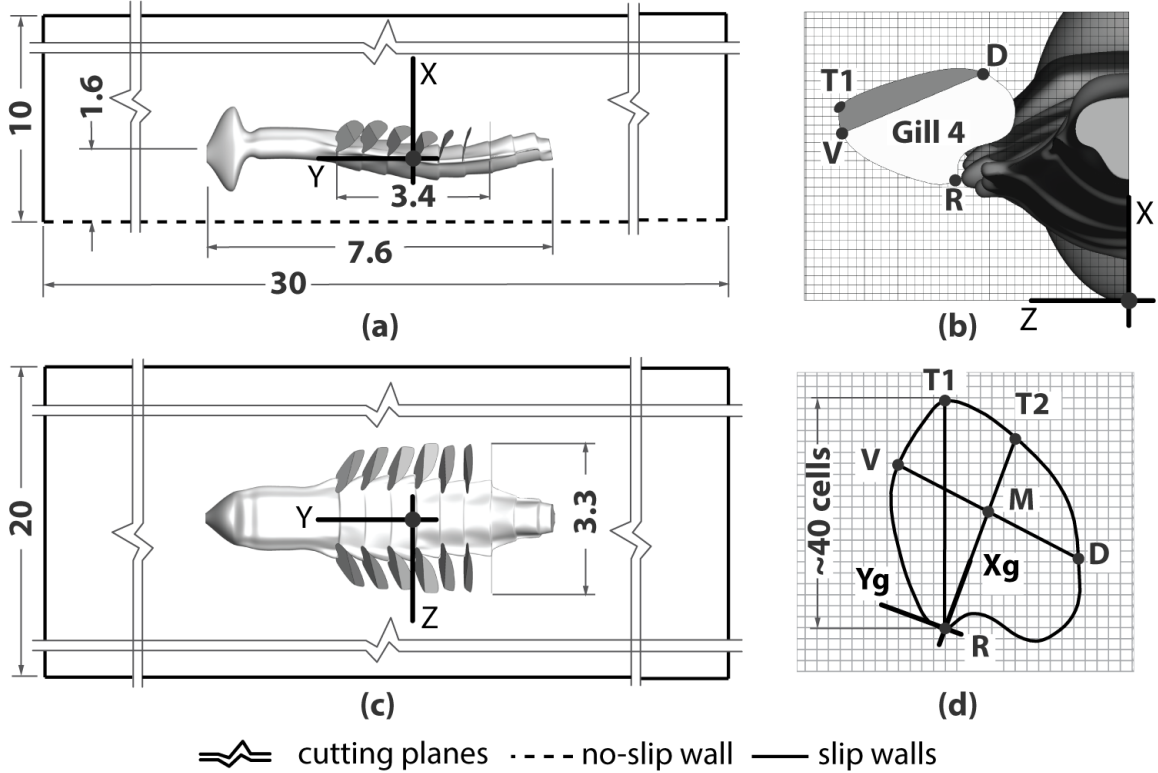


Figure 3.1: Schematic of computational Domain. (a,c) Computational domain lateral and top view. (b) Closeup of mayfly posterior view (back) showing left gill 4. (d) Gill immersed in computational domain. Numerical Grid shown is half the actual density for clarity. (R)Root. (V)Ventral. (D)Dorsal. (M)Midchord. (T1)Tip.

time vary between 5 to 25 days for each simulation.

### 3.4 Comparison with Experiments

The second order accuracy of the NSE solver used in executing the simulations was previously validated and led to a series of publications [8–10, 80–82]. In addition, the accuracy of the IB forcing using the MLS reconstruction as well as the calculus of hydrodynamic forces was established by [68, 69], where it was shown that it preserves the second order accuracy of the numerical schemes. Therefore, in the current work, the main purpose of the comparison with the experiments is to ascertain that the flow

physics observed *in-vivo* are replicated numerically. In other words, the numerical grid is fine enough in order to capture the flow physics or more and the prescribed kinematics are accurate enough to reproduce the main flow features of the rowing and flapping.

Therefore, in the following section, comparisons with previous PIV experiments performed on live mayfly nymphs is presented for both flapping at  $Re_\omega = 21.6$  and rowing at  $Re_\omega = 2.3$ . This will be followed by comparisons with robotic experiments using an idealized rowing type of kinematics at  $Re_\omega = 17.6$ . It will be shown that the physical problem is replicated with sufficient accuracy that enables the execution of other hypothetical situations without the need for further validation. The main goal of the comparisons is to establish confidence in the numerical results. The specific details of the flow fields however, will be deferred to §4.

### 3.4.1 Comparison with *in-vivo* Experiments

Previous experimental work by [57–59] investigated the rowing-flapping transition occurring in *C. triangulifer*. In order to investigate the beating kinematics, 9 nymphs were studied aging 20 – 42 days with  $0.25mm < L < 0.77mm$  and  $2.1 \pm 0.18 < Re_\omega < 21.6 \pm 1.2$ . Oscillation frequencies were in the range 20 – 36Hz with no significant trend associated with  $Re_\omega$ . In reporting the results, the nymphs beating kinematics were classified into three types: 1) rowing for  $Re_\omega < 5$ , which was characterized by a higher pitching range and a negligible hinge flexion angle (of the same order of the digitization error), 2) flapping for  $Re_\omega > 20$ , which was character-

ized by a minimal pitch variation and the formation of a distal flap that appeared to move passively, and 3) intermediate kinematics for  $5 < Re_\omega < 20$ , which marked abrupt and gradual changes in many parameters as for example the hinge flexion angle, which increased from  $17 \pm 2^\circ$  to  $61 \pm 7^\circ$  and decreased stroke plane deviation.

After extracting the beating kinematics, PIV measurements were carried out. The combination of the lenses and the Argon laser provided a light sheet that was approximately  $20mm$  wide and  $0.15 - 0.2mm$  thick. The field of view varied from  $3mm \times 3mm$  for the smallest nymph and up to  $9mm \times 9mm$  for the largest nymph (animal length varied between  $2 - 5.64mm$  excluding the caudal filaments). The vertical light sheet was parallel to the medial plane (vertical) and centered between the lateral and medial extents of the gill plates ( $\pm 0.2mm$ ). Framing rates of  $1kHz$  allowed for cyclical resolution of approximately  $10^\circ$ , with a spatial resolution of approximately  $25\mu m$  for the  $3mm \times 3mm$  field of view. Of the approximately 30 cycles recorded in a typical imaging sequence, an ensemble of  $N = 10$  frame pairs was found to be sufficient to converge velocity fields at the desired resolution. The maximum uncertainty for the velocity was taken to be  $2.5mm/s$  which was typically  $5 - 10\%$  of the maximum velocity.

Restricted by the availability of full and reliable experimental sets, comparisons with two live nymphs were carried out. The first is for a large nymph flapping at  $Re_\omega = 21.6$ , while the second is for a small nymph rowing at  $Re_\omega = 2.3$ . The first comparison was very successful, while the second is less successful, probably due to the higher uncertainties associated with smaller nymphs. For both comparisons, the primary source of discrepancy stems from geometrical dissimilarities between

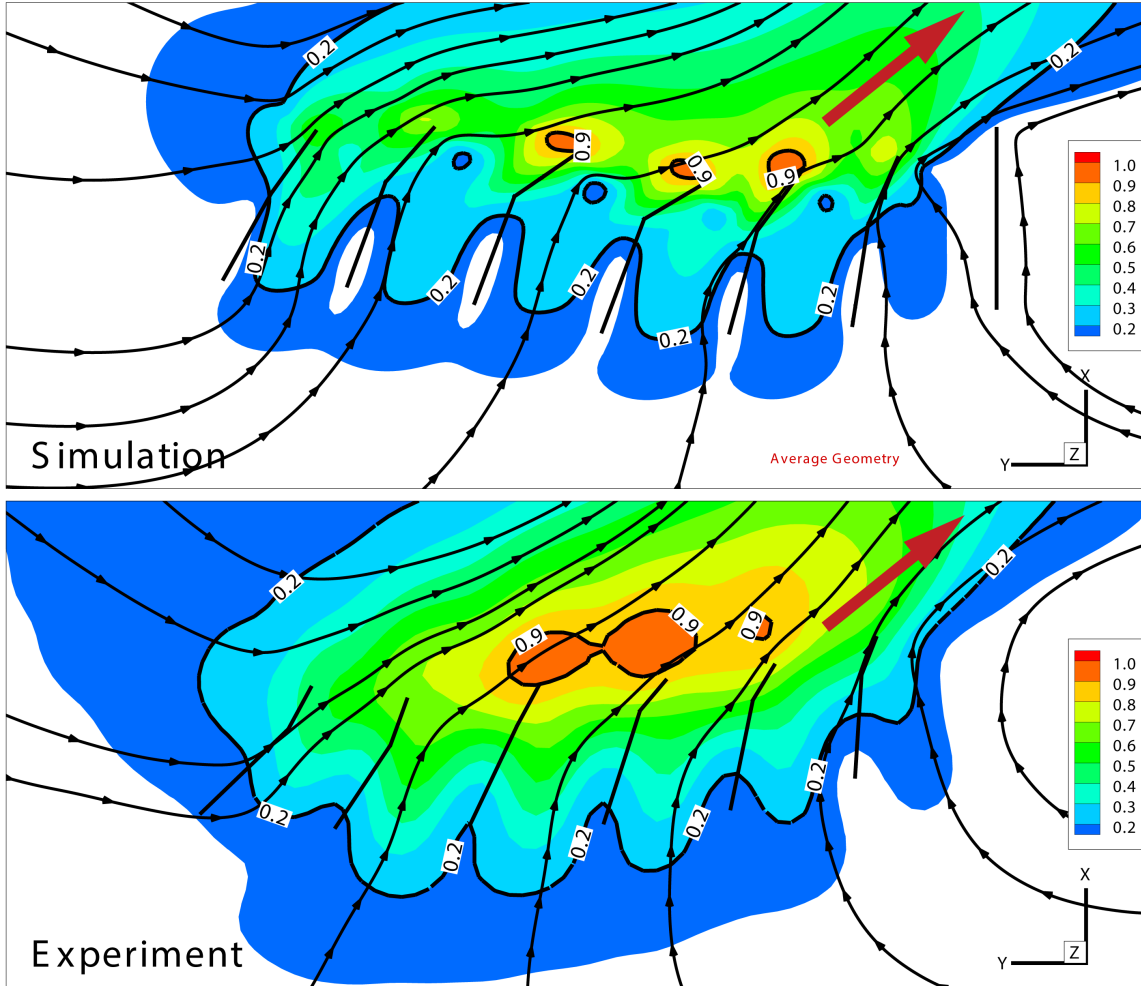


Figure 3.2: Comparison of the time-averaged in-plane velocity magnitude of the flapping kinematics at  $Re_\omega = 21.6$ . Velocity magnitude is normalized by the local maximum. Top: Simulation (showing 7 gills). Bottom: *In-vivo* experiments (showing only 6 gills). Non-moving gill pair 7 was not tracked by experiments. Contour floods below 0.1 are cutoff.

the dissected nymph used to build the computational model and the nymphs used in extracting the kinematics and performing the PIV measurements. In other words, the variability and the morphological changes inherent to the *in-vivo* experiments are the main source of discrepancy. To give an example of such variability, one notices that during the digitization of the flapping kinematics of the large nymphs, the beating frequency was reported at  $37Hz$ , while during the PIV analysis (performed on the

*same* day on the *same* nymph) showed a frequency of  $34Hz$ . Another prevalent source of discrepancy is the vertical distance between the nymphs and the bottom wall. In PIV experiments, this distance was kept constant for all nymphs sizes, which would not achieve geometrical similarity with the water tank since the nymph keeps growing. In numerical simulations, the viscosity of the fluid was manipulated rather than changing the gill size, which maintains geometrical similarity. This is more desirable since it provides a self-consistent set of numerical results that can be analyzed later. One more idealization was introduced to the computational model by maintaining a constant gill length for all 7 pairs. In reality, the mayfly gills get smaller towards the thorax and the tail making gill 1 and 7 the smallest while gill 3 and 4 the biggest. The actual size of gills 1 and 6 could be smaller than the computational model by as much as 10%. The uncertainty in  $Re_\omega$  ( $\approx \pm 1$ ) is another contributing factor that may affect the size of the different structures in all comparisons.

All PIV results presented here were obtained at the mid-section of the gills, i.e. at  $z/L = 1.15$ . Additionally, to mimic the experimental resolution, the numerical results were spatially averaged over a thickness equal to that of the laser sheet, which was approximately  $0.2mm$  or the equivalent of 8 numerical cells. Detailed comparisons of the time-averaged flow fields of the flapping kinematics at  $Re_\omega = 21.6$  are shown in Figures 3.2, 3.3 and 3.4. Figure 3.2 shows the time-averaged velocity magnitude normalized by its local maximum. Overall, the qualitative agreement is acceptable and all the main flow features are reproduced by the computations. As in the experiments, the flow enters from the bottom and left planes (ventral and anterior), while the top and right planes (dorsal and posterior) exhibit both inflow and outflow. Also, the

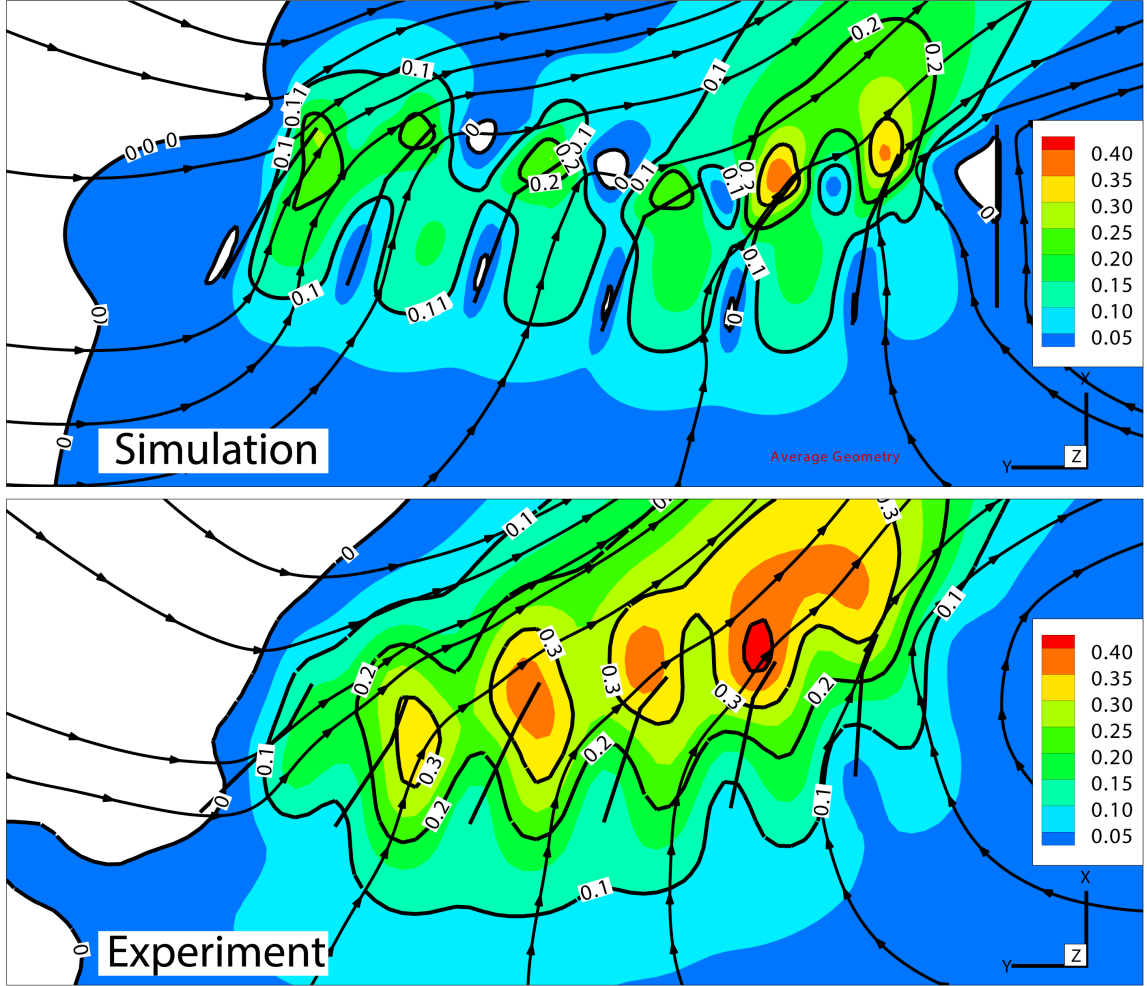


Figure 3.3: Comparison of the time-averaged x-component of the velocity  $u$  for flapping kinematics at  $Re_\omega = 21.6$ . Contour floods below 0.1 are cutoff.

predicted mean outflow direction matches that of the experiments. Quantitatively, the predicted time-averaged velocity magnitude has the correct range and comparable distribution. In the simulations, however, more localized peaks in the velocity magnitude can be observed at the gills dorsal and ventral edges. This could be due to limited experimental resolution or geometrical dissimilarities (inter-gill spacing is smaller in experiments). It should also be noted that the differences in some of the mean gill locations (i.e. gills 2 and 3), are due to the fact that the experimental gills

shown represent an approximate location of the gills (average of intersections with laser sheet), while in the simulations, the exact mean location is shown. Noteworthy is that the simulation shows that the out-of-plane velocity component (also the  $w$  or lateral component) is localized around the distal plates and constitutes no more than 15% of the velocity magnitude at its highest location. In other words, including the lateral velocity component in the velocity magnitude calculation does not have a remarkable qualitative effect on the comparison.

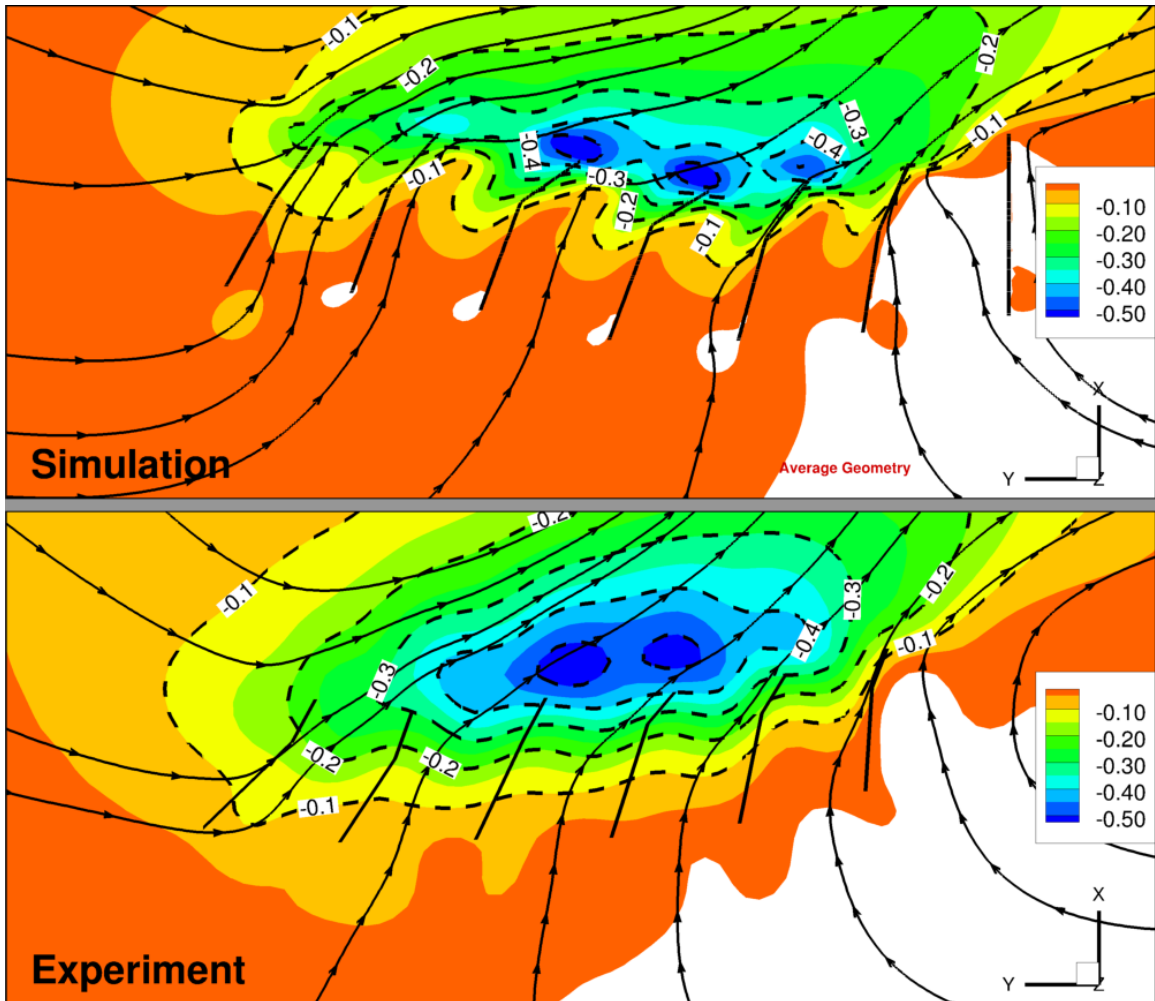


Figure 3.4: Comparison of the time-averaged y-component of the velocity  $v$  for flapping kinematics at  $Re_\omega = 21.6$ . Contour floods above 0.0 are cutoff.

Figures 3.3 and 3.4 show the individual time-averaged velocity components  $u$  and  $v$  respectively. Again, the agreement is quiet remarkable given the variability of the nymphs. The main source of discrepancy is the mean location of the gills. Specifically, gills towards the back of the mayfly (right) are positioned higher in the experiments. This could be due to the mayfly nymphs not oriented horizontally during the experiments and/or a different curvature of the abdomen affecting the mean location of the gills.

For further validation, instantaneous flow fields were also looked at. Figures 3.5 and 3.6 show comparisons of instantaneous vorticity plots at the end of retraction of gill 4 and gill 3 respectively. In both figures, contour floods of the z-component of the vorticity  $\omega_z$ , as well as the instantaneous velocity vectors are shown. The instantaneous position of the gills is shown in both experiments and simulations. Additionally, for the simulations, the extreme positions of the flapping gills are shown in lighter shades.

For both figures, *all* structures are replicated and the instantaneous velocity vectors are in good agreement, most importantly on top of most gills and in the inter-gill spacings. In Figure 3.5, the main difference is the negative vorticity on top of gills 4–6 where in the PIV experiments, the three vortices seems to have started to diffuse together, whereas in the simulations, the three vortices can still be distinguished. The same difference appears also in Figure 3.6 with respect to gills 3–5. Therefore, the numerical results appears less dissipative, with stronger vorticity in proximity of the gills and higher vorticity magnitudes at the vortex cores. This could be attributed to the zero-thickness assumption of the gill plates, to the introduced rigidity of the gills

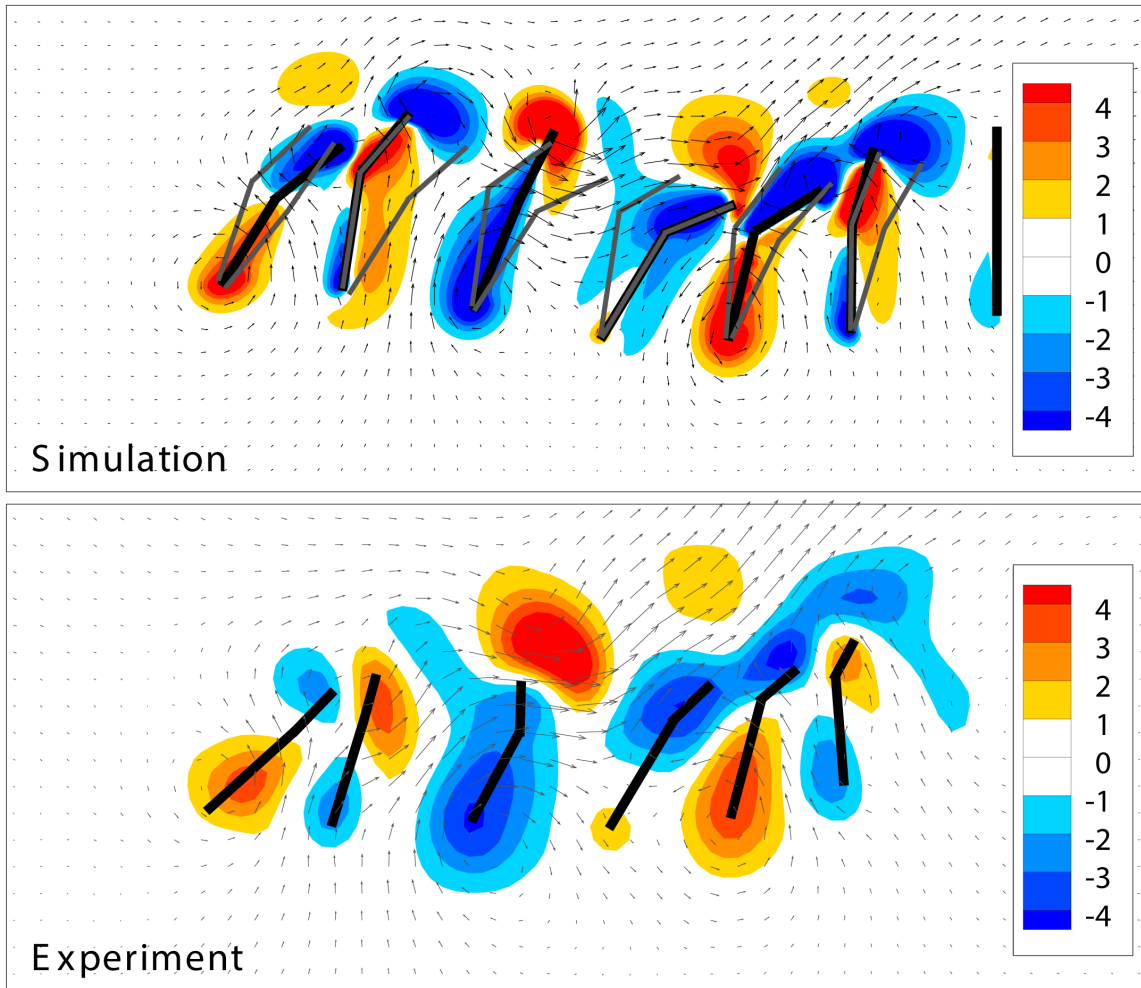


Figure 3.5: Comparison of the instantaneous  $z$ -component of the vorticity vector  $\omega_z$  of the flapping kinematics at  $Re_\omega = 21.6$  and  $t/\tau = 0.102$  (end of retraction of gill number 4).

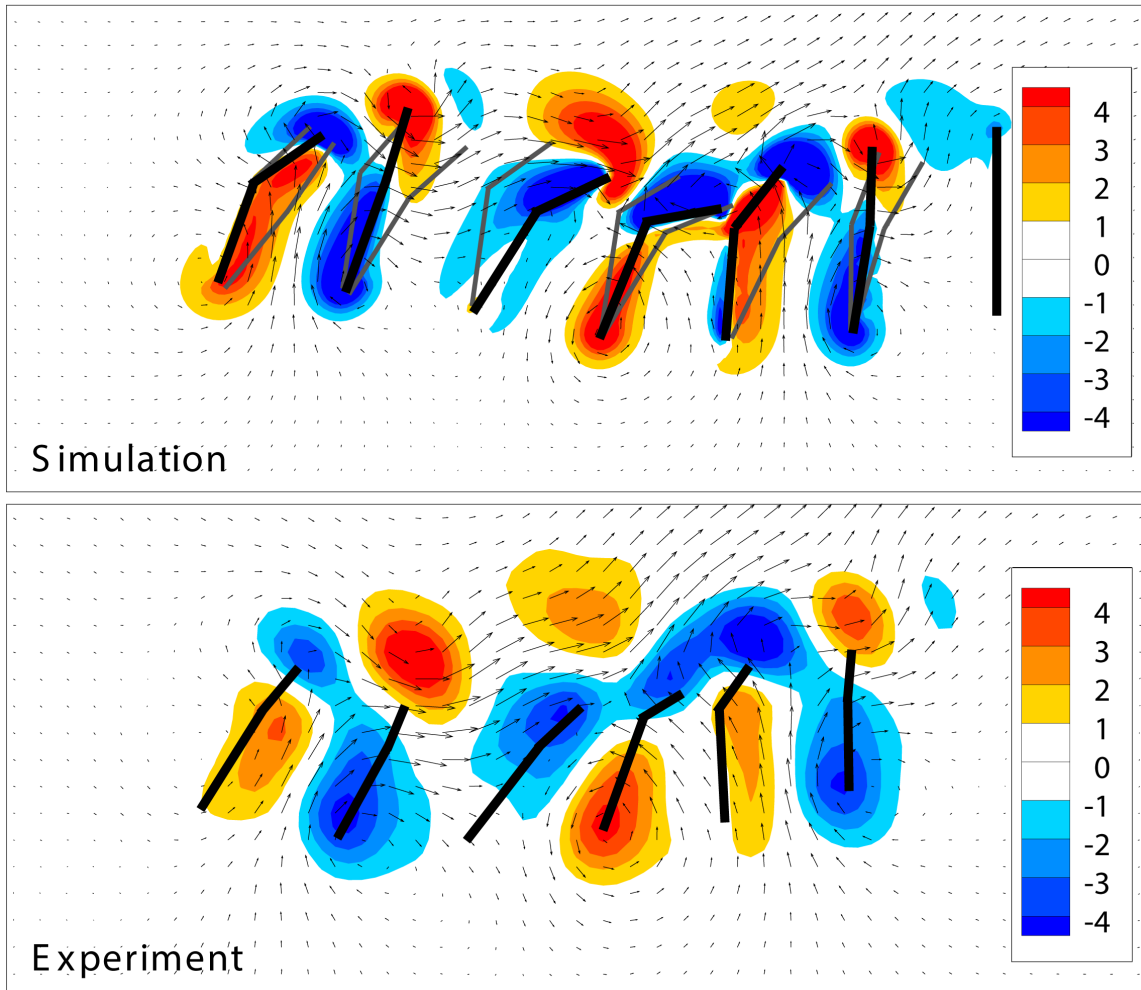


Figure 3.6: Comparison of the instantaneous  $z$ -component of the vorticity vector  $\omega_z$  of the flapping kinematics at  $Re_\omega = 21.6$  and  $t/\tau = 0.326$  (end of retraction of gill number 3).

or to the approximation of the hinge, where the in-gill curvature was neglected and the hinge was approximated as a straight line. As for the location of the gills, gills 2 – 4 in the simulation are lagging their counterparts in the experiment compared to gills 5 and 6, which are well matched. The time lag is, however, less than 5%. This could be explained by the fact that the gill kinematics in the PIV experiments were recorded and extracted at a *different* time than the PIV imaging. In other words, gill kinematics and PIV were not performed simultaneously. Matching the exact timing between the simulations and the experiments proved to be challenging due to the many bodies involved in the flow field. In other words, attempting to match the flow around gills 4 – 6 for example, will cause a slight time lag around gill 1 – 3 or vice versa, which again highlights the variability in the experiments.

Overall, the simulation of a flapping nymph at  $Re_\omega = 21.6$  is able to reproduce the flow physics and the different vortical structures associated with it. The time-averaged flow fields show excellent agreement, while the instantaneous flow fields show acceptable agreement. Most of the discrepancies can be explained and are attributed mainly to insect variability and uncertainties associated with the *in-vivo* experiments. This comparison also shows that the grid resolution is sufficient enough to capture the flow physics, which in turn enables running flapping simulations at lower  $Re_\omega$  provided that the grid resolution is maintained the same.

When it came to comparing the rowing kinematics, there wasn't a full experimental set to work with because none of the rowing nymphs overlapped between the kinematics extraction and the PIV imaging. Therefore, a nymph other than the one used to extract the kinematics had to be selected to perform the flow field compari-

son. The matching was done based solely on the  $Re_\omega$  and qualitative resemblance in the rowing kinematics. In other words, 3 nymphs are involved in the rowing comparison; the nymph used in building the computational model and the two nymphs used by the experiments in extracting the kinematics and performing the PIV imaging. However, all these 3 nymphs are not geometrically similar in the strict sense. This is most noticeable in the ratio between the gill length and the inter-gill spacing.

The above dissimilarities are compounded by the higher uncertainty associated with the smaller nymphs. The largest source of uncertainty may be attributed to the location and orientation of the laser sheet with respect to the gills. The laser sheet thickness was half that of the gill length (compared to one fifth of the gill length in the flapping case) with a conservative uncertainty in its position of  $0.1mm$  (half the gill length). This can actually result in part of the laser sheet not cutting through the gills. Clearly a high level of discrepancy is expected.

The comparison of the time-averaged velocity magnitude for rowing at  $Re_\omega = 2.3$  is shown in figure 3.7. The flow field far from the mayfly agrees well with the experiments. The main flow features are preserved; that is the inflow and outflow locations and magnitudes and the inflow direction. Furthermore, two recirculation zones (bottom left and top right) are present in the flow field and they both reside in regions of low velocity magnitude despite their different location. However, near and around the gills, discrepancies are observed. The most important source of discrepancy in this comparison is the location of the ventral wall (modeled as a no-slip wall) with respect to the nymph. In order to match the mean location of the gills and the inflow direction (top left), the experimental results had to be rotated  $-15^\circ$  around the

z-axis (even though it wouldn't have a similar effect as modeling the nymphs with a different orientation). Additionally, the ventral wall in the simulation is closer to the mayfly when compared to the experiment. This has a combined effect of bending the flow leaving the mayfly at the bottom right away from the ventral wall. Noteworthy is that the recirculation zone at the bottom left disappears at higher Reynolds numbers as observed in simulations (shown later in §4.4), which means that the ventral wall has a major influence on the results (at least on the ventral side of the flow field below the abdomen) and therefore providing a reasonable explanation of the discrepancy.

Another feature that is shown by the simulation is the 'wiggly' shape of the streamlines in the inter-gill spacing. This could be caused by a larger inter-gill spacing in the simulations or a low grid resolution on the experiments. Noteworthy is that the numerical grid resolution in this case is about 4 times that of the experimental grid. I tried to match the experimental results by changing the location where the spatial averaging is performed or changing the depth over which the spatial averaging is performed while remaining parallel to the medial plane (8, 16, 24, 32 cells). The velocity vectors matched the experiments better when the averaging location moved towards the gill tips, where the 'wiggly' effect started to disappear. However the *orientation* of the zone of highest velocity magnitude could not be matched.

As with the flapping at  $Re_\omega = 21.6$ , I looked into instantaneous flow fields for the rowing case at  $Re_\omega = 2.3$ . A comparison of the instantaneous normalized velocity magnitude is shown in Figure 3.8. The instant shown is at  $t/\tau \approx 0.075$ , which is the end of retraction of gill 5 (see Figure 2.10 on Page 46 for rowing kinematics), when the velocity magnitude near the dorsal edge of gill 5 is at its maximum. Given the

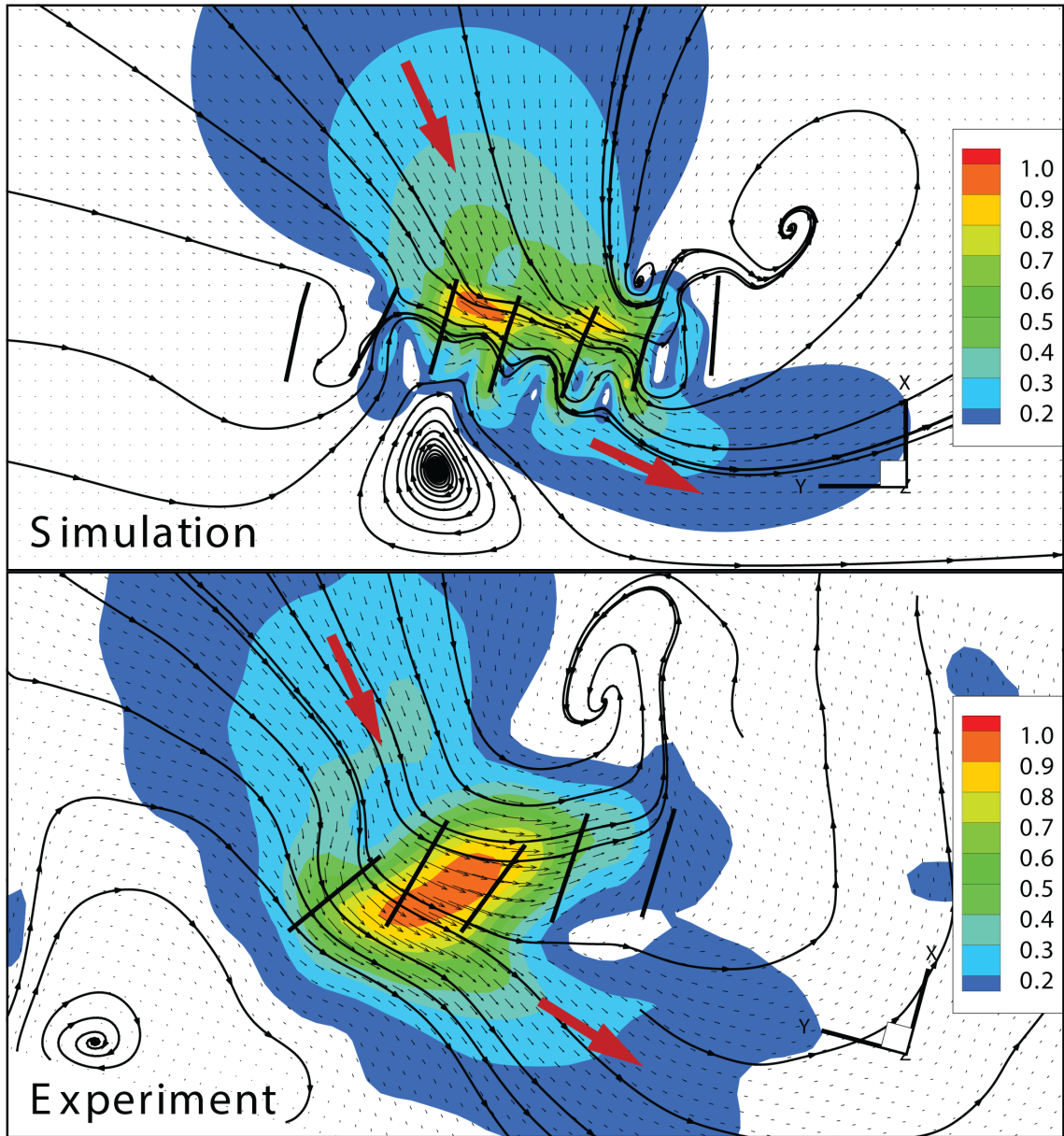


Figure 3.7: Comparison of the time-averaged in-plane normalized velocity magnitude for the rowing kinematics at  $Re_\omega = 2.3$ . Velocity magnitude is normalized by the local maximum. Top: Simulation (showing 7 gills). Bottom: *In-vivo* experiments (showing only 5 gills). Contour floods below 0.1 are cutoff. The sink-like behavior of the streamlines in the simulation is because of the forced 2D integration of the velocity field, which also implies a normal component of the velocity ( $w$ ).

previous discussion, the agreement is still reasonable around most gills.

Overall, the comparison is less remarkable compared to the flapping case at  $Re_\omega = 21.6$  but still acceptable for the purpose of verifying the correct implementation of the kinematics. Outflow direction differs by approximately  $90^\circ$  compared to the flapping kinematics, which was shown by experiments and now substantiated by computations.

To sum up, comparisons with available *in-vivo* experimental data are suggesting a correct implementation of both kinematics and that the grid resolution is sufficient to capture all the flow physics and the general behavior of flapping and rowing mayfly nymphs. In fact, the numerical grid is finer than required when simulating the lower  $Re_\omega$  cases.

### 3.4.2 Comparison with Robotic Experiments

To further validate my numerical code, comparisons were made with mayfly robotic experiments carried out by [43,44]. The robotic mayfly experiment consisted of an array of 5 gills, which were controlled using programmed micro-servomotors. The robot used a simplified version of the rowing kinematics previously introduced in §2.2.3, where the stroke and pitch angles were prescribed, but the stroke plane deviation angle was neglected. Additionally, for all 5 gills, the stroke plane lateral inclination angle  $\epsilon$  was set to  $90^\circ$ , while the stroke plane inclination angle  $\beta$  was  $-60^\circ$ . For all 5 gills, stroke and pitch angles were based on the kinematics of rowing gill number 4 (see Figure 2.10) but varied slightly from each other due to limitations

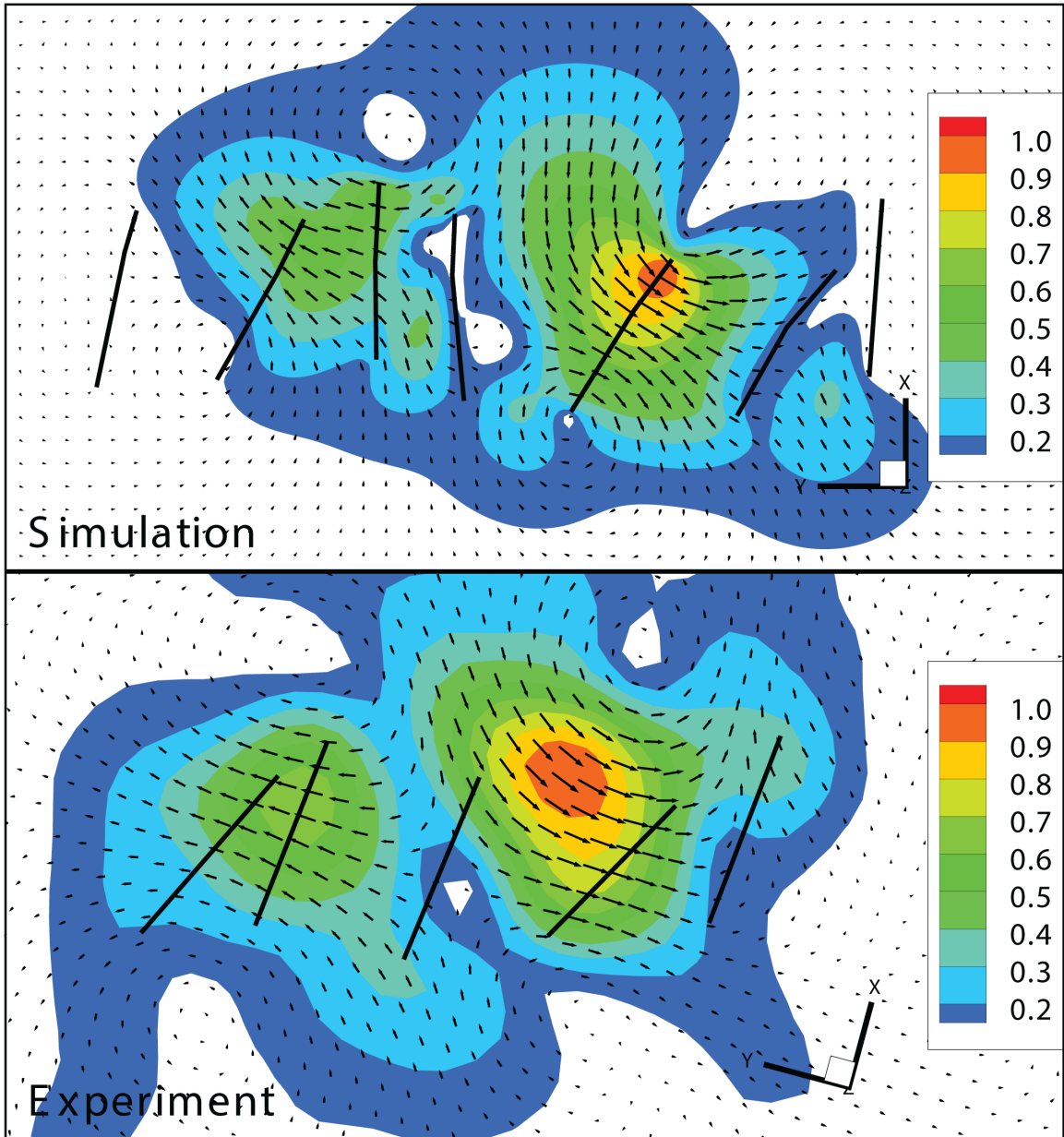


Figure 3.8: Comparison of the instantaneous normalized velocity magnitude for the rowing kinematics at  $Re_\omega = 2.3$  and  $t\tau \approx 0.075$ . Velocity magnitude is normalized by the local maximum. Top: Simulation (showing 7 gills) spatially averaged over  $0.2L$ . Bottom: *In-vivo* experiments (showing only 5 gills). Contour floods below 0.1 are cutoff.

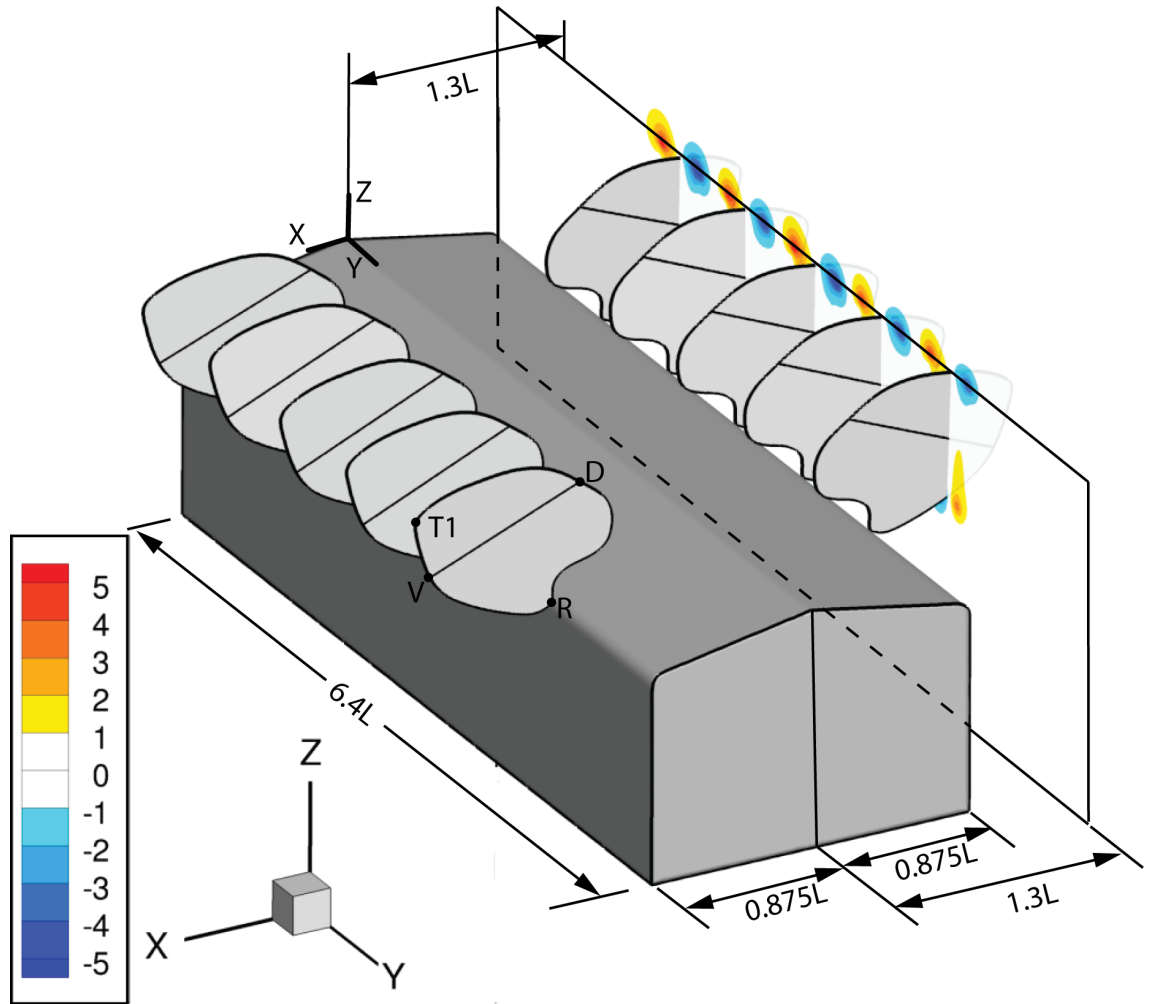


Figure 3.9: Illustration of computational setup and slice at  $z/L = 1.3$

of the servomotors.

The gill plate array had a length of  $96\text{mm}$  (from gill 1 to gill 5) and was immersed in a small aquarium ( $260 \times 310 \times 510\text{mm}$ ) partially filled with mineral oil (depth of fluid =  $200\text{mm}$ ), and oriented such that the bilateral symmetry plane of the mayfly body corresponded with the free surface of the liquid. A simplified body shell for the mayfly was constructed, which only models the abdomen of the mayfly nymph to which the gills are attached. The model was scaled using the oscillating Reynolds

number  $Re_\omega$ . The robotic model dimensions are approximately 54 times those of the original mayfly ( $L = 40mm$ ). Mineral oil with a viscosity of  $175cSt$  was used as the working fluid in order to achieve a  $Re_\omega$  of 17.4. More details about the setup can be found in Appendix A.

In order to simulate the robotic experiment, I constructed another Eulerian grid with dimensions  $6.4L \times 10L \times 12.5L$ . The same grid density introduced in §3.3 was used, i.e. 40 cells per unit length. Consequently, the rectangular domain was discretized with  $258 \times 242 \times 194$  points in the x-, y- and z-directions, which yielded a total of 12 million points. Grid stretching was applied in the x- and z-directions in order to cluster points in the region around the immersed bodies. All domain boundaries are modeled as non-slip walls. An illustration of the computational setup is shown in Figure 3.9.

Figure 3.10 shows a comparison of the time-averaged x-component of the vorticity vector  $\omega_x$ . The results are shown for a medial plane  $z/L = 1.3$ . The location of the slice is illustrated in Figure 3.9. The comparison shows excellent agreement of the vorticity fields, which confirms that a grid density of 40 cells per unit length is sufficient to replicate the flow physics. The comparison is much better than those with the *in-vivo* experiments since the environment is more controllable and uncertainties are much lower than those associated with the *in-vivo* experiments. More comparisons of the instantaneous flow fields as well as integral quantities are available in Appendix A.

This section concludes the comparisons that were performed in order to validate the implementation of the kinematic chain, the two sets of kinematics that will be

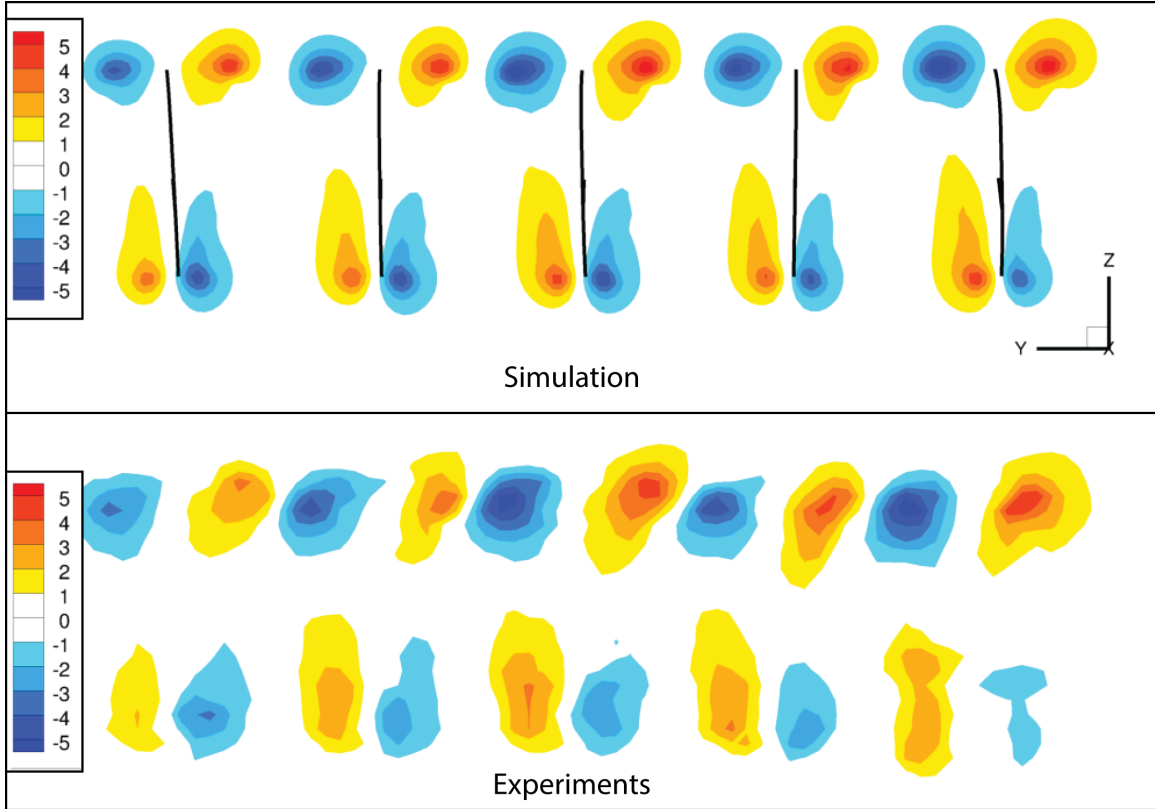


Figure 3.10: Comparison of time-averaged flow fields for simplified rowing at  $Re_\omega = 17.6$ . Contour floods of  $\omega_x$  at  $z/L = 1.3$ . Top: simulation. Bottom: Robotic experiments.

used to carry out the simulations as well as the grid density. With that, the road is paved for numerical experiments that deals with hypothetical scenarios, such as rowing at higher  $Re_\omega$  and flapping at low  $Re_\omega$ . In the other words, the parametric study of the rowing-flapping transition can be executed. In the next section, I will introduce the two parametric spaces that were built throughout this study. This will be followed by the results in §4 and §5.

### 3.5 Parametric Spaces

The primary goal of this study was to investigate the rowing-flapping transition of the mayfly nymph *C. triangulifer*, which was first observed by the PIV experiments. The PIV experiments had reported three types of kinematics throughout the ontogeny of the nymph; rowing, intermediate and flapping kinematics. Therefore 3 different  $Re_\omega$  were selected so that each lies in one of 3 kinematics regimes revealed by the *in-vivo* experiments. These were 2.3, 8.1 and 21.6 belonging to rowing, intermediate and flapping regimes respectively. For each of these 3  $Re_\omega$ , 2 simulations were carried out, one using rowing kinematics and the other using the flapping kinematics, making the total number of simulations 6.

Initially, all simulations were performed using Planform A, which showed some potential to explain the transition but required running two more simulations at a lower  $Re_\omega$  of 1.0 bringing the total number of simulations to 8. Later, the planform shape was found to affect some of the results. Therefore, I decided to study the effect of the gill planform when using rowing kinematics, thereby introducing planforms B and C. This was probably driven by the higher uncertainties associated with rowing nymphs which actually use planforms similar to planforms B and C. Therefore, both planform B and C were used to carry out rowing simulations at the the same 4  $Re_\omega$ , now 1.0, 2.3, 8.1 and 21.6. This brought up the final number of simulations to 16. The rowing-flapping parametric space is summarized in Table 3.1 and the results will be presented in the following chapter; §4. Noteworthy is that optimization techniques would have been ineffective in this study because of the computational cost associated

$Re_\omega$	$Re_f$	Flapping	Rowing	Nature favors	Sample time	Itr/cycle
1.0	0.26-0.82	A	A,B,C	Rowing	10.0	10000-10091
2.3	0.60-1.89	A	A,B,C	Rowing	13.0	4386-4505
8.1	2.11-6.64	A	A,B,C	Transition	16.0	1333-1429
21.6	5.62-17.71	A	A,B,C	Flapping	50.0	562-682

Table 3.1: Parametric space used to explore the rowing-flapping transition. 3 independent variables are investigated: 1)  $Re_\omega$  {1.0,2.3,8.1,21.6}, 2) kinematics {flapping,rowing} and 3) Planforms {A,B,C}.  $Re_\omega = L^2 f / \nu$ .  $Re_f = fAL / \nu$  where A is the stroke amplitude (peak-to-peak). The range in  $Re_f$  for some  $Re_\omega$  is caused by the subtle differences in gills kinematics and different stroke amplitudes between flapping and rowing.

with the simulations and the relatively small number of simulations that were carried out. An optimization approach would have required many more simulations in order to build an initial model. More importantly, the optimized parameter using the current mathematical model was not known *a priori*.

Interestingly, a preliminary run using flapping kinematics at  $Re_\omega = 21.6$  without a hinge was carried out. This was in the testing phase of the kinematics chain, where only two levels have been introduced. The results did not compare well with *in-vivo* experiments and therefore the hinge or the two-plate model was introduced, i.e. the third level of the kinematic chain previously discussed. This resulted in better agreement with the experiments as shown in the previous section (§3.4.1). This also proved the necessity of including the hinge when investigating the rowing-flapping transition of the nymphs.

In light of the above, I decided to investigate the effect of introducing the hinge as a first step towards investigating the flexibility of the gills. After all, flexibility may be achieved in the limit of an infinite number of hinges or plates. Of course,

current experimental data is not sufficient to simulate the slight flexibility present in the flapping gills. On the other hand, the numerical model would require substantial development in order to simulate deforming Lagrangian meshes. With that, I investigated the role of the hinge by running flapping simulations at  $Re_\omega = \{2.3, 21.6\}$  using planform A, with and without the flexural hinge (two-plate vs one-plate model). I also decided to investigate the interaction between the different gills. Therefore, simulations were carried out using the entire gill array (7 pairs) and using only gill pair number 4. This led to a parametric space that encompasses 8 simulations, where 2 of this simulations overlaps with rowing-flapping parametric space. In other words, three independent variable are involved in the second parametric space. These are the  $Re_\omega$ , the flexural hinge (with or without) and the number of gill pairs present in the array (1 or 7). The results of the second parametric space will be summarized in §5.

## Chapter 4: Results I: The Rowing-Flapping Transition

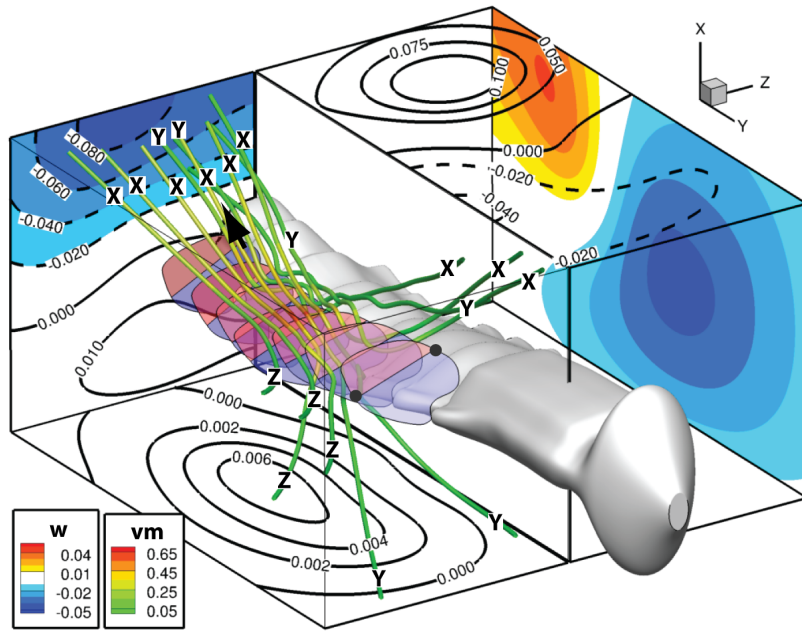
### 4.1 Introduction

The parametric space introduced in this chapter was designed to illuminate the rowing-flapping transition by investigating the effect of 3 different parameters, namely the  $Re_\omega$ , the type of kinematics and the gill planform as summarized in Table 3.1. Originally the goal of this parametric space was to simulate flapping at low  $Re_\omega$  and rowing at high  $Re_\omega$  but was subsequently extended to include the effects of planform morphology. Therefore, this chapter is organized as follows. The first 4 sections deal with mostly qualitative investigation of the different flow fields aiming to provide better understanding of the kinematics and the morphology effects. In specific, the time-averaged flow fields of rowing and flapping are shown in §4.2. This will be followed by a description of the instantaneous fields in §4.3. The effects of varying  $Re_\omega$  is shown in §4.4, while gill planform effects are presented in §4.5. The last section of this chapter provides a quantitative assessment of the micro-pumping using the performance metrics introduced earlier, recaps over the qualitative differences observed and provides a viable explanation of the rowing-flapping transition.

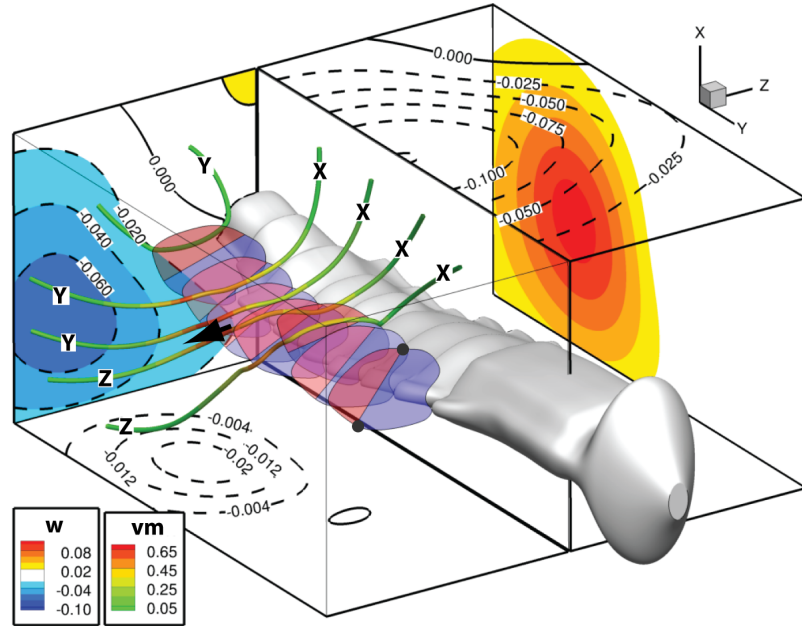
## 4.2 General Description of the Time-averaged Flow Fields

The time-averaged flow field for both flapping and rowing kinematics at Reynolds numbers corresponding to the *in-vivo* experiments is shown in Figures 4.1a and 4.1b respectively. The time-averaged flow field for the flapping kinematics is at  $Re_\omega = 21.6$ , while that for the rowing kinematics is at  $Re_\omega = 2.3$ . Only part of the domain is shown and the left row of gills is omitted for clarity. The sub-domain shown is one unit length away from the gills and extends from  $x = -1.11$  to  $x = 1.89$ , from  $y = -2.71$  to  $y = 2.69$  and from  $z = -2.73$  to  $z = 2.73$ , which constitutes only 1.47% by volume of the entire domain. Also, the right row of gills shown is time-averaged in order to illustrate the average location of the Lagrangian grid. To highlight the differences in the mean flow patterns between flapping and rowing, streamlines are shown. The start and end of many streamlines are marked with a letter corresponding to the plane it intersects at inlet and exit of the sub-domain. The streamlines are colored with the velocity magnitude, which is higher near the gills and decays further away. On the bounding planes, contours (lines or floods) of the velocity component normal to each plane are shown. Dashed isolines indicate a negative velocity component with respect to the inertial frame of reference (and not with respect to the plane normals).

The time-averaged velocity has been integrated across the six different planes of the control surface shown in Figure 4.1. The control surface shown is one unit length ( $L$ ) away from the bounding box of the moving gills. This yields the inflow and outflow of each plane and, in one way, highlights the difference between the two sets of prescribed kinematics. For the flapping case (Figure 4.1a), the integration reveals that the dorsal



(a) Flapping at  $Re_\omega = 21.6$



(b) Rowing at  $Re_\omega = 2.3$

Figure 4.1: Time-averaged flow fields for rowing and flapping.  $w$ : velocity component in the  $z$  direction.  $vm$ : velocity magnitude. Contour floods and lines: velocity component normal to the corresponding plane. Streamlines are colored by velocity magnitude.  $X, Y, Z$  denote intersection of the streamline when entering or exiting the shown sub-domain.  $x = \{-1.11 : 1.89\}$ .  $y = \{-2.71 : 2.69\}$ .  $z = \{-2.73 : 2.73\}$ .

plane ( $x = x_{max}$ ) contributes 60.27% of the total outflow while the posterior plane ( $y = y_{min}$ ) contributes 28.64%. In other words, 88.91% of the outflow goes through a plane which is almost *perpendicular* to the apparent motion of the gills (flapping-like). The remaining outflow exists through the medial planes ( $z = z_{min}$  &  $z = z_{max}$ ) and through the ventral plane ( $x = x_{max}$ ) at 10.94% and 0.15% respectively. As for the inflow, the flow comes into the control surface from the dorsal, anterior, and medial planes at 22.26%, 23.65% and 45.49% respectively. For the rowing case, on the other hand (Figure 4.1b), the primary inflow is through the dorsal plane which contributes approximately 84.93% of the inflow. The anterior plane contributes only 7.31%, and all other planes have negligible inflow. The outflow contribution through the medial, posterior and ventral planes is 59.81%, 31.03% and 7.16% respectively. The mean outflow direction for the rowing kinematics is approximately *perpendicular* to the mean outflow for the flapping kinematics. The contribution of each plane to

Kinematics	Flapping		Rowing	
Figure	4.1a		4.1b	
Mass flow rate	Inflow	Outflow	Inflow	Outflow
Plane	%	%	%	%
Ventral (bottom)	4.44	0.15	1.72	<b>7.16</b>
Dorsal (top)	22.26	<b>60.27</b>	84.93	1.99
Posterior (back)	4.19	<b>28.64</b>	2.12	<b>31.03</b>
Anterior (front)	23.65	0.00	7.31	0.00
Medial (left)	22.75	5.47	1.96	<b>29.93</b>
Medial (right)	22.75	5.47	1.96	<b>29.93</b>

Table 4.1: Table showing the dimensionless mass flow rate across the control surfaces shown in Figure 4.1 for flapping at  $Re_\omega = 21.6$  and rowing at  $Re_\omega = 2.3$ . Boldface notation highlights the major exiting planes and hence the primary difference between the flapping kinematics and the rowing kinematics.

the inflow and outflow is summarized in table 4.1. The above results are in general agreement with what has been observed in experiments and illustrates the difference between the flapping kinematics and the rowing kinematics [57–59].

### 4.3 Dynamics of Rowing and Flapping

Before discussing the parametric spaces and the effect of  $Re_\omega$  and gill planform on the flow field and performance, the micro-pumping dynamics of both flapping and rowing is introduced in order to elucidate the complicated nature of the flow field. This is achieved by looking into the instantaneous flow fields, which will also demonstrate the metachronal wave and consequently highlight the main differences between both kinematics.

Recall that the metachronal wave of the gills starts posteriorly (tail side), i.e. at gill 6. Gill 6 starts its retraction, followed by gill 5 then gill 4 and all the way to gill 1. Also, the phase lag between any two *consecutive* gills is approximately one quarter of the period. Since all 6 pairs of moving gills have similar kinematics (beating, pitching and stroke plane deviation), it is sufficient to follow any of the 6 moving gills in order to elucidate the transient flow field. In addition, the flow field is symmetric about the medial plane ( $z = 0$ ), which means that looking at one side of the mayfly is sufficient to understand the nature of the flow field. In light of that, the flow field around gill 4 is discussed hereunder.

### 4.3.1 Flapping Dynamics at $Re_\omega = 21.6$

The pumping sequence is described in Figure 4.2 through examination of four points in the flapping cycle, covering key features of the gill's interactions with its surrounding neighbors. To provide a sense of the beating direction of the gills, their location at an earlier time step ( $0.15 t/\tau$  earlier) is shown. As gill 4 protraction initiates its motion towards the head ( $t/\tau = 0.102$ ), gill 5 immediately posterior (behind) gill 4 is already near its peak protraction speed, pushing fluid both dorsally and ventrally. At  $t/\tau = 0.476$ , gill 4 is nearing the end of its protraction phase and slowing, while gill 5 initiated retraction and moving toward the tail. This relative motion causes an increasing interstitial volume (volume between adjacent gills) with a strong negative suction pressure, sucking fluid into the widening volume. Note that the biased nature of the hinge (effectively flexing in only one direction), allows the interstitial volume to be blocked from the space dorsal (above) the gill array, forcing the fluid to be entrained from the ventral region. Note that this filling process produces vorticity on the gill surface similar to what would be observed in entrance region of a planar Poiseuille flow. By  $t/\tau = 0.802$ , gill 4 is near its peak retraction speed, while gill 5 has finished retraction is about to reverse direction and start a protraction stroke. This causes a compression of the interstitial volume, and an increase in the interstitial pressure (pressure between adjacent gills) . The flexure on gill 4 allows the distal plate to open, and the fluid is ejected out the dorsal side of the array, carried forward by the inertial bias from the filling event. Lastly, at  $t/\tau = 0.976$ , gill 4 is just past its peak retraction speed, while gill 5 has started its

protraction, producing strong relative closing speeds between the gill tips. Counter-rotating vortices are generated on each adjacent tips (positive vorticity on gill 4, negative vorticity on gill 5), forming a dipole pair that results in a strong ejection jet directed upward and behind (dorsal-posterior) the gill array. This event coincides with peak velocity magnitudes and pressure. The close interaction of the gills and the formation of this dipole pair was identified as a key feature of the flapping array in prior work [59]. Due to the relative phasing of the gills, this process is repeated with each gill, such that the filling and ejection cycle is observed to move in a metachronal wave proceeding from the tail (posterior) end toward the head (anterior), with a spatial wavelength corresponding to 5 gills (4 inter-gill spacings).

The above description of the instantaneous flow field was conventionally presented by moving forward in time and looking at 4 different snapshots of the transient field. However, another way of presenting the instantaneous flow field may be achieved by looking at only one snapshot and riding *spatially* against the metachronal wave. This is possible because the metachronal wave has a spatial wave length equal to 4 inter-gill spacings (distance between 5 consecutive gills). Had the metachronal wave length been longer than the entire gill array, the following method of illustration may have not been possible. Therefore, the pumping sequence may be described if one follows zones A, B, C then D shown in Figure 4.3. Following these zones is the same as following one inter-gill spacing through time (illustrated through Figure 4.2). Inside any of these zones, I refer to the gill at its left as the *lagging* or *anterior* gill and to the gill at its right as the *leading* or *posterior* gill. Zone A: the proximal plate of the lagging gill is starting to protract, while the leading gill is protracting already.

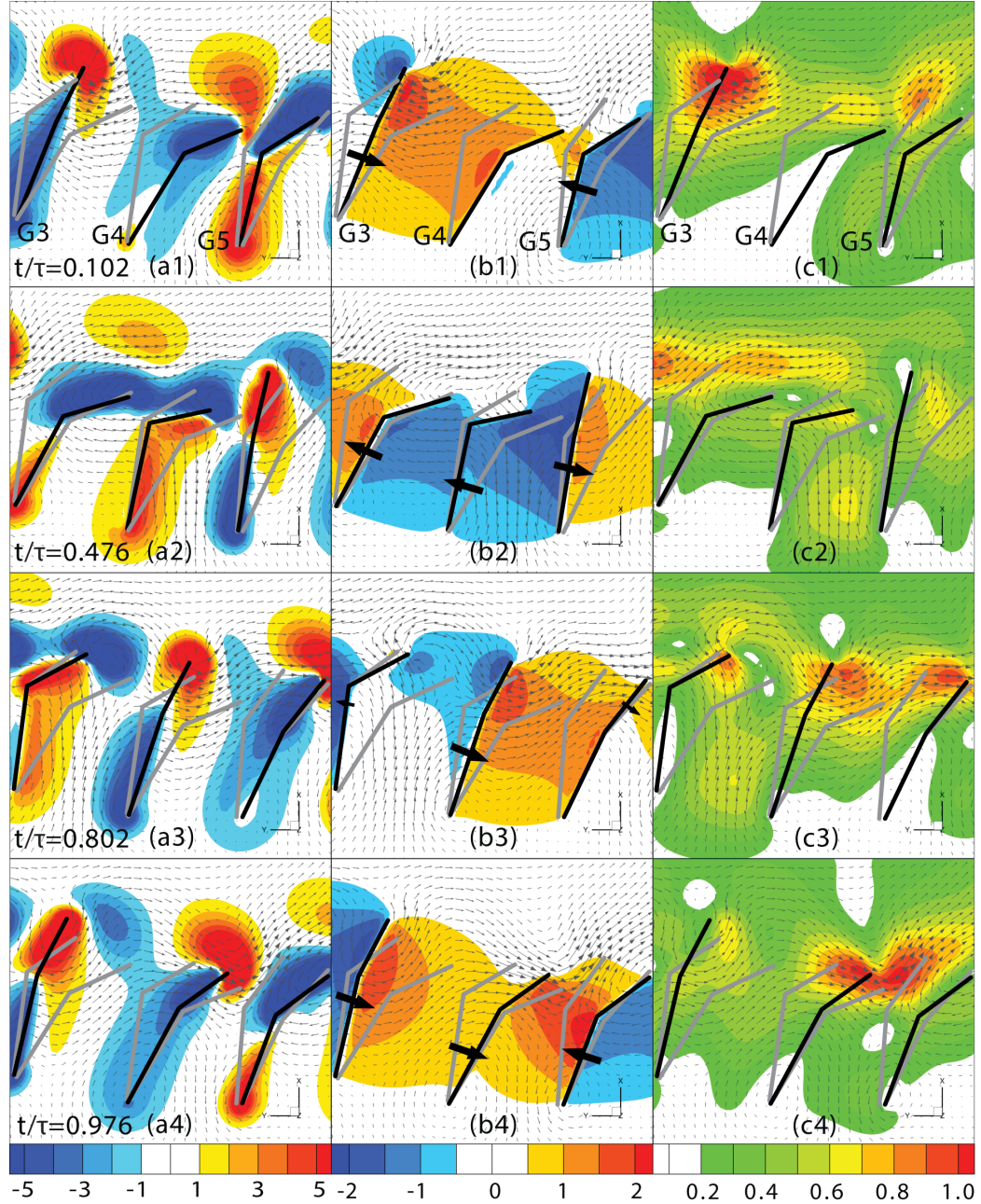


Figure 4.2: Instantaneous flapping dynamics at  $Re_\omega = 21.6$ . Slice at  $z/L = 1.15$  spatially averaged over 8 cells ( $z = \{1.07 : 1.26\}$ ). Focus is on inter-gill spacing 4-5. (Col a) Vorticity component ( $\omega_z$ ). (Col b) Pressure ( $p$ ). (Col c) Velocity magnitude ( $vm$ ). (Row 1)  $t/\tau = 0.102$ : start of protraction (G4). (Row 2)  $t/\tau = 0.476$ : mid-protraction. (Row 3)  $t = 0.802/\tau$ : mid-retraction. (Row 4)  $t/\tau = 0.976$ : approaching end of retraction.

Zone A is marked by lower pressure, low velocity magnitude, no vorticity production at the ventral edge of the lagging gill and positive vorticity generation at the ventral edge of the leading gill. Zone B: the lagging gill is protracting while the leading gill is about to retract. This yields to an effective widening of the inter-gill spacing which causes the fluid particles to accelerate from the ventral side of the mayfly towards the inter-gill spacing. Zone B is marked by the lowest pressures, higher velocity magnitude and the formation of a dipole on the ventral edges of the leading and lagging gills. Noteworthy is that the position of the distal plate of the lagging gill is oriented in such way as to prevent a retrograde flow from the dorsal side towards the inter-gill spacing. Zone C: the lagging gill is about to retract while the leading gill is already retracting. The inter-gill spacing seems to maintain a constant width, where the fluid particles keep moving towards the dorsal side and pushing the distal flap of the lagging gill open. Vorticity is observed along the entire gill surface instead of being focused on the ventral edges and the pressure gradients are at their lowest. Zone D: the lagging gill is retracting while the leading gill is finishing its retraction and about to protract. The effective narrowing of the inter-gill spacing accompanied by the weak inertia of the fluid particles and the dipole forming on the dorsal edges squeezes the fluid particles out to the dorsal side. The above sequence can be observed in any of the 5 inter-gill spacings if one were to follow a specific inter-gill spacing through time. Each inter-gill spacing produces more, or less current, depending on the subtle variations in the kinematics, mean position of the gills and mean inter-gill spacing.

One may summarize the inter-gill micro-pumping sequence as follows. The sequence starts when the inter-gill spacing is widened which creates a pressure drop

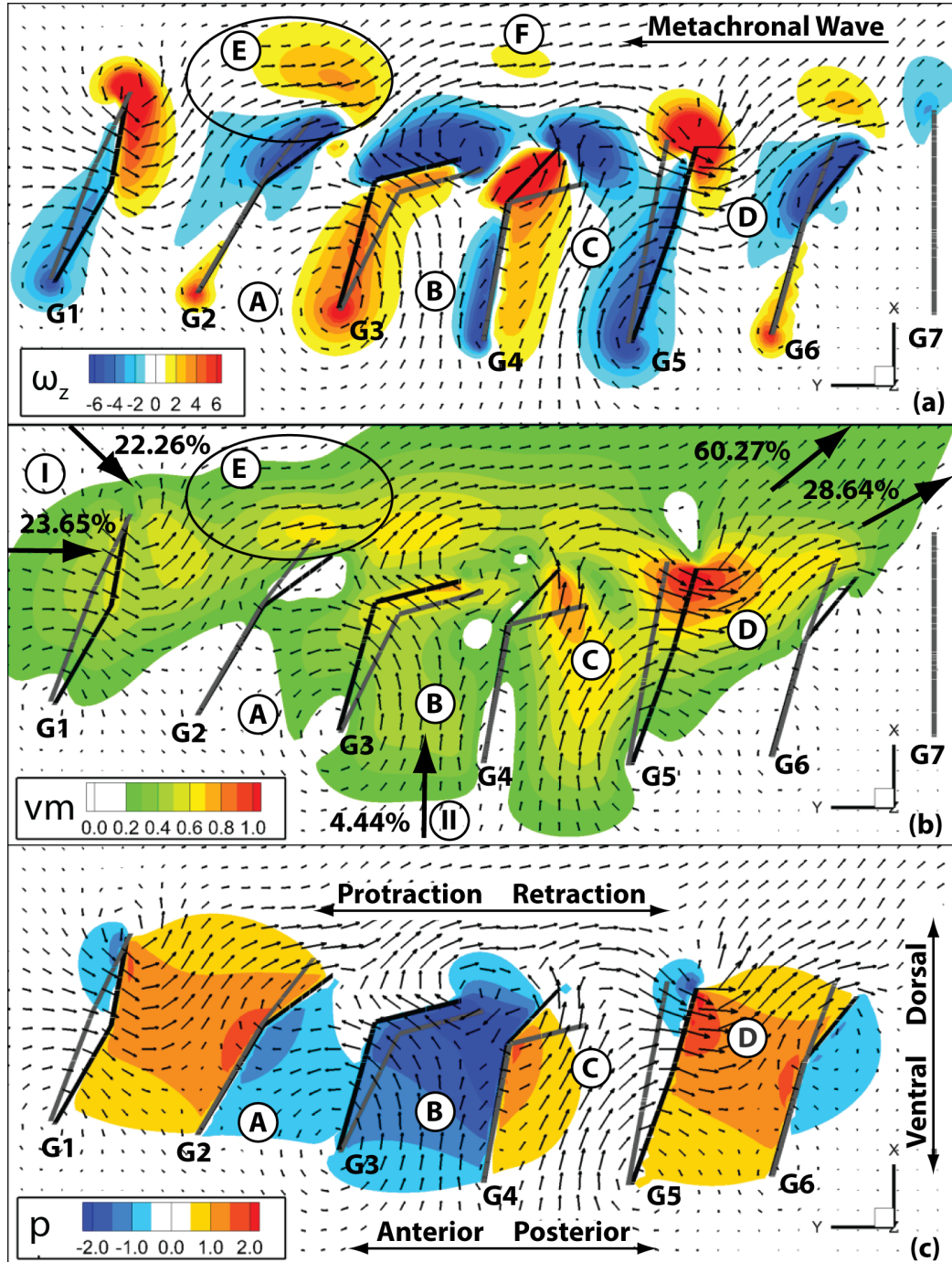


Figure 4.3: Instantaneous fields at  $t/\tau = 0.65$  for flapping kinematics at  $Re_\omega = 21.6$ . Slice at  $z/L = 1.15$ . Gills intersection with slice is shown. Lighter gill shades are from an earlier time step ( $0.15 t/\tau$  earlier). (a)  $z$ -component of the vorticity vector. (b) Velocity magnitude. (c) Pressure. (a-c) Velocity vectors shown are in-plane. G1-G7: Gills 1 through 7. A-D: Pumping sequence for main stream II. E-F: Vortex detachment from gills 2 and 3 respectively assisting main stream I. Percentages shown are for mass inflow or outflow.

inside the inter-gill spacing, pulling the flow from the ventral side. The flow is enhanced by the creation of a dipole at the ventral edge (Figure 4.2, row 2 or Figure 4.3, zone B). During the “suction” phase, the distal flap reduces the amount of retrograde flow into the inter-gill spacing from the dorsal side. The “suction” phase is followed by a “squeeze” or “compression” phase, where the flow is pushed dorsally and posteriorly with a slight retrograde ventrally (Figure 4.2, row 4 or Figure 4.3, zone D). The postero-dorsal flow is enhanced by the creation of a dipole attached to the distal edge of the gill. Interestingly, Eastham had predicted the periods of suction followed by periods of compression in many of his publications about mayfly nymph without actually measuring the pressure and by looking only at velocity fields [15–18]. Eastham prediction is now confirmed by the full numerical simulation presented in this work. Also, Sensenig [57] hypothesized that the distal flap could function as the valve of a pump. Based on the numerical results, the distal flap is acting similar to a non-return valve by reducing the retrograde flow during the “suction” phase. It is impossible to prevent all the retrograde flow due to the shape of the distal plate and the fact that the retrograde flow occurs also laterally.

The periodic widening and narrowing between consecutive gills highlights the first element of synergy between flapping gills, and appears to play an important role in fluid circulation. This type of motion, however, primarily accounts for that part of flow that is directed from the ventral side of the mayfly to the dorsal side (marked by zone II in Figure 4.3), which is relatively small (5% of inflow) as was demonstrated previously by table 4.1. While the inter-gill periodic pumping mechanism is inducing a small percentage of the mass flow rate, its role cannot be overlooked. The periodic

suction and compression of the fluid may have its effect on oxygen transport and gas exchange between the fluid and the tracheal gills (oxygen dissociation).

It turns out that the major contribution of the pumping is induced longitudinally along the dorsal side of the nymph's body, where fluid enters dorsally and anteriorly at 22.26% and 23.65% respectively, flows dorsally along the mayfly, then exits dorsally and posteriorly at 60.27% and 28.64% respectively (see table 4.1). This flow is primarily induced by the antiplectic metachronal wave that starts from the back to the animal. To that effect, the flexing of the distal plate during protraction appears to reduce retrograde flow in the anterior direction. During retraction, the entire gill is pushing fluid posteriorly, while during protraction, the flexing of the distal plate reduces the frontal area of the gill thereby reducing retrograde flow in the anterior direction. In order to illustrate this second element of synergy, namely the antiplectic metachronal wave, pathlines were integrated over 10 flapping periods (after reaching the steady oscillatory state) throughout the near field as shown in Figure 4.4. Seven groups of pathlines are shown, all of which are for particles released near  $z/L = 1.15$ , which is the medial plane cutting through the middle of the gills. Of particular interest is group 'f', where particles were released at the dorsal edge of gill 3. At that instant, gill 3 was retracting and therefore doing work on those particles and pushing them posteriorly towards gill 4. At  $Re_\omega = 21.6$ , it took only one beating cycle for these particles to reach gill 4, which at this point is also retracting and therefore pushing the particles further towards gill 5, which in turn helps ejecting those particles towards the mean flow direction. The above synergy was found to occur between many consecutive gills. One more example is shown by

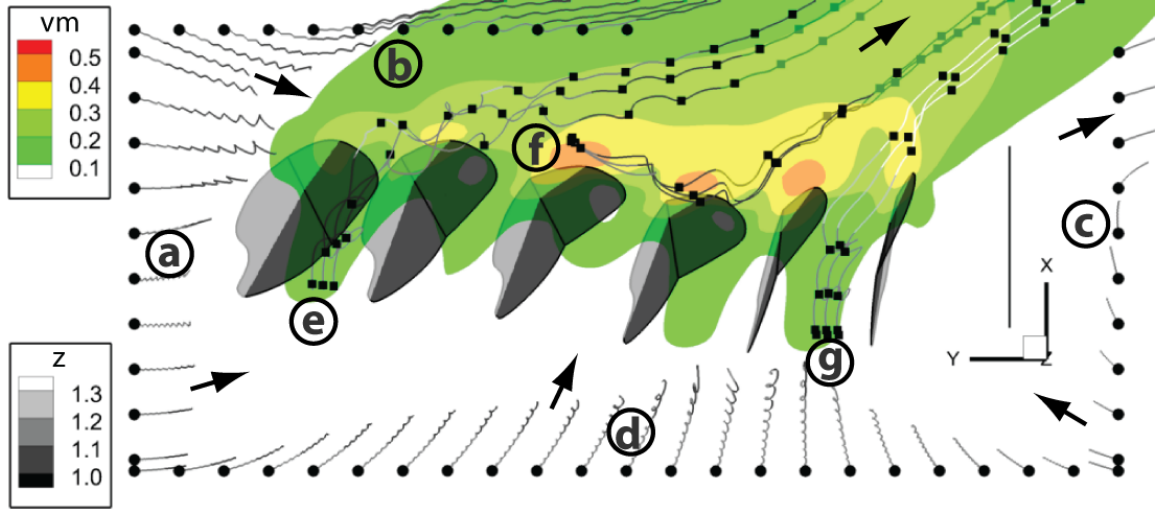


Figure 4.4: Pathlines integration for flapping kinematics over 10 periods at  $Re_\omega = 21.6$ . All particles were released near  $z/L = 1.15$ .  $vm$ : velocity magnitude.  $z$ : depth. Groups a-d: particles released on the edges of the integration domain, i.e. anterior, dorsal, posterior and ventral planes respectively. Group e: particles released in inter-gill spacing 1 – 2. Group f: particles released at the dorsal edge of gill 3. Group g: particles released in inter-gill spacing 5 – 6. Groups e-g: squares highlight one time unit. Contour floods: time-averaged velocity magnitude. Gills are shown at their mean position. Pathlines are colored by depth ( $z$ ).

following group 'e' where synergy between gill 1 and 2 is also evident.

So far, the flapping kinematics have demonstrated two elements of synergy. The first element is the periodic widening and narrowing occurring between any two consecutive gills which leads to a flow directed from the ventral side of the mayfly to its dorsal side. This flow is almost perpendicular to the mayfly axis with a slight posterior tilt depending mostly on the mean position of the corresponding gill. Currently, the contribution of this flow is at 5% of the inflow, but it is speculated to increase if the distance between the mayfly nymph and the ventral wall increases. The second element of synergy is created by the collective effect of the antiplectic metachronal wave which enables almost the entire gill array to work together by doing work on the

same particle as it flows horizontally along the mayfly naiad, which was illustrated in Figure 4.4. Later, when the effect of  $Re_\omega$  is presented, it will be shown that increasing  $Re_\omega$  is actually enhancing both elements of synergies.

Noteworthy is that gills towards the nymph head are tucked closer to the abdomen while those towards the back are extended more laterally with the proximal plates almost parallel to the transverse planes (xz planes). In specific, for gill 1,  $\epsilon = 97.17^\circ$ , while for gill 2,  $\epsilon = 91.37^\circ$ . Also, actual nymphs have smaller gills toward the head and the tail which was not incorporated in the numerical model. It looks that the gradual shift in the mean position of the gills is designed so that gills toward the head are more streamlined with the oncoming flow while those towards the back are designed to redirect the outflow in a postero-dorsal direction which is evident in the time-averaged flow field in Figure 4.1a. In addition, table 4.1 shows that the dorsal and posterior planes contribute to 88.91% of the outflow while the anterior, medial and dorsal planes contribute with 91.41% of the inflow with all three planes showing equal importance for the inflow. These flow ratios complement the speculation about the function of the shift in the gills mean position.

### 4.3.2 Rowing Dynamics at $Re_\omega = 21.6$

To contrast the flapping dynamics, a similar flow sequence is shown for the rowing conditions (also at  $Re_\omega = 21.6$ ) in Figure 4.5. While in general there are similarities with flapping kinematics, the greatest differences to be observed are generated by the asymmetry in the protraction/retraction duration, the pitch range and

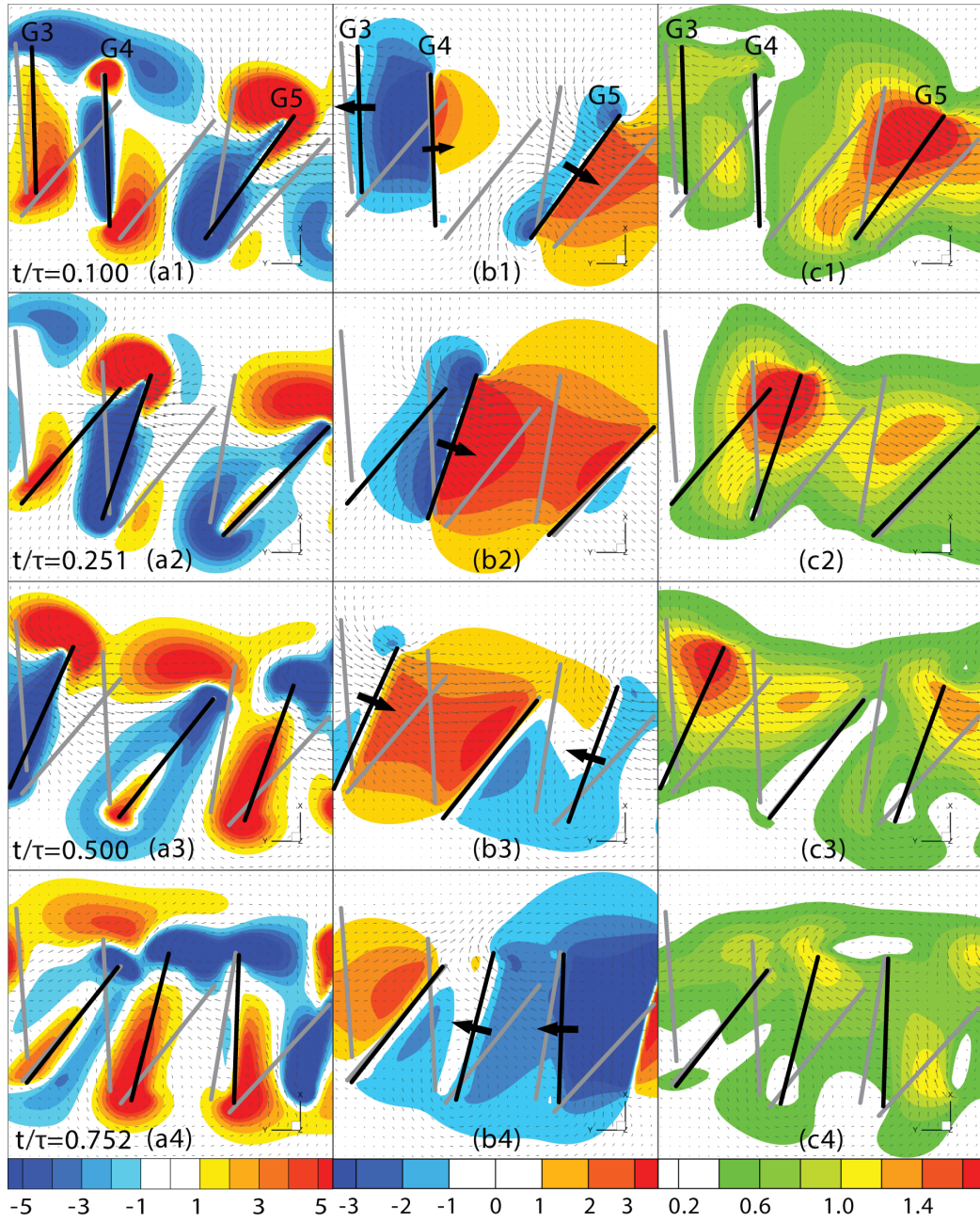


Figure 4.5: Instantaneous rowing dynamics at  $Re_\omega = 21.6$ . Slice at  $z/L = 1.15$  spatially averaged over 8 cells ( $z = \{1.07 : 1.26\}$ ). Focus is on gill 4. (Col a) Vorticity component ( $\omega_z$ ). (Col b) Pressure ( $p$ ). (Col c) Velocity magnitude ( $vm$ ). (Row 1)  $t/\tau = 0.100$ : end of recovery stroke (left), begin power stroke (right) ( $\psi_4 = 1.43^\circ$ ,  $\phi_4 = -79.55^\circ$ ). (Row 2)  $t/\tau = 0.251$ : power stroke, maximum pitch ( $\psi_4 = 13.06^\circ$ ,  $\phi_4 = -99.85^\circ$ ). (Row 3)  $t = 0.500/\tau$ : ending power stroke ( $\psi_4 = 48.31^\circ$ ,  $\phi_4 = -78.04^\circ$ ). (Row 4)  $t/\tau = 0.752$ : recovery stroke, minimum pitch ( $\psi_4 = 33.01^\circ$ ,  $\phi_4 = -63.16^\circ$ ).

the absence of any gill flexion. This, in effect, isolates the gill during its quicker power stroke during retraction, while permitting collective synchronized protraction during the lengthened recovery stroke. In detail, retraction starts for gill 4 at  $t/\tau = 0.100$ , positioned at its maximum forward position, while gill 5 has already started its rearward motion. Similar to the flapping kinematics, this creates a low pressure region within the interstitial space (space between adjacent gills), drawing fluid up from the lower ventral region. Unlike the flapping case, however, the absence of a flexure in the gill plate also allows fluid fill from the region above (dorsal) the gills. As gill 4 reaches mid-retraction ( $t/\tau = 0.251$ ), gill 5 has completed its power stroke and is at its maximum retracted position. Gill 4 is now moving largely in isolation, with a vortex dipole formed on its dorsal (positive vorticity) and ventral (negative vorticity) edges, which is really the signature of a bound vortex ring generated along the periphery of the gill. This creates a dominant induced motion in the direction of the advancing gill, drawing fluid downward and behind the animal. On the anterior space (between gill 3 and 4), a low pressure is created by the expanding interstitial volume, inducing flow up from below the animal and down from above. The pressure in the compressing interstitial space between gill 4 and 5 is now positive, with the flow moving being pushed both downward and outward (perpendicular to the plane of the figure), as evidenced by the mean flow shown in Figure 4.1b and table 4.1. As gill 4 ends its retraction stroke ( $t/\tau = 0.500$ ), the compression phase begins on the anterior side of the gill, reversing the pressure gradient along the anterior surface and also reversing the sign of the vorticity production along the surface, leading to a reversal of the vortex dipole bound to the edge. At  $t/\tau = 0.752$ , gill 4 is in the middle of its

lengthy protraction stroke and is surrounded by two neighboring gills, which are also completing the beginning and ending of the their respective protraction strokes.

During the qualitative analysis of the rowing flow fields, and in contrast with flapping flow field, no form of synergy could be detected that would bring the entire gill array to work together. As mentioned earlier, it seems that each gill performs its quick power stroke in isolation, then slowly retracting while decreasing its pitch during the recovery stroke in order to decrease the viscous drag.

#### 4.4 Viscous and Inertial Effects

In reporting their results, [58] had classified the nymphs beating kinematics into three types: 1) rowing for  $Re_\omega < 5$ , which was characterized by a higher pitching range and a negligible hinge flexion angle (of the same order of the digitization error), 2) flapping for  $Re_\omega > 20$ , which was characterized by a minimal pitch variation and the formation of a distal flap that appeared to move passively, and 3) intermediate kinematics for  $5 \leq Re_\omega \leq 20$ , which marked abrupt and gradual changes in many parameters such as a decreased stroke plane deviation and an increased hinge flexion angle, which increased from  $17 \pm 2^\circ$  to  $61 \pm 7^\circ$ .

In light of the experimental findings by [58], my initial parametric space was selected to include 3 different Reynolds numbers that each lie in a different kinematical regime. Based on the available experimental data, the choice was limited to insects corresponding to  $Re_\omega = \{2.3, 8.1, 21.6\}$ . Following my preliminary findings, the parametric space was subsequently expanded to include a lower  $Re_\omega = 1.0$ . In

other words, in order to investigate the effect of  $Re_\omega$  on the rowing-flapping transition, 4 simulations were carried out at  $Re_\omega = \{1.0, 2.3, 8.1, 21.6\}$  for *each* set of kinematics described in §2.2.

It has long been recognized that all sources of vorticity in homogenous fluids must lie at the boundaries of fluid regions. Studies on vorticity show that its rate of generation involves the tangential pressure gradient within a fluid and the external acceleration of the solid boundary. It is also known that vorticity diffuses neither out of boundaries nor into them, and that the only means of decay is by cross-diffusive annihilation within the fluid [50], such as between two counter-rotating vortices. In light of that, it is speculated that the flapping type of kinematics generate more vorticity compared to the rowing type of kinematics. This is because of the presence of the distal flap, which, during protraction is almost aligned with the mean flow and hence providing more tangential acceleration to the surrounding fluid (see Figure 2.7 at  $t/\tau = \{0.2 : 0.5\}$  for the kinematics and Figure 4.2a2 for the negative vorticity generated). This is in contrast with rowing where most of acceleration is normal to the mean flow and the vorticity generated is used primarily in creating the bound vortex (Figure 4.5).

In order to illustrate the effects of  $Re_\omega$  on the vorticity dynamics of both kinematics, contours of the z-component of vorticity ( $\omega_z$ ) are shown in Figure 4.6 and Figure 4.7 for the flapping and rowing kinematics respectively. The focus is on left gill 4 by the end of its retraction ( $t/\tau = 0.125$  for flapping and  $t/\tau = 0.475$  for rowing).  $\omega_z$  has been normalized by the local maximum that occurs at the core of the positive vortex near the dorsal edge of the gill. A qualitative criteria has been set to

identify vortex detachment. If the local maximum of  $\omega_z$  remains close (attached) to the dorsal edge of the gill by the end of retraction, then it is concluded that the generated vorticity is quickly diffused or annihilated by its neighboring counter-rotating negative vortex. In other words, the momentum diffusion is high enough that no vortical 'structure' could detach from the gill. On the contrary, if the local maximum of  $\omega_z$  slightly convects away from the dorsal edge and lasts for at least 5% of the period, then it is concluded that the bound vortex have detached from the gill and have survived cross-diffusion. The attached or detached distinction can be compared to flow behind cylindrical structures, where at low  $Re$ , two counter-rotating vortices or recirculation bubbles remain attached to the cylinder, while at higher  $Re$ , instability develops leading to the von Kármán street vortex and vortex detachment [60].

With reference to Figures 4.6 and 4.7, it is noted that the vortex detachment occurs at  $Re_\omega \geq 8.1$  for *both* types of kinematics. In both Figures parts (a) and (b), the positive vortex has detached from gill 4, while in parts (c) and (d), the vortex remains visibly attached and lose coherence quickly under viscous diffusion. Granted the detached vortex core has smaller magnitude compared to the negative vorticity being generated by the distal flap, it marks the onset of weak inertia. Also, this detachment occurs more or less for all six gill pairs when  $Re_\omega \geq 8.1$  and therefore its relation to the rowing-flapping transition is unlikely to be coincidental.

The subtle detachment of any of the aforementioned vortices for  $Re_\omega \geq 8.1$  has a noticeable effect on the velocity vectors because of its slight interaction with the negative vorticity being generated by the gill as it ends its retraction and initiates its protraction. For both types of kinematics, the short-lived instantaneous dipole

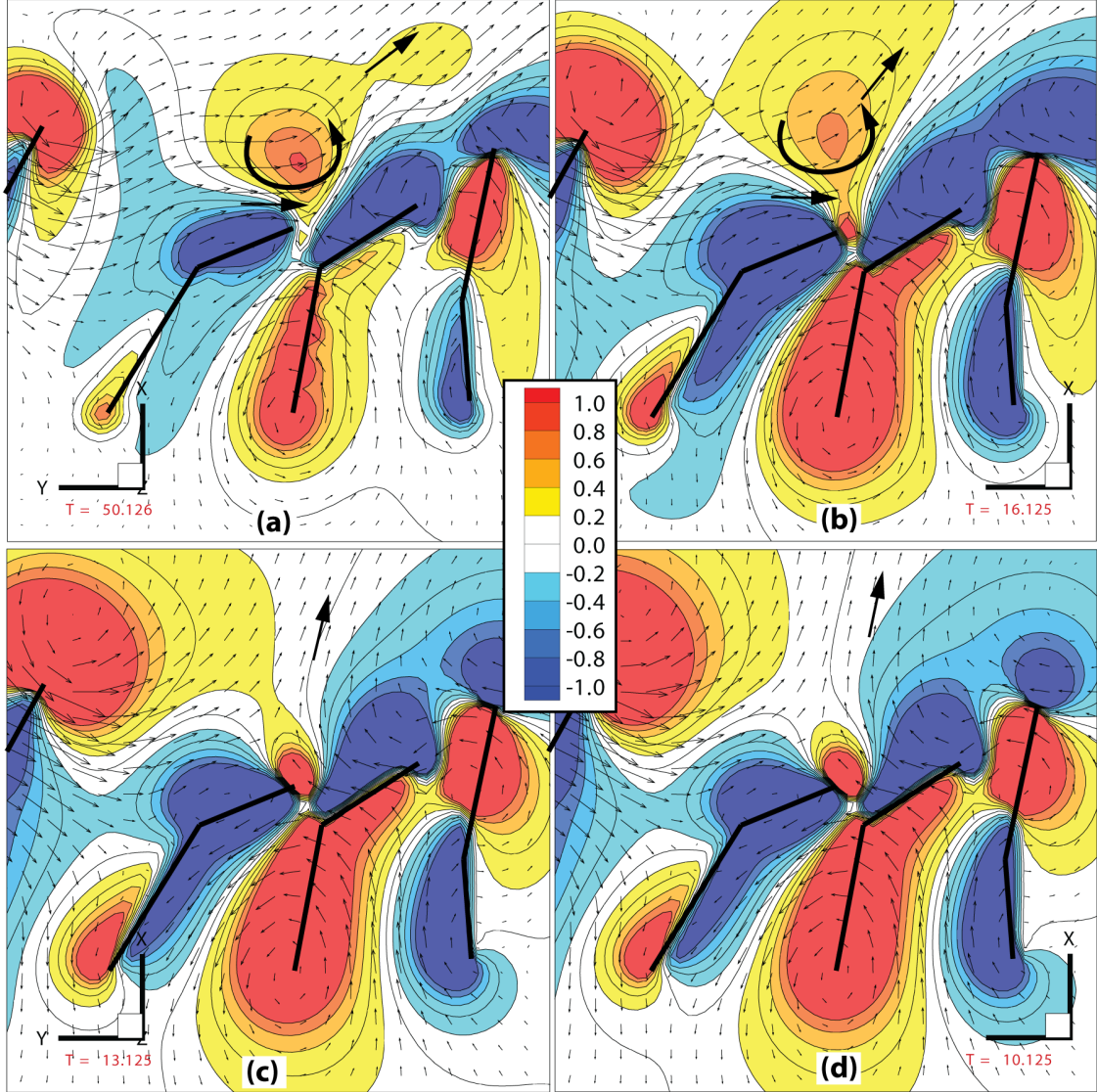


Figure 4.6: Effect of  $Re_\omega$  on  $\omega_z$  for flapping kinematics. Contours floods and lines of  $\omega_z$  normalized by its local maximum (positive vortex core near the dorsal edge).  $t/\tau = 0.125$ : end of left gill 4 retraction. Orthogonal view of a  $z$ -slice at  $z/L = 1.15$ . Vectors shown are in-plane velocity vectors. (a)  $Re_\omega = 21.6$ . (b)  $Re_\omega = 8.1$ . (c)  $Re_\omega = 2.3$ . (d)  $Re_\omega = 1.0$ .

is expelling fluid in a horizontal direction (left to right), which acts in favor of the flapping kinematics, but not so much in favor of the rowing kinematics. Figure 4.6 illustrates the effect on the velocity vectors in the right vicinity of the dipole, where at low  $Re_\omega$  (parts (c) and (d)), the vectors are pointing more upwards, but with

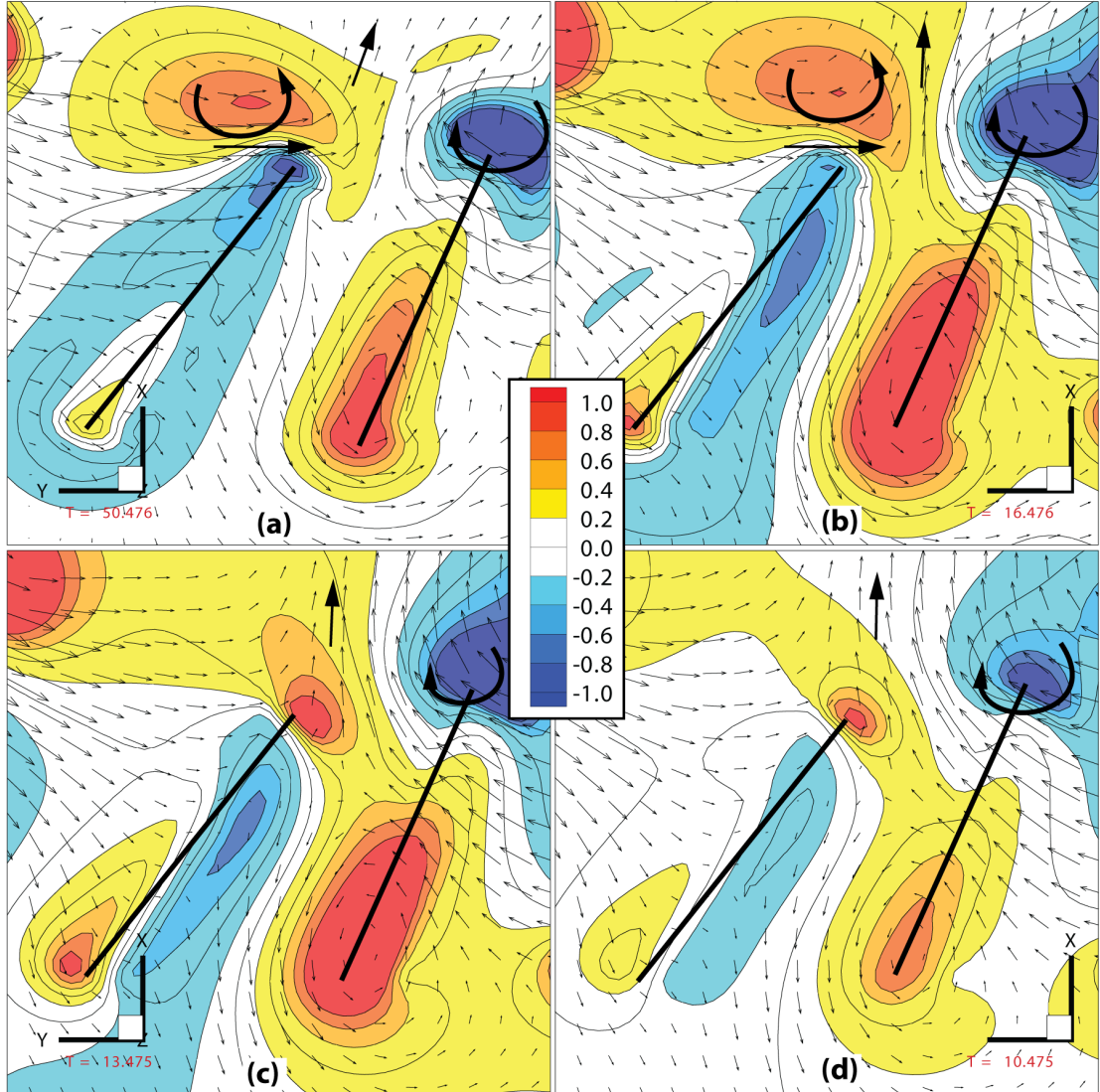


Figure 4.7: Effect of  $Re_\omega$  on  $\omega_z$  for rowing kinematics. Contours floods and lines of  $\omega_z$  normalized by its local maximum (positive vortex core near the dorsal edge).  $t/\tau = 0.475$ : end of left gill 4 retraction. Orthogonal view of a  $z$ -slice at  $z/L = 1.15$ . Vectors shown are in-plane velocity vectors. (a)  $Re_\omega = 21.6$ . (b)  $Re_\omega = 8.1$ . (c)  $Re_\omega = 2.3$ . (d)  $Re_\omega = 1.0$ .

increasing  $Re_\omega$ , they start to point more horizontally (parts (a) and (b)). The velocity vectors at  $Re_\omega < 8.1$  at this instant are also affected by the leading gill (gill 5) because of the higher diffusion inherent to the lower  $Re_\omega$ . Overall, this instant demonstrates a combined effect of the oncoming fluid inertia (from the left), the instantaneous vortex

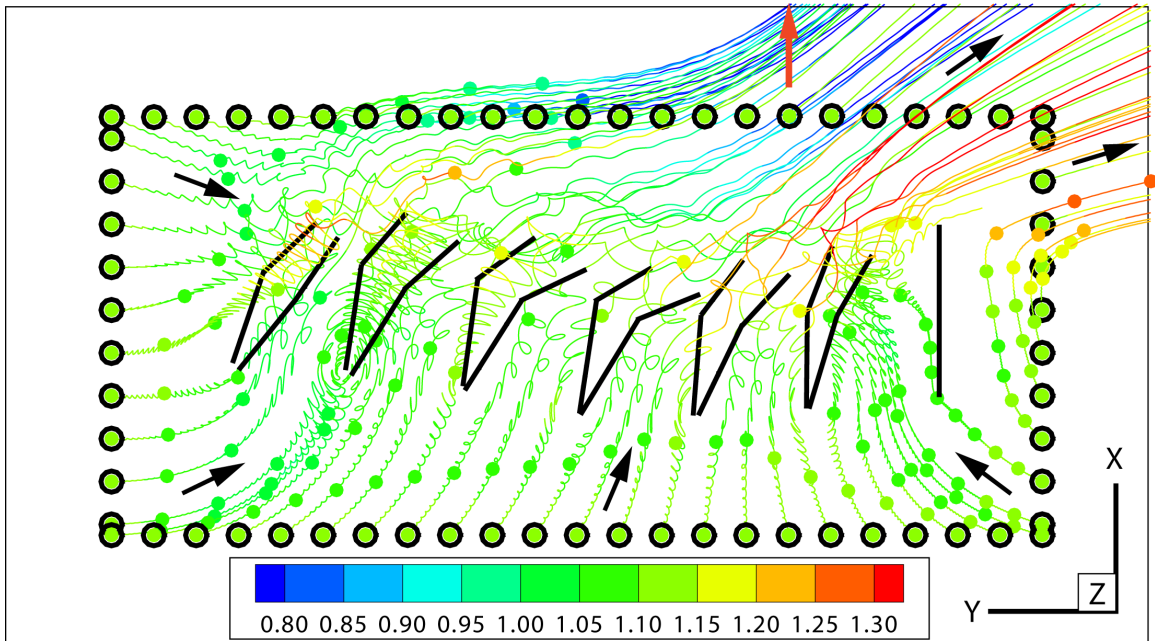
and the interaction with the leading gill. The short-lived instantaneous dipoles along with the asymmetry introduced by the distal flap occurring over the entire array explains the fact that most of the outflow for the flapping kinematics is occurring in the dorsal direction (see table 4.1). In contrast, for the rowing kinematics (Figure 4.7), the detached vortex is acting behind the retracting gill so that the instantaneous dipole is not providing an obvious function so as to help the mean flow.

The previous discussion of vortex detachment (shedding) or attachment was found to be close to some recent studies. The most similar work is reported by Roper [54] in §4.2 and precisely Figure 4.4. Using COMSOL, a tethered 2D asymmetric fin, which is a proxy for *Clione antarctica* [12], was forced to oscillate (flap) up and down in a time-reversible fashion. The foil was then able to exert a net pumping force upon the fluid in a direction orthogonal to the plane of flapping. Two flapping regimes were identified which were signaled by a reversal in the direction of the time averaged pumping force at  $Re_\omega = 20$ . It was concluded that the pumping mechanism is effective even at arbitrarily low rates of energy expenditure. At higher frequencies ( $Re_\omega > 20$ ), the flow rate is supplied by vortex dipoles shed from the fin edges on alternating halves of the fin stroke. However, positive thrust is generated only above a critical flapping Reynolds number ( $Re_\omega > 20$ ) coinciding with the work in [1, 12, 66, 67]. Roper [54] pointed out, however, that the mechanism for thrust production is *not* illuminated by examination of the instantaneous flow field, since at each half of the fin beat, vortices build up on the fin edges, but are eliminated by viscous diffusion too quickly to be shed (Hence, my depiction earlier in 4.6 and 4.7 using normalized vorticity).

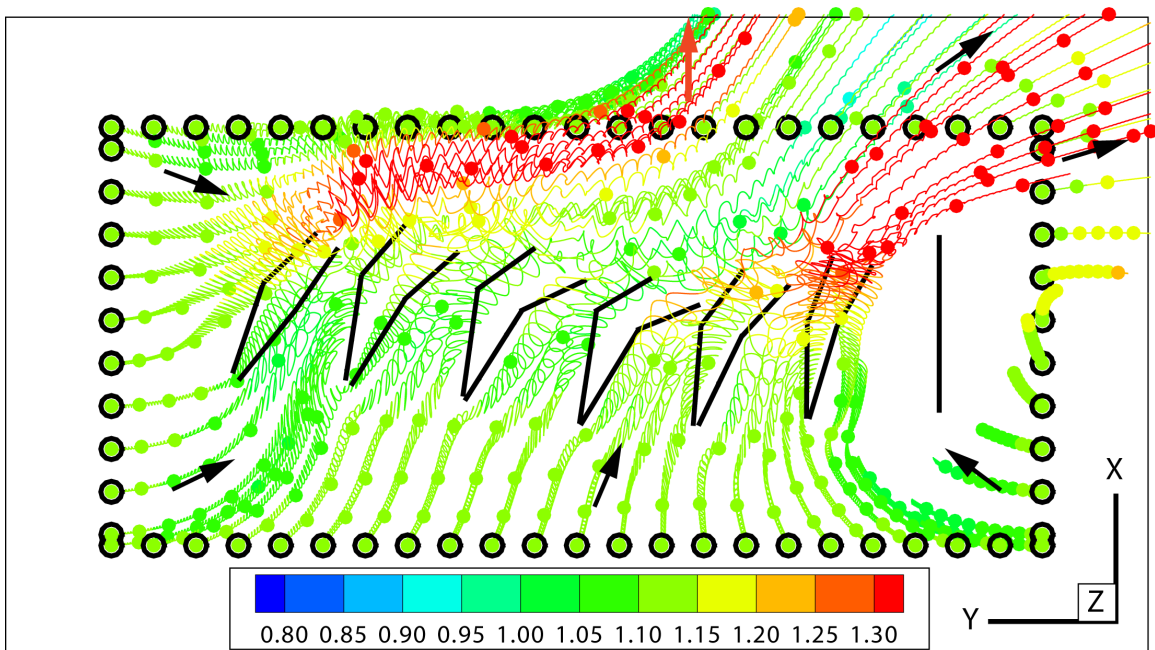
Another similar work pertaining to locomotion only (no net pumping investi-

gated) was presented in [1]. [1] used *in-silico* experiments to study a 2D flapping ellipsoidal body. By introducing a perturbation normal to the flapping direction, they showed that at sufficiently large  $Re_f$ , unidirectional locomotion emerges as an attracting state. Locomotion was shown to be generated in two stages: first, the fluid field loses symmetry by an instability similar to the classical von Kármán instability; and second, precipitous interactions with previously shed vortical structures push the body into locomotion. Based on my current work and previous studies, it may be concluded that net pumping occurs even at low  $Re_\omega$  provided some sort of asymmetry is introduced. However, locomotion occurs only above a certain critical  $Re_\omega$ .

To further illustrate the effect of  $Re_\omega$  on the flapping kinematics, pathlines have been integrated after reaching the steady oscillatory state for both the highest and lowest  $Re_\omega$  available ( $Re_\omega = 21.6$  and  $Re_\omega = 1.0$  respectively) over 100 periods. The result of the integration is shown in Figure 4.8. In Figure 4.8, particles were released all around the gill array at  $z/L = 1.15$ , then integrated over 100 periods. The initial position of the particles is outlined by black circles ( $\circ$ ), and the pathlines are colored by depth  $z$ . Also, the location of the particles is shown every 10 periods ( $\bullet$ ). In comparing  $Re_\omega = 21.6$  with  $Re_\omega = 1.0$ , one may spot the increasing inertial effects and decreasing viscous effects by noticing two features of the pathlines. The first feature is where the particles or pathlines exit the dorsal plane (top or  $x_{max}$ ). At  $Re_\omega = 21.6$ , the particles have been displaced further to the right compared to  $Re_\omega = 1.0$  by about  $0.5L$ , which is highlighted by the red arrows. The second feature is the oscillating motion of the particles, which is present everywhere for  $Re_\omega = 1.0$ , but only at inflows for  $Re_\omega = 21.6$ . Both these features indicate higher inertia present



(a)  $Re_\omega = 21.6$



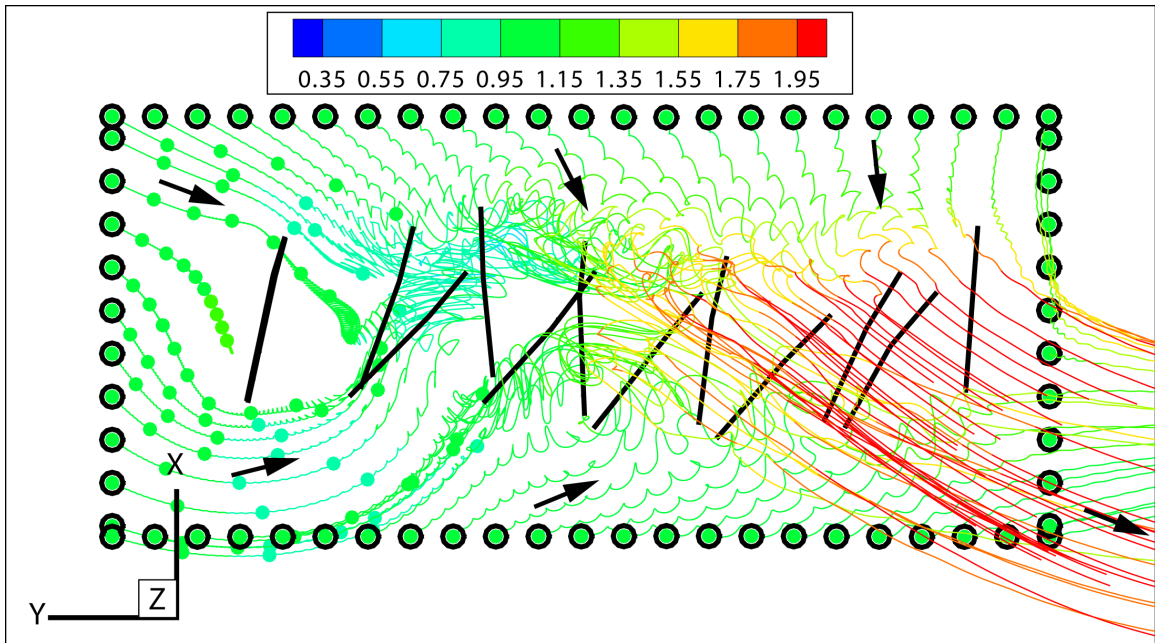
(b)  $Re_\omega = 1.0$

Figure 4.8: Pathlines integration for flapping kinematics over 100 periods. (a)  $Re_\omega = 21.6$ . (b)  $Re_\omega = 1.0$ . Pathlines are colored by depth  $z$  (blue: inwards, red:outwards).  $\circ$ : Particles initial seeding position at  $z/L = 1.15$ .  $\bullet$ : Particles location each 10 periods. Black arrows indicate mean flow direction. Section of gills shown is at  $z/L = 1.15$  and illustrates their extreme flapping positions.

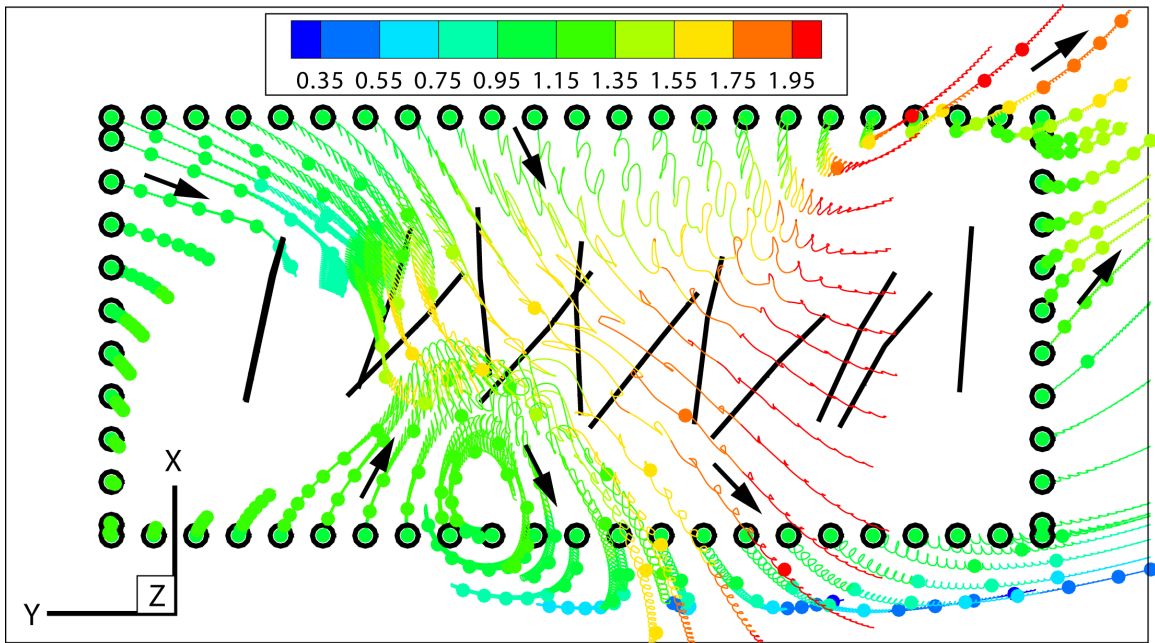
in the flow. In addition, the oscillating motion of the particles with respect to the actual displacement is an indication of how well or efficient the micro-pumping is. In specific, it takes on average 4 beating periods for the particles located on the ventral side (bottom or  $x_{min}$ ) to reach the inter-gill spacings when  $Re_\omega = 1.0$ , but it takes fewer than 2 periods when  $Re_\omega = 21.6$ . Qualitatively, it may be concluded that the flow field for  $Re_\omega = 21.6$  provides a higher mass flow rate because of the smaller oscillations, is doing less work in moving particles because of the fewer number of periods required to move particles around, and is therefore more efficient than the flow field for  $Re_\omega = 1.0$ . This will be substantiated later when the performance metrics are presented.

Noteworthy is that the second feature discussed above highlights the second element of synergy previously discussed in §4.3.1 and how the increased inertial effects are acting in favor of enhancing the antiplectic metachronal wave. Noteworthy also is that not all inter-gill spacings are performing the same. Close examination of Figure 4.8 will reveal that inter-gill spacings 4-5 and 5-6 are pushing more fluid than their counterparts, followed by inter-gill spacing 3-4, then 2-3 and then 1-2. This is equally true for both  $Re_\omega = 1.0$  and  $Re_\omega = 21.6$ .

To contrast, pathlines integration for the rowing kinematics using the same planform (planform A) for  $Re_\omega = 21.6$  and  $Re_\omega = 1.0$  is performed and is shown in Figure 4.9. According to Figure 4.9, changing the  $Re_\omega$  has a stronger effect on the rowing kinematics compared to the flapping kinematics. In Figure 4.9b ( $Re_\omega = 1.0$ ), a small recirculation zone is present on the ventral side of the mayfly, below gill pair 2 and 3. This recirculation zone does not extend all the way in the  $z$  direction but



(a)  $Re_\omega = 21.6$



(b)  $Re_\omega = 1.0$

Figure 4.9: Pathlines integration for rowing kinematics over many periods. (a)  $Re_\omega = 21.6$ . (100 periods) (b)  $Re_\omega = 1.0$  (75 periods). Pathlines are colored by depth  $z$  (blue: inwards, red: outwards).  $\circ$ : Particles initial seeding position at  $z/L = 1.15$ .  $\bullet$ : Particles location each 10 periods. Black arrows indicate mean flow direction. Section of gills shown is at  $z/L = 1.15$  and illustrates their extreme rowing positions.

extends only from the mid-section of the gills ( $z/L \approx 1.15$ ) to the their tips ( $z/L \approx 1.68$ ). The recirculation zone was also observed when  $Re_\omega = 2.3$ , but disappeared for  $Re_\omega \geq 8.1$ . It is interesting that this feature is 'toggled' during the rowing-flapping transition, but no apparent connection could be established. The recirculation zone is probably due to the increasing effect of the no-slip ventral wall located at  $\approx 1.5L$  below the gill array when decreasing  $Re_\omega$ .

Another effect of increasing the  $Re_\omega$  is the ratio between the medial (lateral) flow rate to the posterior (back) flow rate. The higher the  $Re_\omega$ , the higher the flux through the posterior plane as shown in Figure 4.9a. On the contrary, the lower the  $Re_\omega$ , the higher the flux through the medial planes as shown in Figure 4.9b. This is probably due to the increased interaction between the gills, where a retracting gill faced by a non-moving or slowly protracting gill will tend to squeeze fluid out medially rather than pushing fluid posteriorly. In numerical terms, the magnitude of the y-component of the velocity vector is higher for higher  $Re_\omega$ , which aligns with the direction of the power stroke of the gills while the z-component is higher for lower  $Re_\omega$ . The mass flow rates will be quantified later in §4.6.

The rowing flow fields exhibit one feature that is similar to the flapping kinematics previously shown in Figure 4.8, which is the amount of oscillations present along a pathline with respect to the net displacement of a particle. The higher the  $Re_\omega$ , the higher the net displacement of most particles with respect to the amplitude of oscillations. This is the telltale sign of increasing fluid inertia. Again, just by looking at both cases, one may speculate that the higher  $Re_\omega$ , the more efficient is the mayfly in moving fluid around.

Finally, at  $Re_\omega = 21.6$  and in comparison with flapping, particles are leaving the integration domain faster. In Figure 4.9a, particles released on top of the mayfly naiad left the integration domain in fewer than 10 periods (medially or posteriorly), while for the flapping case at the same  $Re_\omega$  (Figure 4.8a), most of the particles resided in the integration domain for more than 20 periods. This is primarily due to the higher accelerations present in retracting half-stroke of the rowing kinematics and the higher tip velocities associated with the longer strokes.

To summarize this section, one may conclude a few points about the effect of  $Re_\omega$ . First and foremost and for both kinematics, the higher the  $Re_\omega$ , the more efficient the fluid is moved around. This was indicated by the smaller oscillations with respect to the net displacement associated with higher  $Re_\omega$  and the fewer number of periods required to move particles around. In other words, both kinematics are enhanced by increasing fluid inertia and decreased viscous effects. Second, the flapping flow structure is not affected much by increasing the  $Re_\omega$ , while the rowing flow structure shows more sensitivity, though insignificant overall. Finally, the rowing type of kinematics is able to move fluid around faster and is therefore inducing higher mass flow rates.

## 4.5 Planform Morphology

Initially, the parametric space designed to investigate the rowing-flapping transition had only the  $Re_\omega$  as an independent parameter,  $Re_\omega = \{1.0, 2.3, 8.1, 21.6\}$ , yielding only 8 simulations, 4 for flapping and 4 for rowing. After the quantitative

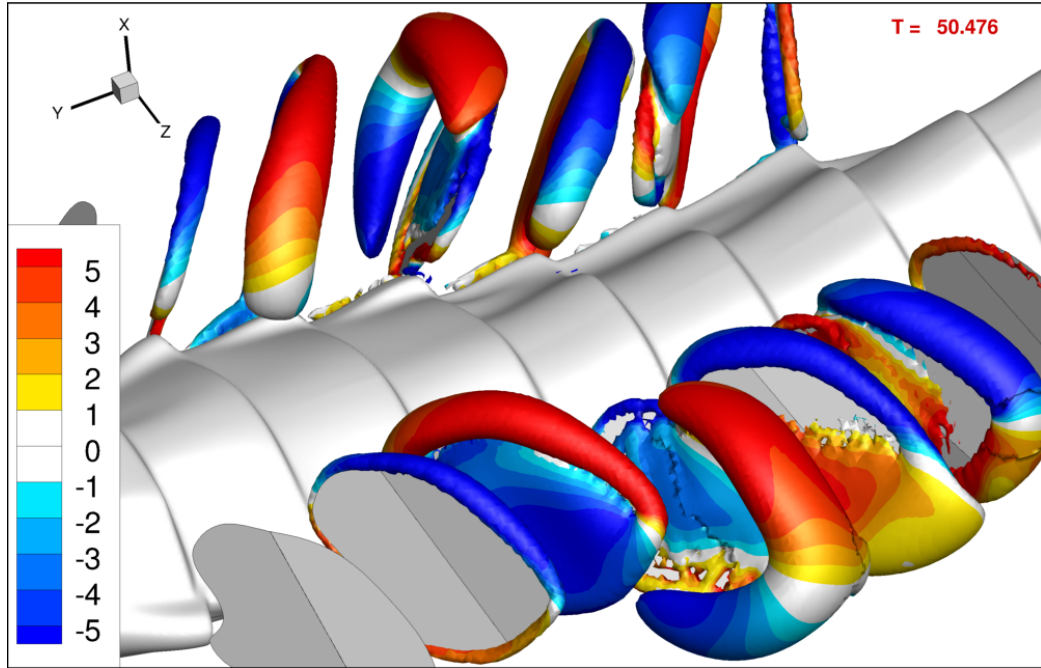
assessment using the performance metrics introduced in §2.4, which will be shown later, the results showed some potential to explain the transition, but did not match the experimental findings very well. In specific, the quantitative results favored a transition between  $1.0 < Re_\omega < 2.3$  when using only planform A (see Figure 2.3 for planform illustration), which is lower than the regime reported by the PIV experiments ( $3 < Re_\omega < 8$ ). Knowing that young nymph possess narrower gills than what was used in the simulations, I decided to investigate the effect of the gill shape or planforms. Therefore, two more planforms were introduced, which are planforms B and C (see Figure 2.3 for planform illustration). Planform B was reported by experiments and is used by younger (smaller) nymphs. Planform C is a numerically distorted version of planform B, obtained by scaling down planform B, but only in its local x axis. Hence, the area of planform C is 20.72% smaller than B and its aspect ratio is 26.01% higher than planform B.

The direction of investigating the gill planform was a result of a few key points. First, there were only **two** planforms reported by the experiments, namely planforms A and B for old nymphs and young nymphs respectively. This means that there is a degree of uncertainty associated with the shape of those gills. In other words, there is no guarantee that the gill planform is exactly the same across different nymphs or even within the same nymph. Given that *C. triangulifer* molts more than a few times during its aquatic phase, it seems more likely that the gill shape or planform undergo some sort of 'smooth' transition rather than jumping directly from planform B to planform A. This was also speculated because the structural properties of the gills undergo a transition (bigger gills exhibit more flexibility) and because of the existence

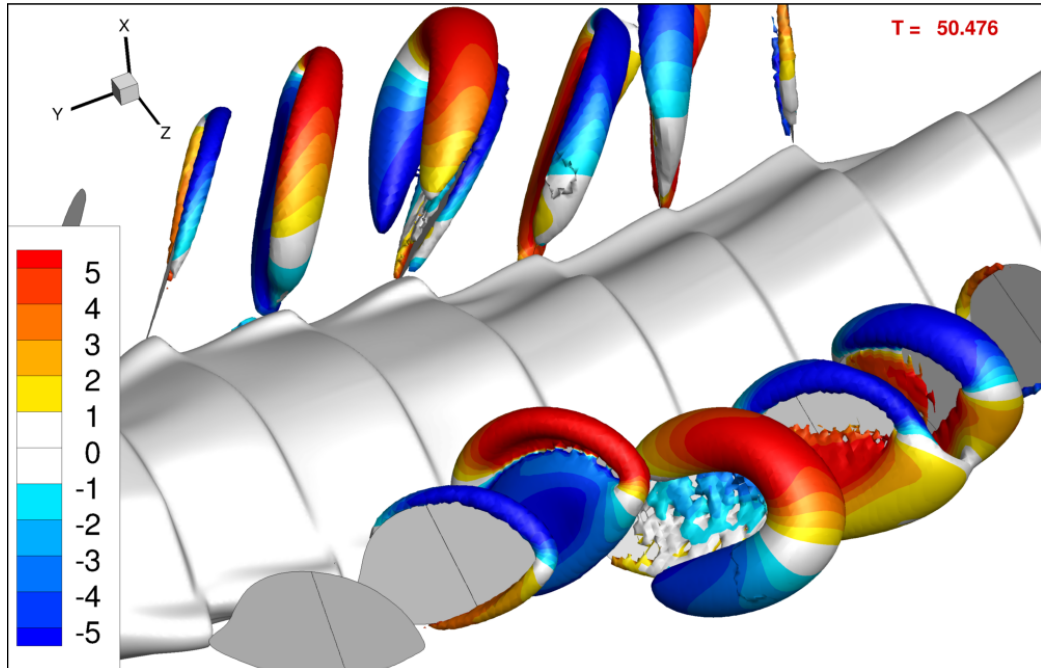
of an intermediate kinematics regime. Second, the gill length is not constant within the same nymph (gill 3 and 4 are the biggest, then gills tend to decrease in size posteriorly and anteriorly). Finally, during the replication of the rowing kinematics, I investigated the average location of landmarks 'D' and 'V' with respect to the root 'R' and tried to fit those on planforms A and B. This investigation was completely independent of the Eulerian angles extraction or the kinematic chain. I was simply calculating the norms of the different segments ( $\overline{RV}$ ,  $\overline{RD}$ ,  $\overline{DV}$ ) and overlaying them on gill planform B. This in turn suggested that the gills needed to be narrower in order to better fit the rowing kinematics I was using.

In light of the above, and knowing that the uncertainty in the experimental work for younger (smaller) nymphs is higher than the uncertainty related to older (larger) nymphs, I investigated the effect of the gill planform using the rowing kinematics. In specific, 8 more simulations using the rowing kinematics were carried out, 4 using planform B and 4 using planform C, both planforms at  $Re_\omega = \{1.0, 2.3, 8.1, 21.6\}$ , with the purpose of comparing those with previous rowing simulations using planform A. With the introduction of the planform uncertainty, variability or morphology, the final parametric space encompassed 16 simulations and 3 independent variables, which are the  $Re_\omega \{1.0, 2.3, 8.1, 21.6\}$ , the gill planform {A,B,C} and the beating kinematics {flapping, rowing}.

As discussed earlier in §2.1, the area of planforms A, B and C are 0.638, 0.449, and 0.356 (length squared) respectively and the corresponding aspect ratio is 1.57, 2.23, and 2.81 respectively. Most of the qualitative differences that show up in comparing the flow field of different planforms can be attributed to the variation in their

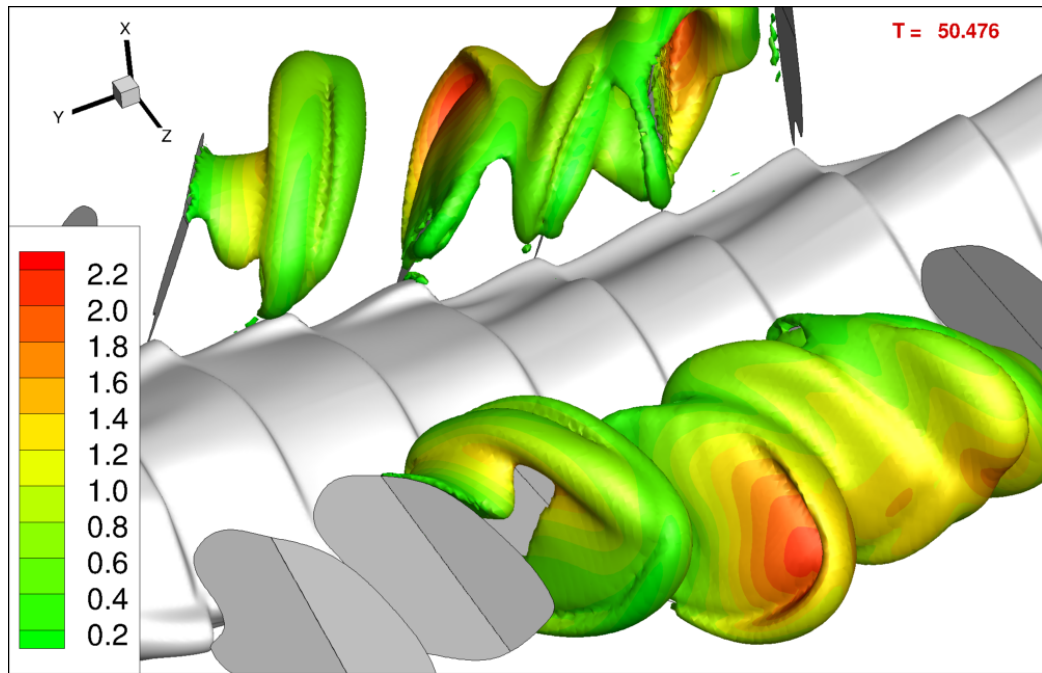


(a) Planform A

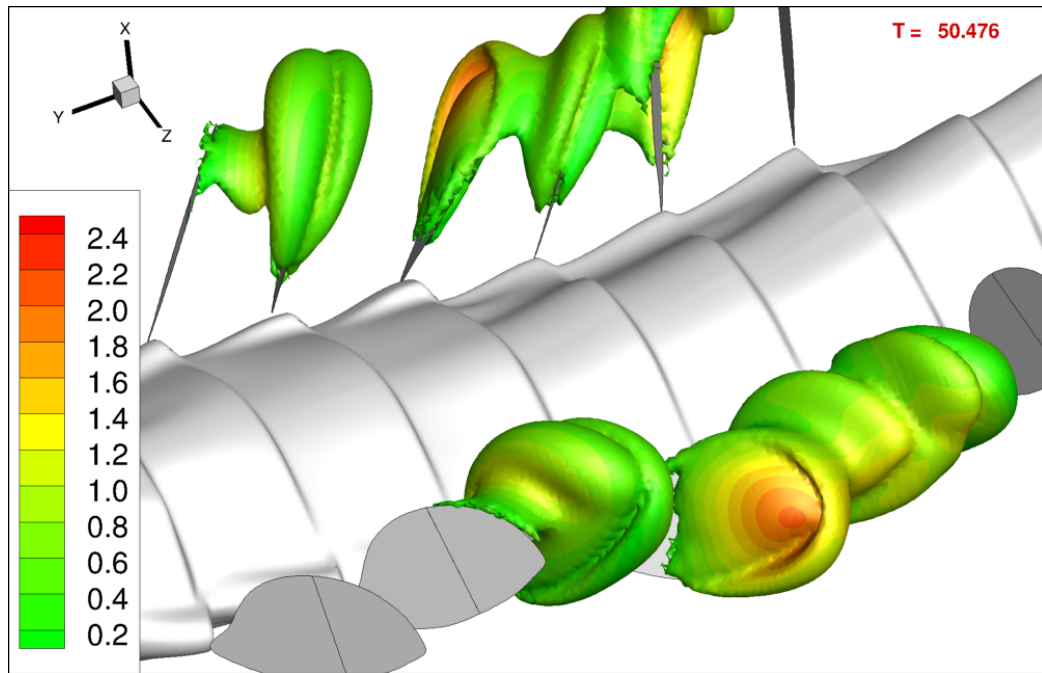


(b) Planform C

Figure 4.10: Effects of planform morphology on flow fields for  $Re_\omega = 21.6$  at  $t/\tau = 0.476$ . Iso-surfaces of the second invariant of the velocity gradient tensor ( $Q_2=5$ ), flooded by the  $z$ -component of the vorticity vector  $\omega_z$ . (a) Planform A. (b) Planform C.



(a) Planform A



(b) Planform C

Figure 4.11: Effects of planform morphology on flow fields for  $Re_\omega = 21.6$  at  $t/\tau = 0.476$ . Iso-surfaces of the viscous dissipation rate ( $\phi = 5 \times 10^{-5}$ ), flooded by the velocity magnitude. (a) Planform A. (b) Planform C.

surface area and their aspect ratio. After all, this is the only independent variable or parameter that is being changed. For example, the (spatial) average velocity magnitude behind a retracting gill is higher, when using bigger planforms, i.e. a bigger mass of fluid is being pushed posteriorly. This will have a direct effect on the mass outflow exiting the gill array behind the nymphs. The higher the surface of the planform, the higher the mass flow rates induced for the 3 planforms investigated. A second qualitative measure is seen when iso-surfaces of flow structures are plotted. In Figure 4.10, instantaneous iso-surfaces of the second invariant of the velocity gradient tensor (also known as the Q2 criterion [33]) are shown for the largest planform (A) and the smallest planform (C) both operating at the highest  $Re_\omega$  ( $Re_\omega=21.6$ ). Also, the iso-surfaces are colored by the z-component of the vorticity vector,  $\omega_z$ . In addition, both left and right rows of gills are shown to provide better visualization (remember that the flow field is symmetric around the medial plane). Generally speaking, the coherent structures for planform A are bigger, which is most evident by the presence of the bound vortices around gills 3-6. Not only the vortices are larger, but also the magnitude of vorticity is higher for bigger planforms as indicated by the colored contours.

The instantaneous field picked in Figure 4.10 ( $t/\tau = 0.476$ ) actually coincides with the instantaneous field previously shown in 4.7a when presenting the effect of  $Re_\omega$  on the flow field. At that instant, which is the end of retraction of gill 4, the onset of vortex detachment was shown, which is illustrated here by the iso-surfaces of the Q2 criterion. The bound vortex has detached from gill 4 and will quickly lose coherence into the surrounding field. Again, the detached vortex for planform A is

larger than for planform C and exhibits higher vorticity magnitude especially when moving farther from the gill tip.

With the higher velocities and bigger structures associated with bigger planforms, one may speculate that the rate of viscous dissipation is also higher. For that purpose, Figure 4.11 shows iso-surfaces of the viscous dissipation rate ( $\phi = 5 \times 10^{-5}$ ) flooded by the velocity magnitude at the same instant as Figure 4.10, i.e. at the end of retraction of gill 4 ( $t/\tau = 0.476$ ). Clearly, the viscous dissipation rate is higher (evident by the larger iso-surfaces) for planform A at that  $Re_\omega$ . This is in fact true for all  $Re_\omega$  considered. The higher velocities near the tip of gill 4 is also evident as well as gills 5 and 6.

In my efforts to relate the effects of planform morphology to known physical parameters or dimensionless groups, I found that as many as three Reynolds numbers could be defined for this particular problem. The first  $Re$  is the oscillating  $Re$  (previously defined as  $Re_\omega = L^2 f/\nu$ ). The second  $Re$  could be based on some tip velocity (maximum or mean), which would take into account the difference between the two types of kinematics (including the hinge development) and would surely correlate with  $Re_f = fAL/\nu$  (sometimes reported as the flapping or frequency  $Re$ ). A third  $Re$  may be defined using some chord length (for example  $\overline{DV}$ ) or the gill aspect ratio, which would take into account some of the variation in the planform shape. In an overly simplified situation, each of the 3 independent parameters in this parametric space ( $Re_\omega$ , planform and kinematics) represents some ratio between the viscous forces and the inertia in one way or another and all 3 parameters are playing a role in explaining the rowing-flapping transition. Noteworthy is that in insect locomotion, where a

forward velocity is clearly defined, a manipulation of the first two Reynolds numbers would yield the so-called advance ratio or reduced frequency, but for a stationary insect like the mayfly nymph, these parameters do not show up normally.

To sum up this section, the effect of planform morphology was investigated by simulating 3 different planforms using the rowing kinematics. This was mainly driven by the higher uncertainty present in smaller nymphs which are known to employ the rowing type of kinematics and use narrower planforms such as planforms B and C. It was concluded that larger planforms are inducing higher mass flow rates and bigger vortices according to the Q2 criteria. The presence of a bound vortices speculated by previous PIV experiments [57–59] is now corroborated. The effect of increasing the aspect ratio of the gills may be analogous to decreasing the inertial effects, because of the smaller fluid mass associated with it (smaller added mass).

## 4.6 Micro-pumping and Performance Metrics

The results presented in the previous sections attempted to introduce the complicated nature of the flow field while qualitatively comparing the effects of the different independent parameters involved in the rowing-flapping parametric space. In other words, the effect of varying the  $Re_\omega$ , the gill planform and the type of kinematics employed was investigated only by looking at the flow fields of the different scenarios. In fact, the different snapshots of the flow fields were hand-picked from dozens of animations that were batch-created and inspected in my attempt to explain the transition. Unfortunately, all of these qualitative results cannot ascertain

any possible reason behind the transition reported by the PIV experiments. What was established qualitatively, with a good degree of certainty, is that higher  $Re_\omega$  simulations are more efficient than lower  $Re_\omega$  for *both* kinematics which doesn't say much about the transition. In fact, it is well established that lower  $Re_\omega$  are associated with lower efficiencies [45, 53], including roto-dynamic pumps. It was also illustrated that the rowing kinematics are able to push fluid faster in comparison with the flapping kinematics when operating at the same  $Re_\omega$ . This was mainly due to the higher accelerations and longer beating strokes present in the rowing kinematics, where the effect of latter will appear in  $Re_f$  (rowing kinematics have higher  $Re_f$  than flapping kinematics when both are operating at the same  $Re_\omega$ ). It can be speculated that the rate of work done by the rowing kinematics is going to be higher than its flapping counterpart when both kinematics are employing the same planform (planform A). This, again doesn't say much about the transition, since the rowing kinematics induces higher mass flow while and, at the same time, does more work compared to its flapping counterpart. The effect of increasing the planform aspect ratio on the rowing kinematics is inducing less mass flow rate and probably doing less work. Narrower planforms will decrease the interaction between the gills, which might act in favor of the rowing kinematics since the rowing kinematics does not display much synergy. On the other hand, the flapping kinematics were shown to have two elements of synergy, where the first allows two consecutive gills to work together, and the second brings the entire array to work together by enhancing the antiplectic metachronal wave.

In light of the above, it was necessary to look into quantitative measures that try to assess the performance of each combination of independent variables. Any

quantitative measure ought to be realizable by the current mathematical model, which solves only for conservation of momentum and mass. This is still acceptable owing to the exploratory nature of the project and the higher cost associated with simulating mass transport. Future extensions may be able to tackle the problem with more complicated models, but only after some understanding of the flow fields have been reached and the important parameters have been identified.

However, most of the metrics that exist for biological taxa and fluid mechanics assume the existence of a clear forward velocity, upon which, the metric itself is based. Obvious examples are the lift and drag coefficients associated with insects and airplanes. On the other hand, metrics associated with transport are clearly not an option. This leaves room only for purely innovative, and possibly approximate, approaches. With the nature of the flow field, which is a periodically moving body in stagnant fluid, the first engineering approach that was thought of is a CV (control volume) approach. More importantly, since efficiency is at question, the first metric aimed to use the conservation of mechanical energy, even though the energy equation was not part of the mathematical model that solves for the flow around the mayfly nymph. In the next section, the results of the first metric,  $\eta$ , is introduced along with the sensitivity of the metric itself to the control volume size.

#### 4.6.1 Mechanical Efficiency

The first performance metric is based on the integral form of the mechanical energy equation over a fixed volume [41], namely the mechanical efficiency of a control

volume. The metric was previously introduced in §2.4.1 and reads:

$$\eta(\%) = \frac{\overline{\int_{outer} E\mathbf{u} \cdot d\mathbf{A}} - \overline{\int_{outer} u_i \tau_{ij} dA_j}}{\overline{\int_{gills} u_i \tau_{ij} dA_j}} \times 100 \quad (4.1)$$

where 'outer' refers to the surfaces defined by the six planes corresponding to the rectangular control volume (Figure 2.11 on Page 50) and 'gills' refer to the control surface in contact with the moving gills. The overbar denotes time-averaged quantities. The effect of the CV size on the metric was investigated by computing  $\eta$  for 3 different CVs. Each CV is larger than the bounding box containing the moving gill array but does not include them. The 3 CVs are simply rectangular prisms and are approximately  $0.5L$ ,  $1.0L$  and  $2.0L$  away from the bounding box containing the moving gill array. The 3 CVs are defined by the following coordinates respectively:

- CV1: extends from  $(-0.59, -1.70, -2.21)$  to  $(1.41, 1.70, 2.21)$ .
- CV2: extends from  $(-1.09, -2.70, -2.71)$  to  $(1.91, 2.70, 2.71)$ .
- CV3: extends from  $(-1.40, -3.70, -3.73)$  to  $(2.95, 3.70, 3.71)$ .

where CV1 is the smallest and CV3 and is the largest.

The mechanical efficiency for the rowing-flapping parametric space is shown in Figure 4.12 for all 3 CVs as a function of  $Re_\omega$ . For all 3 planform types and across the regime considered, the mechanical efficiency of the rowing kinematics is always higher than that of the flapping kinematics. Also, within the 12 rowing simulations, larger planforms result in a higher mechanical efficiency. The results of the mechanical efficiency is not analogous to the kinematic transition in insect locomotion, where a similar propulsive efficiency favors flapping above some critical Reynolds number [12].

Therefore, it is concluded that the transition from rowing to flapping kinematics, that has been observed *in-vivo*, is probably not done on the basis of optimizing the mechanical efficiency.

While the trends of  $\eta$  did not provide a viable explanation to the kinematics transition, they still provide some insight on the fluid behavior in the regime investigated. Therefore, the different terms involved in computing the mechanical efficiency were investigated independently in an attempt to explain the trends observed, especially the increase of  $\eta$  for small CVs at the low  $Re_\omega$  side. Recalling that all the terms are dimensionless and that the findings are for the investigated regime ( $1.0 \leq Re_\omega \leq 21.6$ ), the key features of the different terms are highlighted hereunder: For the same CV, an increase in  $Re_\omega$  from 1.0 to 21.6 will result in:

- a decrease in the average rate of viscous work done by the moving gills by approximately one order of magnitude.
- a decrease in the average rate of pressure work done by the moving gills by approximately one order of magnitude.
- a decrease in the average rate of viscous dissipation by approximately one order of magnitude.
- an increase in the average kinetic energy flux through the control surface by one to two orders of magnitude depending on the control volume size. In other words, the fluid gains more kinetic energy as it leaves the control volume.
- an increase in the average rate of work done by the control volume on the

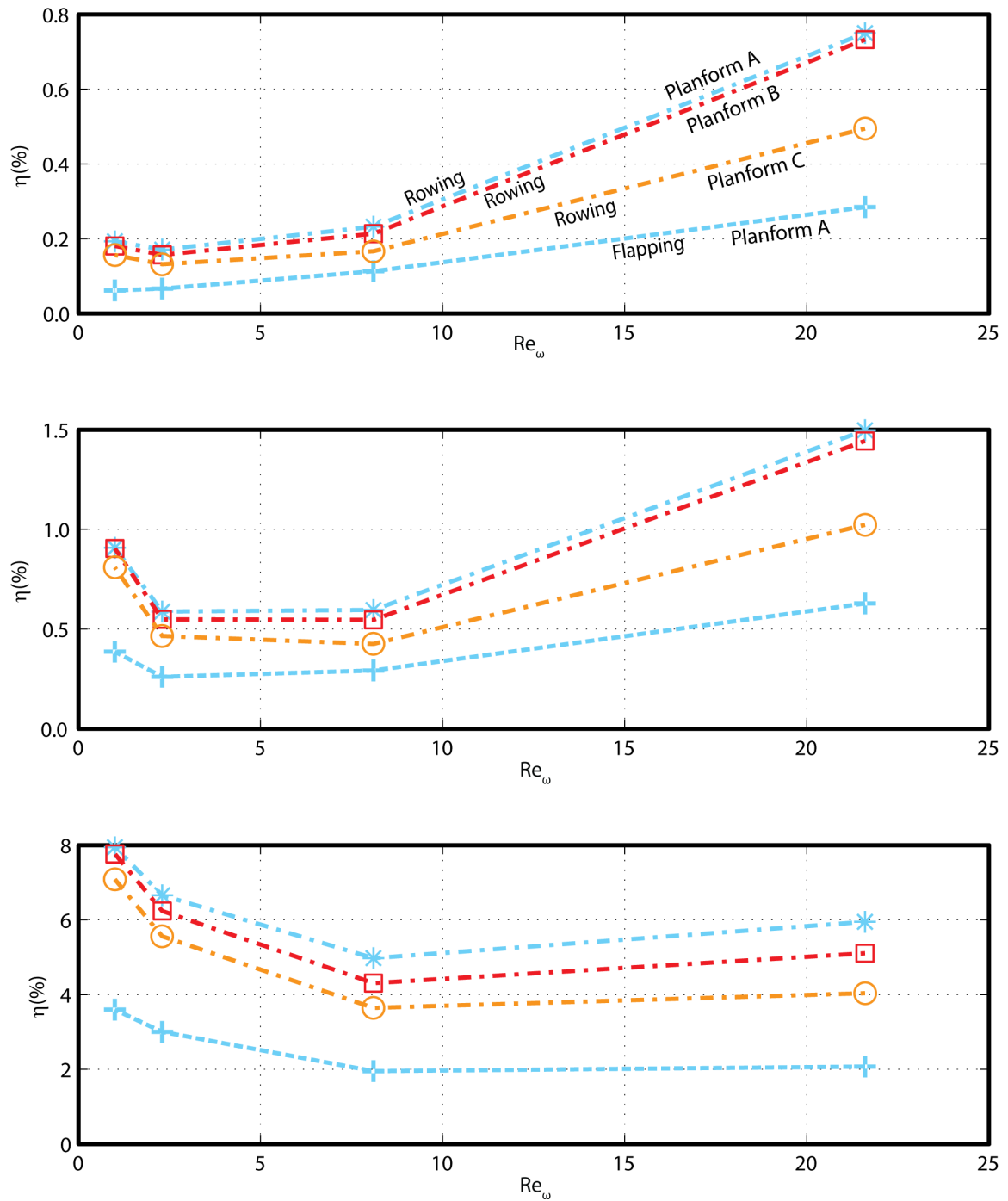


Figure 4.12: Mechanical efficiency,  $\eta$ , for 3 control volumes. \*: Rowing using planform A.  $\square$ : Rowing using planform B.  $\circ$ : Rowing using planform C. +: Flapping using planform A. Top: CV1 (0.5L away). Middle: CV2 (1.0L away). Bottom: CV3 (2L away).

surrounding fluid by one to two orders of magnitude depending on the control volume size.

Also, for the same  $Re_\omega$ , an increase in the CV size from CV1 to CV3 resulted in:

- a decrease in the average kinetic energy flux through the control surface by one to two orders of magnitude depending on the  $Re_\omega$ . The lower  $Re_\omega$ , the faster the decrease.
- a decrease in the average rate of work done by the control volume on the surrounding fluid by one to two orders of magnitude depending on the  $Re_\omega$ . The lower  $Re_\omega$ , the faster the decrease. Only rowing using planform A exhibits a decrease by three orders of magnitude at the lowest  $Re_\omega$ .
- a negligible change in the average rate of viscous dissipation. In other words, most of the energy loss is occurring in the near field around the moving gills.

The above provides a numerical explanation to the observed trends of  $\eta$  with respect to  $Re_\omega$ . On the high end of  $Re_\omega$ , both the average kinetic energy flux and the average rate of work done by the control volume on the surrounding fluid are of the same order of magnitude, but the former is increasing its order of magnitude while the latter is decreasing it. The end result is an increase in the mechanical efficiency  $\eta$  on the high end of  $Re_\omega$ . In other words, for  $Re_\omega \geq 21.6$ ,  $\eta$  is driven mainly by the average kinetic flux, while for lower  $Re_\omega$ ,  $\eta$  is driven by the average stress work on the outer six planes. Otherwise put, the first term in the numerator of equation 4.1 is dominating at high  $Re_\omega$ , while the second term is dominating for lower  $Re_\omega$ . For bigger CVs,

both terms in the numerator are approaching zero and the competition between these two terms is washed out by their relatively dwindling values. In fact, bigger CVs will require higher order interpolation and integration schemes in order to compute  $\eta$ . The trends observed when increasing  $Re_\omega$  align with inertial flows, as for example in turbo-machinery, where the second term in the numerator is neglected along with the viscous effects resulting in the so-called hydraulic power or the pressure work rate on the boundaries. The increasing mechanical efficiency for  $Re_\omega \geq 8.1$  also agrees with known trends in inertial flows, where the viscous dissipation keeps decreasing for increasing  $Re_\omega$ .

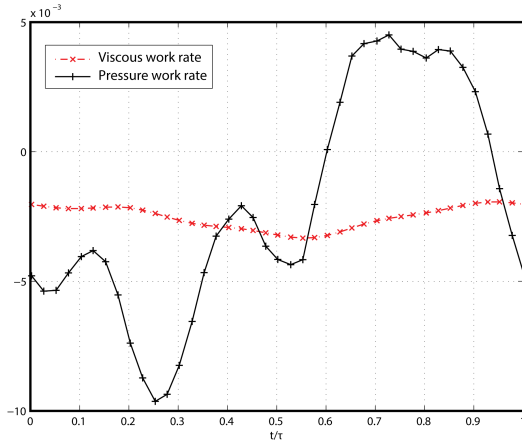
The analysis of the different terms also showed that for the same  $Re_\omega$  and the same CV, all terms that appear in equation (4.1) (kinetic energy flux, stress work rate and gill work rate) are the highest for rowing using planform A, followed by rowing using planform B, then rowing using planform C and finally flapping using planform A. With the order of magnitude discussion above, this would explain why the rowing kinematics have higher mechanical efficiency than the flapping kinematics.

Noteworthy is that the average total stress work (pressure and viscous) on the outer six planes was always negative for the entire parametric space. In other words, the CV was, on average, doing work on the surrounding fluid. However, the instantaneous values of the work rate behave differently. To illustrate that, the viscous work rate and pressure work rate on a plane below the mayfly is shown in Figure 4.13. Figure 4.13 shows the viscous and pressure work rate of both kinematics using planform A at the highest and lowest  $Re_\omega$  at a plane located at  $x/L = -0.59$ . This is one of the six planes that define the smallest CV of the 3 CVs discussed earlier (CV1). With

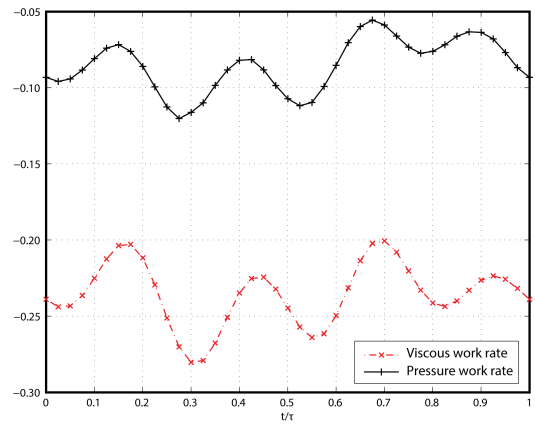
reference to Figure 4.13, it can be seen that, for that plane and for  $Re_\omega = 1.0$ , the magnitude of the viscous work rate is comparable to the pressure work rate, while for  $Re_\omega = 21.6$ , the magnitude of the pressure work rate is relatively higher. In addition the fluctuation and the average viscous work rate is decreasing with increasing  $Re_\omega$ , which is just another indication of decreased deformation work or viscous dissipation. Furthermore, it can be seen that both the pressure and viscous work rate are higher for the rowing kinematics for both  $Re_\omega$ .

Interestingly, the signature of the metachronal wave or the beating gills could be detected for some of the planes of integration defining the CV. For example, with reference to Figure 4.13b, the observed 4 local maxima of the pressure and viscous work rate at  $t/\tau \approx \{0.16, 0.45, 0.7, 0.92\}$  correspond approximately to the end of the retraction half-stroke of gills  $\{4, 3, 2\&6, 1\&5\}$  respectively (see Figure 2.8, on Page 44 for flapping kinematics). Likewise, in Figure 4.13d, the observed 4 local maxima of the viscous work rate at  $t/\tau \approx \{0.25, 0.25, 0.45, 0.75\}$  correspond approximately to the end of the retraction half-stroke of gills  $\{6, 5, 4, 3\}$  respectively (see Figure 2.10, on Page 46 for rowing kinematics). The local maxima of the stress work become more difficult to spot for higher  $Re_\omega$  or bigger CVs due to inertial and viscous effects respectively.

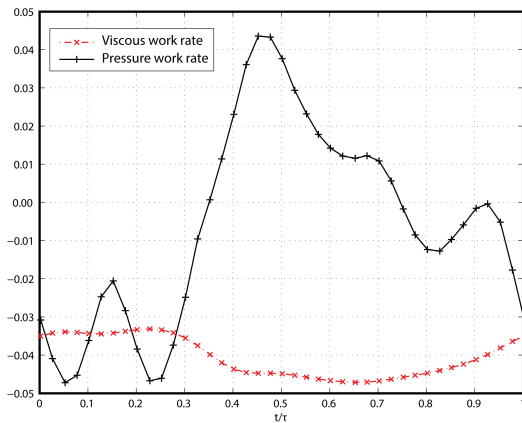
The fact that the mechanical efficiency failed to explain the rowing-flapping transition is still interesting on a fundamental level. While it may be completely intuitive that the mayfly nymphs are not optimizing for mechanical efficiency since it is already established that mayfly nymphs beat their gills in order to enhance their metabolic respiration, the question that remains is that why efficient mixing was not



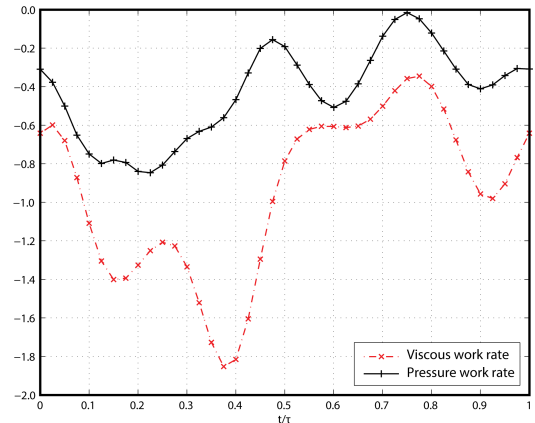
(a) Flapping at  $Re_\omega = 21.6$



(b) Flapping at  $Re_\omega = 1.0$



(c) Rowing at  $Re_\omega = 21.6$



(d) Rowing  $Re_\omega = 1.0$

Figure 4.13: Viscous and pressure work rate on the ventral plane ( $x/L = -0.59$ ) for flapping and rowing kinematics using planform A.

associated with an optimized mechanical efficiency? A possible answer was discussed by Purcell [53], where he pointed out that in tiny propelling organisms, the energy invested in moving around represents a small fraction of their total energy budget. In other words, propelling insects may not care about mechanical efficiency as much as engineers do. The most likely outcome of the analysis of the mechanical efficiency of the mayfly is that enhanced mixing does not correlate with an optimized mechanical efficiency in the investigated regime. An outcome that is only verifiable using more

specific tools such as the Lagrangian Coherent Structures approach [29]. The results of the mechanical efficiency concluded that the rowing-flapping transition does not occur due on energetic reasons only, and that another factor must be involved. Consequently, a second performance metric was devised, namely the specific mass flow rate.

#### 4.6.2 Specific Mass Flow Rate

With the failure of the mechanical efficiency in explaining the rowing-flapping transition, a metric that combines both energy and mass was thought of. The specific mass flow rate  $\xi$  was presented in §2.4.2 and reads:

$$\xi = \frac{\overline{\dot{m}}}{\overline{\dot{W}}_{gills}}, \quad (4.2)$$

where  $\dot{m}$  is the mass flow rate leaving (or entering) the control volume, and  $\dot{W}_{gills}$  is the rate of work done by the six pairs of moving gills.  $\xi$  is interpreted as the dimensionless time-averaged mass flow rate leaving the mayfly divided by the dimensionless time-averaged rate of work done by the gills.

The metric was inspired from a known performance parameter in internal combustion engines, namely the specific fuel consumption. In internal combustion engines, the specific fuel consumption is the flow rate of fuel consumed by the engine (say in gallons/minute) divided by the output power obtained at the vehicle's tires (say in Horsepower), which translates to the vehicle speed depending on the drag force. The lower the specific fuel consumption, the more efficient is the moving vehicle. The opposite holds of course. It is well known that this metric is lower on a

'highway' and higher 'in city' and hence a vehicle running at highway speeds consumes less fuel per unit distance and is, consequently, more desirable.

The metric introduced here carries the same idea, except that a higher specific mass flow rate is desirable. In other words, the higher the flow rate induced by the mayfly nymph per unit power expended by the moving gills, the more 'efficient' is the mayfly nymphs in circulating water. Again, the metric is limited by the mathematical model and carries the assumption that a higher flow rate across the control volume and hence across the mayfly translates into better inter-gill flow, enhanced ventilation and gas exchange. The main advantage of this metric compared to the mechanical efficiency is that it incorporates both mass flow and energy, where the former may be related to gas exchange, while the latter is be related to metabolism and energy expenditure.

As with the mechanical efficiency,  $\eta$ , the specific mass flow rate,  $\xi$  was computed for 3 different CVs in order to investigate its sensitivity to the CV size. The same CVs used to compute the mechanical efficiency were used to compute  $\xi$ . These are CV1, CV2 and CV3 which are approximately  $0.5L$ ,  $1L$  and  $2L$  away from the moving gills. Note that for both metrics, only the numerator is function of the CV size, since all selected CVs are bigger than the bounding box containing the moving gill array. Therefore, only the numerator is sensitive to the CV size. First, the results for CV2 ( $1L$  away) are introduced. This is followed by a discussion of the sensitivity of  $\xi$  to the CV size. Last, a more detailed quantification of the mass flow rates that occur across the control surface is presented.

Figure 4.14 illustrates the metric  $\xi$  computed for CV2, where the abscissa is

the average rate of work done by the moving gills (denominator in (4.1)) and the ordinate is the mass flow rate induced across the control volume (numerator in (4.1)). Therefore, the slope at any data point in the figure represents  $\xi$ . Furthermore, the figure shows the metric for the entire parametric space (i.e. 16 data points) and hence introduces the 2 dependent variables (average mass flow rate and average rate of work done) as function of the 3 independent variables being studied ( $Re_\omega$ , kinematics and planform). Otherwise put, the plot introduces a total of 5 variables.

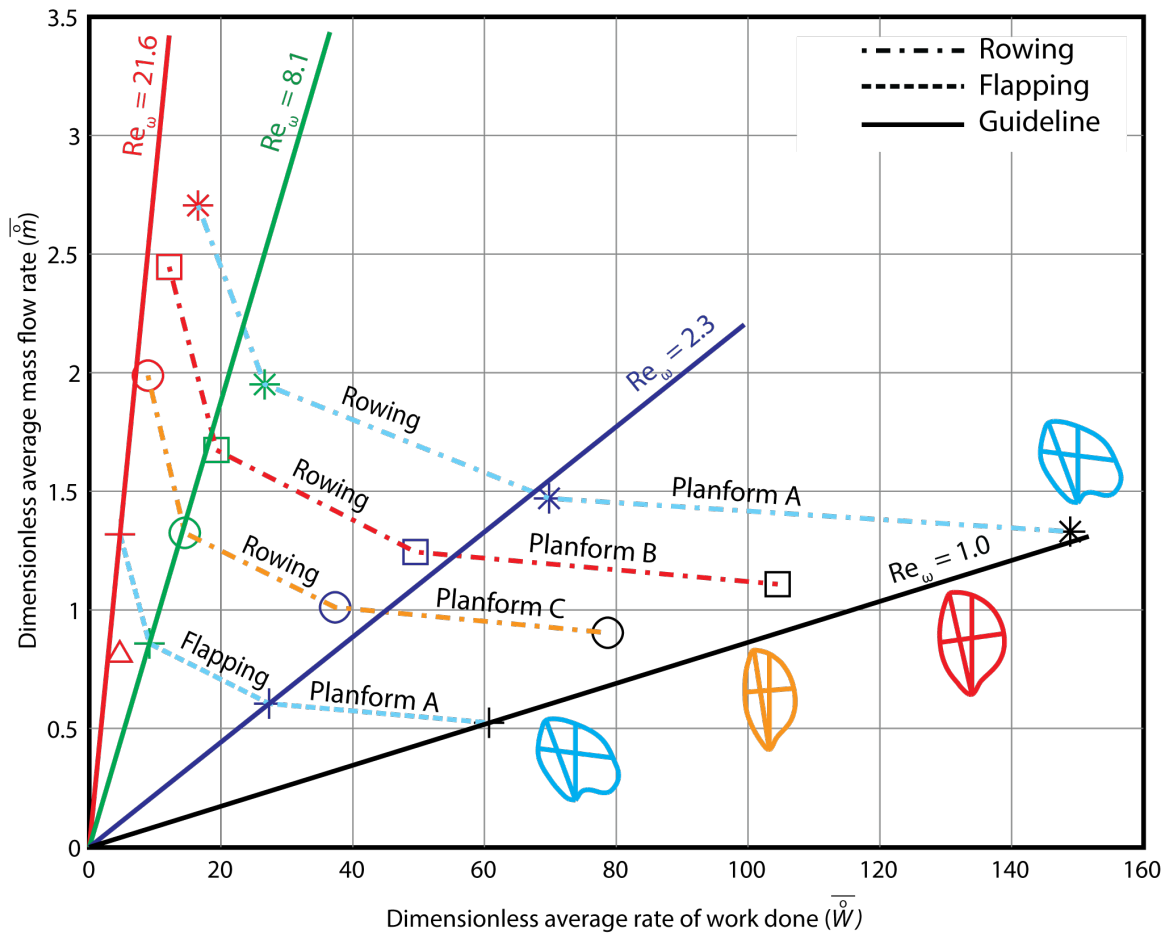


Figure 4.14: Specific mass flow rate  $\xi$ , for the rowing-flapping parametric space. \*: Rowing using planform A.  $\square$ : Rowing using planform B.  $\circ$ : Rowing using planform C. +: Flapping using planform A.

First, we consider the four data points corresponding to the flapping kinematics with planform A (+), which will serve as a baseline case for later comparison with the rowing kinematics. In this case, the average rate of work done increases ( $\overline{W}_{gills} = \{4.66, 9.11, 27.30, 60.68\}$ ) with decreasing  $Re_\omega$  ( $Re_\omega = \{21.6, 8.1, 2.3, 1.0\}$ ). In fact, one order of magnitude drop in  $Re_\omega$  causes an order of magnitude increase in the rate of work done. Both pressure and viscous work are contributing to the rate of work done with the ratio between the former and the latter being  $\{5.80, 5.47, 5.38, 5.36\}$  respectively. On the other hand, the average mass flow rate through the control volume is decreasing ( $\overline{m} = \{1.32, 0.86, 0.60, 0.52\}$ ) probably due to the increase in the average rate of viscous dissipation. Note the four straight lines in the figure, each starting at the origin and going through one of the four points of the flapping kinematics. The slope of each line is equal to  $\xi$ , which is decreasing with decreasing  $Re_\omega$  ( $\xi = 1e - 03\{281.88, 94.04, 22.15, 8.63\}$ ). In particular,  $\xi$  drops two orders of magnitude with one order of magnitude drop in  $Re_\omega$ . Overall for the flapping kinematics, the performance based on  $\xi$  is highest at the maximum  $Re_\omega$  considered, which nicely coincides with the qualitative observation of the pathlines previously presented in §4.4 and with the results of the mechanical efficiency  $\eta$  in §4.6.1.

Second, we consider the twelve remaining cases with rowing kinematics (three different planforms at four different  $Re_\omega$ ). The same symbols are used for each planform (\*,  $\square$  and  $\circ$  for planforms A, B and C respectively). Note that the symbols for the same  $Re_\omega$  have the same color and are clustered in the neighborhood of the corresponding lines introduced above, whose slope is the specific mass flow rate,  $\xi$ , for

the flapping kinematics. Overall, the same trends observed in the flapping kinematics can also be seen for the rowing kinematics. An increase in  $Re_\omega$ , for example, causes an increase in the average mass flow rate and a decrease in the average rate of work done. Among the things to note, is that for any planform and while fixing  $Re_\omega$ , the average rate of work done of the rowing case is higher than the flapping case and so is the average mass flow rate. Also, as previously discussed in §4.6.1, the bigger the planform area, the higher the rate of work done.

Now, we compare the specific mass flow rate of the rowing cases to the corresponding flapping kinematics. Let us consider clusters of data points for the same  $Re_\omega$ , and use the line going through the flapping kinematics point as a reference. When the data point for the rowing kinematics is: i) below the line for the particular  $Re_\omega$  then  $\xi$  for this case is smaller and it is less efficient than flapping; ii) above the line for the particular  $Re_\omega$  then  $\xi$  for this case is larger and it is more efficient than flapping. Starting at the lowest  $Re_\omega$  ( $Re_\omega = 1.0$ , black in the figure), we see that all data points for the rowing kinematics are above the line indicating that  $\xi$  is higher and therefore rowing is more efficient than flapping for all three planforms considered. As  $Re_\omega$  increases to  $Re_\omega = 2.3$ , the data point for planform A moves below the corresponding line, indicating that rowing using planform A at this Reynolds number is now less efficient than flapping. Planforms B and C (which are closer in morphology to the ones found in younger nymphs) are still more efficient than flapping. At the two highest Reynolds numbers, all data points are on or below their corresponding lines. For  $Re_\omega = 21.6$ , and for all planforms, flapping is always more efficient than rowing, while for  $Re_\omega = 8.1$  flapping is equally or more efficient than rowing depend-

ing on the planform. In other words, if a mayfly were to have gills in the shape of planform A throughout its entire aquatic phase, the specific mass flow rate metric would favor a switch from rowing to flapping within  $1.0 < Re_\omega < 2.3$  as it grows. Of course, the gill undergoes a change in shape from planform B or C to that of A, in which case  $\xi$  suggests a demarcation from rowing to flapping somewhere within  $2.3 < Re_\omega < 8.1$ . Simulations at  $Re_\omega = 2.3$  clearly show the effect of the planform on the kinematics; planform A favors flapping, while planforms B and C favor rowing. Strictly speaking, and based on the numerical results alone, the *transition* regime from rowing to flapping kinematics is  $2.3 < Re_\omega < 8.1$ .

Another way of presenting the previous results is shown in Table 4.2, where the average rate of work done by the gills, the average mass flow rate and the specific mass flow rate,  $\xi$ , are listed for all rowing cases, normalized by their flapping counterparts at the same  $Re_\omega$ . Although it was shown that with increasing  $Re_\omega$ , the average mass flow rate increases and the average rate of work done for either kinematics decreases, the normalized rate of work done: i) is increasing with increasing Reynolds number; ii) and the normalized mass flow rate is decreasing, indicating that rowing is falling behind with increasing  $Re_\omega$  no matter which planform is used thereby indicating an imminent switch to flapping.

To further illustrate the effect of planform morphology on the different dependent parameters like the rate of work done  $\overline{W}$ , the induced mass flow rate  $\overline{m}$  and the specific mass flow rate  $\xi$ , Figure 4.14 was re-plotted while normalizing both axis by the total surface area of the moving gills ( $24 \times$  the planform area). In other words, the x-axis is now the dimensionless time-averaged rate of work done per unit area of

$Re_\omega$	$\frac{\overline{W}_{row,A}}{\overline{W}_{flp,A}}$	$\frac{\overline{W}_{row,B}}{\overline{W}_{flp,A}}$	$\frac{\overline{W}_{row,C}}{\overline{W}_{flp,A}}$	$\frac{\overline{m}_{row,A}}{\overline{m}_{flp,A}}$	$\frac{\overline{m}_{row,B}}{\overline{m}_{flp,A}}$	$\frac{\overline{m}_{row,C}}{\overline{m}_{flp,A}}$	$\frac{\xi_{row,A}}{\xi_{flp,A}}$	$\frac{\xi_{row,B}}{\xi_{flp,A}}$	$\frac{\xi_{row,C}}{\xi_{flp,A}}$
1.0	2.45	1.72	1.30	2.54	2.12	1.73	<b>1.03</b>	1.23	1.33
2.3	2.55	1.81	1.37	2.43	2.06	1.67	<b>0.95</b>	<b>1.13</b>	<b>1.22</b>
8.1	2.91	2.11	1.58	2.27	1.95	1.54	0.78	<b>0.92</b>	<b>0.97</b>
21.6	3.49	2.55	1.88	2.05	1.85	1.51	0.58	0.71	0.79

Table 4.2: Table showing the average rate of work done  $\overline{W}_{gills}$ , average mass flow rate  $\overline{m}$ , and specific mass flow rate  $\xi$  for the rowing cases normalized by their flapping counterparts. row:rowing. flp: flapping. A,B,C: planforms A,B,C. **Boldface** notation ( $\xi \approx 1$ ) highlights the transition.

the 6 pairs of moving gills while the y-axis is the dimensionless time-averaged induced flow rate per unit area of the 6 pairs of moving gills. The result of this normalization is shown in Figure 4.15. Inspecting Figure 4.15 doesn't change any of the conclusions deduced from its non-normalized version in terms of the rowing-flapping transition, i.e. the Figure still suggests a transition in the range  $2.3 < Re_\omega < 8.1$  if the effects of planform morphology are taken into account. Figure 4.15 illustrates clearly the effect of planform morphology on rowing simulations. On a per unit surface area basis, the rate or work done does not change much by changing the planform area especially for higher  $Re_\omega$  cases. On the contrary the mass flow rate (again per unit gills area) is decreasing with increasing planform A. This is, in fact, the exact opposite behavior of the non-normalized version of this figure, i.e the increase in planform area results in a decrease in the mass flow rate per unit area. Evidently, the increased inertial effect associated with bigger planforms is not favored by a rowing type of kinematics. This may also explain why planform A favors a switch that is earlier than the one observed *in-vivo*. The normalized results are particularly interesting since the surface

area of the gills is definitely tied to the amount of gas exchange that occurs across its surface.

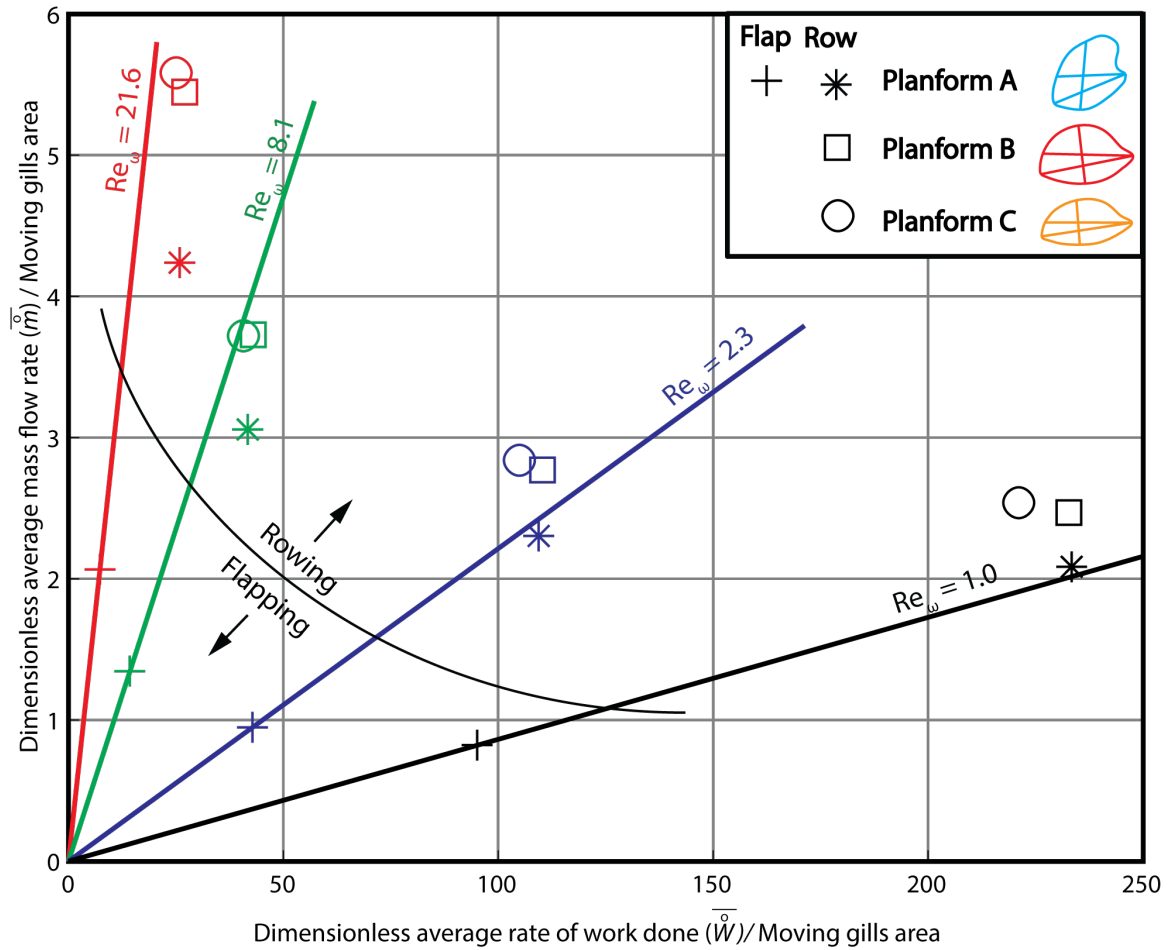


Figure 4.15: Specific mass flow rate  $\xi$ , for the rowing-flapping parametric space. Rate of work done and mass flow rate are normalized using the surface area of the moving gills. \*: Rowing using planform A. □: Rowing using planform B. ○: Rowing using planform C. +: Flapping using planform A.

Overall, the results indicate a strong correlation between  $Re_\omega$  and the proposed metric,  $\xi$ , which in turn provides a surprisingly simple, yet elegant explanation of the kinematic switch observed *in-vivo*. However, before finalizing this result, the effect of the control volume size on  $\xi$  had to be investigated. Therefore,  $\xi$  was analyzed for CV1 (0.5L away) and CV3 (2L away) and plotted the same way as for CV2. The plots are

shown in Figure 4.16. Analysis of Figure 4.16 yields almost the same result obtained when analyzing Figure 4.14. This is because  $\xi$  still favors a switch from rowing using planform B or C to flapping using planform A in the same regime  $2.3 < Re_\omega < 8.1$  suggested by CV2. In addition, when using planform A for both rowing and flapping,  $\xi$  based on smallest CV (CV1) still favors a switch within  $1.0 < Re_\omega < 2.3$  which is the same regime suggested by CV2. The only data point that seems to weaken the sensitivity analysis belongs to the rowing kinematics using planform A at  $Re_\omega = 1.0$  for the biggest CV (CV3), where this point actually suggests that the transition from rowing using planform A to flapping using planform A occurs at  $Re_\omega < 1$  as opposed to the smaller CVs which suggested a transition at  $1.0 < Re_\omega < 2.3$ .

The existence of this point, which represents 1 point out of 48 points, does not conflict with the *in-vivo* observations. This is simply because mayflies nymphs don't use planform A to row. In fact, they use a planform closer in shape to planform B or C. Hence, whether the rowing-flapping transition using planform A occurs at  $1.0 < Re_\omega < 2.3$  (suggested by the two smaller CVs) or at  $Re_\omega < 1.0$  (suggested by the biggest CV) may not be important to mayflies in specific. However, on a fundamental level, it would be much more desirable to show that the kinematics switch occurs even if the planform shape remains the same, i.e. the dependance is only on the  $Re_\omega$ . At this point, there were two choices: 1) run simulations at  $Re_\omega < 1.0$  which is more expensive and wouldn't guarantee that bigger control volumes (bigger than CV3) won't suggest more conflicting results or 2) keep working on the sensitivity analysis and look into why  $\xi$  behave the way it does, which would bring more understanding to the flow field and  $\xi$ . The second choice was favored because it provides more insight

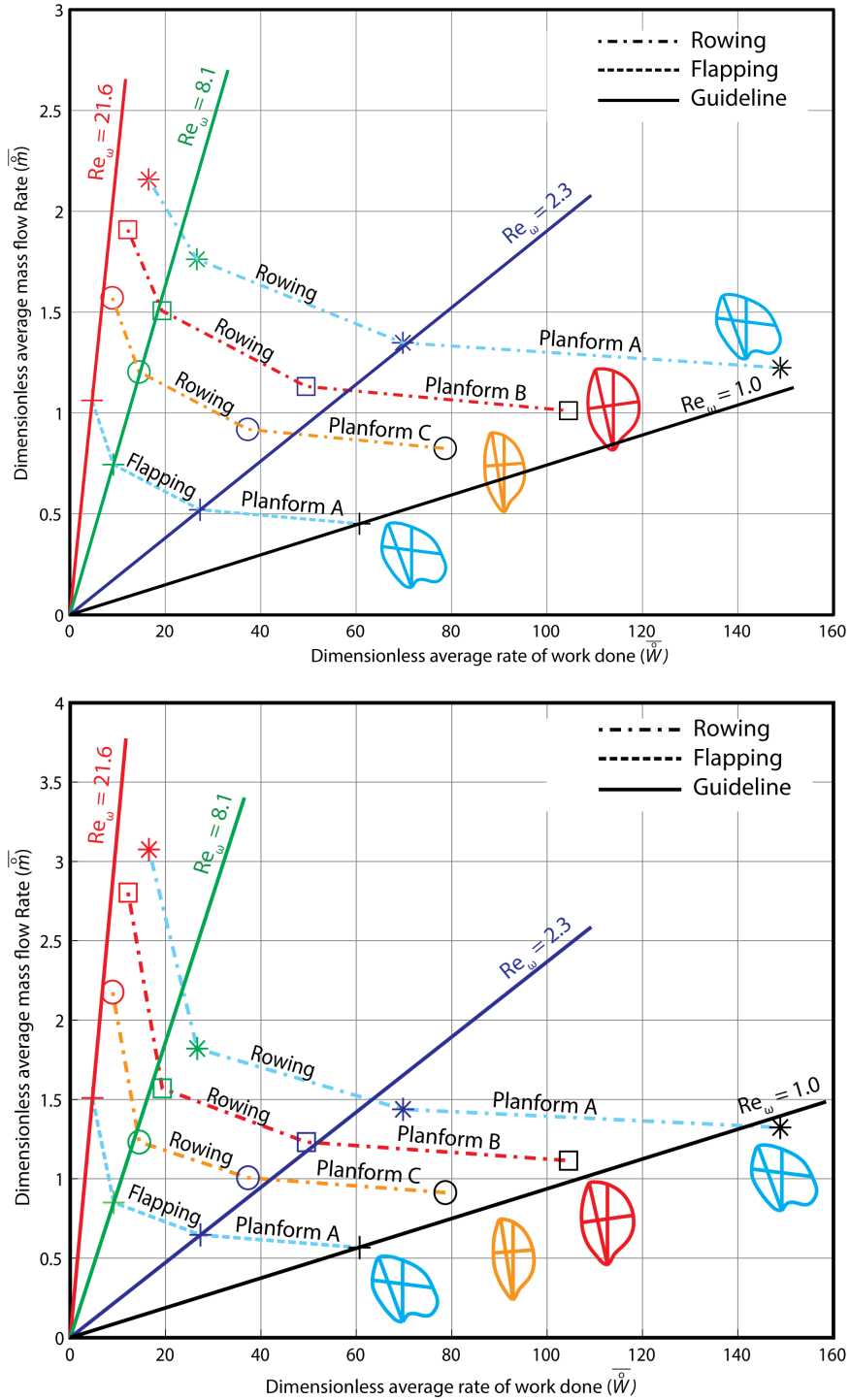


Figure 4.16: Sensitivity of specific mass flow rate  $\xi$  to the control volume size. \*: Rowing using planform A.  $\square$ : Rowing using planform B.  $\circ$ : Rowing using planform C. +: Flapping using planform A. Top: CV1 ( $0.5L$  away). Bottom: CV3 ( $2L$  away).

and actually studies the proposed metric.

Recalling that only the mass flow rate through the control volume affects the value of  $\xi$ , it is clear that one needs only to address how the mass flow varies with the choice of CV, the kinematics and the  $Re_\omega$ . It is clear that the mass flow rate will start to drop as one gets further away from the mayfly and that as the CV size approaches the entire domain size, the mass flow rate, and therefore  $\xi$ , is going to be effectively zero owing to the no penetration boundary conditions. To explore that effect, the contribution from each plane of the CV was analyzed for all CVs and all 16 simulations and graphed in manner aimed to quantitatively highlight this difference. The plots are shown in Figure 4.17 and Figure 4.18.

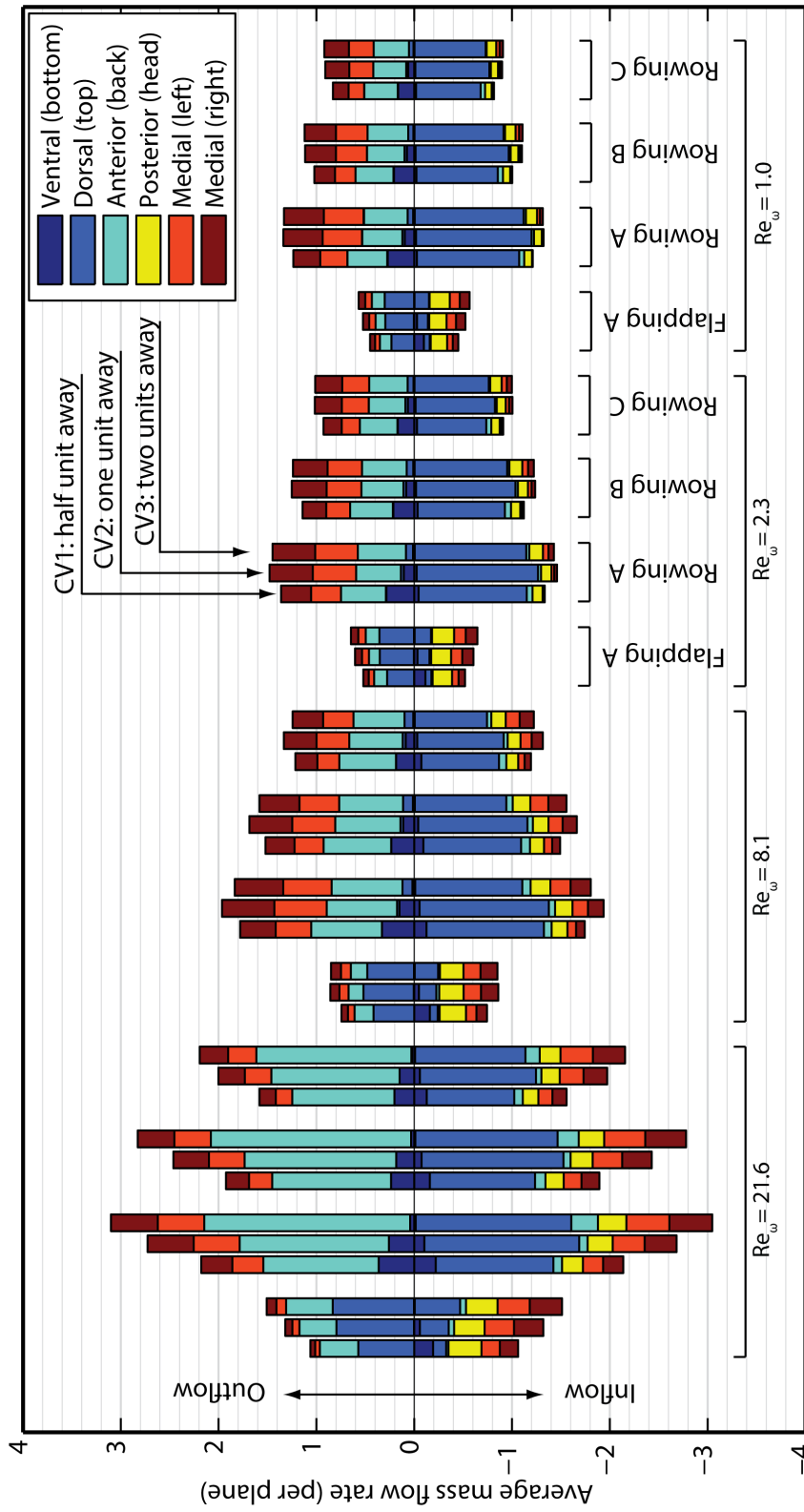


Figure 4.17: Illustration of the mass flow rate through the control surface for the rowing-flapping parametric space. 576 data points were used to build this figure (16 simulations  $\times$  3 control volumes  $\times$  6 planes for each control volume  $\times$  inflow and outflow for each plane = 576 points). Note the slightly declining mass outflow (or inflow) for rowing using planform A for CV3 at  $Re_w \leq 8.1$ .

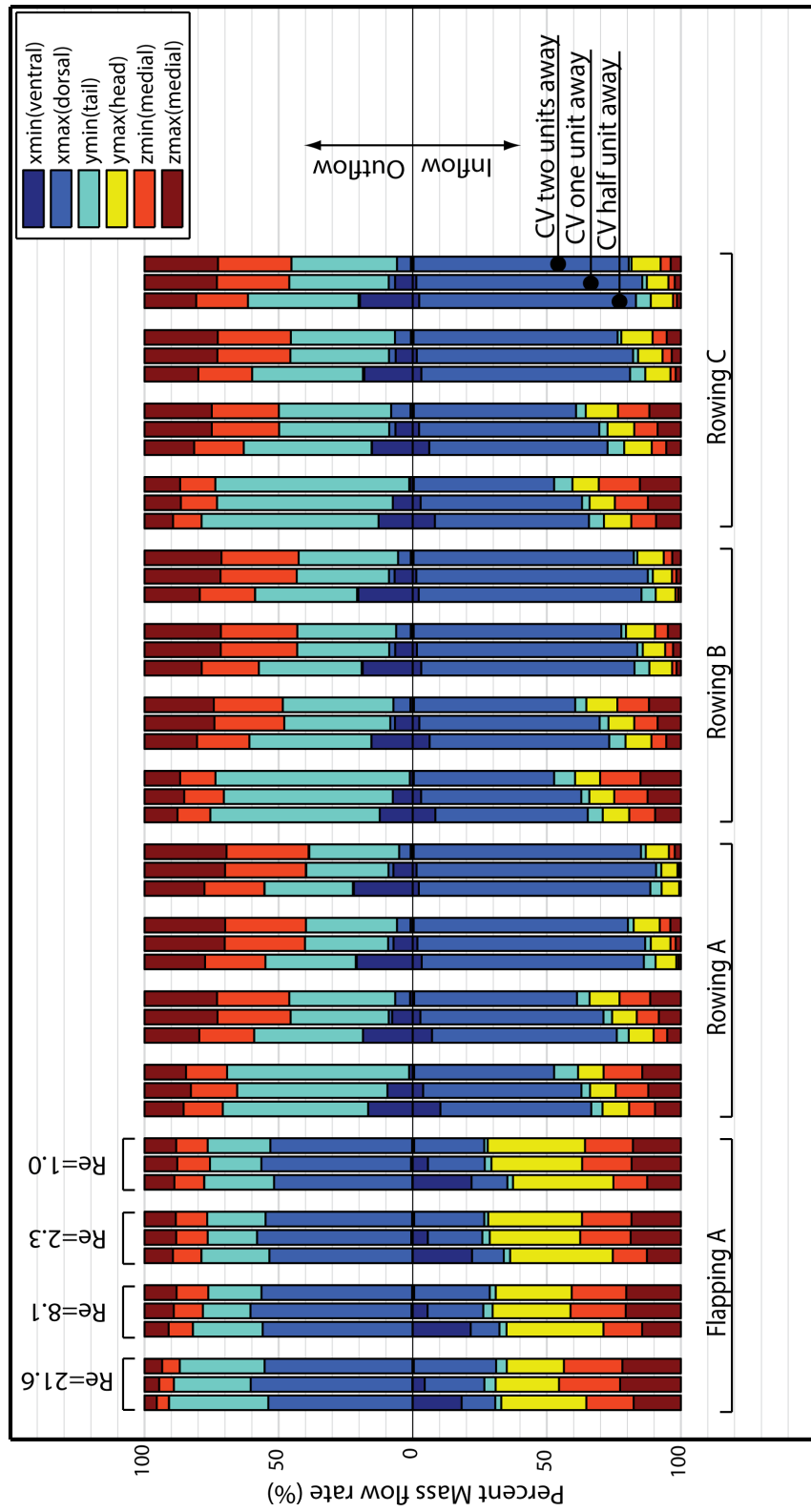


Figure 4.18: Illustration of the mass flow rate through the control surface for the rowing-flapping parametric space. Percentage is of total inflow or outflow. 576 data points were used to build this figure (16 simulations  $\times$  3 control volumes  $\times$  6 planes for each control volume  $\times$  inflow and outflow for each plane = 576 points).

Figure 4.17 summarizes the effect of the  $Re_\omega$ , the planform and the beating kinematics on the total inflow and outflow to the different control volumes, a quantification of earlier qualitative comparisons of flow fields. In addition, it illustrates the contribution from each plane of the CV to the total inflow and outflow separately. In the horizontal direction, the figure contains 4 sets, one set for each  $Re_\omega$ . Each set is divided into 4 subsets corresponding to flapping using planform A, rowing using planform A, rowing using planform B and rowing using planform C. Finally, each subset is divided into 3 sub-subsets corresponding to CV1, CV2 and CV3. Vertically, each sub-subset is a bar plot colored by the plane location and illustrates the contribution of each plane to the inflow (negative) and outflow (positive). In total, the plot is based on 576 data points. Needless to mention that mass is conserved through the CV, which is indicated by the top-bottom symmetry of the figure. Also, the left-right symmetry of the flow is indicated by the equal length of the left and right medial planes (orange and red).

By looking only on the *total* inflow and outflow of all simulations, most of the general trends discussed qualitatively earlier can be deduced from Figure 4.17. For example, for both kinematics and all planforms, increasing  $Re_\omega$  increases the mass flow rate. Also, for rowing kinematics, bigger planforms result in higher mass flow rates. Furthermore, it can be seen that flapping kinematics produces lower mass flow rates compared to rowing and that for lower  $Re_\omega$  the difference becomes more pronounced, i.e. rowing is getting better in comparison with flapping as  $Re_\omega$  is decreased.

Now, looking on the contribution of each plane within each sub-subset can provide us with more details about the changes occurring in the flow field. Most

interestingly is the contribution of the medial planes to the total outflow in the rowing kinematics (orange and red). The mass outflow through this planes does not change much with decreasing  $Re_\omega$ , which means that the medial component of the flow is increasing with respect to the total outflow as  $Re_\omega$  decreases. This was qualitatively illustrated earlier using pathlines integration for rowing at the highest and lowest  $Re_\omega$  (Figure 4.9). One can also tell the major contributions from the different planes that highlight the main difference in kinematics. For rowing, the outflow is mainly occurring anteriorly (cyan) and medially (orange and red), while the inflow is mainly dorsally (blue) and medially (orange and red). In contrast, for flapping, the major contributors for outflow are the dorsal plane (blue) and the anterior plane (cyan), while the inflow is distributed among the medial planes (orange and red) and the posterior plane (yellow).

By far, the most important observation from this figure is how the mass flow changes in going from CV2 to CV3 when rowing using planform A. For  $Re_\omega \leq 8.1$ , the mass flow through the largest control volume (CV3) is smaller than that through the medium-sized control volume (CV2). The same can't be said about flapping using planform A, i.e. CV3 is yielding higher flow than CV2. In short, for  $Re_\omega \leq 8.1$  and for CVs equal or greater to CV3, the mass flow through the control surface for rowing using planform A is already declining as one gets further away from the mayfly, while that for flapping is not. This is caused primarily by the smaller outflow from the ventral integration plane (dark blue), which is getting closer to the domain boundaries (ventral integration plane for CV3 is at  $x = -1.4$ , while domain boundary is at  $x = -1.5$ ).

Figure 4.18 is very similar to Figure 4.17, but instead of plotting the absolute values of the mass flow rate through the different control surfaces, the percent contribution of the control surfaces of the outflow or inflow is shown. In addition, the bar plots have been reshuffled so that the highest 4 sets denote flapping using planform A, rowing using planform A, rowing using planform B and rowing using planform C. In addition, the subsets are arranged by the  $Re_\omega$  and then the sub-subsets are arranged by the control volume. Again, the different trends can be observed by inspecting this figure such as the effect of decreasing  $Re_\omega$  on the rowing type of kinematics using any of the 3 planforms, which is an decreased medial inflow and an increased medial outflow.

With the quantitative analysis of the different mass fluxes and the sensitivity analysis of  $\xi$  to 3 different CVs, it is concluded that the observed trends of  $\xi$  are a good representative of the 3 independent parameters and that its sensitivity to the CV size is not a major factor.

To sum up the results of this chapter, first the main differences in the flow fields were introduced qualitatively. This included a detailed discussion of the 3 independent parameters being studied, namely the type of kinematics used in §4.3, which was followed by a discussion of the viscous and inertial effects in §4.4 and finally the effects of planform morphology in §4.5. Time-averaged flow fields were discussed and illustrated clearly the primary difference between both types of kinematics in that the resulting outflows are perpendicular with respect to each other. Pathlines integration showed that both types of kinematics are enhanced by increasing inertial effects. Pathlines integration also pinpointed one of the effects of decreasing the  $Re_\omega$

on the rowing kinematics, which is an increased medial outflow, which is probably due to increased gill interaction. Vorticity fields showed that vortex detachment occurs during the reported transitional regime for both kinematics and is unlikely to be coincidental. Iso-surfaces of the second invariant of the velocity gradient tensor showed that bigger planforms were associated with bigger coherent structure and higher vorticity magnitudes. Instantaneous fields showed that flapping offers a more synergistic micro-pumping mechanism by bringing the entire array to work together. Instantaneous fields also showed that rowing gills tend to work in isolation.

Second, quantitative metrics have been devised and computed for the entire rowing-flapping parametric space. The metrics were restricted by the mathematical model used, which basically solves for mass and momentum conservation without incorporating mass transport due to the cost-prohibition of the latter at the time of the study. The first metric, namely the mechanical efficiency  $\eta$ , failed to present any explanation behind the transition. This was in contrast to propelling animals where the mechanical efficiency of flapping animals is higher. The first metric, however, indicated that energetic reasons may not be the only reason behind the transition and that transport may not necessarily correlate with the mechanical efficiency within the investigated regime. Therefore, other factors must be involved and hence the specific mass flux  $\xi$  was introduced.

As simple as it may be, the specific mass flux showed a strong correlation with the mayfly nymph kinematics and hence favored a kinematic switch within  $2.3 < Re_\omega < 8.1$ , which matches surprisingly well with the observed *in-vivo* experiments ( $Re_\omega \approx 5$ ). The regime will be  $1.0 < Re_\omega < 2.3$  if planform morphology is *not* taken

into account. The sensitivity of the second metric to the control volume size was meticulously inspected and it was concluded that the control volumes closest to the gills do provide an adequate interpretation of the results. In addition, the sensitivity analysis shed more light on the effects of the different independent variables on the flow field.

Future studies should look into solving for transport while avoiding the higher computational cost associated with it. This may be achieved by using specialized tools (e.g. Lagrange Coherent Structures or Monte Carlo simulations), which would themselves require rigorous validation. Additionally, a study that incorporates transport while studying mayfly nymphs is confronted by another challenge, which is the unknown mass transport boundary condition on the gills surface and the correct formulation to treat this boundary condition within an immersed boundary formulation. Only with these types of studies that the actual relation between  $\xi$  and mass transport can be revealed. I expect that some relation exists when the mass transport is convection-dominated but vanishes for diffusion-dominated flows. The  $Pe$  for the diffusion of dissolved oxygen in water at 25°C varies from  $\approx 10^3$  for small nymphs to more than  $10^4$  for larger nymphs, i.e. more than one order of magnitude change, which might profoundly alter the mass transport physics throughout ontogeny. Undoubtedly, there is room for future improvement.

## Chapter 5: Results II: Flexibility and the Role of the Hinge

### 5.1 Introduction

In the first stages of the project, the kinematic chain introduced to simulate the gills motion contained only two levels, where the second level describes the motion of the *entire* gill with respect to the abdomen. However, comparison with *in-vivo* experiments wasn't that successful. Therefore, the third level was introduced, which describes the orientation of the distal plate with respect to the proximal plate by introducing the hinge flexion angle  $\gamma(t)$ , while the second level describes the orientation of the proximal plate with the respect to the abdomen (as opposed to the entire gill in the first stage). The rowing-flapping parametric space was then executed using the 3-level kinematic chain. Recall that the flexural hinge is coupled only with the flapping kinematics, while the rowing kinematics has negligible hinge flexion.

The investigation of the rowing-flapping transition showed a favorable effect of the flexural hinge, in that the location of the instantaneous dipoles formed by the end of a retracting gill enhances the second element of synergy discussed in §4.3.1. In specific, the flexural hinge enables the instantaneous dipole to eject water in a more horizontal direction, which aligns the flow partially to the next posterior gill, thus increasing synergy between neighboring gills. However, I couldn't ascertain if such

short-lived instantaneous dipole is a result of the gill motion only or is a consequence of the oncoming flow possessing increasingly 'weak' inertia or a combination of both. Is it possible that the oncoming flow decreases the vorticity decay near the dipole, thereby enabling the dipole to live longer? How important is the interaction of the neighboring gills? What is exactly the role of the hinge? [57] argued that the distal flap acts as a non-return valve that decreases the retrograde dorsal flow into the inter-gill spacing. Is there another role associated with the hinge development? With that in mind, the second parametric space was born. Noteworthy is that the introduction of the hinge is a step towards a more flexible gill, since it adds one degree of freedom to the entire gill.

The second parametric space is a set of 8 simulations, 4 running at  $Re_\omega = 21.6$  and 4 running at  $Re_\omega = 2.3$ . Each subset of 4 simulations includes 2 simulations using the full array of 7 gill pairs (6 pairs moving and 1 pair fixed) and 2 simulations using only gill pair 4 (i.e. gills 1-3 and 5-7 are removed). Finally, each sub-subset of 2 simulations includes 1 simulation that uses the one-plate model (without flexural hinge) and 1 simulation that uses the two-plate model (flexural hinge). The mayfly body (abdomen, thorax and head) was included in all simulations. Planform A was used for all 8 simulations and the proximal plates are prescribed with the same flapping kinematics previously discussed. As with the rowing-flapping parametric space, three independent parameters are at play. These are the  $Re_\omega$  ( $\{2.3, 21.6\}$ ), the number of gills ( $\{1, 7\}$ ) and the flexural hinge ( $\{\text{with hinge, without hinge}\}$ ). In short, each of the three independent parameters is varied once making the total number of simulations 8 ( $2^3$ ), where 2 of these overlaps the rowing-flapping parametric space.

The 8 simulations were adequate to elucidate the role of the hinge. Simulations using different numbers of gills will be required if one were to determine the optimum number of gills in an array, but this was not the primary goal of this investigation.

As with the rowing-flapping parametric space, first, the different flow fields are presented and compared qualitatively. This will be followed by a discussion of the specific mass flow rate and the different forces acting on the gills and finally concluding remarks.

## 5.2 Qualitative Investigation

To elucidate the effect of the spatial asymmetry introduced by the flexural hinge within the full array of gills, time-average flow fields for both cases are shown at  $Re_\omega = 21.6$  in Figure 5.1 and Figure 5.2. In both figures the two-plate model (with flexural hinge) is compared with the one-plate model (without flexural hinge). Also, in both figures, time-averaged streamlines, gills location and their intersection with the slice ( $z/L = 1.15$ ) are shown. Additionally, the dipole centers (vortex cores) are connected with solid lines in order to illustrate their average location. In both figures, it is evident that the introduction of the flexural hinge increases the antero-posterior component of the velocity ( $v$ ), which is illustrated by the colored arrows on the dorsal side.

Figure 5.1 shows the time-averaged z-component of the vorticity  $\omega_z$ , while Figure 5.2 shows the time-averaged normalized velocity magnitude. With reference to both figures, many features may be distinguished. The first feature is the average

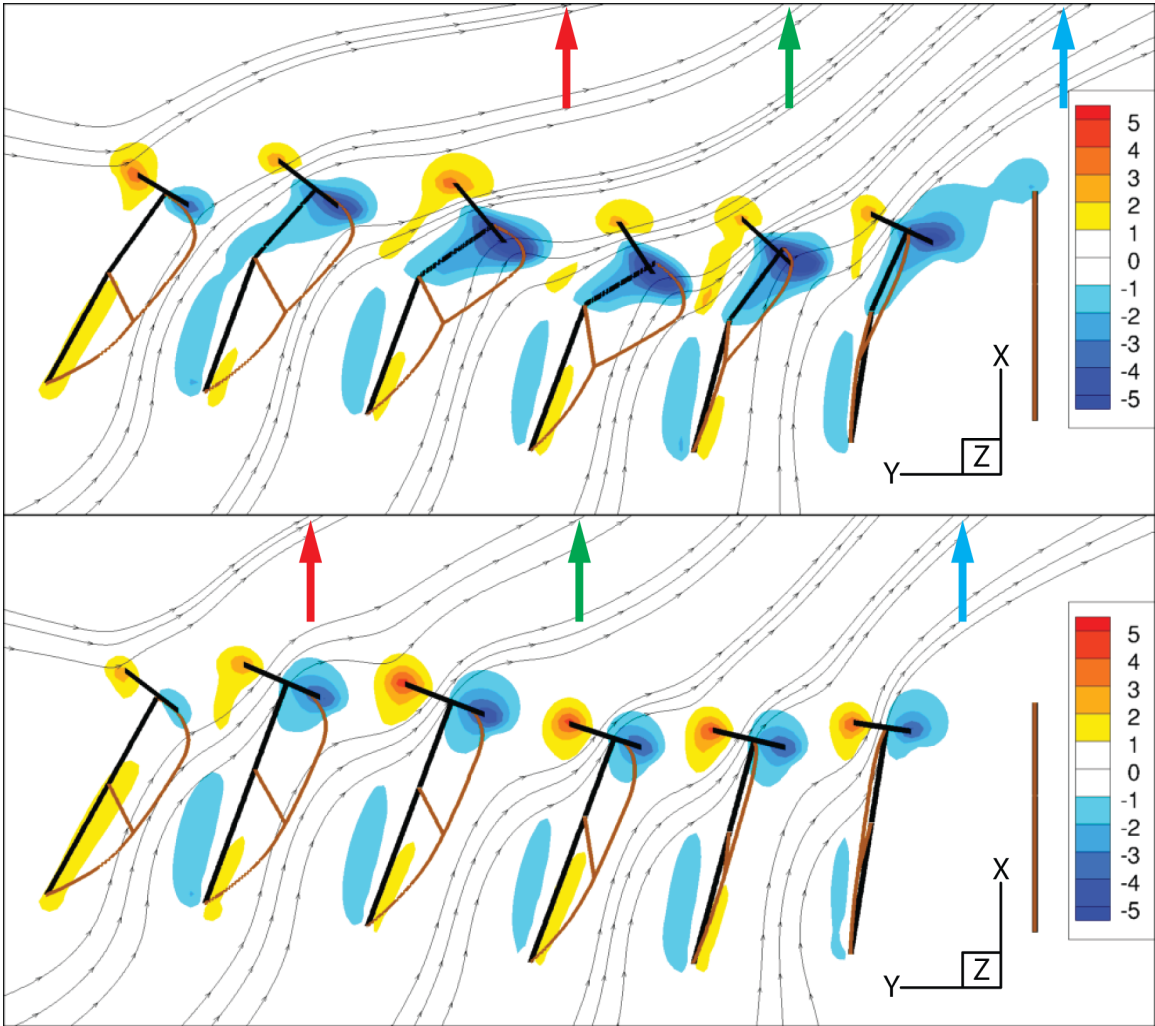


Figure 5.1: Time-averaged vorticity component  $\omega_z$  for  $Re_\omega = 21.6$  using the full array of gills. Slice at  $z/L = 1.15$ . Gill edges are shown in brown. Gills intersection with slice is shown in black. Average dipole centers are connected with black lines. Streamlines going through each inter-gill spacing are shown. Top: with flexural hinge. Bottom: without flexural hinge.

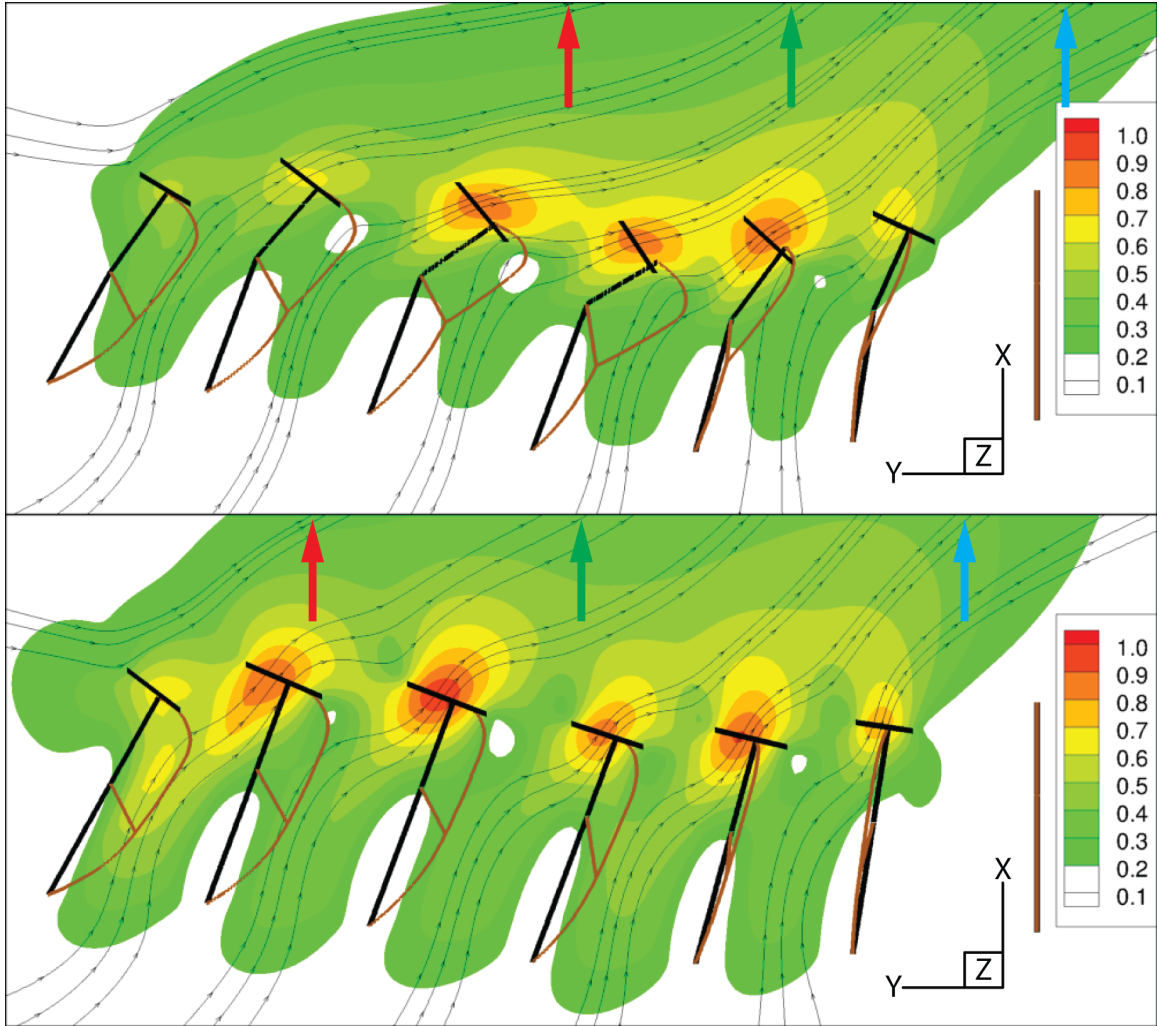


Figure 5.2: Time-averaged normalized velocity magnitude for  $Re_\omega = 21.6$  using the full array of gills. Velocity magnitude is normalized by the local maximum. Slice at  $z/L = 1.15$ . Gill edges are shown in brown. Gills intersection with slice is shown in black. Average dipole centers are connected with black lines. Streamlines going through each inter-gill spacing are shown. Top: with flexural hinge. Bottom: without flexural hinge.

magnitude of both cores of the dipole. The negative vorticity, which is generated during the protraction of the gill, is, on average, higher for the two-plate model in comparison with the one-plate model (global minimum is  $-6.71$  vs.  $-4.94$ ) and is stretched along the distal plate. This is most evident for gills 3-6. This is primarily caused by the protracting distal plate being tangential to the flow as opposed to the one-plate model. On the other hand, the positive vorticity, which is generated during the retraction of the gill is, on average, slightly lower for the two-plate model (global maximum is  $4.13$  vs.  $4.67$ ). This is primarily due to the time-averaging process since the instantaneous fields show that the vorticity magnitude is higher for the two-plate model at all times.

The second feature is the orientation of the dipole, where in the two-plate model, the orientation is more vertical, when compared to the one-plate model. The more vertical orientation was highlighted in the first parametric space in §4, which enhances the second element of synergy by aligning the flow from a preceding gill to the next one. This has the effect of increasing the antero-posterior component of the velocity ( $v$ ), which is illustrated by the colored arrows on the dorsal side.

The third feature pertains to the normalized velocity magnitude, where in the one-plate model, local maxima seem to be isolated near the dorsal edge of each gill, while in the two plate model, the local maxima near gills 3-5 seem to blend together. This is primarily due to the longer tip trajectory associated with the two-plate model, which allows the distal plates to be closer to each other. One also notes that the local maxima of the normalized velocity magnitude occurs at the center of the time-averaged dipoles, which indicates that the dorsal dipoles are much stronger than the

ventral dipoles for both models.

Based on the above discussion, it is still inconclusive which model is performing better. We know that the two-plate model shows better agreement with the *in-vivo* experiments. We also know that the two-plate model increases the y-component of the velocity by breaking the spatial symmetry (distal flap). Moreover, we know that both models break the 'orientational' symmetry with respect to the ventral wall. Knowing that the flow induced in the inter-gill spacing is much lower (5%) than the antero-posterior flow, one may speculate that the two-plate model induces higher mass flow rates. To further elucidate the effect of the flexural hinge, comparisons using only gill pair number 4 flapping at  $Re_\omega = 21.6$  are shown next.

Figure 5.3 shows the time-averaged normalized velocity magnitude and streamlines for both models (left column). It also shows pathlines integration in proximity of gill 4 along with time-averaged in-plane velocity vectors (right column). Part (c) clearly shows that the velocity magnitude for the one-plate model is symmetric about the mean position of the gill (left-right). At this  $Re_\omega$ , the gill is still able to circulate water, where the outflow is aligned with the gill plane and exits mostly in the dorsal direction. On the other hand, the two-plate model in part (a) illustrates the broken spatial symmetry where the outflow is now directed more posteriorly than dorsally. Both models are inducing flow in the dorsal direction due to the broken symmetry with respect to the ventral wall.

Pathlines integration shown in parts (b) and (d) also demonstrates the effect of the hinge on the surrounding field. The specific zone shown was selected because the time-averaged streamlines (or velocity vectors) approximately coincides for both

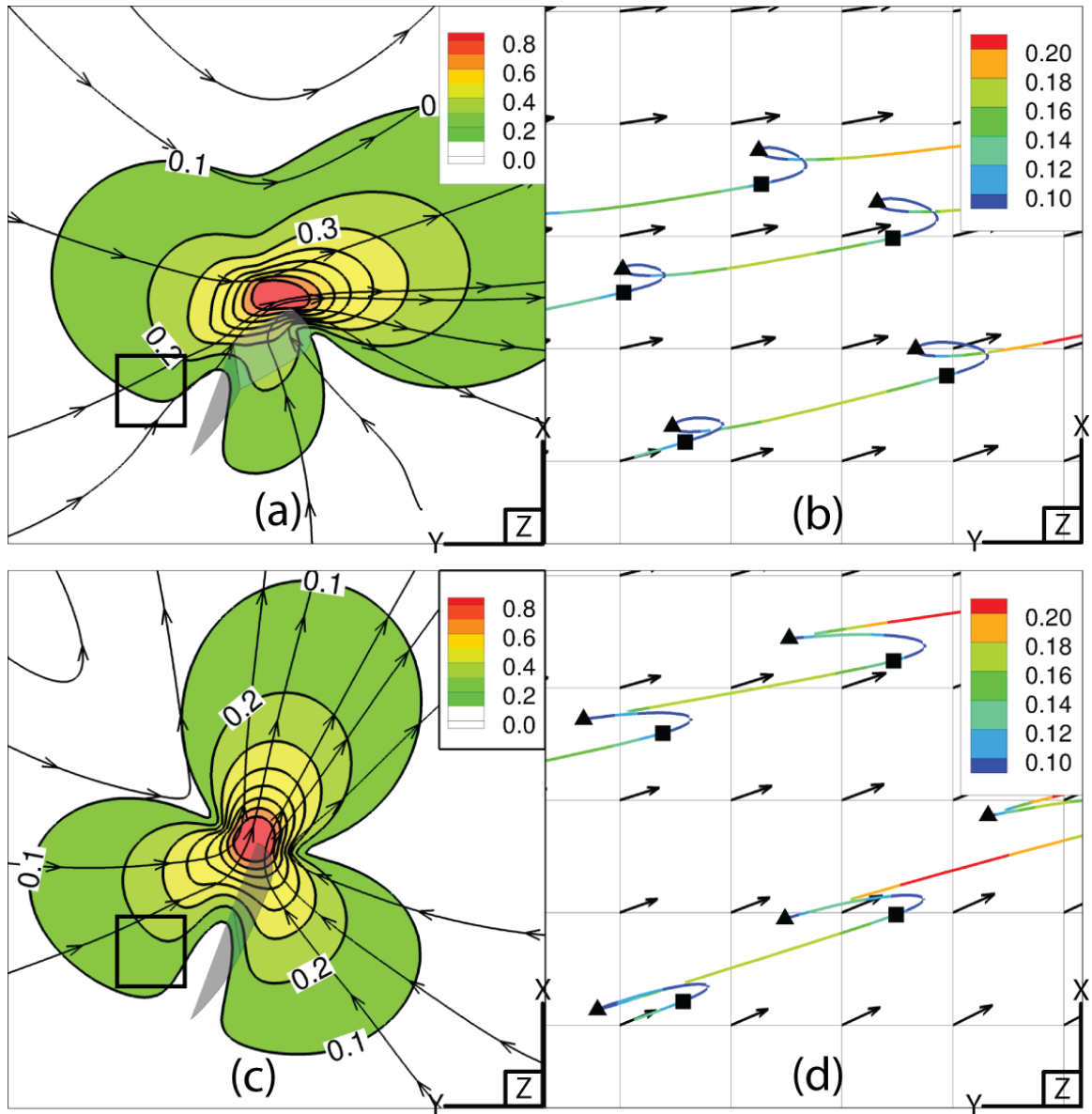


Figure 5.3: Time-averaged normalized velocity magnitude for  $Re_\omega = 21.6$  using gill pair 4 and pathlines integration. Top: with flexural hinge. Bottom: without flexural hinge. Left: normalized velocity magnitude and streamlines. Right: in-plane pathlines colored by velocity magnitude and time-averaged in-plane velocity vectors for insets shown in (a) and (c). ( $\blacktriangle$ ) begin retraction. ( $\blacksquare$ ) begin protraction.

models. Also, Pathlines are colored by the velocity magnitude. More importantly, landmarks highlighting the beginning of retraction ( $\blacktriangle$ ) and protraction ( $\blacksquare$ ) have been added. The advantage of the broken spatial symmetry is evident when comparing the particle displacement during protraction (by following a particle from  $\blacksquare$  to  $\blacktriangle$ ) with the time-averaged velocity vectors. For the one-plate model the particles retrograde displacement is 4-5 times the amount of retrograde displacement of the two-plate model. In addition, the retrograde displacement of the one-plate model is mostly opposite to the mean flow, while the retrograde displacement of the two-plate model has a vertical upwards component that helps the mean flow. The latter is probably due to the upward movement of the distal flap during protraction. For both models, the magnitude of retrograde displacement was found to be higher for particles closer to the gill. When comparing the net displacement after a full stroke, one notices that the net displacement is about 2.5 and 2 numerical cells for the two-plate and one-plate models respectively. This is about 25% increase in the net displacement of particles.

Interestingly, the average magnitude of the velocity of the gill tip (T1) in the two-plate and the one-plate model is about 0.75 and 0.64 respectively, which is about 17% increase. This means that the enhanced flow of the two-plate model is not only due to the increased tip velocity and that the asymmetry introduced by the distal flap is playing a major role. Therefore, one may conclude that the two-plate model is more efficient than the one-plate model due to the smaller retrograde displacement introduced by the former.

Noteworthy is that the vortex detachment illustrated in the rowing-flapping

parametric space (§4.4, Figure 4.6) for  $Re_\omega \geq 8.1$  is still present in simulations using *only* gill pair 4 and in simulations using the one-plate model for  $Re_\omega = 21.6$ . The 4 simulations running at  $Re_\omega = 2.3$  exhibit the same behavior discussed in 4.4, most notably the increased amount of oscillations with respect to the actual displacement of the particles. The next step now is to explore the behavior of the specific mass flow rate  $\xi$  within this parametric space.

### 5.3 Quantitative Assessment

To further evaluate the performance of this parametric space, and based on findings from §4, the specific mass flow rate is computed for all 8 simulations. Figure 5.4 shows  $\xi$ , where both axis are normalized. Recall that the normalization is done using the total surface area of the moving gills, which means that  $\overline{m}$  and  $\overline{W}$  are simply divided by  $24\times$  the planform area when using the full array or by  $4\times$  the planform area when using gill pair 4. In addition, the results shown are for CV2, which is  $1L$  away from the bounding box of the moving 6 pairs of gills. Note that the normalization of  $\overline{m}$  and  $\overline{W}$  does not affect the numerical value of  $\xi$ .

One feature in Figure 5.4 actually matches with the rowing-flapping parametric space, which is the increase of  $\xi$  when  $Re_\omega$  is increased. This is equally true whether the full gill array is used or only gill pair 4. This also holds true whether the flexural hinge is introduced or not. Furthermore, when comparing the two-plate model with the one-plate model when using the full gill array at  $Re_\omega = 21.6$ , one notes that  $\overline{m}$  has increased by 64.31%, whereas  $\overline{W}$  has increased by only 3.14%. Similarly when

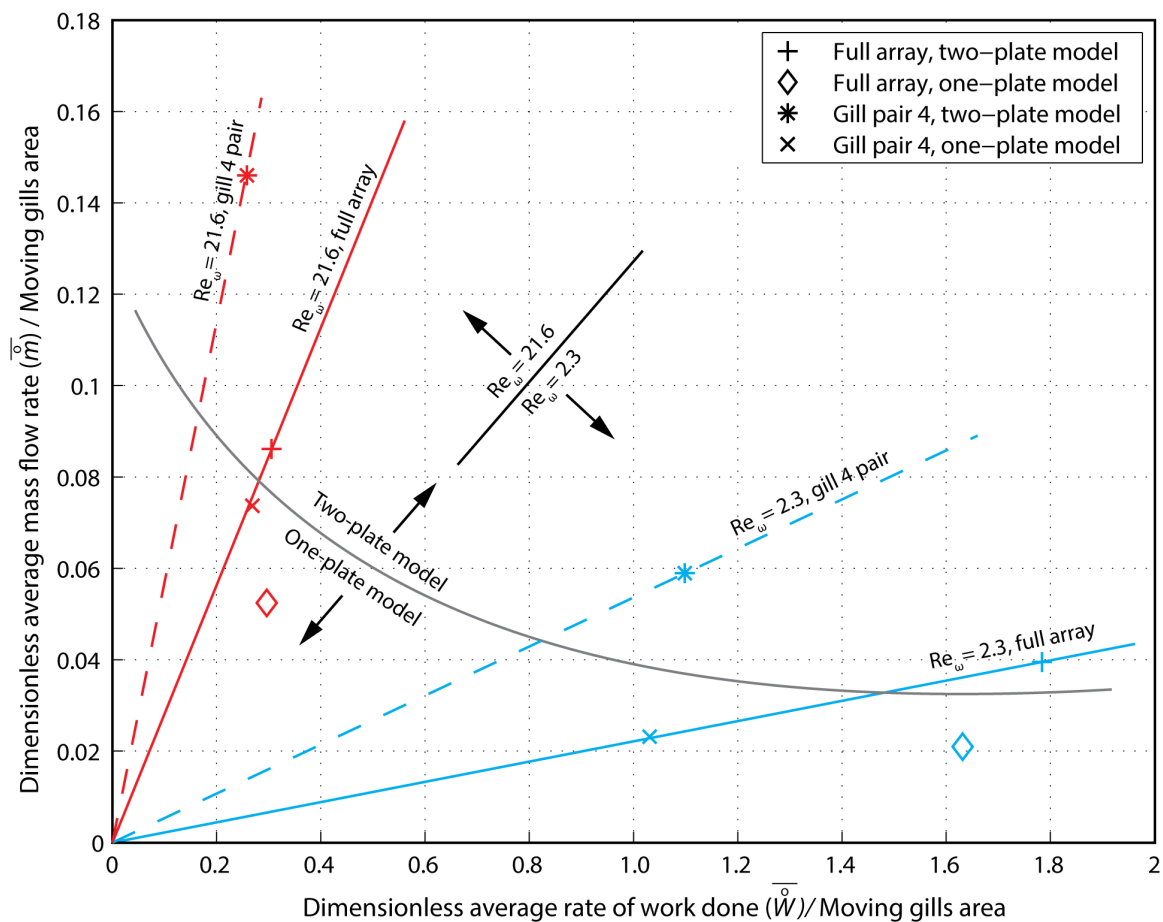


Figure 5.4: Specific mass flow rate  $\xi$  for the parametric space (normalized axis). Rate of work done and mass flow rate are normalized by the surface area of the moving gills. Solid lines: full array, two-plate model. Dashed lines: gill pair 4, two-plate model. Scattered symbols: one-plate model.

comparing the two-plate model with the one plate model when using gill pair 4 at  $Re_\omega = 21.6$ , one notes that  $\bar{m}$  has increased by 98.10%, whereas  $\bar{W}$  has *decreased* by 3.94%. In short, the introduction of the flexural hinge increases the average mass flow rate by 64.31% – 98.10% with a negligible change in the average rate of work done. This results in an increase in  $\xi$  by 59.31% and 106.23% for the full array and gill 4 pair respectively when introducing the flexural hinge at  $Re_\omega = 21.6$ .

Likewise, on the lower end of  $Re_\omega$ , the introduction of the flexural hinge (two-plate model) increases the average mass flow rate by 88.10% and 153.88% when using the entire gill array and gill pair 4 respectively in comparison with the one-plate model. The corresponding increase in the average rate of work done is 9.34% and 6.53% only. This yields an increase in  $\xi$  of 72.03% and 138.32% respectively.

The above quantification shows that  $\xi$  favors the two-plate model over the one-plate model when using gill pair 4. This coincides with known physics in that the unbroken spatial symmetry of the one-plate model is disadvantageous. However, the one-plate model is still able to circulate water at low  $Re$ , which is probably caused by the broken 'orientational' symmetry with respect to the ventral wall. Based on my work and the work of [46] and [54], I speculate that the one-plate model will still induce a mass flow at much lower  $Re_\omega$  as long as the orientational symmetry with respect to the ventral wall is broken.

The above results show that when the full array of gills is used,  $\xi$  favors the two-plate model. However,  $\xi$  shows that the introduction of the hinge when gill pair 4 is used is more advantageous than when introducing it within the full gill array. In other words, the removal of the flexural hinge from an entire gill array is not as

bad as removing the flexural hinge from one pair of beating gills. This is because the full array may still benefit from the asymmetry introduced by the metachronal wave. Moreover, whether using the full array of gills or only gill pair 4, the lower the  $Re_\omega$ , the more beneficial is the introduction of the hinge. In other words lowering the  $Re_\omega$  will worsen the effect of removing the flexural hinge.

Overall, the introduction of the flexural hinge is beneficial for all cases considered as illustrated in Figure 5.4. In addition, the importance of the flexural hinge becomes more pronounced at lower  $Re_\omega$  and when using a single pair of flapping gills in comparison with the entire array. Furthermore,  $\xi$  favors flapping with gill pair 4 rather than flapping with an entire array whether the flexural hinge exists or not. A detailed discussion of the hydrodynamic forces acting on the gills follows.

Figure 5.5 shows the different hydrodynamic forces acting on the mayfly when flapping at  $Re_\omega = 21.6$  using gill pair 4 for the one-plate and two-plate models. Part (a) shows the tip velocity magnitude along with its  $u$  (ventral-dorsal) and  $v$  (posterior-anterior) components. Part (b) shows the rate of viscous and pressure work done by the gill pair (or mayfly) on the surrounding fluid. Part (c) shows the total hydrodynamic force acting on the mayfly.

Recall that the proximal plate has the exact same kinematics in the one-plate and the two-plate model. With reference to Figure 5.5a, one immediately distinguishes the different behavior of the gill tip velocity. For the one-plate model, the symmetry is evident in both velocity components, where their signs are reversed every  $\approx 0.5\tau$ . On the contrary, in the two-plate model, the  $v$  component of the tip remains positive for  $\approx 0.6\tau$ . While the proximal plate starts to protract at  $t/\tau \approx 0.575$ , part

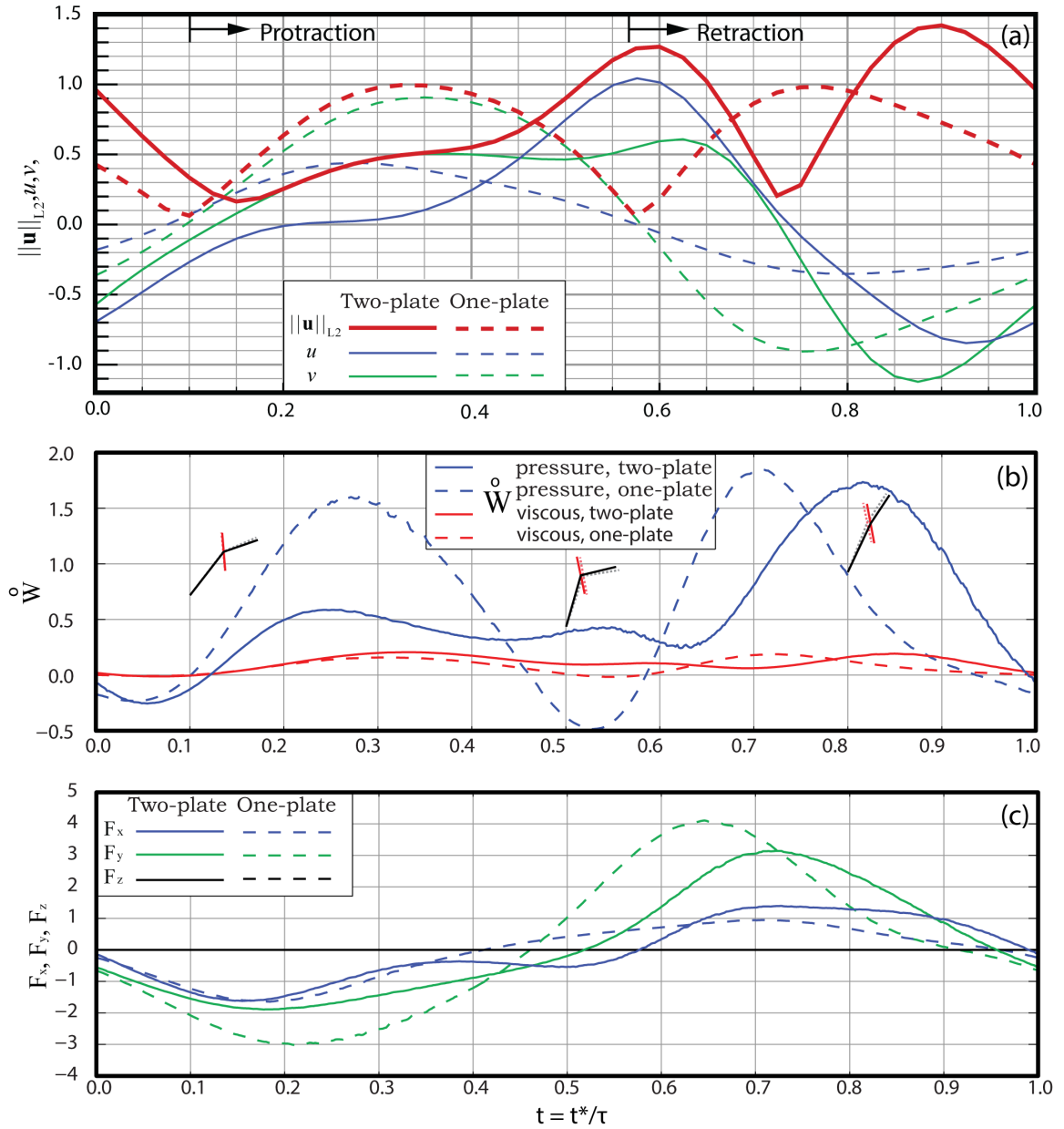


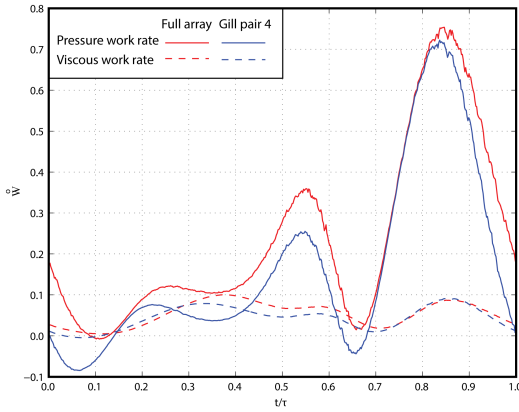
Figure 5.5: Flapping using gill pair 4 at  $Re_\omega = 21.6$ . (a) tip (T1) velocity ( $u$ : ventral-dorsal,  $v$ : posterior-anterior,  $\|\mathbf{u}\|_{L2}$ : velocity magnitude). (b) total pressure and viscous rate of work done by the mayfly (1 pair of gills), gill 4 position is shown at  $\{0.1, 0.5, 0.8\}$ . (c) total force acting on the mayfly. Dashed lines: one-plate model. Solid lines: two-plate model.

of the distal plate is still moving anteriorly until  $t/\tau \approx 0.725$ , when the distal plate completely reverses its direction and the tip starts to accelerate posteriorly. This results in the asymmetry of the velocity magnitude and delayed maxima in comparison with the one-plate model.

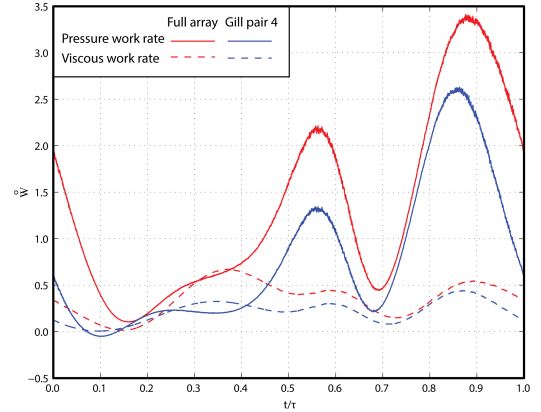
With reference to Figure 5.5b, the effect of the flexural hinge on the rate of work done is illustrated. The primary effect is observed on the rate of work done by the mayfly to overcome the pressure forces, where the maximum rate of work done during protraction is about one third that of the one-plate model. This simply means a lower pressure drag on the distal plates due to their orientation during protraction. Furthermore, in both models, negative rate of work done is observed by the end of retraction owing to the deceleration of the gill. However, only the one-plate model exhibits a negative work done by the end of protraction. As for the forces acting on the mayfly (Figure 5.5c), the distinction between both models is not as pronounced as with the rate of work done. Note that the z-component of the force acting on the mayfly body is zero owing to the medial symmetry.

Now, a detailed look on the rate of work done by the proximal and distal plates of left gill 4. Figure 5.6 shows the rate of work done to overcome pressure and viscous forces for the two-plate model at  $Re_\omega = 2.3$  and  $Re_\omega = 21.6$  when flapping using gill pair 4 or flapping using the entire array. All curves present the results when using the two-plate model.

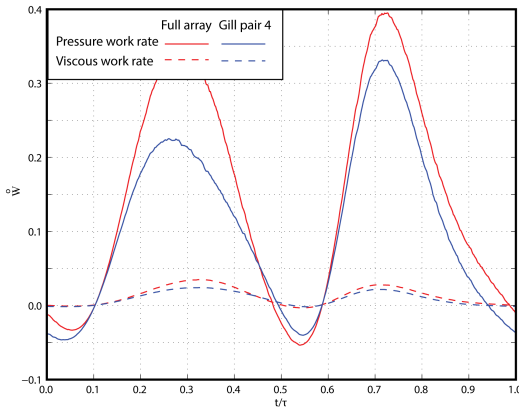
The first feature to notice in Figure 5.6 is how the amount of negative work done behaves when decreasing  $Re_\omega$ . Let us focus on the rate of work done when flapping using gill pair 4 only (blue curves). In part (b), the fluid is not able to exert any



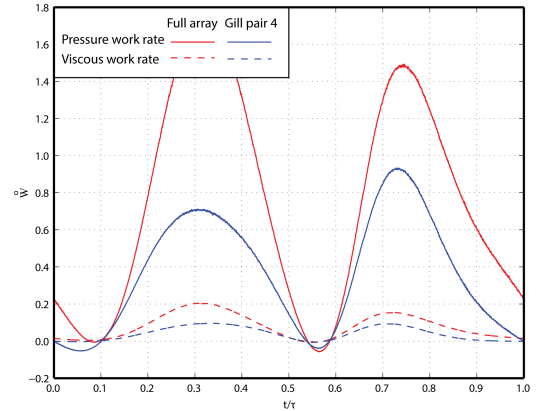
(a) Distal plate,  $Re_\omega = 21.6$



(b) Distal plate,  $Re_\omega = 2.3$



(c) Proximal plate,  $Re_\omega = 21.6$



(d) Proximal plate,  $Re_\omega = 2.3$

Figure 5.6: Rate of work done by gill 4. Left column:  $Re_\omega = 21.6$ . Right column:  $Re_\omega = 2.3$ . Top row: distal plate of gill 4. Bottom row: proximal plate of gill 4. Red curves: entire array. Blue curves: gill pair 4. Solid curves: pressure work rate. Dashed curves: viscous work rate.

work on the distal plate especially by the end of protraction and beginning retraction (at  $t/\tau \approx 0.65$ ). The negative pressure work rate occurs only during  $\approx 0.07\tau$  when  $Re_\omega = 2.3$  compared to  $\approx 0.19\tau$  when  $Re_\omega = 21.6$  (part (a)). This simply translates from the weakening inertia of the surrounding fluid. In other words, the surrounding fluid cannot 'store' energy in order to send it back to the gill. Coupled with the negligible mass of the gill, this illustrates why small organisms need to keep moving around at small  $Re_\omega$  in order to propel themselves or circulate water as discussed

in [53]. The same is true for the proximal plate shown in parts (c) and (d), where the amount of negative pressure work rate lasts  $\approx 0.15\tau$  and  $\approx 0.20\tau$  for  $Re_\omega = 2.3$  and  $Re_\omega = 21.6$ .

Now, let us compare the work rate of the proximal and distal plates of left gill 4 when it is flapping alone or when it is flapping within the full array of gills (blue curves vs. red curves). Since the kinematics of gill 4 are exactly the same in both scenarios, any differences observed between the curves are attributed to the interaction with the neighboring gills (left gills 3 and 5). For all 4 parts, the rate of work done is higher when gill pair 4 is present within the entire flapping array. The use of an entire flapping array has increased the average rate of work done by the proximal plate by 41.71% and 107.20% for  $Re_\omega = 21.6$  and  $Re_\omega = 2.3$  respectively in comparison with flapping using gill pair 4 only. Also, the average rate of work done by the distal plate has increased by 35.27% and 70.15% for  $Re_\omega = 21.6$  and  $Re_\omega = 2.3$  respectively. This shows that the lower the  $Re_\omega$ , the more interacting the gills are and therefore the higher the rate of work done.

Previously, Figure 5.4 showed that  $\xi$  favors the scenarios in which gill pair 4 is flapping alone when compared to the flapping using the entire gill array. Now, Figure 5.6 shows that the interaction between the gills leads to higher work rates. This simply means that the increase of the rate of work done due to increased interaction between the gills does not yield a proportional increase in the induced mass flow rate. Additionally, in §4, it was pointed that the flow due to inter-gill pumping contributes with only 5% of the inflow (see Figure 4.18). The most likely outcome of all of the above is that the presence of the entire array of flapping gills becomes increasingly

unfavorable at lower  $Re_\omega$ . In specific, introducing the full array of flapping gills decreases  $\xi$  by 50.14% and 58.73% for  $Re_\omega = 21.6$  and  $Re_\omega = 2.3$  relative to flapping using only gill pair 4.

## 5.4 Last Remarks

The primary goal of this chapter was to investigate the effect of the flexural hinge on the flow field, on the flapping kinematics and on the specific mass flow rate  $\xi$ . This was achieved by comparing 8 simulations where one half of these simulations uses the flexural hinge, while the other half doesn't (Figure 5.4). The results clearly illustrated the benefit of introducing the flexural hinge because of the broken spatial symmetry. Furthermore, the results point to the effect of the orientational asymmetry, where flapping without the flexural hinge is still inducing a mass flow rate at the low  $Re_\omega$  of 2.3. The main benefit of the flexing of the distal plate was a reduced pressure drag during protraction while increasing the induced mass flow rate.

The investigation of the hydrodynamic forces on the proximal and distal plates of gill 4 elucidated the interaction between neighboring gills (Figure 5.6). It was deduced that the increased interaction between neighboring gills increases the rate of work done by the mayfly while not yielding a proportional increase in the induced mass flow rate. Therefore,  $\xi$  favors cases where gill pair 4 is flapping alone rather than cases where the entire gill array is flapping metachronally. Based on  $\xi$ , the optimum number of gills may still be more than 1 but seems to be fewer than 7.

To conclude this chapter, two more simulations were performed. These were

rowing with gill pair 4 only (i.e. gills 1-3 and 4-7 are removed) while using planform A at  $Re_\omega = 21.6$  and  $Re_\omega = 2.3$ . These two simulations were compared with simulations using the entire rowing gill array previously shown in the rowing-flapping parametric space (§4). Interestingly, the use of an entire rowing array seems to decrease  $\xi$  in comparison with rowing using only gill pair 4. However, the lower the  $Re_\omega$ , the lesser is the effect of using the entire rowing array. In specific, introducing the full array of rowing gills decreases  $\xi$  by 33.96% and 24.53% for  $Re_\omega = 21.6$  and  $Re_\omega = 2.3$  relative to rowing using only gill pair 4.

The above trends are in contrast with the flapping results. Otherwise said, using the entire array as opposed to using only gill pair 4 has a worsening effect on  $\xi$  for both flapping and rowing in the investigated regime. In comparison with beating using gill pair 4 only, the use of a flapping array has decreased  $\xi$  by 50.14% and 58.73% for  $Re_\omega = 21.6$  and  $Re_\omega = 2.3$  respectively, while the use of a rowing array has decreased  $\xi$  by 33.96% and 24.53% for  $Re_\omega = 21.6$  and  $Re_\omega = 2.3$  respectively. The observed trends are opposing each other. In short, while the introduction of the full gill array decreases  $\xi$  for both kinematics, a decrease in  $Re_\omega$  is *beneficial* for the rowing kinematics but is *detrimental* for the flapping kinematics, all due to higher interactions between neighboring flapping gills. Therefore, one may speculate that there exist a certain  $Re_{array} (< 2.3)$  at which using an entire rowing array will *not* change  $\xi$  in comparison with rowing using only gill pair 4 only. At that same  $Re_{array}$ , using a flapping array will decrease  $\xi$  by more than 58.73%. Furthermore, if one were to carry the rowing simulations of gill pair 4 using planforms B and C, it is expected that  $Re_{array}$  is going to be higher than that using planform A. This is

because planform B and C will exhibit less interaction with other due to their smaller areas.

In going from planform A to B to C, the aspect ratio of the gill has increased from 1.57 to 2.23 to 2.81. Increasing the aspect ratio much further will approach that of a cilium ( $\approx 50$ ), which always uses a rowing type of kinematics. The results of  $\xi$  suggest that rigid structures (gills in small nymphs) are unable to work cooperatively at low  $Re_\omega$  due an undesirable increase in their interaction yielding a much higher rate of work done. Therefore, rowing 'independently' using narrower gills may be the solution. Only at a certain  $Re_{array}$  that the interaction of wider gills may be tolerated and a switch to flapping kinematics is therefore favorable.

Finally, recall that all simulations were executed using prescribed kinematics. Lowering  $Re_\omega$  further will yield higher forces and moments that may not be withstood by the actual gills. Hence, further evaluation of the above results will definitely require a strongly coupled Fluid-Structure-Interaction model with properly known structural properties of the gills.

## Chapter 6: Conclusions and Future Work Suggestions

Mayfly nymphs are an attractive living testbed for a variety of phenomena related to the rowing-flapping dichotomy. They operate in the less studied intermediate Reynolds number regime and abruptly switch kinematics throughout ontogeny. *In-vivo* experiments on *C. triangulifer* have revealed a switch from antiplectic rowing to flapping, where the latter is coupled with the development of a flexural hinge. In this study, and building upon the earlier experimental work by [58,59], an accurate numerical model was built. The numerical results for cases matching the *in-vivo* and robotic experimental conditions were found to reproduce the basic flow physics within the uncertainty of the experiments. Afterward, numerical 'experiments' were executed, where rowing and flapping kinematics for different gill planforms are used, for a range of Reynolds numbers not occurring in nature. The result-driven simulations led to two distinct parametric spaces, where the first investigates the rowing-flapping transition of the full gill array, while the second looks into the role of the flexural hinge and the interaction between neighboring gills.

Based on the rowing-flapping parametric space discussed in §4, the following is concluded<sup>+</sup> or corroborated<sup>\*</sup>:

- A newly introduced performance metric,  $\xi$ , is being optimized throughout the

rowing-flapping transition of *C. triangulifer*, which shows that the rowing-flapping transition minimizes the rate of work done by the nymph per unit mass flow rate induced throughout its ontogeny<sup>+</sup>. In other words, the switch from rowing to flapping is most favorable or desirable by  $\xi$ .

- To optimize  $\xi$  while maintaining planform A, the rowing-flapping transition of *C. triangulifer* would be  $1.0 < Re_\omega < 2.3^+$ .
- To optimize  $\xi$  while morphing from planform A to planform B or C, the rowing-flapping transition of *C. triangulifer* is  $2.3 < Re_\omega < 8.1^+$ .
- Planforms with higher aspect ratio will delay the rowing-flapping transition, i.e. the transition will occur at a higher Reynolds number<sup>+</sup>.
- The rowing-flapping transition is coupled with the onset of vortex detachment for both rowing<sup>+</sup> gills and flapping<sup>\*</sup> gills. The vortex detachment was observed for  $Re_\omega \geq 8.1$ .
- Within the investigated regime, the rate of work done, rate of viscous dissipation and induced mass flow rate by metachronally rowing gills is much higher than the rate of work done by metachronally flapping gills<sup>+</sup>.
- Contrary to locomotion in animals, the rowing kinematics in ventilating mayfly nymphs *C. triangulifer* results in a higher mechanical efficiency than the flapping kinematics<sup>+</sup>.
- Contrary to locomotion in flapping animals, where locomotion occurs only above some critical Reynolds number, a net flow rate may be induced by flapping at

Reynolds numbers below the transition regime as long as spatial or orientational symmetry is broken\*.

- Low Reynolds number flows have very low mechanical efficiencies due to the high rate of viscous dissipation\*.

Based on the rowing-flapping parametric space discussed in §5, the following is concluded<sup>+</sup>, corroborated\* or highly speculated<sup>!</sup>:

- The introduction of the flexural hinge into a flapping gill or an array of flapping gills increases  $\xi$ , i.e. increases the induced mass flow rate per unit power<sup>+</sup>.
- The flexural hinge results in a different distribution of vorticity and instantaneous dipoles that increases the synergy between flapping gills<sup>+</sup>.
- The flexural hinge reduces the maximum pressure drag on the distal plates while maintaining the same induced mass flow rate in comparison with rigid gills<sup>+</sup>.
- The lower the Reynolds number, the more beneficial is the flexural hinge\*.
- To optimize  $\xi$  while morphing from planform A to planform B or C without developing a flexural hinge, the rowing-flapping transition of *C. triangulifer* would occur at  $Re_\omega > 21.6^+$ .
- In the investigated regime,  $\xi$  favors gills rowing or flapping alone rather than gill arrays rowing or flapping in a metachronal wave<sup>+</sup>.

- For flapping kinematics, the lower the  $Re_\omega$ , the more detrimental is the effect of having an array of gills on  $\xi$  in comparison of having only one gill<sup>1</sup>.
- For rowing kinematics, the lower the  $Re_\omega$ , the less detrimental is the effect of having an array of gills on  $\xi$  in comparison of having only one gill<sup>1</sup>.
- Orientational asymmetry with nearby walls is allowing a symmetrically flapping gill to induce a net mass flow rate at Reynolds numbers as low as 2.3<sup>+</sup>.

Throughout this study, it became clear that some parameters are affecting the flow physics more than others. Future studies may include some of these parameters as an independent variable in the parametric space. In order of importance, the following parameters are worth looking at: 1) The inter-gill spacing with respect to the gill length. 2) The distance from the ventral (bottom) wall with respect to the gill length. 3) The orientation of the ventral (bottom) wall with respect to the nymph. 4) The location of the flexural hinge. 5) The orientation and shape of the hinge. 6) The size of the domain. 7) The number of gills. 8) The varying length of the gills within the same mayfly. 9) Much higher and much lower Reynolds numbers. 10) Gills with much higher aspect ratios. 11) An idealized shape of the gill (e.g. ellipse). 12) The phase lag between neighboring gills (studied by [43]). 13) The function of the fixed pair of gills (gill pair 7). Most of the preceding points are specific to *C. triangulifer*, while only 10-12 would benefit the rowing-flapping transition in general. Point 1 is strongly affecting the interaction between the neighboring gills and is the most important parameter if one were to explain the rowing-flapping transition within

an array (by looking at forces). Point 2 plays a role with orientational symmetry and might affect the mass flow rate through the inter-gill spacing. The long list of independent variables coupled with the variability of mayflies might actually provide an explanation why the observed *in-vivo* transition occurs in a regime rather than at a specific critical Reynolds number.

Future work should include a fluid-structure interaction model since the analysis performed on the work done by the gills in §5 is very sensitive to the extracted kinematics, the shape of the gill and their mean locations with respect to each other. However, the structural properties of the gills throughout ontogeny are not known and would require substantial measurements. Future studies should also aim to incorporate oxygen transport into the computational model, which is, likewise, confronted by an uncommon boundary condition on the surface gills, where the physiology governing the concentration of oxygen inside the tracheal tubes is not well studied. Currently, a portion of the data generated by the first parametric space is being investigated by Rodolphe Chabreyrie<sup>1</sup> using Lagrangian coherent structures and passive scalar transport. This will result in new quantitative metrics that may substantiate the current work.

---

<sup>1</sup>Rodolphe Chabreyrie, PhD. Department of Aerospace and Mechanical Engineering. The George Washington University, Washington, DC.

# Effect of metachronal phasing on the pumping efficiency of oscillating plate arrays

Mary Larson · Ken T. Kiger · Khaled Abdelaziz · Elias Balaras

Received: 16 June 2013 / Revised: 28 April 2014 / Accepted: 28 April 2014 / Published online: 16 May 2014  
© Springer-Verlag Berlin Heidelberg 2014

**Abstract** A programmable oscillating plate array was constructed in order to study the detailed hydrodynamics of external pumping by a series of oscillating plates at Reynolds numbers on the order of 10. The array was modeled after the geometry and kinematics found in the nymphal mayfly (Ephemeroptera) *Centroptilum triangulifer*, and consisted of five plates, each of which could be actuated independently for stroke and pitch. Scaled tests were performed at a Reynolds number,  $Re = fL_g^2/\nu = 18$ , with a single stroke kinematic pattern modeled after the living animal. In mayflies, and in many other oscillating plate systems, an antiplectic metachronal wave is used with a phase delay of approximately  $90^\circ$ , which corresponds to a travelling wave that moves from posterior to anterior with a wavelength of approximately four plates. In order to better understand possible reasons for why the animal system might favor the observed phase lag, ensemble-correlation stereo PIV measurements were made to reconstruct the unsteady three-dimensional phase averaged flow field at a resolution that allowed a uniform and converged estimate of the net pumped flux and the total energy dissipation within and around the vicinity of the gill array. The results indicate that the baseline case offered an optimal spot in the mass flux of fluid pumped through the array per unit energy expended, while also providing a great deal of flexibility in modifying the stroke amplitude without interference effects from adjacent gills.

M. Larson · K. T. Kiger (✉) · K. Abdelaziz  
Department of Mechanical Engineering, University of Maryland,  
College Park, MD 20742, USA  
e-mail: kkiger@umd.edu

E. Balaras  
Department of Mechanical and Aerospace Engineering, The  
George Washington University, Washington, DC 20052, USA

## 1 Introduction

Small-scale chemical sensors and micro-reactors intrinsically rely on pumping and scalar mass transport to accomplish their design goals (Vitko et al. 2004). Traditionally, the size and flowrate through the mechanical components used for these functions have been large enough that inertial convective mechanisms can be effectively used, as exemplified by devices such as centrifugal fans. One challenge faced by continually shrinking packages, however, is a concurrent decrease in the operational Reynolds number and a transit towards viscous pumping mechanics where such inertial mechanisms are ineffective (Quin and Grimes 2008). A variety of micropump mechanisms have been studied for these applications with the most prevalent concepts being reciprocating diaphragm pumps (Thomas and Bessman 1975; van Lintel et al. 1988; Bourouina et al. 1997), electrohydrodynamic pumps (Bart et al. 1990), electroosmotic pumps (Jiang et al. 2002; Wang et al. 2009), and magnetohydrodynamic pumps (Jang and Lee 2000). Many of these pumps exhibit effective fluid transport for particular conditions, but are limited to fluids with specific chemical properties, finite volumes of fluid or small flow rate ranges (Laser and Santiago 2004; Woias 2005). The development of a versatile micropump that can be effective over a wide range of pumped volumes, flow rates, and fluid properties in the range of Reynolds number  $<100$  is desirable but has not yet emerged.

One approach to exploring improved pump performance across the transition from inertial to viscous dominated regimes is to observe how animals at this intermediate scale cope with similar requirements. Animals frequently use oscillating appendages for propulsion or pumping across the entire range of Reynolds number, from inertialess creeping flow ( $Re \ll 1$ ) to inviscid potential flow

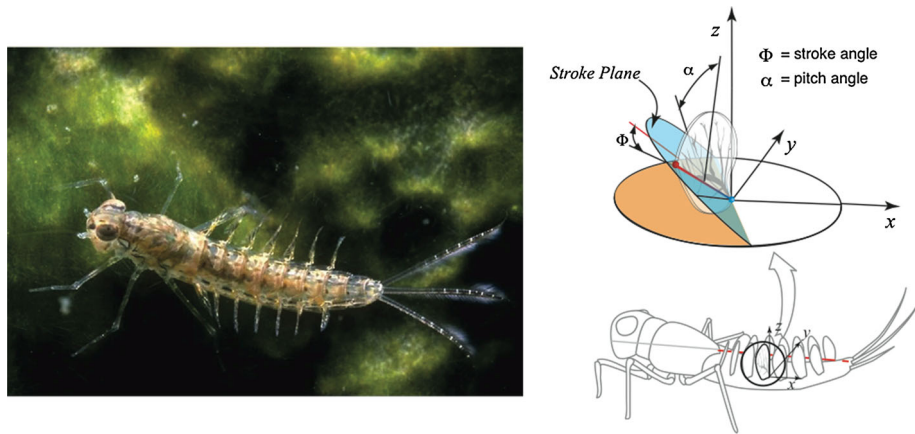
( $Re \gg 1$ ) (Childress 1981). Distinct patterns of appendicular motion have been observed on either side of this intermediate transition region, dividing stroke kinematics into two main categories: flapping and rowing. Flapping is generally defined as a motion where the net thrust is perpendicular to the stroke plane and is predominantly exhibited at higher Reynolds number ( $Re > 100$ ). In contrast, rowing is categorized as a drag-based mechanism with the net thrust being parallel to the stroke plane, and is found to be prevalent at low Reynolds numbers (Walker 2002). Rowing necessitates use of asymmetry in the motion or geometry of the appendage, generally with distinct power and recovery strokes, while flapping can frequently allow for symmetric motions and still generate a net thrust.

While the simplest geometry calls for a single pair of oscillating appendages, many animals (such as ciliated organisms, crustacea and arthropods) use appendage arrays. This introduces limb spacing and the relative phase difference between adjacent appendages as additional parameters for the design. For low Reynolds numbers, cilia frequently beat out of phase when positioned in large groups as a result of hydrodynamic coupling of independent adjacent oscillators (Gueron et al. 1997). A phase lag between adjacent cilia creates a motion referred to as a metachronal wave, and is one means to introduce a non-time-reversible parameter that is necessary to generate flow under creeping flow conditions (Childress 1981). Two-dimensional simulations of discrete cilia confined within a channel have been conducted to study the effect of the metachronal phasing and appendage spacing under creeping flow conditions for both symmetric (Khaderi et al. 2012) and asymmetric (Khaderi et al. 2011) stroke motions. The results of the work show clearly that a net pumping can be induced approximately perpendicular to the appendages by purely symmetric individual motions when used in conjunction with a metachronal wave (thus breaking the symmetry), which for the particular conditions studied yielded an optimal flow rate for  $\lambda/L = 4$ . Allowing for asymmetric stroke motions provided an increase in the net flowrate over equivalent symmetric conditions. It also showed at closer appendage spacings a favorable bias of antiplectic metachrony, where the wave propagates in the opposite direction of the effective stroke, over symplectic metachrony, where the wave propagates in the same direction as the effective stroke. A computational study by Hussong et al. (2011) developed a continuum porous media model for symmetric beating cilia actuated in a metachronal manner, extending the previous works to observe the influence of inertia. The results show that this motion is an effective transport method for flow in a channel well into the inertially dominated regime, also demonstrating increasing flow for decreased metachronal wavelengths. At a

much higher Reynolds number ( $Re \sim 800$ ), a study on the locomotion of krill compared how using synchronized or metachronal pleopod motion affected the efficiency of propulsion. It was found that the metachronal wave is the most efficient and also produces the highest body velocities for the krill (Alben et al. 2010). The metachronal wave is exhibited on animals that function both in low and high Reynolds number ranges and may be an important contributor to effective pumping in both cases.

The current study focuses on a specific animal (the mayfly nymph *Centroptilum triangulifer*) that functions across the intermediate range of Reynolds numbers, transitioning from a viscous to an inertial dominated regime. This animal uses seven pairs of external gill plates (see Fig. 1) to pump water around its body in order to maintain an acceptable oxygen concentration necessary for respiration. This particular animal is interesting because previous studies on live mayflies have shown that they exhibit a distinct shift in their appendage kinematics at a Reynolds number ( $Re_f = L_g^2 f / \nu$ , where  $L_g$  is the root to tip gill length,  $f$  is the frequency of oscillation and  $\nu$  is the kinematic viscosity) of order 10 (Sensenig et al. 2009). Although the flow generated by the animal has been documented in prior studies, the limited range of behavior of the animal prevented a detailed understanding of why and how such a pumping mechanism might be optimized. One specific question concerning the kinematics of the array is what is the optimal phase delay of the adjacent gills for a given set of stroke kinematics? In the mayfly *C. triangulifer*, a phase delay of  $\Delta\phi = 60^\circ\text{--}90^\circ$  was observed throughout its life cycle, which corresponds to cycle wavelength to plate length of  $\lambda/L_g = 2.3$ . A similar phase shift has been noted in other animals using arrays of appendages operating in a similar Re range, such as copepods ( $\Delta\phi = 64^\circ$ ,  $\lambda/L_g = 3$ , Van Duren and Videler 2003), remipedes ( $\Delta\phi = 30^\circ$ ,  $\lambda/L_g = 3.9$ , Kohlhage and Yager 1994) and ctenophores ( $\Delta\phi = 40^\circ$ ,  $\lambda/L_g = 4.5$ , Barlow et al. 1993), but no detailed explanation has been given for why this particular phasing may represent a favorable range of operation at these transitional conditions. The previous detailed studies on cilia array provide some guidance, but it is not immediately clear that their two-dimensional results can be generalized to three-dimensional conditions. Moreover, we wish to ask a slightly different question than what has been addressed in previous work: does this phase difference somehow represent an optimal efficiency point in terms of the cost of pumping fluid? In order to determine the influence of individual kinematic and geometric characteristics of a cost-based pumping efficiency, further experiments that allow for isolated variation of different properties are necessary. The current study focuses on the effects of the phase delay in between the gills.

**Fig. 1** Mayfly (Ephemeroptera) *Centroptilum triangulifer* (left, photo courtesy of David Funk), as well as kinematic angle and coordinate system definitions for stroke motion (right, after Sensenig et al. 2009)



## 2 Experimental design and setup

In order to perform proposed studies, it was first necessary to develop a device that could both replicate the nominal kinematics of typical mayfly gills as well as extend the range beyond what was exhibited in nature. The array of gills used for this experiment was designed using a simplified geometry compared to the live mayfly, which was controlled using programmed micro-servomotors. The kinematics and physical design of the gill plate array was taken from Sensenig et al. (2009). Kinematic definitions from this previous study can be seen in Fig. 1.

For simplicity, only the most significant kinematic parameters were considered. Examining the stroke, pitch and stroke plane deviation angles revealed that the stroke range was a dominant kinematic parameter throughout the mayfly's life cycle (Sensenig et al. 2009). For the lower Reynolds number conditions, the pitch range appears to have comparable significance to that of the stroke angle range, while for the higher Reynolds number case, the pitch variation is comparably small. The stroke plane deviation is the least significant factor in both cases. By retaining stroke and pitch functionality, the device has the ability to replicate simplified kinematics for both the high Reynolds number case and the low Reynolds number case.

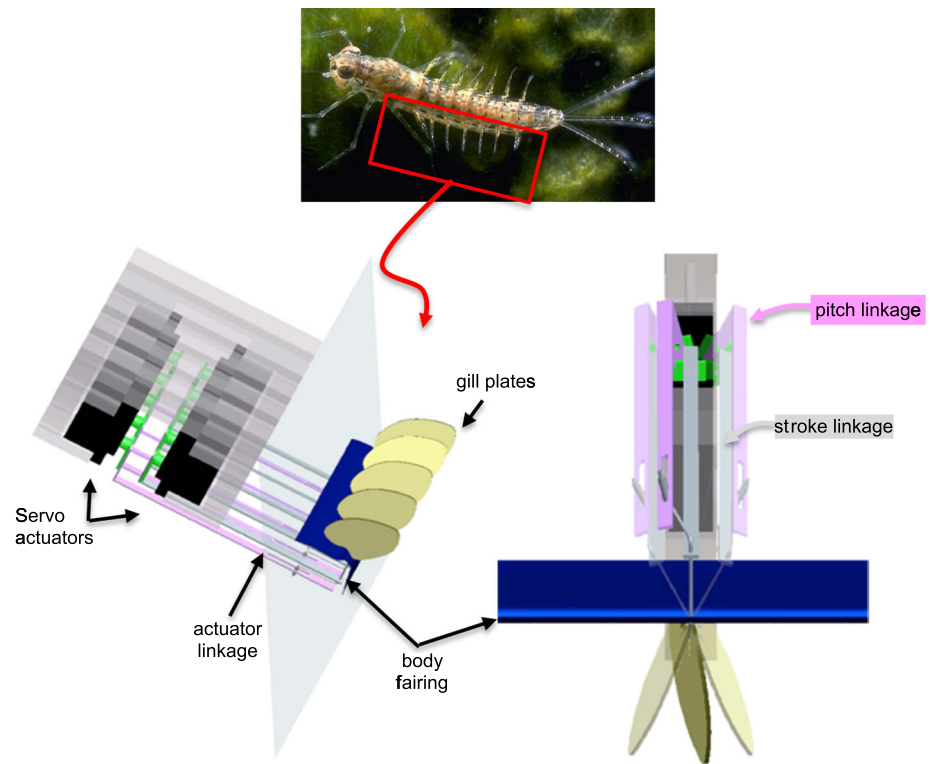
To simplify the construction, identical gill planform shape and kinematics were used for all gills. These were based on the kinematics of gill 4 examined by Sensenig et al. (2009), as this was located in the mid-point of the array. Although the living animal consistently used an intragill phase delay of  $\Delta\phi = 60^\circ\text{--}90^\circ$ , the current study focuses on effect of varying the phase delays between the gills, which imposes limitations on the kinematics. It was necessary to reduce the range of the stroke and the pitch to 64 % of their original values to prevent collision between adjacent gills and control linkages for the conditions of  $\Delta\Phi = 180^\circ$  (asynchronous motion).

The robotic gill array achieves the desired kinematics using two micro-servomotors, crank arms and sliding linkages to control each gill (see Fig. 2). A brief description of the design is given below, and further details can be found in Larson (2011). The linkage is designed such that correlated motion of both servos changes the stroke of the gill, while a differential movement provides the pitch variation. To control the stroke of the gills, the servomotors are arranged such that the motor rotation axis is perpendicular to the stroke plane of the gill. A steel extension arm is attached to each servomotor and connected to a thin metal push-rod that is embedded in the gill, passes through the stroke extension arm, and terminates after an *s*-bend within a slot of the pitch extension arm. When the servo arm moves, the extension arm rotates, which then moves the gill push-rod the same angular displacement as the servo arm. The pitch is controlled by varying the difference in the angle between the two servo arms. When the two servos move together so that the extension arms connected to them stay parallel, the pitch remains fixed at  $\alpha = 90^\circ$ . When there is a differential movement of the two arms, the metal rod in the gill is forced to rotate to compensate for the difference, which causes the pitch of the gill to change. Therefore the angles of the servo arms used to control the pitch are calculated relative to the positions of the stroke servo.

An important aspect of the pumping done by mayfly gills is the effect of combining the gills into an array. For this reason, five gills were used for the experiment to provide three "internal" gills free of end effects. On a live mayfly, there is some slight variation for the distance between the roots of the gills, but for this simplified model the gills are equally spaced with a root separation to gill length ratio of 0.6. The gill plates for the robot were fabricated out of transparent, UV cured acrylic (Loctite 3525).

The flow generated by the live mayfly nymph is bilaterally symmetric, so it was only necessary to construct a single side of the mayfly. The gill plate array (length from

**Fig. 2** Mayfly (Ephemeroptera) *Centroptilum triangulifer* (top, photo courtesy of David Funk), programmable oscillating plate array (left), and details of linkage assembly at three different positions in the stroke cycle (right). The programmable array mimics the mayfly geometry, but can be programmed with arbitrary kinematics for the stroke and pitch motion



gill 1 to gill 5 = 96 mm) was immersed in a small aquarium (260 × 310 × 510 mm) partially filled with mineral oil (depth of fluid = 200 mm), and oriented such that the bilateral symmetry plane of the mayfly body corresponded with the free surface of the liquid. A simplified body shell for the mayfly was constructed, which only models the abdomen of the mayfly nymph to which the gills are attached. This geometry allows for a gimbaled motion about the gill root, which provides for variation of the stroke plane inclination angle ( $\beta$ ) relative to the fixed body. In the current work, the stroke plane inclination angle was fixed at 60°.

The model was scaled using the oscillating Reynolds number  $Re_f = L_g^2 f/\nu$ . Considering the velocity ranges of the servomotors and the spacing necessary to prevent them from colliding, the robotic model dimensions are approximately 54 times those of the original mayfly ( $L_g = 40$  mm). Mineral oil with a viscosity of 175 cSt was used as the working fluid for this experiment to achieve a Reynolds of 17.4.

Three-dimensional velocity field data was obtained using stereo PIV, where two cameras (LaVision Imager Pro 4 M cameras, 2,048 × 2,048 pixels, 50 mm lens) equipped with Scheimpflug mounts were placed on the same side of the laser sheet (approximately 2 mm thick) with an enclosed angle of 66° between them. Because of the shape of the tank and the index of refraction between mineral oil and air, it was necessary to construct prisms so that the

camera lenses were normal to the windows (Prasad and Jenson 1995), giving a resulting field of view of approximately 154 × 90 mm. Data was taken at 32 planes (nineteen planes across a single gill) with a 2 mm spacing between planes, in order to obtain a three-dimensional volume of flow data around the array of gill plates. Each image was interrogated using a multipass algorithm with a final interrogation window size of 32 × 32 pixels with 0 % overlap, which gave an effective in-plane spatial resolution of approximately 2 mm. The largest uncertainty in the measurements was due to the variability in the position of individual gills at specific instances in the cycle (typically <1 mm), resulting from the tolerances in the individual linkages and the effects of friction. To minimize the impact of this, 40 images were acquired at the same phase angle (17 phase angles were acquired over a single cycle), processed individually, and then median sorted to remove outliers from the set. The  $N = 30$  vector fields which exhibit a minimum deviation from the median vector field were averaged to produce the ensemble-averaged velocity field at a given phase angle of the stroke cycle. The uncertainty of this velocity field is taken by the uncertainty of the mean of the ensemble, which was found to be less than or equal to  $\sigma_u/N^{0.5} = \pm 0.05$  pixels or  $\pm 0.18$  mm/s for all the data, where  $\sigma_u$  is the square root of the variance of the ensemble. See Larson (2011) for details of the analysis. Flux data was directly calculated from this set. For spatial velocity gradients, the three-dimensional fields were first

smoothed using an average of the neighboring cells before the derivatives were computed using a standard second-order finite difference. To check the consistency of the velocity field constructed from the minimum deviation from the median sample described above, the divergence of the three-dimensional velocity field was calculated and found to vary <10 % of the typical velocity gradient magnitudes. There were isolated locations where spurious vectors near the gill tips caused errors close to 100 %, but these were rare and constituted <0.02 % of vectors in a typical volume.

As a check on the above procedure, a direct numerical simulation for the case of  $\Delta\Phi = 90^\circ$  was conducted, using the measured kinematics reported above in Fig. 3. The Navier–Stokes equations for viscous incompressible flow are solved on a Cartesian grid using an exact projection method. Both the advective and diffusive terms are advanced explicitly using a third-order, low-storage, Runge–Kutta scheme. All spatial derivatives are discretized using second-order central differences on a staggered grid (Balaras 2004). The body and the oscillating plate array are immersed into the Cartesian grid, and boundary conditions are imposed using an immersed boundary formulation, which utilizes a moving least-squares (MLS) reconstruction procedure (Vanella and Balaras 2009). The overall numerical scheme is second-order accurate both in space and time. The rectangular computational domain has dimensions of  $6.4L_g$ ,  $10L_g$  and  $12.5L_g$ , and is discretized with  $258 \times 242 \times 194$  points in  $x, y, z$  directions

respectively (total of 12 million points). Grid stretching is applied in the  $x$  and  $z$  directions in order to cluster points in the region around the immersed bodies so that the domain density is 40 cubic cells for each gill length ( $L_g$ ) around the plate array and the body (which is approximately twice the spatial resolution of the experiments). Grid refinement tests (not shown here) showed that the above resolution was sufficient to capture the dynamics of the flow. All domain boundaries are modeled as non-slip walls to mimic experimental conditions.

A comparison of the experimental and numerical results is shown in Fig. 4. As can be observed, the typical vorticity distribution is virtually indistinguishable between the experiment and DNS (Fig. 4a, b). Quantitatively, however, there are discrepancies, most notably near the core of the vortices produced near the tips of the gills (Fig. 4c). This is a result of the slight under-resolution of the interrogation window size and the smoothing applied prior to calculating spatial velocity derivatives. Since one of the main goals of the work is to track the dissipation produced by these flow structures, Fig. 4d shows a comparison of the temporally varying dissipation integrated within a control volume bounding the gills (see Sect. 3.3 for details). By this measure, both flows track within about 10 % of each other, with the experimental value tending to be systematically larger than the DNS results. Thus although the values at the very core of a vortex are underestimated, the slight overestimate in the larger region outside the center compensates and reduces the net error.

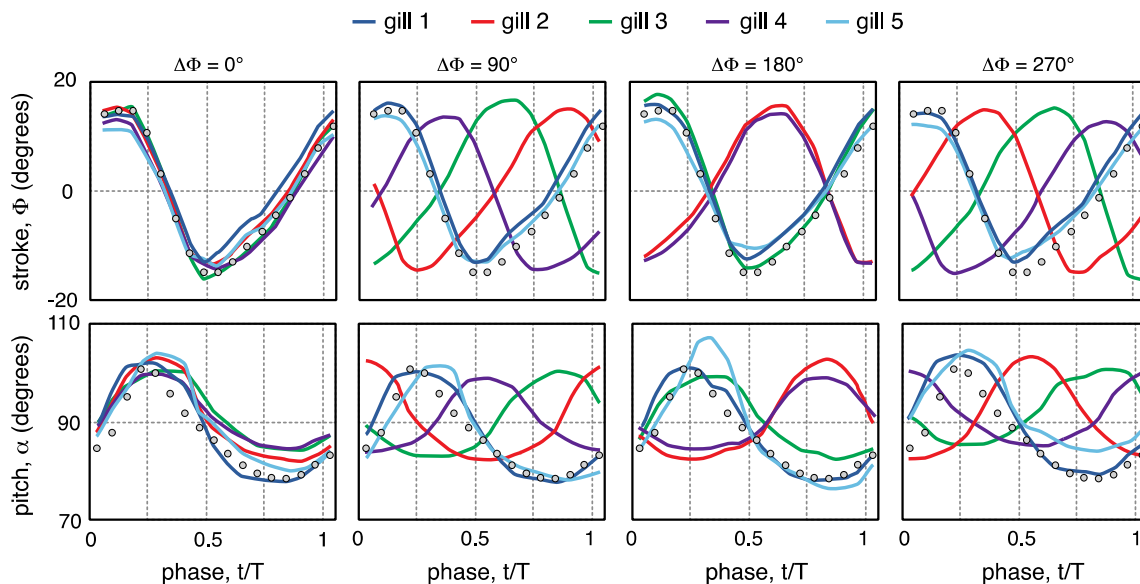


**Fig. 3** Stroke kinematics for the robotic mayfly, showing the stroke and pitch program achieved for each of the 5 gills in the array for each of the four intergill phase delays ( $\Delta\Phi$ ) tested. *Solid lines* indicate the

measured motion extracted from the stereo images during testing, while the *dotted line* indicates the intended program

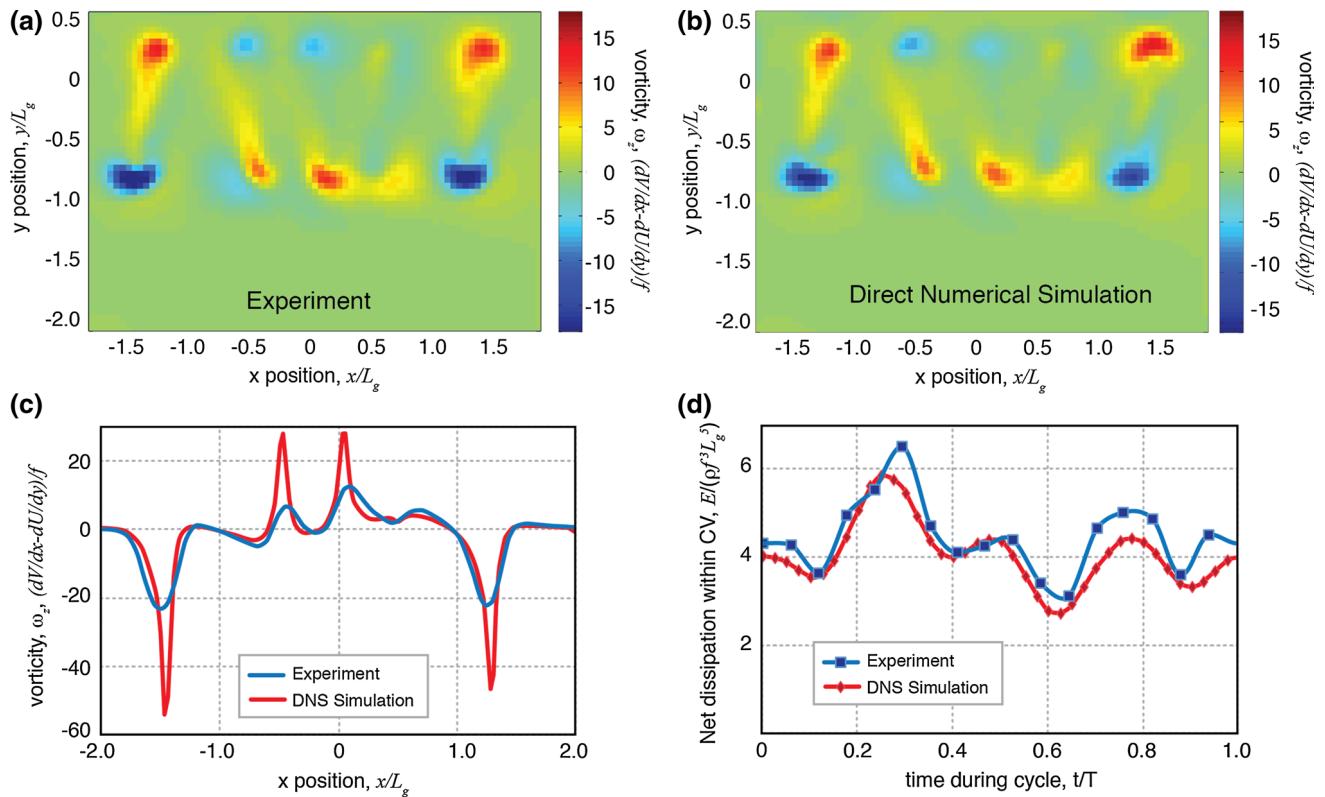


**Fig. 4** **a** Experimental measurement of vorticity, **b** DNS result for same location and time from the experiment shown in **(a)**, **c** line profile of vorticity extracted from  $y/L_g = -0.79$ , and **d** comparison of the net dissipation rate within the control volume for both the experiment and DNS

### 3 Results

The results of this experiment contain flow field data for four different test conditions. In these four tests, the amplitude of the stroke and pitch are kept consistent for each case, but different phase lags are used in between each gill. The phase lags tested are approximately  $0^\circ$ ,  $90^\circ$ ,  $180^\circ$  and  $270^\circ$ . The actual stroke and pitch of each gill plate achieved in the experiment will differ from gill to gill from the specified motion due to variations in the tolerance of the actuator construction.

The kinematics realized during the experiment were documented by tracking 38 points on each gill using the images from the PIV measurements. Even though the index of refraction of the gill material ( $n_{\text{gill}} = 1.49$ ) was similar to that of the oil used in the experiments ( $n_{\text{oil}} = 1.47$ ), the edge of the gill still scattered sufficient light to be visible in the PIV image. These points were recorded for the five gills at every phase angle and every plane where the laser sheet intersected with the gill plates. The results of this kinematic tracking for each test case (distinguished by their phase delay,  $\Delta\Phi$ ) can be seen in Fig. 3. The black circles indicate the position commands that were sent to the servomotors. The same pattern was sent for each gill, just at different times, depending on the phase delay between the gills.

#### 3.1 Phase-resolved and time-averaged velocity

The phase-resolved velocity fields within the X–Y (coronal) planes for the four different phase delays, as well as the corresponding mean flow, is shown in Fig. 5. For all cases, the flow near an individual gill is fairly similar, with negative vorticity generated at the lateral tip ( $-y$ ) furthest from the root during retraction (motion towards  $+x$ ), and a positive vortex during protraction (motion toward  $-x$ ). A weaker vortex of opposite sign is generated near the root of the gill closest to the medial plane ( $+y$ ). The primary difference of the flows then stems from the timing of the interactions of these vortices with their surrounding neighbors. For the case of synchronous gill motion ( $\Delta\Phi = 0^\circ$ ), all of the gills peak their circulation at the same point in time, leading to the formation of an array of vortices of the same sign, which may be viewed as a time-varying discretized vortex sheet extending along the  $x$ -direction. As it peaks near mid-retraction ( $t/T = 0.24$ ) the two oppositely signed sheets (positive at the gill root, negative at the gill tip) lead to a region of uniform streaming within the gill region. As the gills decelerate and reverse direction ( $t/T = 0.47$ ), the vorticity at the gill tip diffuses into the outer flow and the external flow is redirected toward the anterior direction. As protraction starts, a

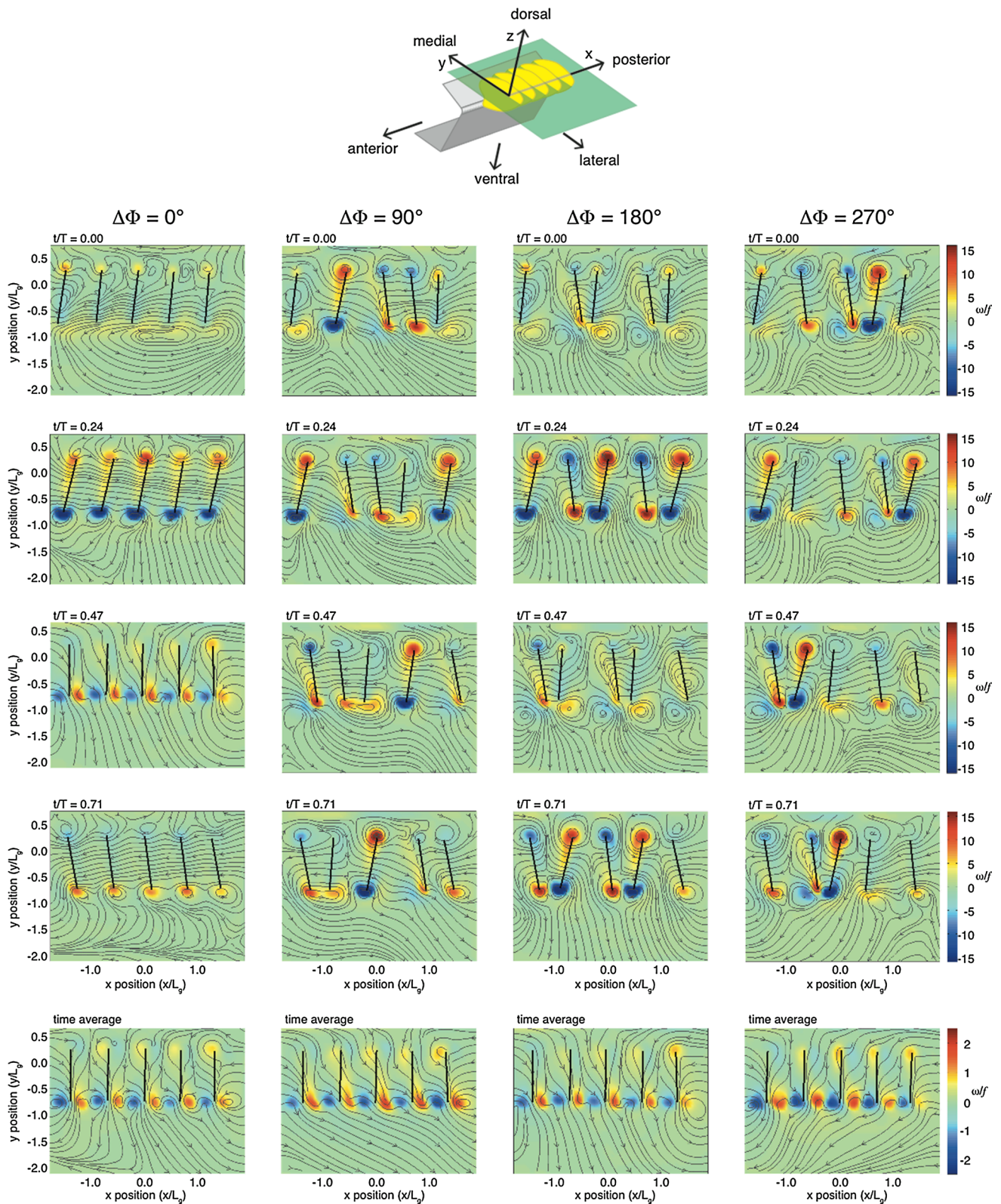


**Fig. 5** Phase-resolved and time-averaged flow through the coronal plane of the gill array. Streamlines are shown with the background colored by the non-dimensional vorticity,  $\omega_z/f$ . For the phase-resolved fields, only 4 of the 17 sampled phases are shown

similar but somewhat weaker flow is repeated in the opposite direction. The protraction is weaker due to the asymmetry in the stroke velocity (see Fig. 3).

The  $\Delta\Phi = 90^\circ$  is most similar to the actual animal conditions, and the gill motion propagates as an antiplectic metachronal wave with a wavelength of  $\lambda/L_g = 2.4$ . As noted by Sensenig et al. (2010), this phasing places the retracting plate in relative isolation of its neighbors during the retracting power stroke, creating a dominant dipole about the root and lateral tip *on the same gill*, creating an induced flow in the posterior (+ $x$ ) direction. The posteriorly directed jet follows the metachronal wave anteriorly during the cycle. During the weaker protraction, the plates are in their closest proximity and interfere with one another to prevent significant anteriorly directed backflow.

For  $\Delta\Phi = 180^\circ$ , the array operates in a nearly anti-symmetric fashion (the pitch and stroke programs are not symmetric with respect to each half-cycle, breaking the symmetry this standing wave), with plates making their closest approach to neighboring gills at the beginning and mid-point of the stroke cycle. This leads to dipole pairs on neighboring gills that produce alternating lateral and medial directed jets, with a dominant lateral ( $-y$ ) outward direction. Finally,  $\Delta\Phi = 270^\circ$  is similar to the  $\Delta\Phi = 90^\circ$  condition except that the wave exhibits a symplectic metachronism. This now places the protracting recovery stroke in isolation, producing a weaker anterior ( $-x$ ) directed jet that travels in the posterior direction. The stronger retraction power stroke occurs in close proximity to its neighboring gills, preventing effectively directed pumping.

The time-average of the 17 different equally spaced samples in the cycle gives a representation of the net flow through the gill array. In general the flow is seen to enter the array from the medial plane as well as the anterior ( $x < 0$ ) and posterior ( $x > 0$ ) regions to the left and right of the array. The outflow is generally directed laterally away from the array (transverse to the attachment line of the gills along  $y = 0$ ), but is biased towards anterior or posterior direction depending on the antiplectic (posterior flow bias) or symplectic (anterior flow bias) metachronal kinematics. This is qualitatively in agreement with the findings of Khaderi et al. (2012), who found that the net flow induced within their channel was in opposition to the metachronal wave direction. They argued this resulted from an effective mean pressure gradient that was created by a spatial asymmetry between the peak compression (high pressure) and expansion (low pressure) regions near the tip of the appendages. While there are undoubtedly similar high and low pressure regions between the gill plates of the current system, the comparison can only be speculative due to the absence of an enclosing channel and the higher Reynolds number of the current system. Finally, it is observed that

while the symmetric and antisymmetric cases should, in principle, produce a symmetric flow, there is a slight posterior-directed bias to the outflow due to the fact that the specified kinematics of the plates are not themselves symmetric.

### 3.2 Flux

In order to properly measure the effective efficiency of the system, one needs to first consider what is being optimized. For living systems such as a mayfly, the oscillating appendages are presumably used to pump fresh oxygenated water close to the skin to enhance the uptake of oxygen into the animal (Bäumer et al. 2000). In this sense, the animal would seem to benefit most by maximizing the uptake of oxygen with a minimal expenditure of energy. To calculate this, one would need to measure (1) the scalar absorption rate of oxygen onto the surface of the gill plates and the body of the animal, and (2) the amount work done by the plates on the working fluid.

The first of these points would require tracking a scalar with suitable boundary conditions on the plates and the far field. Such an experiment is beyond the scope of the current work. Instead, we assume the absorption rate would be tied to the local volume flux of fluid through a control volume surrounding the extents of the plate array. Figure 6 shows three of the six surfaces of the bounding control volume used for this calculation, which shows similar trends to the horizontal slices depicted in Fig. 5. Specifically for all cases, inflow is largely from the dorsal direction and close to the body from the anterior and posterior direction. The outflow is directed laterally and dorsally, but is biased toward the posterior for the antiplectic wave and biased anteriorly for the symplectic wave. The symmetric and antisymmetric cases are slightly biased toward the anterior direction.

The net flux through the array was then calculated by multiplying the time-averaged out-of-plane velocity components on each surface by the area surrounding each vector, then summing separately all of the flow entering into the Control Volume (CV, defined as a subset of the PIV interrogation domain, given by  $-1.8 < x/L_g < +1.9$ ,  $-1.5 < y/L_g < 0.6$  and  $-0.3 < z/L_g < +1.2$ ) and all of the flow moving out of the CV. In the equation below,  $Q_{in,k}$  represents the volumetric flowrate going into one side of the control volume with a unit normal vector in the  $k$  direction:

$$Q_{in,k} = \iint \bar{U}_{k_{in}} dx_i dx_j \cong \sum_{l_{in}=1}^{N_{in}} \bar{U}_{k_{in,l}} \delta x_i \delta x_j \quad (1)$$

where  $i$ ,  $j$  and  $k$  represent the directions relevant to the surface on the volume being analyzed, and  $l$  represents the

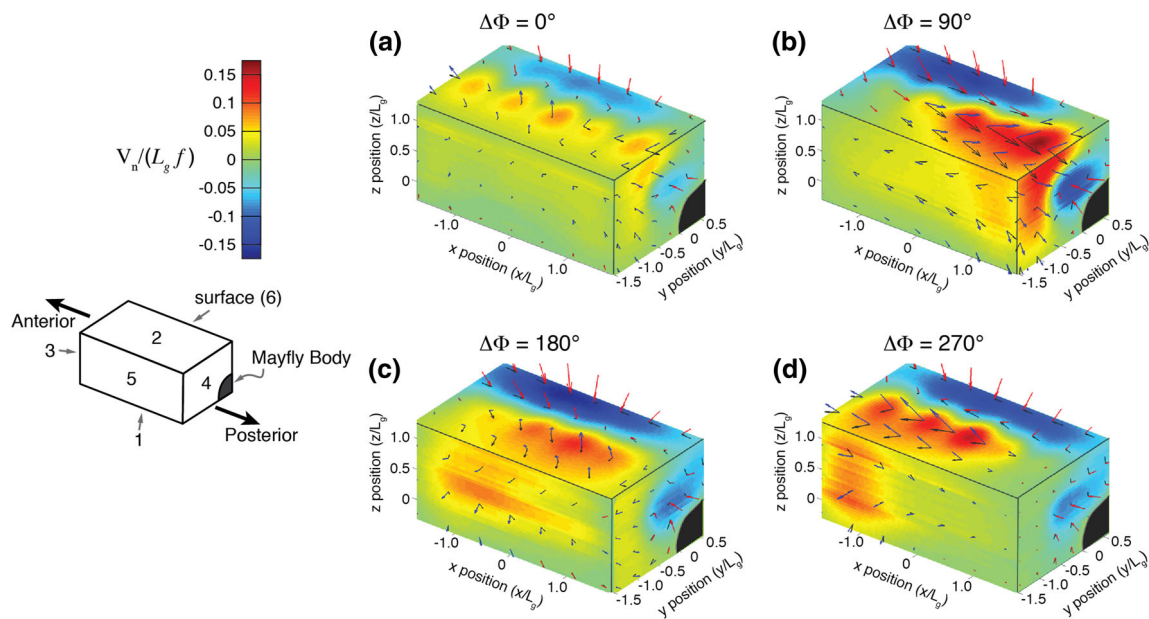


**Fig. 6** Time-averaged volume flux across a control volume bounding the gill array (red = outflow, blue = inflow). Select three-component velocity vectors are shown on the surface, along with their projection

onto the surface to convey the net three-dimensional flow. The velocity magnitude is made non-dimensional by  $v/fL_g$ . **a**  $\Delta\Phi = 0^\circ$ , **b**  $\Delta\Phi = 90^\circ$ , **c**  $\Delta\Phi = 180^\circ$ , and **d**  $\Delta\Phi = 270^\circ$

index over all inward pointing vectors on the surface.  $i$  and  $j$  represent the components in this plane, while  $k$  represent the out-of-plane component. The total volume of fluid moving into the control volume ( $Q_{in}$ ) is then given by:

$$Q_{in} = \sum_{l=1}^{N_{sides}=6} Q_{in,l} \tag{2}$$

A similar expression is used for the fluid moving out of the control volume. The results were made non-dimensional by dividing the volumetric flowrate by  $L_g^3 f$ , where  $L_g$  is the gill length, 0.04 m, and  $f$  is the frequency, 1.85 Hz. Owing to mass conservation, the sum of the flow in and out of the CV should equal zero, which is not exactly achieved due to the accumulated error in the measurement. The total uncertainty of the measurement was propagated through the flux calculations using the standard error from the variation in the flow field calculated from the ensemble of 30 images acquired at a single phase in the cycle. This results in an uncertainty of about  $\pm 1\%$  of the average of the total flow in and out of the control volume, consistent with the observed discrepancy.

The amount of fluid that the array in each test case pumps is given by the average of the magnitudes of the total flow in and the total flow out (see Table 1). Comparing this value for the different test cases, a phase delay of  $\Delta\Phi = 90^\circ$  produced the greatest magnitude, followed closely by  $\Delta\Phi = 180^\circ$  ( $Q_{net,180} = 0.96Q_{net,90}$ ) and then  $\Delta\Phi = 270^\circ$  ( $Q_{net,270} = 0.94Q_{net,90}$ ). The synchronous case ( $\Delta\Phi = 0^\circ$ ) had a distinctly lower volume flux with  $Q_{net,0} = 0.60Q_{net,90}$ . The marked decrease for the

synchronous case is indicative of the pumping benefit provided by the relative isolation and close approach that occurs for the non-synchronous cases. In that the symplectic case is only 5 % less than the antiplectic case is somewhat surprising, as the pitch program is biased to favor the antiplectic conditions, due to the fact that the individual gill kinematics were based on the live animal. To answer questions of the benefit provided by using a closely-spaced array, it would be of interest to perform future studies with a single gill.

### 3.3 Dissipation

The second parameter calculated is the amount of dissipation in a fluid system, which is the amount of energy lost due to irreversible viscous shear work done on the fluid. This is calculated by:

$$\begin{aligned} \varepsilon = \mu & \left[ 2 \left( \frac{\partial U}{\partial x} \right)^2 + 2 \left( \frac{\partial V}{\partial y} \right)^2 + 2 \left( \frac{\partial W}{\partial z} \right)^2 + \left( \frac{\partial V}{\partial x} + \frac{\partial U}{\partial y} \right)^2 \right. \\ & \left. + \left( \frac{\partial W}{\partial y} + \frac{\partial V}{\partial z} \right)^2 + \left( \frac{\partial U}{\partial z} + \frac{\partial W}{\partial x} \right)^2 \right] \end{aligned}$$

Due to the relatively small inertia of the fluid in these flows, the energy imparted to the fluid by the gill plate motion is dissipated within a short distance of the gill surface. In a companion study to the work of Sensenig et al. (2010), direct numerical simulations of a mayfly gill array confirm that the average work done by the mayfly gills over a cycle is within 2 % of the total dissipation of energy over

**Table 1** The non-dimensionalized volumetric flow rate going in and out for six sides of a control volume for the four different test cases

Phase lag ( $\Delta\Phi$ )	0°		90°		180°		270°	
	In	Out	In	Out	In	Out	In	Out
Surface 1	-0.0926	0.0331	-0.0993	0.0426	-0.0377	0.0915	-0.0988	0.0546
Surface 2	-0.1330	0.1640	-0.2550	0.2770	-0.2900	0.2350	-0.2500	0.2440
Surface 3	-0.0781	0.0503	-0.1580	0.0000	-0.1510	0.0087	-0.1180	0.0648
Surface 4	-0.0364	0.0410	-0.0757	0.1090	-0.0850	0.0279	-0.0935	0.0000
Surface 5	-0.0094	0.0713	-0.0006	0.1780	-0.0046	0.2130	-0.0023	0.1970
Surface 6	-0.0130	0.0086	-0.0146	0.0026	-0.0227	0.0035	-0.0135	0.0052
Total	-0.362	0.368	-0.604	0.609	-0.591	0.580	-0.576	0.565
Avg. magnitude of flow In and Out, $Q_{net}$	0.365		0.606		0.585		0.570	

These were non-dimensionalized by dividing by  $f \cdot L_g$ , where  $f$  is the frequency of the cycle, 1.85 Hz, and  $L_g$  is the length of the gill 0.04 m

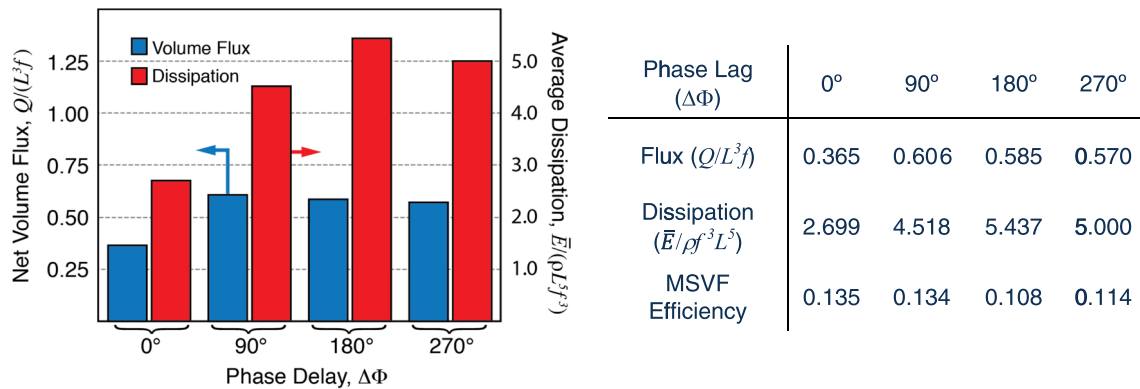


**Fig. 7** Non-dimensional average dissipation and net pumped flux through the control volume

a complete cycle in a volume within 1 gill length of the array boundary. Using this information, it is possible to compare the average amount of work done by the gill arrays for each test case using the time-average dissipation within the control volume as an equivalent surrogate for the work performed by the gills.

The average rate of power dissipated within the control volume is calculated as:

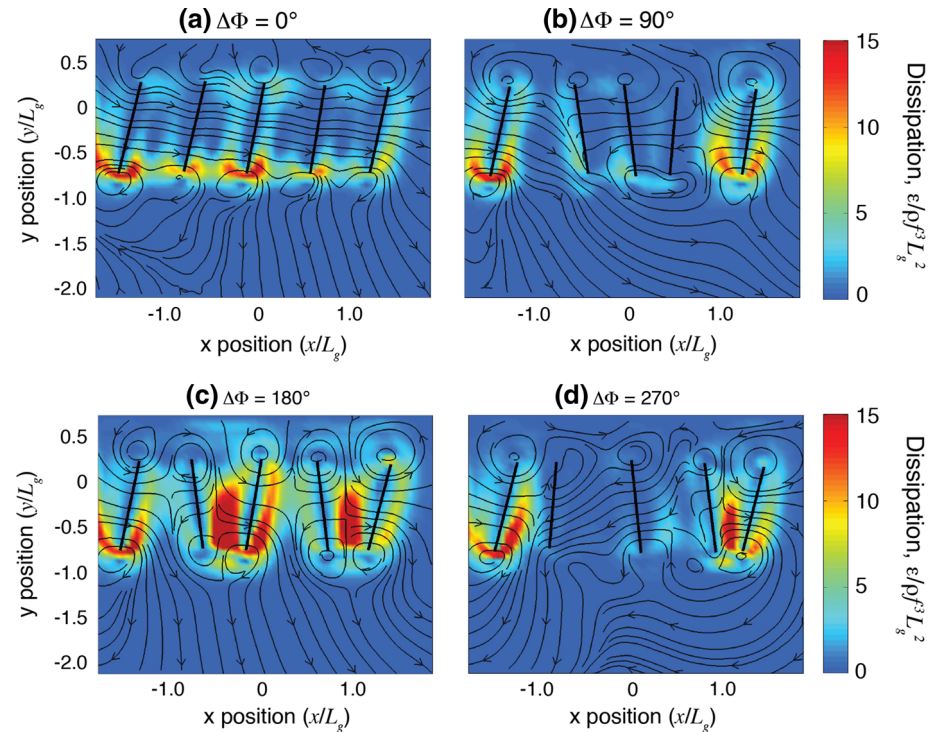
$$\bar{E} = \frac{1}{T} \int_0^T \int_{z_1}^{z_2} \int_{y_1}^{y_2} \int_{x_1}^{x_2} \varepsilon(x, y, z, t) dx dy dz dt$$

where the subscripts 1 and 2 indicates the boundaries of the control volume used in the previous flux calculation. The resulting average dissipation were non-dimensionalized by  $\rho f^3 L_g^5$ , where  $\rho$  is the density,  $f$  is the frequency of the cycle, and  $L_g$  is the gill length. These results are listed in Fig. 7. Comparing the time averages of the dissipation shows that the gills in the  $\Delta\Phi = 0^\circ$  case did the least amount of work. The  $\Delta\Phi = 180^\circ$  degree test case required the most work followed by the  $\Delta\Phi = 270^\circ$  and  $90^\circ$  test case, respectively.

To understand why the average dissipation exhibited the above trend, it is instructive to observe the peak phase-resolved dissipation for the each case, as shown in Fig. 8. The peak dissipation is formed when each gill is performing its power stroke, and the maximum value is largest when the gill performing its power stroke is relatively close to adjacent gills. Observing the results of the  $180^\circ$  degree test case, which generated the most dissipation, the gills beginning their power strokes are relatively close to an adjacent gill beginning to move in the opposite direction. When they end their power strokes, they are moving towards a gill once again moving in the opposite direction. These high velocities in opposite directions at close proximity to each other cause high gradients, resulting in the largest amounts of dissipation.

A similar observation can be made when comparing the dissipation generated by the  $\Delta\Phi = 90^\circ$  and  $270^\circ$  phase delay cases. For the  $90^\circ$  case, the antiplectic wave allows the retracting gill to be relatively far away from adjacent gills when performing its power stroke for the  $90^\circ$  case, while the symplectic wave for  $\Delta\Phi = 270^\circ$  places the plates comparatively closer during the power stroke. This causes smaller velocity gradients for the  $90^\circ$  phase lag case, which

**Fig. 8** Phase-resolved dissipation rates during power stroke for **a**  $\Delta\Phi = 0^\circ$ , **b**  $\Delta\Phi = 90^\circ$ , **c**  $\Delta\Phi = 180^\circ$  and **d**  $\Delta\Phi = 270^\circ$  at time  $t/T = 0.24$



results in lower peak and total dissipation. The test case with a phase lag of  $0^\circ$  resulted in the lowest dissipation for the same reason. The gills are always equidistance from each other and they are always moving in the same direction. This synchronized motion results in the lowest gradients, and therefore produces the least amount of dissipation.

### 3.4 Efficiency

To determine which case exhibits the best overall performance, a metric to describe the “pumping efficiency” as a Mass-Specific Volume Flux (MSVF) is introduced. The MSVF was calculated by dividing the net pumped volume flux by the average dissipation (representing the work done by the gills). Uncertainty propagation resulted in uncertainties in the MSVF of  $\pm 0.001$ . The calculated MSVF values are listed in Fig. 7. This calculation reveals that the phase lags that yield the highest efficiency are  $0^\circ$  and  $90^\circ$ . With the given uncertainty, there is no statistical difference between the efficiencies for these two phase delays. The lowest efficiency was produced by the  $\Delta\Phi = 180^\circ$ , which is about 20 % lower than the  $90^\circ$  phase delay efficiency.

Based on observation of natural pumping systems such as the mayfly, one may hypothesize that the case with a phase delay of  $90^\circ$  would function with the highest pumping efficiency. While this is true, a phase delay of  $0^\circ$  resulted in a similar pumping cost per unit of fluid moved over the array. A mayfly nymph uses its gills to circulate

water around its body in order to maintain the necessary amount of oxygen in it that allows it to breathe, and hence the absolute magnitude of the amount of pumped fluid is also relevant. Since the amount of fluid that the array pumps with a phase delay of  $0^\circ$  is 40 % lower than the amount pumped with the array that uses the  $\Delta\Phi = 90^\circ$ , the  $90^\circ$  phase delay would be more effective for this purpose. In order to determine if this is a substantial explanation, a study that specifically focuses on the scalar mass transport to the surface of the mayfly (and therefore delivers oxygen to the body) would have to be performed. Finally, one may also note that the smaller phase delays may be favored to provide a greater range of flexibility in terms of stroke amplitude. The current tests were all conducted at a common stroke amplitude that was reduced from the equivalent animal case owing to the fact that for the antisymmetric and symplectic cases, the gills would have collided. Having the flexibility to increase the stroke amplitude, and presumably the net volume flux, would be a useful advantage if additional flux were required by the animal.

## 4 Conclusions

In order to further explore the pumping mechanisms of a set of mayfly gills, a two-degree-of-freedom robotic oscillating plate array was constructed, allowing for an examination on the effect of gill phasing on the pumping performance of the array. Stereo PIV was used for four

different test cases to measure all three components of the unsteady phase averaged velocity field over a three-dimensional volume surrounding the array. Data was taken using four different phase delays: the  $\Delta\Phi = 0^\circ, 90^\circ, 180^\circ$  and  $270^\circ$ , all with the same programmed stroke and pitch amplitude. The quantitative measurements acquired for each case allowed for the net pumping rate, flow induced dissipation and a ratio of these two, representing a specific flux efficiency, to be directly computed.

A number of trends emerged when examining which phase delay resulted in the highest efficiency, highest flux and highest dissipation. Phase delays that cause the gills to move asynchronously (and therefore to generate counter-rotating vortex pairs on adjacent gill tips), were observed to generate significantly higher amounts of flux. The phase delay with the gill performing the power stroke the furthest from adjacent gills, the  $\Delta\Phi = 90^\circ$ , produced the highest amount of flux. This makes smaller phase delays, which allow higher stroke and pitch amplitudes to be reached without collision, to be advantageous for applications where high flow rates are required. Synchronized motion ( $\Delta\Phi = 0^\circ$ ) produces the least amount of dissipation, which for this low Reynolds number experiment can be equated to the amount of work done within a region near the gill array. The total amount of dissipation increases as the phase delay causes the space between adjacent gills with large velocity gradients between them to decrease.

These trends show that adjacent gills must have velocity gradients between them to achieve high flow rates, but that if the high gradients are accompanied by close proximity to adjacent gills, the amount of work required will increase, and the amount of pumping will decrease. This combination causes a decrease in efficiency. For an optimized pumping device, it would be necessary to determine the best balance for spacing and velocity pattern to achieve beneficial vortex pumping, while minimizing detrimentally high dissipation.

**Acknowledgments** This material in this article is based upon work supported by the National Science Foundation under Grants Nos. CBET1067066 and CBET0730907.

## References

- Alben S, Spears K, Garth S, Murphy D, Yen J (2010) Coordination of multiple appendages in drag-based swimming. *J R Soc Interface* 7:1545–1557
- Balaras E (2004) Modeling complex boundaries using an external force field on fixed Cartesian grids in large-eddy simulations. *Comput Fluids* 33(3):375–404. doi:10.1016/S0045-7930(03)00058-6
- Barlow D, Sleight MA, White RJ (1993) Water flows around the comb plates of the ctenophore *Pleurobrachia* plotted by computer: a model system for studying propulsion by antiplectic metachronism. *J Exp Biol* 177:113–128

- Bart SF, Tavrow LS, Mehregany M, Lang JH (1990) Microfabricated electrohydrodynamic pumps. *Sens Actuators A* 21(1):193–197
- Bäumer C, Pirow R, Paul RJ (2000) Respiratory adaptations to running-water microhabitats in mayfly larvae *Epeorus sylvicola* and *Ecdyonurus torrentis*, Ephemeroptera. *Phys Biochem Zoo* 73(1):77–85
- Bourouina T, Bosseboeuf A, Grandchamp JP (1997) Design and simulation of an electrostatic micropump for drug-delivery applications. *J Micromech Microeng* 7:186–188
- Childress S (1981) The mechanics of swimming and flying. Cambridge University Press, Cambridge, MA
- Gueron S, Levit-Gurevich K, Liron N, Blum JJ (1997) Cilia internal mechanism and metachronal coordination as the result of hydrodynamical coupling. *Proc Natl Acad Sci USA* 94(12):6001–6006
- Hussong J, Breugem WP, Westerweel J (2011) A continuum model for flow induced by metachronal coordination between beating cilia. *J Fluid Mech* 684:137–162. doi:10.1017/jfm.2011.282
- Jang JS, Lee SS (2000) Theoretical and experimental study of MHD (magnetohydrodynamic) micropump. *Sens Actuators A* 80:84–89
- Jiang L, Mikkelsen J, Koo JM, Huber D, Yao S, Zhang L, Zhou P, Maveety JG, Prasher R, Santiago JG, Kenny TW, Goodson KE (2002) Closed-loop electroosmotic microchannel cooling system for VLSI circuits. *IEEE Trans Compon Packag Technol* 25(3):347–355
- Khaderi SN, den Toonder MJM, Onck PR (2011) Microfluidic propulsion by the metachronal beating of magnetic artificial cilia: a numerical analysis. *J Fluid Mech* 688:44–65. doi:10.1017/jfm.2011.355
- Khaderi SN, den Toonder MJM, Onck PR (2012) Fluid flow due to collective non-reciprocal motion of symmetrically beating artificial cilia. *Biomicrofluidics* 6:014106. doi:10.1063/1.3676068
- Kohlhage K, Yager J (1994) An analysis of swimming in remipede crustaceans. *Philos Trans Biol Sci* 346(1316):213–221
- Larson M (2011) Effect of kinematic variation on viscous pumping by a robotic gill plate array. MS Thesis Dissertation, University of Maryland
- Laser DJ, Santiago JG (2004) A review of micropumps. *J. Micromech Microeng* 14(6):35–64
- Quin D, Grimes R (2008) The effect of reynolds number on microaxial flow fan performance. *J Fluids Eng* 130:101101. doi:10.1115/1.2953300
- Prasad AK, Jensen K (1995) Scheimpflug stereocamera for particle image velocimetry in liquid flows. *Appl Optics* 34(30):7092–7099
- Sensenig A, Shultz J, Kiger KT (2009) The rowing-to-flapping transition: ontogenetic changes in gill-plate kinematics in the nymphal mayfly *Centroptilum triangulifer* (Ephemeroptera, Baetidae). *Zool J Linn Soc* 98(3):540–555
- Sensenig A, Kiger KT, Shultz J (2010) Transitional ventilation mechanisms in nymphal mayfly *Centroptilum triangulifer*. *J Exp Biol* 213(19):3319–3331
- Thomas LJ, Bessman SP (1975) Prototype for an implantable micropump powered by piezoelectric disk benders. *Trans Am Soc Artif Organs* 21:516–520
- Van Duren LA, Videler JJ (2003) Escape from viscosity: the kinematics and hydrodynamics of copepod foraging and escape swimming. *J Exp Biol* 206:269–279
- van Lintel HTG, van de Pol FCM, Bouwstra S (1988) A piezoelectric micropump based on micromachining of silicon. *Sens Actuators* 15:153–167
- Vanella M, Balaras E (2009) A moving-least-squares reconstruction for embedded-boundary formulations. *J Comput Phys* 228(18):6617–6628. doi:10.1016/j.jcp.2009.06.003

- Vitko J, Franz DR, Alper M, Biggins PDE, Brady LD, Bruckner-Lea C, Burge HA, Ediger R, Hollis MA, Laughlin LL, Mariella RP, McFarland AR, Schaudies RP (2004) Sensor systems for biological agent attacks: protecting buildings and military bases. The National Academies Press, Washington, DC
- Walker JA (2002) Functional morphology and virtual models: physical constraints on the design of oscillating wings, fins, legs, and feet at intermediate Reynolds numbers. *J Integr Comp Biol* 42:232–242
- Wang X, Wang S, Gendhar B, Cheng C, Byun CK, Li G, Zhao M, Liu S (2009) Electroosmotic pumps for microflow analysis. *Trends Anal Chem* 28(1):64–74
- Woiass P (2005) Micropumps—past, progress and future prospects. *Sens Actuators B Chem* 105(1):28–38

## Bibliography

- [1] S. Alben and M. Shelley. Coherent locomotion as an attracting state for a free flapping body. *Proceedings of the National Academy of Sciences of the United States of America*, 102(32):11163–11166, Aug. 2005.
- [2] G. Astarita. Dimensional analysis, scaling, and orders of magnitude. *Chemical Engineering Science*, 52(24):4681–4698, Dec. 1997.
- [3] E. Babák and O. Foustka. Untersuchungen über den Auslösungsreiz der Atembewegungen bei Libellulidenlarven (und Arthropoden überhaupt). *Pflüger, Archiv für die Gesamte Physiologie des Menschen und der Thiere*, 119(9-11):530–548, Sept. 1907.
- [4] E. Balaras. Modeling complex boundaries using an external force field on fixed Cartesian grids in large-eddy simulations. *Computers & Fluids*, 33(3):375–404, Mar. 2004.
- [5] M. Baltussen, P. D. Anderson, F. Bos, and J. den Toonder. Inertial flow effects in a micro-mixer based on artificial cilia. *Lab on a chip*, 9(16):2326–31, Aug. 2009.
- [6] D. Barlow, M. A. Sleight, and R. J. White. Water flows around the comb plates of the ctenophore *Pleurobrachia* plotted by computer: a model system for studying propulsing by antiplectic metachronism. *J. Exp. Biol.*, 177(1):113–128, 1993.
- [7] M. F. Beatty. *Principles of Engineering Mechanics: Volume 1: Kinematics*. Mathematical Concepts and Methods in Science and Engineering. Springer, 1986.
- [8] N. Beratlis. *Direct Numerical Simulations of Transitional Pulsatile Flows in Stenotic Vessels*. PhD thesis, University of Maryland, College Park, 2008.
- [9] N. Beratlis, E. Balaras, and K. T. Kiger. Direct numerical simulations of transitional pulsatile flow through a constriction. *Journal of Fluid Mechanics*, 587:425–451, Aug. 2007.

- [10] N. Beratlis, K. Squires, and E. Balaras. Numerical investigation of Magnus effect on dimpled spheres. *Journal of Turbulence*, 13(July 2014):N15, Jan. 2012.
- [11] S. Childress. *Mechanics of swimming and flying*. Press Syndicate of the University of Cambridge, New York, 1st edition, 1981.
- [12] S. Childress and R. Dudley. Transition from ciliary to flapping mode in a swimming mollusc: flapping flight as a bifurcation in  $Re_\omega$ . *Journal of Fluid Mechanics*, 498:257–288, Jan. 2004.
- [13] J. den Toonder, F. Bos, D. Broer, L. Filippini, M. Gillies, J. de Goede, T. Mol, M. Reijme, W. Talen, H. Wilderbeek, V. Khatavkar, and P. D. Anderson. Artificial cilia for active micro-fluidic mixing. *Lab on a chip*, 8(4):533–41, Apr. 2008.
- [14] M. H. Dickinson. Unsteady mechanisms of force generation in aquatic and aerial locomotion. *American Zoologist*, 36(6):537–554, 1996.
- [15] L. Eastham. Currents produced by the gills of mayfly nymphs. *Nature*, page 58, 1932.
- [16] L. Eastham. Metachronal Rhythms and Gill Movements of the Nymph of *Caenis horaria* (ephemeroptera) in Relation to Water Flow Proceedings of the Royal Society of London . Series B , Containing Papers of a Biological. *Proceedings of the Royal Society of London.*, 115(791):30–48, 1934.
- [17] L. Eastham. The rhythmical movements of the gills of nymphal *leptophlebia marginata* (ephemeroptera) and the currents produced by them in water. *J. Exp. Biol.*, 13:443–449, 1936.
- [18] L. Eastham. The gill movements of nymphal *ecdyonurus venosus* (ephemeroptera) and the currents produced by them in water. *J. Exp. Biol.*, 14:219–228, 1937.
- [19] L. Eastham. Gill movements of nymphal *ephemera danica* (ephemeroptera) and the water currents caused by them. *J. Exp. Biol.*, 16:18–33, 1939.
- [20] L. Eastham. The Abdominal Musculature of Nymphal *Chloeon Dipterum* L. (Insecta: Ephemeroptera) in Relation to Gill Movement and Swimming. *Proceedings of the Zoological Society of London*, 131(2):279–291, Aug. 1958.
- [21] C. P. Ellington. The aerodynamics of hovering insect flight. I. The quasi-steady analysis. *Philosophical Transactions of the Royal Society of London. B, Biological Sciences*, 305(1122):1–15, 1984.
- [22] C. P. Ellington. The Aerodynamics of Hovering Insect Flight. II. Morphological Parameters. *Philosophical Transactions of the Royal Society B: Biological Sciences*, 305(1122):17–40, Feb. 1984.

- [23] C. P. Ellington. The Aerodynamics of Hovering Insect Flight. III. Kinematics. *Philosophical Transactions of the Royal Society B: Biological Sciences*, 305(1122):41–78, Feb. 1984.
- [24] C. P. Ellington. The Aerodynamics of Hovering Insect Flight. IV. Aerodynamic Mechanisms. *Philosophical Transactions of the Royal Society B: Biological Sciences*, 305(1122):79–113, Feb. 1984.
- [25] C. P. Ellington. The Aerodynamics of Hovering Insect Flight. V. A Vortex Theory. *Philosophical Transactions of the Royal Society B: Biological Sciences*, 305(1122):115–144, Feb. 1984.
- [26] E. Fadlun, R. Verzicco, P. Orlandi, and J. Mohd-Yusof. Combined Immersed-Boundary Finite-Difference Methods for Three-Dimensional Complex Flow Simulations. *Journal of Computational Physics*, 161(1):35–60, June 2000.
- [27] J. H. Ferziger and M. Perić. *Computational Methods for Fluid Dynamics*. Springer London, Limited, 2002.
- [28] D. T. Greenwood. *Principles of Dynamics*. Pearson College Division, 1988.
- [29] R. Grigoriev and H. G. Schuster. *Transport and Mixing in Laminar Flows: From Microfluidics to Oceanic Currents*. Annual Reviews of Nonlinear Dynamics and Complexity (VCH). Wiley, 2012.
- [30] S. Gueron and K. Levit-Gurevich. Computation of the internal forces in cilia: application to ciliary motion, the effects of viscosity, and cilia interactions. *Biophysical journal*, 74(4):1658–76, Apr. 1998.
- [31] S. Gueron and K. Levit-Gurevich. Energetic considerations of ciliary beating and the advantage of metachronal coordination. *Proceedings of the National Academy of Sciences*, 96(22):12240–12245, Oct. 1999.
- [32] S. Gueron, K. Levit-Gurevich, N. Liron, and J. J. Blum. Cilia internal mechanism and metachronal coordination as the result of hydrodynamical coupling. *Proceedings of the National Academy of Sciences of the United States of America*, 94(12):6001–6, June 1997.
- [33] J. Jeong and F. Hussain. On the identification of a vortex. *Journal of fluid mechanics*, 285:69–94, 1995.
- [34] H. Jiang. Numerical study of the feeding current around a copepod. *Journal of Plankton Research*, 21(8):1391–1421, Aug. 1999.
- [35] H. Jiang. Chemoreception and the deformation of the active space in freely swimming copepods: a numerical study. *Journal of Plankton Research*, 24(5):495–510, May 2002.

- [36] H. Jiang. Hydrodynamic interaction between two copepods: a numerical study. *Journal of Plankton Research*, 24(3):235–253, Mar. 2002.
- [37] H. Jiang. The flow field around a freely swimming copepod in steady motion. Part II: Numerical simulation. *Journal of Plankton Research*, 24(3):191–213, Mar. 2002.
- [38] S. N. Khaderi, M. H. M. Baltussen, P. D. Anderson, J. M. J. den Toonder, and P. R. Onck. Breaking of symmetry in microfluidic propulsion driven by artificial cilia. *Physical Review E*, 82(2):027302, Aug. 2010.
- [39] S. N. Khaderi, J. M. J. den Toonder, and P. R. Onck. Microfluidic propulsion by the metachronal beating of magnetic artificial cilia: a numerical analysis. *Journal of Fluid Mechanics*, 688:44–65, Oct. 2011.
- [40] K. Kohlhage and J. Yager. An Analysis of Swimming in Remipede Crustaceans. *Philosophical Transactions of the Royal Society B: Biological Sciences*, 346(1316):213–221, Oct. 1994.
- [41] P. K. Kundu and I. M. Cohen. *Fluid Mechanics*. Elsevier Science, 2001.
- [42] P. Lancaster and K. Salkauskas. Surfaces generated by moving least squares methods. *Mathematics of Computation*, 37(155):141–141, Sept. 1981.
- [43] M. Larson, K. T. Kiger, K. Abdelaziz, and E. Balaras. Effect of metachronal phasing on the pumping efficiency of oscillating plate arrays. *Experiments in Fluids*, 55(5):1741, May 2014.
- [44] M. A. Larson. *Effect of kinematic variations on viscous pumping by a robotic gill plate array*. PhD thesis, University of Maryland, College Park, 2011.
- [45] D. J. Laser and J. G. Santiago. A review of micropumps. *Journal of Micromechanics and Microengineering*, 14(6):R35–R64, June 2004.
- [46] E. Lauga. Continuous breakdown of Purcells scallop theorem with inertia. *Physics of Fluids*, 19(6):061703, 2007.
- [47] J. Lenarcic, T. Bajd, and M. M. Stanišić. *Robot Mechanisms*. Intelligent Systems, Control and Automation: Science and Engineering. Springer, 2012.
- [48] A. Lilienthal, A. Zell, M. Wandel, and U. Weimar. Sensing odour sources in indoor environments without a constant airflow by a mobile robot. In *Proceedings 2001 ICRA. IEEE International Conference on Robotics and Automation (Cat. No.01CH37164)*, volume 4, pages 4005–4010. IEEE, 2001.
- [49] G. Liu and Y. T. Gu. *An Introduction to Meshfree Methods and Their Programming*. Springer-Verlag, Berlin/Heidelberg, 2005.
- [50] B. Morton. The generation and decay of vorticity. *Geophysical & Astrophysical Fluid Dynamics*, 1984.

- [51] C. S. Peskin. Flow patterns around heart valves: A numerical method. *Journal of Computational Physics*, 10(2):252–271, Oct. 1972.
- [52] C. S. Peskin. The immersed boundary method. *Acta Numerica*, 11, July 2003.
- [53] E. M. Purcell. Life at low Reynolds number. *American Journal of Physics*, 45(1):3–11, 1977.
- [54] M. L. Roper. *Symmetry breaking and un-breaking in microhydrodynamical systems: swimming, pumping and bio-ballistics*. PhD thesis, Harvard University, 2007.
- [55] S. P. Sane. The aerodynamics of insect flight. *J. Exp. Biol.*, 206(23):4191–4208, Dec. 2003.
- [56] K. E. Sapsford, Z. Liron, Y. S. Shubin, and F. S. Ligler. Kinetics of antigen binding to arrays of antibodies in different sized spots. *Analytical chemistry*, 73(22):5518–24, Nov. 2001.
- [57] A. T. Sensenig. *Kinematics of the Mayfly Nymph Gill Array: An Intermediate Reynolds Number Ventilation Pump*. PhD thesis, University of Maryland, College Park, 2009.
- [58] A. T. Sensenig, K. T. Kiger, and J. W. Shultz. The rowing-to-flapping transition : ontogenetic changes in gill-plate kinematics in the nymphal mayfly *Centroptilum triangulifer* ( Ephemeroptera , Baetidae ). *Biological Journal of the Linnean Society*, 98:540–555, 2009.
- [59] A. T. Sensenig, K. T. Kiger, and J. W. Shultz. Hydrodynamic pumping by serial gill arrays in the mayfly nymph *Centroptilum triangulifer*. *The Journal of experimental biology*, 213(Pt 19):3319–31, Oct. 2010.
- [60] B. M. Sumer and J. Fredsø e. *Hydrodynamics Around Cylindrical Structures*. Advanced series on ocean engineering. World Scientific, 1999.
- [61] P. N. Swarztrauber. A Direct Method for the Discrete Solution of Separable Elliptic Equations. *SIAM Journal on Numerical Analysis*, 11(6):pp. 1136–1150, 1974.
- [62] P. N. Swarztrauber. FFT Algorithms for Vector Computers. *Parallel Comput.*, 1(1):45–63, Aug. 1984.
- [63] L. Tang, H. J. Kwon, and K. A. Kang. Studies on effect of sample circulation on sensing performance of protein C immunosensor. In *Proceedings of the Second Joint 24th Annual Conference and the Annual Fall Meeting of the Biomedical Engineering Society* [Engineering in Medicine and Biology, volume 3, pages 1805–1806. IEEE, 2002.

- [64] M. Uhlmann. An immersed boundary method with direct forcing for the simulation of particulate flows. *Journal of Computational Physics*, 209(2):448–476, Nov. 2005.
- [65] L. A. van Duren and J. J. Videler. Escape from viscosity: the kinematics and hydrodynamics of copepod foraging and escape swimming. *Journal of Experimental Biology*, 206(2):269–279, Jan. 2003.
- [66] N. Vandenberghe, S. Childress, and J. Zhang. On unidirectional flight of a free flapping wing. *Physics of Fluids*, 18(1):014102, 2006.
- [67] N. Vandenberghe, J. Zhang, and S. Childress. Symmetry breaking leads to forward flapping flight. *Journal of Fluid Mechanics*, 506:147–155, May 2004.
- [68] M. Vanella. *A Fluid-Structure Interaction Strategy with Application to Low Reynolds Number Flapping Flight*. PhD thesis, University of Maryland, College Park, 2010.
- [69] M. Vanella and E. Balaras. A moving-least-squares reconstruction for embedded-boundary formulations. *Journal of Computational Physics*, 228(18):6617–6628, Oct. 2009.
- [70] R. A. Vijayendran, F. S. Ligler, and D. E. Leckband. A computational reaction-diffusion model for the analysis of transport-limited kinetics. *Analytical chemistry*, 71(23):5405–12, Dec. 1999.
- [71] J. J. Vitko, D. R. Franz, M. Alper, P. D. Biggins, L. D. Brandt, C. Brucknerlea, H. A. Burge, R. Ediger, M. A. Hollis, L. L. Laughlin, R. P. J. Mariella, A. R. McFarland, and R. P. Schaudies. *Sensor Systems for Biological Agent Attacks: Protecting Buildings and Military Bases*. The National Academies Press, Washington, D.C., 2005.
- [72] J. A. Walker. Functional morphology and virtual models: physical constraints on the design of oscillating wings, fins, legs, and feet at intermediate reynolds numbers. *Integrative and comparative biology*, 42(2):232–42, Apr. 2002.
- [73] J. A. Walker and M. W. Westneat. Mechanical performance of aquatic rowing and flying. *Proceedings. Biological sciences / The Royal Society*, 267(1455):1875–81, Sept. 2000.
- [74] J. A. Walker and M. W. Westneat. Kinematics, dynamics, and energetics of rowing and flapping propulsion in fishes. *Integrative and comparative biology*, 42(5):1032–43, Nov. 2002.
- [75] Z. J. Wang. Dissecting Insect Flight. *Annual Review of Fluid Mechanics*, 37(1):183–210, Jan. 2005.
- [76] T. Weis-fogh. Quick estimates of flight fitness in hovering animals, including novel mechanisms for lift production. *J. Exp. Biol.*, 59:169–230, 1973.

- [77] F. M. White. *Viscous Fluid Flow*. McGraw-Hill, third edition, 2006.
- [78] T. A. Williams. A Model of Rowing Propulsion and the Ontogeny of Locomotion in Artemia Larvae. *Biological Bulletin*, 187(2):164, Oct. 1994.
- [79] T. A. Williams. Locomotion in developing Artemia larvae: mechanical analysis of antennal propulsors based on large-scale physical models. *The Biological Bulletin*, 187(2):156–163, 1994.
- [80] J. Yang. *An Embedded-Boundary Formulation for Large-Eddy Simulation of Turbulent Flows Interacting with Moving Boundaries*. PhD thesis, University of Maryland, College Park, 2005.
- [81] J. Yang and E. Balaras. An embedded-boundary formulation for large-eddy simulation of turbulent flows interacting with moving boundaries. *Journal of Computational Physics*, 215(1):12–40, June 2006.
- [82] J. Yang, S. Preidikman, and E. Balaras. A strongly coupled, embedded-boundary method for fluidstructure interactions of elastically mounted rigid bodies. *Journal of Fluids and Structures*, 24(2):167–182, Feb. 2008.
- [83] J. Yen and J. R. Strickler. Advertisement and concealment in the plankton: what makes a copepod hydrodynamically conspicuous? *Invertebrate Biology*, 115(3):191–205, 1996.
- [84] C. Zhou. Accessory gills in mayflies (Ephemeroptera). *Stuttgarter Beiträge zur Naturkunde A, Neue Serie*, pages 79–84, 2010.